Imaging small-scale mantle heterogeneities using seismic arrays

Hannah Louise Marie Bentham

Submitted in accordance with the requirements for the degree of
Doctor of Philosophy

The University of Leeds
School of Earth and Environment
26 September 2013

Declaration

The candidate confirms that the work submitted is his own and that appropriate credit has been given where reference has been made to the work of others.

Chapter 4 contains material from the accepted publication:

Bentham, H. L. M. and Rost, S. (2014), Scattering beneath Western Pacific subduction zones: Evidence for oceanic crust in the mid-mantle, *Geophysical Journal International*.

In this paper, Hannah Bentham carried out the data processing and analysis and wrote the paper, whilst Sebastian Rost provided some data and codes and contributed to writing.

Acknowledgements

It goes without saying that this project would not have been possible without the help and guidance from many people. Firstly, thank you to my supervisor, Sebastian Rost, who came up with the project "Where do slabs go to die?" and has guided me towards answering this question. His vast knowledge of the subject has supported me through the technical stages and his patience and persistence has helped me endlessly through my battles with the written word. I also thank Graham Stuart and Doug Angus for their advisory roles in the project; their critiques and support have been more than appreciated.

Many thanks to Mike Thorne for hosting me in Salt Lake City while undertaking the global stacking project and for providing a collection of codes that have helped me endlessly. I acquired many other codes from generous donors, but a special thank you to Peter Shearer and Fenglin Niu for their modelling and ray-tracing codes respectively.

I was very fortunate to be part of IGT, an institute that is full of great minds and data repositories, and so in no particular order, thanks to Jon Mound, Roger Clark, Dave Cornwell (DC), Dave Thompson (DT), Chris Davies and Liz Vanacore for chats, discussions and data. Furthermore, thanks to DERG members for providing feedback on my work and blowing my mind with updates on core dynamics. In addition, Richard Rigby have been marvellous in moping up my computer errors and truly deserves a medal.

Completing this thesis would not be possible without the comradery of the PhD gang; past and present. Julia, Fran and Haggis have been there from beginning to end, sharing every laugh and tear during this roller-coaster journey. Sandra and Karen, have kindly supported and helped me through some difficult situations. Office pals: Andy P, Dave C, Dave W, Grace, Muneef, Will and Yangwen, as well as old-timers Ben and Tom, have provided coping mechanisms of heated debate, ridiculousness and beer. Other shout-outs to Matty, Barbara, Emma, Luke, Becky and Jo for being part of the adventure.

A special thank you to some of my oldest friends, Mary, Nikki, Steph and Rob who have allowed me to be fickle, distant and crabby at times, and yet they are still there to keep me going. I'm looking forward to getting things back to normal.

Coming to a close, my lovely family should be acknowledged for being the best family in the world. I am spoilt with 5 siblings to keep me entertained and with loving parents and grandparents who do whatever they can to make me happy. Love you all,

Mum, Dad, Jon, Dan, Lil, Josh, Joe, Grandma, and Gramps, and of course the dogs, Patch, Harley and Islay.

My last and most important thank you is for my David: my cook, my cleaner, my chauffeur, my proof reader and most importantly, my fire-blanket. Your patience, humour and love have been essential in completing this work; without you I'm not sure I could have done it. Köszönöm szépen.

Abstract

In recent years seismology has been used extensively to detect and locate the small scale (∼10 km) structure of the Earth. In the mantle these structures likely represent chemical heterogeneity and are essential in our understanding of mechanical mixing processes within mantle convection. As subducted crust is chemically distinct from the background mantle, imaging the remains of the crust provides a tracer for convectional flow. In this study global and regional seismic heterogeneities in the mantle are found by processing teleseismic earthquake data through array seismology methods. Scattered energy from shallow earthquakes that arrives as *PP* precursors is studied in a 100 s quiet window before the main *PP*.

Global average stacks of the *PP* wavefield are formed using data recorded at a global distribution of seismic arrays, for distances 70-120°. The resultant global stacks of *PP* have revealed that precursors to *PP* exist for all distances with the amplitudes increasing with distance and time. Regional stacks for the Pacific and Atlantic Oceans are found to contain very similar patterns of *PP* precursors suggesting scattering observed here does not vary with tectonic region. Global averages of *PP* precursors are modelled using a Monte Carlo phonon method that generates statistical scattering models for random media. Modelling results show that heterogeneities in the crust and mantle contribute to scattered *PP* wavefield. The best models found have 1% scattering strength in the crust, with reduced scattering strength of 0.8% in the uppermost mantle and an increase in scattering strength to 1% at ∼700 km. Correlation length also varies from 2 km in the crust to 6 km in the mantle. The extent of the deeper mantle layer of heterogeneity is not well resolved and may be determined using larger epicentral distances.

Regional patterns of heterogeneity are found from *PP* precursors that are scattered from small-scale heterogeneities in subduction zones. Array methods are applied to data in the epicentral distance range of 90°-110° from Eielson Array in Alaska, to calculate directivity and to enhance weak arrivals. Coherent precursors are selected automatically based on a semblance weighted beampower spectrum. Assuming single *P*-to-*P* scattering and using the directivity information from array processing, the origin of scattering is found by ray-tracing through a 1D velocity model. Most scatterers are imaged in western Pacific subduction zones with evidence for ∼300 small-scale heterogeneities in the region around the present day Japan, Izu-Bonin, Mariana and West Philippine subduction zones. Most of the detected scatterers are located in the crust and upper mantle, but 6% are located deeper than 600 km. Scatterers in the transition

zone correlate well with edges of fast features in tomographic images and subducted slab contours derived from slab seismicity. Deeper scatterers are located beneath the Izu-Bonin/Mariana subduction zones, which outline a steeply dipping pseudo-planar feature to 1480 km depth, and beneath the ancient (84-144 Ma) Indonesian subduction trench down to 1880 km depth. The cause of scattering is likely the underside reflection of the subducted Moho of subducted crustal material and are related to past and present subduction providing evidence that the subducted crust does descend into the lower mantle at least for these steeply dipping subduction zones.

Combining the findings from both global and regional studies, it is likely that the heterogeneities detected in these studies are related to different stages of the mantle mixing cycle. As such a simple model for mid-mantle heterogeneity applicable to subduction zones has been suggested, with a well mixed mid-mantle of 6 km scale heterogeneities that have been thinned through mechanical stirring and a steeply dipping slab with attached crust penetrating to the lower mantle.

Contents

List of Figures

List of Tables

Chapter 1

Introduction

1.1 Overview

For more than half a century there has been significant development in the modelling of mantle convection flows from purely thermal models to the current generation of thermo-chemical convection models, providing the ideal platform for studying the mantle mixing processes. Subducted slabs are the major drivers introducing chemical heterogeneity into the upper mantle and in part into the lower mantle (Hofmann, 1997, van Keken et al., 2002, Helffrich, 2006, Rapp et al., 2008). On the other hand, isotopic heterogeneity in the mantle must have been preserved by distinct long-lived reservoirs of primitive or early recycled material that are isolated from the convection processes (Silver et al., 1988). Studying the structure and dynamics of the compositional heterogeneity represented by subducted slabs and chemical reservoirs is important for our understanding of the dynamics, structure and chemical evolution of the mantle. Seismic tomography has been very successful in imaging the large scale 3D structure of the interior of the Earth but the method cannot reveal the small-scale structure associated with mantle heterogeneity. This Chapter provides an overview of mantle structure, convection and heterogeneity revealed from multiple geoscience disciplines, and introduces the need for the seismological detection of the small-scale structure as explored in this thesis.

1.2 Mantle structure

Since the early 1900s, travel-time data of global seismic phases have been used to determine the 1D seismic velocity structure of the Earth and can be used in characterising

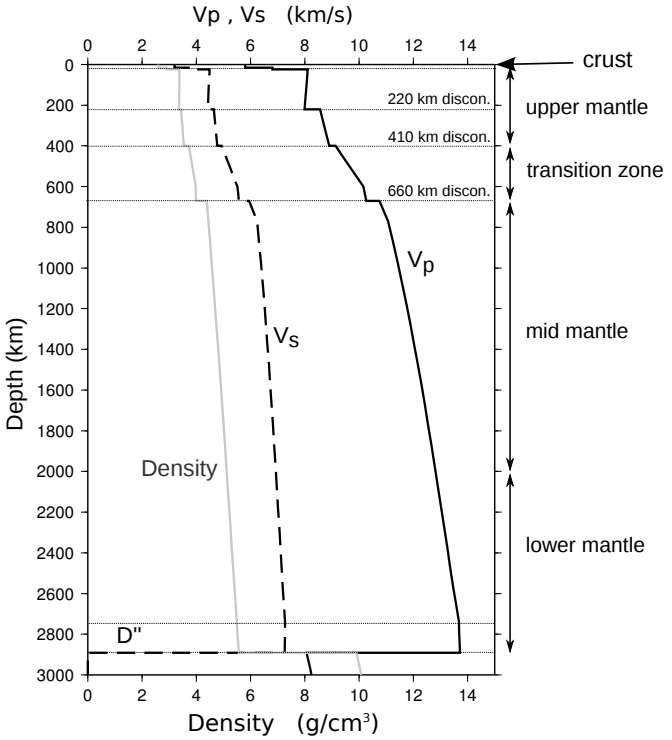

Figure 1.1: Mantle structure with P and S wave velocities and density profiles from PREM (Dziewonski and Anderson, 1981).

Earth's composition. In the 1940s Jeffrey-Bullen (JB) used seismic data for a large range of distances and recognised that the Earth is separated into spherical shells of different compositions, velocities and densities. Later studies with larger datasets and more seismic phases have derived other Earth reference models with the addition of seismic discontinuities (Figure 1.1). Models such as PREM (Dziewonski and Anderson, 1981), IASP91 (Kennett and Engdahl, 1991) and ak135 (Kennett et al., 1995) are widely used in seismology studies as the predicted traveltimes of global seismic phases closely match the observed traveltimes (Figure 1.2).

PREM, IASP91 and ak135 reference models contain many common features, in particular the gradual increase of P and S wave velocities with depth throughout the crust and mantle (e.g. PREM Figure 1.1). The models contain noticeable sharp increases in P and S wave velocities at 410 km and 660 km depth, corresponding to seismic discontinuities. These discontinuities have been explained by phase changes of olivine (Figure 1.3) as discovered through high pressure experiments (e.g. Ringwood, 1970). The sharp velocity increase at the 410 km discontinuity correspond to the phase change of olivine to wadsleyite occurring at the boundary between the upper mantle and the mantle

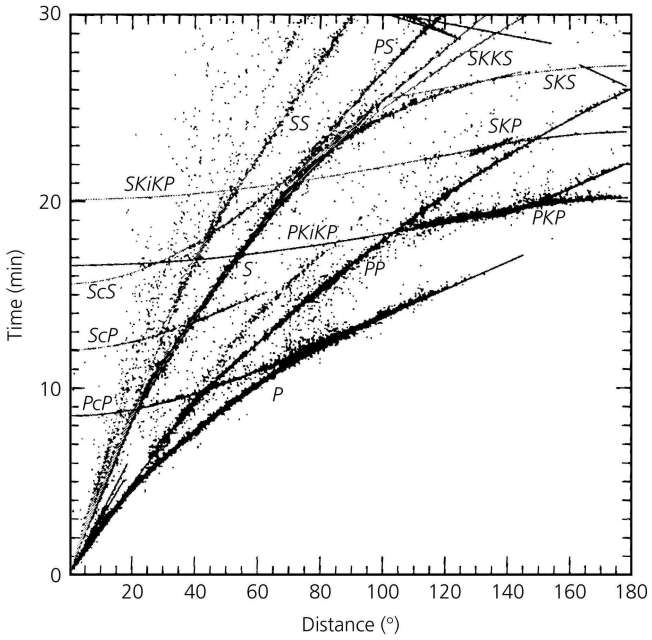

Figure 1.2: IASP91 model travel time curves and observed global travel time picks. Reproduced with permission from Kennett and Engdahl (1991), Figure 6.

transition zone. The sharp velocity increase at the 660 km discontinuity corresponds to the depth where ringwoodite undergoes a phase change to perovskite at the base of the transition zone.

In contrast to the upper mantle and transition zone, models show P and S velocities increase gradually (without sharp changes) from 660 km until a few hundred kilometres above the core mantle boundary, CMB (Figure 1.1) suggesting there are no compositional or phase changes here. Gradual increase of velocity increases until the lowermost mantle where a sharp velocity increase at 250-350 km above the CMB is observed: called the D" seismic discontinuity (Lay and Helmberger, 1983). The D" region is thought to exist due to the solid-state phase change from perovskite to post-perovskite (Murakami et al., 2004, Oganov and Ono, 2004) coinciding with the thermal boundary layer at the CMB.

These observations demonstrate that Earth reference models have been important in linking seismological observations with high pressure studies of mineral physics revealing the large scale composition of the mantle. However, there are traveltime observations that are not represented by the models (e.g. IASP91 Figure 1.2) and these anomalies are evidence that the Earth contains laterally varying structures that can be

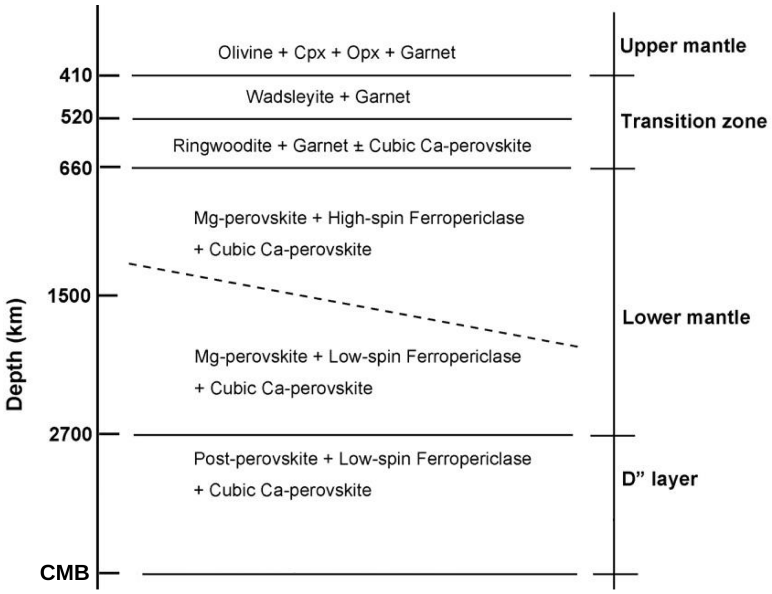

Figure 1.3: Key phase changes at various depths in the mantle. After Ono (2008).

observed seismically

Lateral velocity can be studied using tomographic inversions of traveltime and waveform data producing impressive 3D velocity images. Tomography has demonstrated that there are strong velocity variations in the crust, which probably exist due to chemical and structural heterogeneities. Whereas in the upper mantle and transition zone, linear features of fast seismic velocity are observed. These anomalies have been shown to correlate well with the locations of past and current subduction zones (van der Hilst and Seno, 1993).

Many more tomographic images have revealed linear sheets of anomalously fast velocity, which are widely interpreted as subducted slabs descending from ocean trenches into the mantle (e.g. Dziewonski and Woodhouse, 1987, Wen and Anderson, 1995, van der Hilst et al., 1997, Kárason and van der Hilst, 2001, Wortel and Spakman, 2000, Grand, 2002, Huang and Zhao, 2006, Sugioka et al., 2010, Ritsema et al., 2011). The characteristics of such fast velocity features have been found to vary with tectonic regions. A large number of studies have imaged shallow dipping linear structures that lie flat within the transition zone (e.g. Zhao, 2004, Huang and Zhao, 2006, Sugioka et al., 2010) as shown in Figure 1.4. These structures are interpreted as slabs that have been deflected at the 660 km discontinuity due to the increased density (and viscosity) of perovskite.

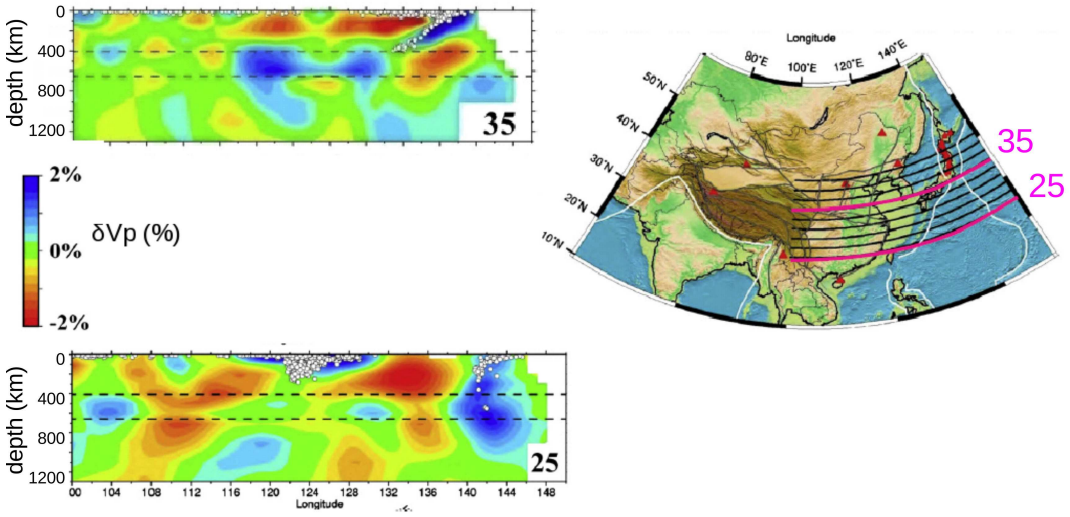

Figure 1.4: *P* wave tomography beneath SE Asia showing horizontal fast velocity feature in the transition zone (cross section at latitude 25°) and a steep linear fast velocity anomaly that is present from the surface until depths of 1000 km (cross section at latitude 35°) (Huang and Zhao, 2006). Reprinted from Zhao and Ohtani (2009). Copyright 2009, with permission from Elsevier and International Association for Gondwana Research.

Other studies have found evidence of fast velocity bodies that are not connected to any surface ocean trench and are interpreted as detached slabs (Wortel and Spakman, 2000, Widiyantoro et al., 1999). Furthermore, some studies have produced images of steeply dipping fast velocity structures that extend from ocean trenches into the lower mantle (Dziewonski and Woodhouse, 1987, Engdahl et al., 1995, Grand, 2002) and some of these extend to the CMB (Figure 1.5) (van der Hilst et al., 1997). The variety of fast velocity features show that subducted slabs can descend to different depths of the mantle. As subducted slabs are drivers of mantle convection, the variability in their dynamics show that mantle flow is complex and heterogeneities associated with subduction can be found in the mantle where slabs exist and may accumulate at boundaries that inhibit slab flow.

Tomography has also imaged significant large scale negative anomalies in the lowermost mantle (Ishii and Tromp, 1999, Trampert et al., 2004, Ritsema et al., 2004). These large low shear velocity provinces (LLSVPs) are consistent in most tomographic images beneath the Pacific and Africa and thought to be linked to plume generation. Therefore LLSVPs, as well as fast velocity features, are 3D velocity structures that are important for studying convective flow in the mantle.

With the increasing number of seismic stations installed, e.g. USArray (IRIS, 2010), compared to the sparse global station distribution, tomography will play an even more

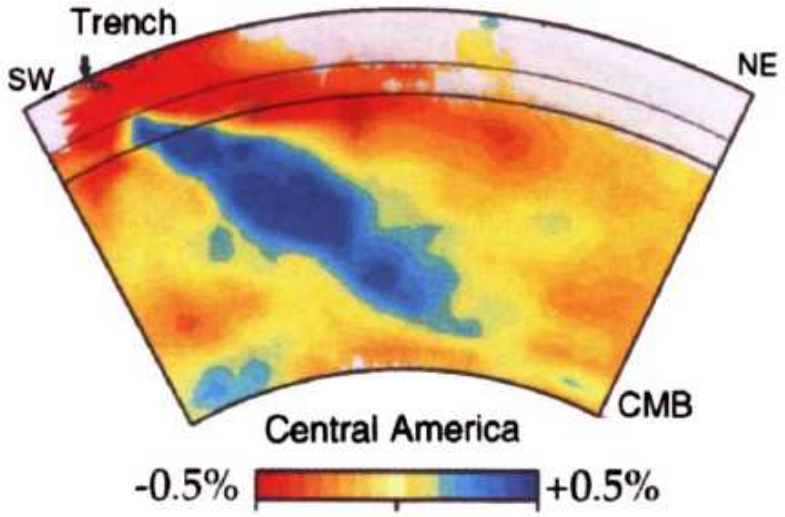

Figure 1.5: *S* wave tomography beneath Central American (van der Hilst et al., 1997) shows a broad fast velocity anomaly extending from the mantle transition zone to the lowermost mantle. Reprinted by permission from Nature Publishing Group: Nature, van der Hilst et al. (1997), copyright 1997.

important role in revealing details of lateral variations in the subsurface. Though tomography is a very powerful tool for revealing large scale (∼100 km) velocity structures, the models may be unconstrained in regions with limited source-receiver paths. In addition, limited range of ray angles can result in poor vertical resolution as well as model artifacts that are difficult to distinguish from real structure. As a result, vertical resolution and artifacts could limit the confidence in the interpretation of deep penetrating slabs, for example those in Figures 1.4 and 1.5. Furthermore, tomography cannot resolve small scale (∼10 km scale) structures that may help in resolving deep penetrating slabs and the dynamics of mantle flow.

1.3 Mantle convection

The fast velocity linear features extending into the lower mantle imaged in tomographic studies shows that material is subducted into the deep Earth and indicates that convection is not confined to the upper mantle. Numerical models can produce whole mantle convection systems that are driven by penetrative downwellings (e.g. Christensen and Yuen, 1984, Tackley et al., 1993, 1994, Simmons et al., 2006). Though the phase change at 660 km discontinuity has been suggested to inhibit slab flow, Christensen and Yuen

(1984) demonstrated that a subducted slab could penetrate the 660 km discontinuity without deflection (and possibly continue to the CMB) if the slab is highly viscous and has negative thermal buoyancy. Furthermore, studies by Tackley et al. (1993, 1994) suggest that the endothermic nature of the 660 km discontinuity will delay transport of subducting slabs but the material would ultimately descend into the lower mantle through episodic avalanches. In addition, Tackley et al. (1994) demonstrated that the exothermic phase boundary at 410 km would accelerate slabs through the transition zone causing slab avalanches to be more frequent. Simmons et al. (2006) computed multiple numerical models considering cases of whole mantle convection and cases with impenetrable flow boundaries in the lower mantle. By comparing these numerical models to velocity models from joint inversion of global seismic and geodynamical data sets, they found that the whole-mantle flow scenario fits the data best.

As whole mantle convection may tend to homogenise the mantle, the model can be in conflict with geochemical observations (Silver et al., 1988). From isotope studies exploring $^{87}Sr/^{86}Sr$ and $^{143}Nd/^{144}Nd$ ratios of mid ocean ridge basalts (MORB) and ocean island basalts (OIB), it has been suggested the upper mantle is depleted of such isotopes (e.g. Hart et al., 1973, Schilling, 1973). Noble gas helium ratios ($^{3}He/^{4}He$) (e.g. Kurz et al., 1982) and Ne concentrations (e.g. Honda et al., 1991) also differ between MORB and OIB, and indicate that OIB are derived from a more primitive source. Different source rocks for MORB and OIB therefore can be explained by several compositional layers in the mantle with a shallower depleted convecting layer potentially bounded at the 660 km discontinuity and a deeper large reservoir of preserved primitive material that is isolated from the surface (e.g. Schilling, 1973) (Figure 1.6A). However, a boundary to flow at 660 km depth is disputed by geodynamical and tomographical constraints, causing Davies and Richards (1992) to prefer whole mantle convection (Figure 1.6B).

Through developing mantle convection models, an important observation is the persistent requirement of recycled crust (Figure 1.6). Geochemical studies analysing osmium have proposed that recycled crust can be entrained into upwellings and reach the Earth's surface (e.g. Hauri and Hart, 1993). Osmium is highly incompatible and recent studies show that osmium isotope ratios in MORB and OIB are higher than osmium isotope ratios in mantle periodotite (e.g. Shirey and Walker, 1998, Day et al., 2009). These observations provide evidence that OIB contain chemical signatures of

subducted crust. If such heterogeneities related to recycled crust can be detected in subduction zones, storage reservoirs and in volcanic rocks at the surface, then recycled crust can be used as a tracer for the mixing cycle.

1.4 Models of mantle heterogeneity

As geochemical observations require the survival of primitive material and ancient recycled crust, whole mantle convection models have been adapted to allow for long-lived chemical heterogeneity. One of the earliest models with incorporated heterogeneity was presented by Davies (1984) who argued that distributed heterogeneity could be produced from chemically distinct subducted material. The heterogeneity would be small scale and could be passively convected and dispersed randomly throughout the mantle (Davies, 1984).

Since the work by Davies (1984), several studies have proposed different mechanisms of how heterogeneity may be distributed in the mantle. Becker et al. (1999) suggested that primitive material could be contained in viscous blobs that contribute up to 35-65% of the total mantle volume (Figure 1.6C). Due to mixing inefficiency, blobs that are 10 to 100 times more viscous than the background depleted MORB mantle (DMM), can remain unmixed for billions of years (Manga, 1996). However a problem with this model is that these blobs have not been detected in seismic imaging studies.

Another model considers that the subducted lithosphere could create a high $^{3}He/^{4}He$ layer in the lower mantle containing the missing heat producing elements and this material would rest on an enriched recycled crust (ERC) layer on top of the CMB (Figure 1.6D) (Coltice and Ricard, 1999). However, it is unclear as to what type of convective system would allow the recycled lithosphere and recycled crust to separate into two layers.

In contrast to the viscous blob model, primitive material could reside in a reservoir at the CMB. If the viscosity of such a reservoir is about 100 times the upper mantle viscosity the primitive source could explain the geochemistry observations while surviving in a convecting mantle (Davies and Gurnis, 1986). Two piles of hot primitive material could exist as a result of radiogenic heating (Figure 1.6E) and may correspond to the two megaplumes beneath the Pacific Ocean and Africa (Tackley, 1998). These piles are featured in many other thermal-chemical convection models (Hirose et al., 2005, McNamara and Zhong, 2005, Deschamps et al., 2011) and could correspond to LLSVPs

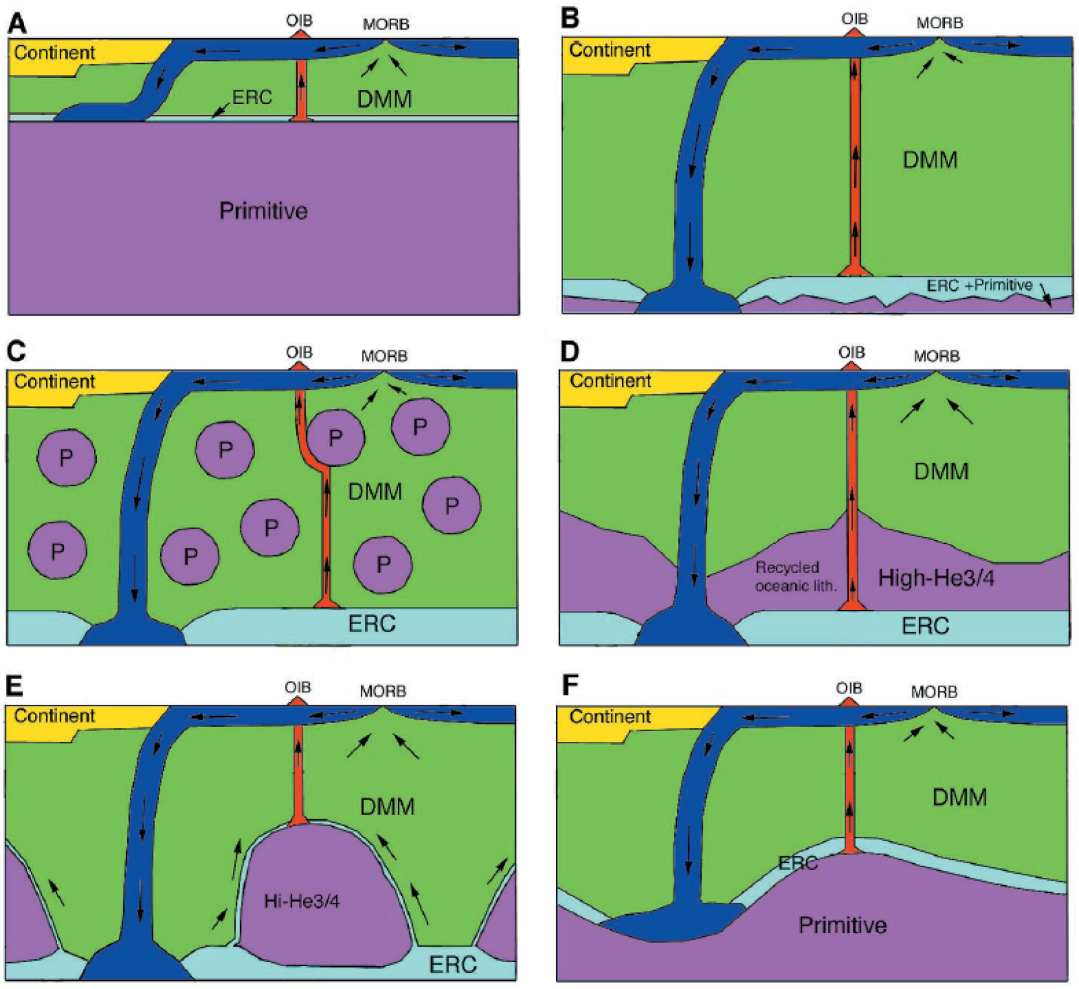

Figure 1.6: Models of the distribution of heterogeneity in the mantle and how these reservoirs of heterogeneity are related to mantle dynamics. From Tackley (2000). Reprinted with permission from AAAS. The convective features are downwelling slabs (blue) and upwelling plumes (red). Geochemical reservoirs are depleted MORB mantle, DMM (green), primitive mantle with high $^3He/^4He$ (purple) and enriched recycled crust, ERC (light blue). A) Model with two layers bounded at 660 km depth where each layer has a different reservoir signature and convection system. B) Model with a homogeneous mantle of DMM except for a mixture of ERC and primitive material at the base of the mantle. C) Model containing blobs of primitive material (Becker et al., 1999). D) Model with complete recycling of subducted crust and lithosphere (Coltice and Ricard, 1999). E) Model containing piles of primitive material (Tackley, 1998). F) Model with a deep layer of primitive material that is disconnected from the main convective system (Kellogg et al., 1999).

as observed in tomography. Furthermore, these structures would be long-lived, allowing the ancient subducted crust entrained into the upwelling plumes to provide the primitive signature of OIB that is required by geochemical observations (Figure 1.7).

Alternatively, Kellogg et al. (1999) suggested that a global primitive layer of ∼1300 km thick (and undulating by up to 1000 km) could exist and would be large enough to contain the missing heat producing elements required (Figure 1.6F). However, such a boundary layer has not been been imaged seismically (van Keken et al., 2002). The discrepancy between geochemical and seismic observations could be resolved using a time evolving convection system as observed through laboratory thermo-chemical experiments (Le Bars and Davaille, 2004) which represent the models in Figure 1.6. Nonetheless the present day snapshot of mantle convection obtained through seismology is in support of the LLSVP/primitive piles interpretation.

1.5 Survival of mantle heterogeneity

Numerical models have demonstrated that mantle convection controls the transport of heterogeneities, with subducted crust introduced into the mantle at subduction zones and entrained into plumes or passively rising to the surface at mid ocean ridges. Analysing the life cycle of heterogeneity requires knowledge as to how heterogeneity can survive in a high pressure, high temperature, chemically diverse and dynamic setting. In the mantle, heterogeneities can be destroyed through chemical diffusion and mechanical stirring, and can accumulate in chemically distinct reservoirs or piles that are resistive to mantle convection flows (Figure 1.7).

Ultimately, chemical diffusion controls the lifetime of heterogeneity and the chemical diffusion rate varies depending on composition and temperature of the material (Hofmann and Hart, 1978). For silicates, the chemical diffusion coefficient (D) varies little over the mantle: $D \approx 1 - 17 \times 10^{-15}$ cm^2 s^{-1} (Allegre and Turcotte, 1986, Stixrude and Lithgow-Bertelloni, 2012). Chemical diffusion is extremely slow and this can be demonstrated through the expression:

$$\ell = \sqrt{D\tau} \tag{1.1}$$

where ℓ is the lengthscale that diffusion can operate in time interval τ. Since the formation of Earth, ℓ would only reach 1 m when assuming D to be valid for a

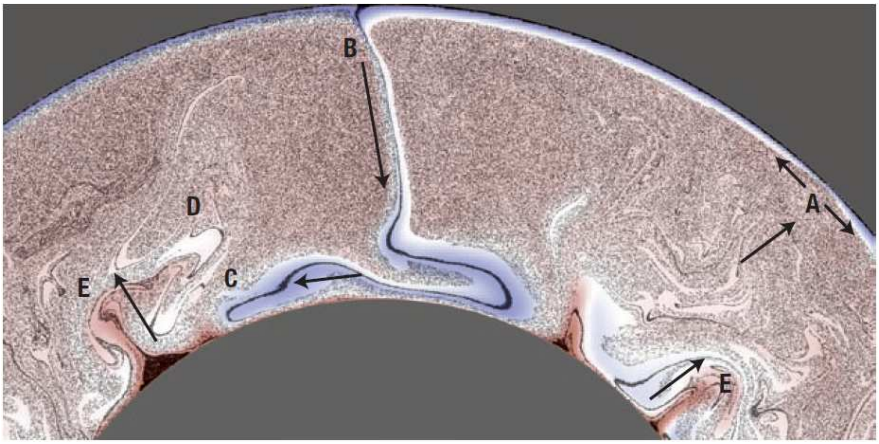

Figure 1.7: Numerical thermo-chemical modelling of mantle convection with chemically distinct oceanic crust (black lines). Basaltic crust is formed at the mid-ocean ridge (A) and is introduced into the mantle at subduction zones (B). The crust is present in the lower mantle (C) and is recycled to the rest of the mantle (D). Crust is brought up by plumes to ocean island hotspots (E) or passively at mid-ocean ridges (B - again). Image reprinted by permission from Nature Publishing Group: Nature Geoscience, Plank and van Keken (2008), copyright 2008, using models from Brandenburg and van Keken (2007).

magnesium rich silicate perovskite (Stixrude and Lithgow-Bertelloni, 2012), taking into account the increase effectiveness of chemical diffusion in the lowermost mantle due to the properties of post-perovskite (Ammann et al., 2010). In any case, chemical diffusion operates on lengthscales that are substantially smaller than the thickness of subducted crust (Stixrude and Lithgow-Bertelloni, 2012), therefore this process alone is unlikely to break down subducted MORB.

In contrast mantle stirring is more efficient at re-distributing MORB reducing the thickness of the crust exponentially to diffusion length scales (e.g. 1 m) after 1-10 Ga (Kellogg and Turcotte, 1990, Stixrude and Lithgow-Bertelloni, 2012). The normal strain rate, $\dot{\varepsilon}$, of a material can be used to find the thickness after stirring, h, from the initial thickness h_0, at a specified time, τ, through the equation from Spence et al. (1988):

$$h = h_0 \exp(\dot{\varepsilon}\tau) \tag{1.2}$$

Using $\dot{\varepsilon} = 6 \times 10^{-16} \mathrm{s}^{-1}$ as derived from mantle convection calculations Spence et al. (1988) in equation 1.2, the crustal thickness is not significantly altered until at least 10 Ma of mixing and remains on the order of kilometre scale until ∼500 Ma (Figure 1.8). Stirring remains the dominant process for the destruction of heterogeneity since heterogeneity is continuously introduced into the mantle.

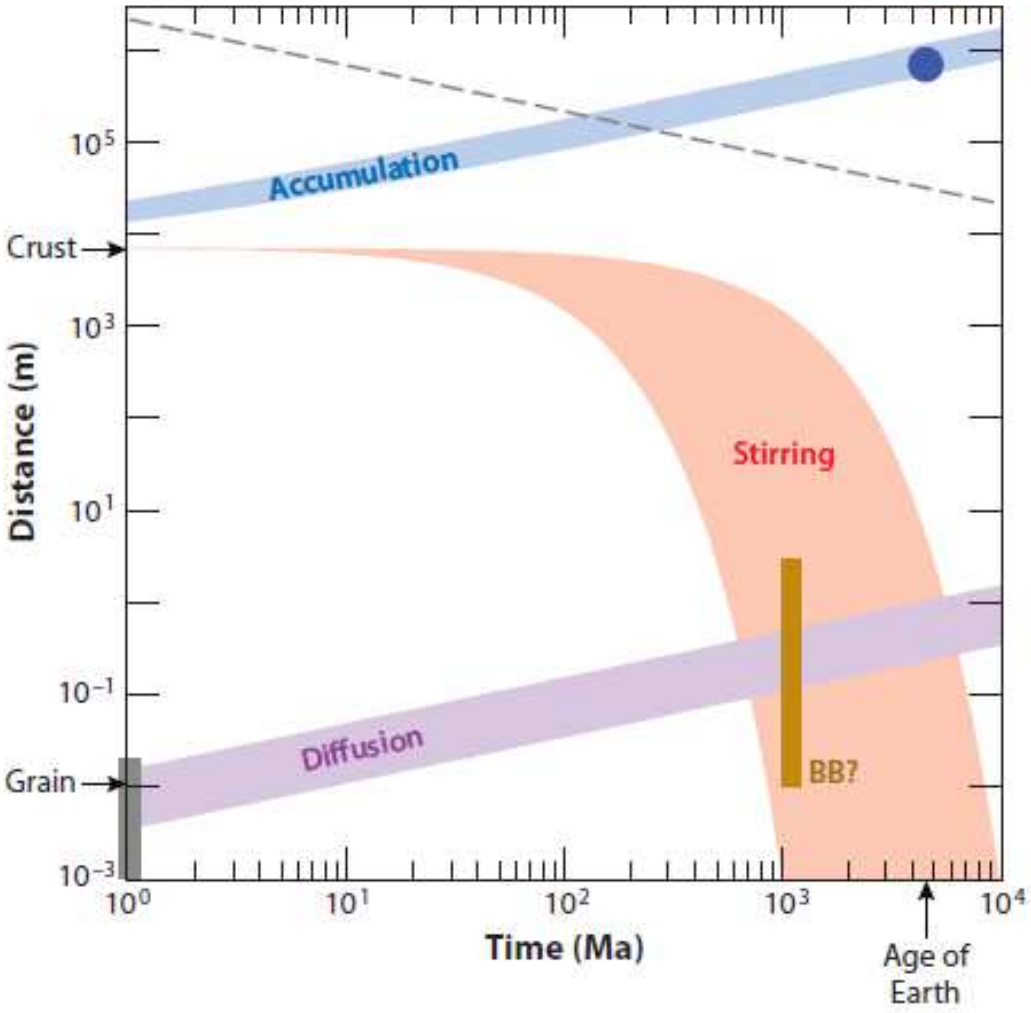

Figure 1.8: Evolution of lengthscales relevant to the survival of heterogeneity in the mantle. Mechanical stirring (orange band) starts to reduce the lengthscale of oceanic crust after 200 Ma, and continues to dominate the mixing process until 1 Ga when the crust is thinned to grain size (cm scale) and diffusion (purple band) becomes effective. Accumulation of heterogeneity (blue band) is approximated by calculating the increase in volume of a cylindrical piece of basalt at the core-mantle boundary over time. The change in radius of the basalt is found by $\sqrt{vh_ct}$ where $v \approx 1-10$ cm/yr, $h_c = 8$ km and t =4.8 Ga, assuming that the basalt separates from the harzburgite efficiently and is not entrained into mantle flow (Stixrude and Lithgow-Bertelloni, 2012). As a result, the maximum accumulation of heterogeneity over the age of Earth ranges from 620 km to 1960 km, depending on rate of accumulation. Republished with permission of Annual Reviews, from Stixrude and Lithgow-Bertelloni (2012); permission conveyed through Copyright Clearance Center, Inc.

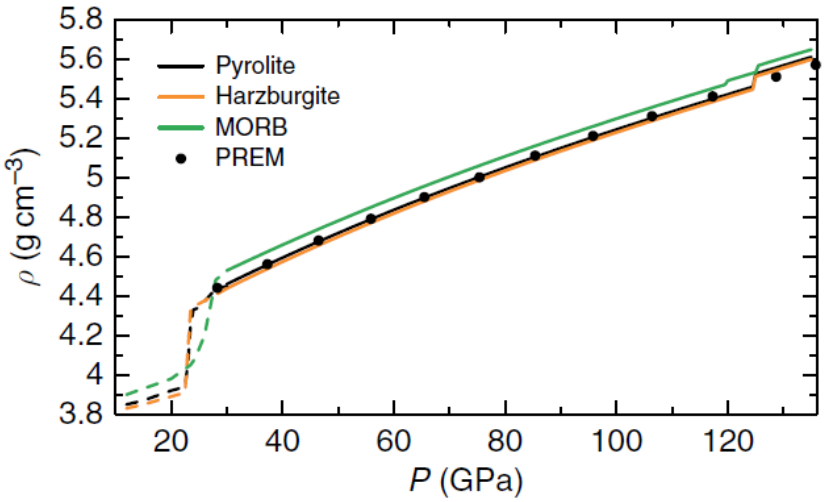

Figure 1.9: Density variations of basalt (green), harzburgite (orange) and pyrolite (black) in contrast to PREM (black dots). Reprinted from Irifune and Tsuchiya (2007), Copyright (2007)

Subducted crust is stretched into many different scalelengths after 1 Ga, ranging from centimetre to kilometre scale (Figure 1.8). The smaller scale heterogeneities may become part of a well-mixed mantle resembling the plum-pudding (Figure 1.6C) or mechanical mixture mantle models (Figure 1.7). The maximum accumulation of subducted crust may be increased up to ∼1900 km over the age of the Earth (Figure 1.8) (Stixrude and Lithgow-Bertelloni, 2012). Accumulation opposes thinning and may permit the crust to survive at kilometre scalelengths for longer than 1 Ga. For accumulation of crust to occur, the crust may need to become separated from the underlying lithosphere. Additionally, crust may only accumulate at the base of the mantle where basalt is negatively buoyant, or at the base of the transition zone where basalt is neutrally buoyant (Figure 1.9).

Crust could accumulate and remain at the CMB (Christensen and Hofmann, 1994) due to the 1% increase of the density of the crust at these depths. Thermochemical modelling has shown that accumulation of crust at the CMB could coincide with LLSVP and could be the source of recycled crust entrained into thermal upwellings (Figure 1.7) (Brandenburg and van Keken, 2007). Accumulation may require crust to be delaminated from the underlying subducted lithosphere at lower mantle depths and this could occur due to increases in mantle viscosity and aided by the soft rheology of post-perovskite (Ammann et al., 2010).

Some studies suggest that stirring alone could not delaminate the crust on such rapid

timescales in the transition zone (Jin et al., 2001, van Keken et al., 1996). However, combining stirring with the presence of a weak (van Keken et al., 1996) or serpentinite layer between crust and underlying lithosphere could result in basalt delamination within the transition zone (Lee and Chen, 2007). In addition, mixing could aid the accumulation of crust through entrainment of crust towards the shallower parts of the mantle.

The survival of heterogeneity is partially governed by viscosity of ambient mantle and reservoirs, and the time scale for mixing large scale compositional anomalies may correlate with the age of the Earth (Olson et al., 1984). The viscosity of these long-lived reservoirs in a whole mantle convective system could be 10-100 times the viscosity of the surrounding mantle (Manga, 1996) and they could exists as blobs (Becker et al., 1999) or as rounded super plumes of dense material in the lower mantle (McNamara and Zhong, 2005).

1.6 Seismic detection of heterogeneity

Heterogeneities associated with subducted crust may be seismically visible due to significant impedance contrasts between MORB and the ambient mantle. Impedance is dependent on the density structure (Figure 1.9) and velocity structure (Figure 1.10). Subducted MORB is more dense than harzburgite and pyrolite for most of the mantle, which may indicate that MORB is seismically detectable (Figure 1.9). MORB and pyrolite velocities profiles generally increase with depth but contain sharp velocity increases, particularly in the upper mantle and lowermost mantle, and these velocities influence the detection of MORB.

For the upper mantle, the velocity profile of pyrolite (or mechanically mixed) mantle has sharp increases in velocity at 410 km, 520 km and 660 km corresponding to phase transitions in the transition zone (Section 1.2). The velocity of subducted MORB also increases with depth but sharp increase are observed at 300 km depth and ∼800 km depth due to phase changes from MORB to stishovite (300 km) and MORB to perovskite and calcium-ferrite respectively (Figure 1.10). Generally, the velocities and densities of MORB and ambient mantle are different in the upper mantle and transition zone (Figure 1.9), and thus MORB may be seismically detectable at these depths. Indeed, for most of the mid and lower mantle, MORB velocity is greater than the velocity of perovskite except at the D" discontinuity where the velocity of MORB sharply

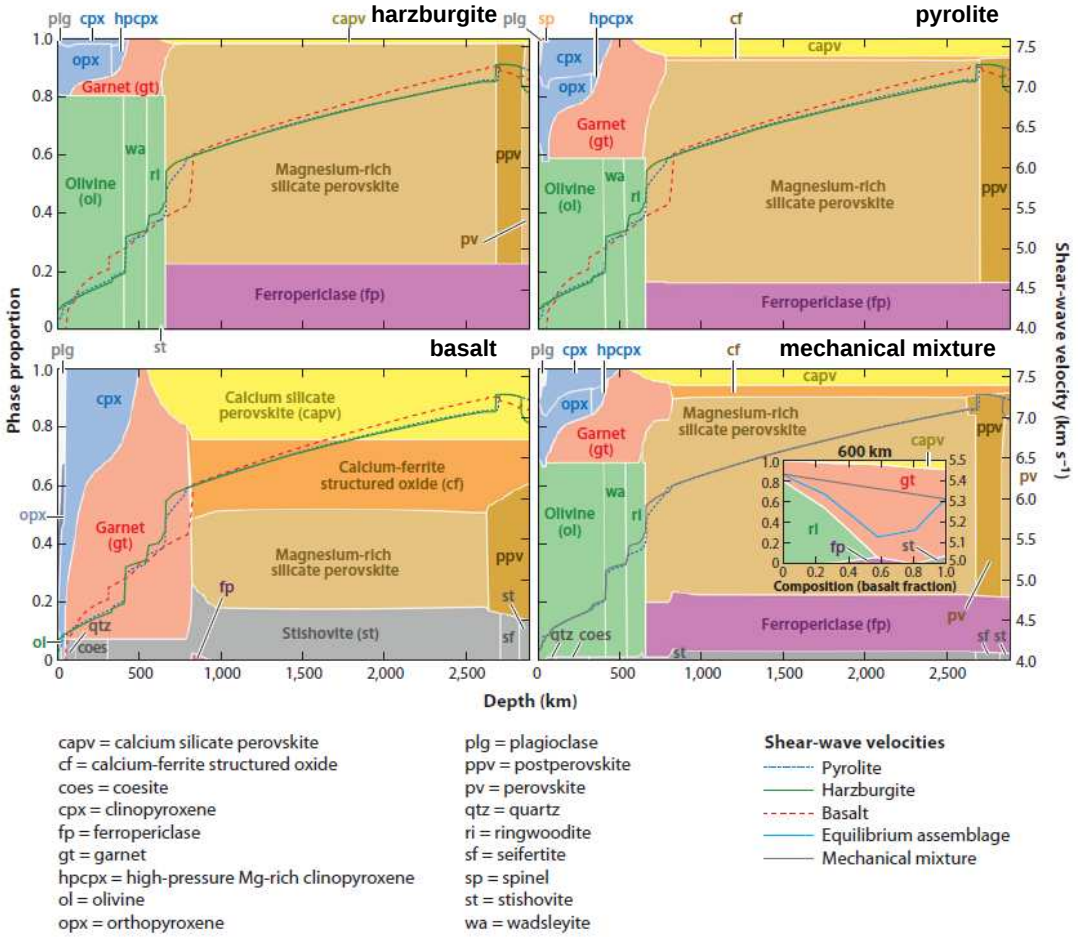

Figure 1.10: Phase proportions of four types of compositions: harzburgite, pyrolite, basalt and mechanical mixture (18% basalt and 82% harzburgite, in equal overall bulk composition to pyrolite). Superimposed are shear-wave velocitys (as indicated in the S-wave velocities legend), and are shown in each panel for comparison. Republished with permission of Annual Reviews, from Stixrude and Lithgow-Bertelloni (2012); permission conveyed through Copyright Clearance Center, Inc.

decreases (Figures 1.10). Therefore MORB may also be detected at these depths.

MORB and pyrolite velocities are significantly different for most of the mantle suggesting that the mineral physics would not prevent seismic detection. This supports the findings from seismology studies, which have detected small scale features interpreted as chemical heterogeneities (e.g. Weber and Wicks, 1996, Kaneshima and Helffrich, 1999, Krüger et al., 2001, Rost et al., 2008, Kaneshima, 2009).

1.7 Thesis aims

Mantle heterogeneity is important in characterising the mantle mixing processes and knowledge of heterogeneity in the upper and mid-mantle would improve our understanding of how material is transported from the surface to the CMB. Uncovering the pattern of mid-mantle heterogeneous structures is crucial for geophysicists to compare observations of small scale structure to numerically derived flows in mantle mixing models. Small scale structure is below the resolution level of tomography but these features can be detected using scattered seismic waves (Chapter 2).

In this thesis the main aims are:

1. to obtain global signatures of mantle heterogeneity through analysing and modelling seismic scattering in global stacks.

2. to obtain regional signatures of mantle heterogeneity through processing individual coherent scattered arrivals and use array processing of the wavefield to locate the source of scattering.

3. to discuss how the global and regional patterns of heterogeneities may be useful for understanding the mixing processes in the mid-mantle as presented in numerical models.

In Chapter 2, I discuss the theory behind seismic scattering and how one can detect scattering using global networks and smaller seismic arrays. In Chapter 3, I present the method and results of obtaining global averages of the *PP* scattered wavefield through stacking global seismic datasets. In addition, I describe how these stacked datasets can be used to derive models of mantle heterogeneity and discuss which models of heterogeneity can produce the observed *PP* scattered wavefield. In Chapter 4, I present the method and results in locating individual seismic scatterers in the upper and mid-mantle, with a particular focus on western Pacific subduction zones. The scatterers are analysed and discussed using other geophysical evidence and provide constraints on the history of subduction dynamics. In Chapter 5, I discuss the implications of the global and regional patterns of heterogeneity, combining the information to present a simple heterogeneity model for the mid-mantle. Finally, in Chapter 6, I summarise the key findings of this thesis and present objectives for future work.

Chapter 2

Studying seismic heterogeneity in the mantle

2.1 Overview

Our knowledge about the seismic structure of the interior of the Earth comes from the analysis of the direct body waves that travel along paths governed by the long wavelength structure of Earth's interior. From these observations, 1D velocity profiles (e.g. PREM, IASP91, ak135) and tomographic inversions of P and S wave travel times have revealed characteristics of the 3D velocity structure of the planet. However, there are other coherent arrivals in the short period data that account for some of the total seismic energy, which arise from scattering off the smaller scale structure (1-10 km). Scattering tends to appear as coda or precursory energy to the main phases, and on Earth scattering is relatively weak as evidenced by the energetic and visible primary arrivals in contrast to the strong scattering on the moon (e.g. Latham et al., 1970). These arrivals abide by scattering laws as described in this Chapter.

In addition, off-azimuth reflections from discrete structures or dipping reflectors can generate weak anomalous arrivals in the precursory and coda wavefields. Though off-azimuth arrivals are explained by Snell's Law rather than scattering theory, for this study it is not important to distinguish between these mechanisms.

This Chapter includes a summary of the fundamentals of scattering theory and the approximations that are used to apply such theories to scattering in perturbed elastic media. In addition I provide an overview into how one can observe and model scattering through global stacking methods, and how one can observe and locate individual regional scatterers through small seismic array methods.

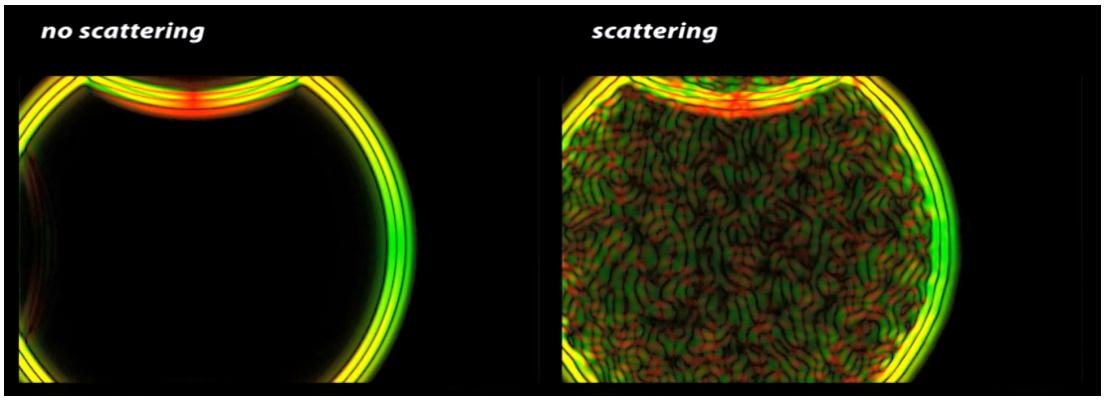

Figure 2.1: Seismic wavefront travels through a box of homogeneous medium and reflects off the sides of the box (left). In a medium of small-scale heterogeneities, the wavefront encounters scatterers and the high frequency wavefield is scattered (Thorne et al., 2013).

2.2 Seismic scattering

2.2.1 Scattering theory

Seismic scattering occurs when the incident wavefield interacts with heterogeneities and alters the high frequency wavefield (Figure 2.1). The equation of motion (equation 2.1) is used to describe the displacement of a homogeneous medium in reaction to a stress. This equation has to be modified to include the effects of perturbed properties of a heterogeneous media. As scattering from the Earth's interior is typically weak, the effects of scattering can be studied using the Born Approximation. In this description 3D propagation and wave conversions between P and S waves are considered.

Seismic scattering theory has been greatly explored for more than half a century and has been useful in describing properties of the wide-range of material that exists in the Earth. The scattering fundamentals as described by Aki and Richards (1980) are extensive and this section provides a summary of such work. For further detailed derivations, see Aki and Richards (1980), in addition to Wu and Aki (1985, 1988), Shearer (1999), Stein and Wysession (2003) and Sato et al. (2012), and references therein.

Scattering can be explored by considering the wave equation for a wave travelling in a homogeneous medium,

$$\frac{\partial \sigma_{ij}(\boldsymbol{x},t)}{\partial x_j} = \rho \frac{\partial^2 u_i(\boldsymbol{x},t)}{\partial t^2}, \tag{2.1}$$

where i and j range from 1 to 3 (corresponding to x, y and z), u_i is displacement,

ρ is density and σ_{ij} is the stress tensor for isotropic media defined as

$$\sigma_{ij}(\boldsymbol{x},t) \;=\; \lambda\theta\delta_{ij} \;+\; 2\mu e_{ij}(\boldsymbol{x},t). \tag{2.2}$$

The stress tensor depends on the strain tensor, e_{ij}; dilatation (volume change), θ; the Kronecker delta function, δ_{ij}; and the Lamé parameters, λ and μ. Solving the partial derivatives for each x, y and z component of the stress tensor yields a general wave equation for an isotropic inhomogeneous elastic medium (Aki and Richards, 1980):

$$\rho\frac{\partial^2 u(\boldsymbol{x},t)}{\partial t^2} \;=\; \frac{\partial}{\partial x_j}\left[\lambda\nabla\cdot u(\boldsymbol{x},t)\right] \;+\; \frac{\partial\left[\mu(\frac{\partial u_i}{\partial x_j}+\frac{\partial u_j}{\partial x_i})\right]}{\partial x_j} \tag{2.3}$$

The total combined wavefield, $u(\boldsymbol{x},t)$, in a inhomogeneous media is defined through the Born Approximation, which is the sum of the incident (homogenenous) wavefield $u^H(\boldsymbol{x},t)$ and the perturbed (scattered) wavefield $u^S(\boldsymbol{x},t)$:

$$u(\boldsymbol{x},t) \;=\; u^H(\boldsymbol{x},t) \;+\; u^S(\boldsymbol{x},t). \tag{2.4}$$

For the homogeneous media ρ_0, λ_0 and μ_0 are assumed to be constant. The perturbed component contains very small variations in average values of ρ_0, λ_0 and μ_0 as a function of space, i.e. $\delta\rho(\boldsymbol{x}), \delta\lambda(\boldsymbol{x}), \delta\mu(\boldsymbol{x})$:

$$\rho(x) = \rho_0 + \delta\rho(\boldsymbol{x}) \qquad \lambda(x) = \lambda_0 + \delta\lambda(\boldsymbol{x}) \qquad \mu(x) = \mu_0 + \delta\mu(\boldsymbol{x}). \tag{2.5}$$

Substituting these values into equation 2.3 and collecting perturbed values on the right hand side, one can obtain an expression for the total wavefield in inhomogeneous medium,

$$\begin{aligned}\rho_0\frac{\partial^2 u_i}{\partial t^2} \;-\; (\lambda_0+\mu_0)\frac{\partial(\nabla\cdot u)}{\partial x_i} \;-\; \mu_0\nabla^2 u_i \;=\; & -\delta\rho\frac{\partial^2 u_i}{\partial t^2} \;+\; (\delta\lambda+\delta\mu)\frac{\partial(\nabla\cdot u)}{\partial x_i} \\ & +\; \delta\mu\nabla^2 u_i \;+\; \frac{\partial(\delta\lambda)}{\partial x_i}\nabla\cdot u \\ & +\; \frac{\partial(\delta\mu)}{\partial x_i}\left(\frac{\partial u_j}{\partial x_j}+\frac{\partial u_j}{\partial x_i}\right)\end{aligned} \tag{2.6}$$

As the Born Approximation assumes that $|u_i^S| << |u_i^H|$, the total wavefield can be decomposed into the unperturbed wavefield u^H:

$$\rho_0 \frac{\partial^2 u_i^H}{\partial t^2} \;-\; (\lambda_0 + \mu_0)\, \frac{\partial \left(\nabla \cdot u^H\right)}{\partial i} \;-\; \mu_0 \nabla^2 u_i^H \;=\; 0. \tag{2.7}$$

and the scattered wavefield u^S:

$$\rho_0 \frac{\partial^2 u_i^S}{\partial t^2} \;-\; (\lambda_0 + \mu_0)\, \frac{\partial \left(\nabla \cdot u^S\right)}{\partial i} \;-\; \mu_0 \nabla^2 u_i^S \;=\; F_i \tag{2.8}$$

where

$$\begin{aligned} F_i \;=\; & -\delta\rho \frac{\partial^2 u^H}{\partial t^2} \;+\; (\delta\lambda + \delta\mu) \frac{\partial(\nabla \cdot u_i^H)}{\partial x_i} \;+\; \delta\mu \nabla^2 u_i^H \\ & +\; \frac{\partial(\delta\lambda)}{\partial x_i} \left(\nabla \cdot u^H\right) \;+\; \frac{\partial(\delta\mu)}{\partial x_i} \left(\frac{\partial u_j^H}{\partial x_j} + \frac{\partial u_j^H}{\partial x_i} \right). \end{aligned} \tag{2.9}$$

Equation 2.8 is essentially the equation of motion in homogeneous, unbounded, isotropic and elastic medium with an additional body force term, F_i. The components of F_i are connected to the perturbed parameters $\delta\rho$, $\delta\lambda$, $\delta\mu$ and their partial derivatives.

Considering P wave energy only, the displacement of an incident P wave travelling in x_1 direction (in terms of α_0, the P wave speed in perturbed media) is defined as:

$$u_i^0 \;=\; \delta_{1i} \exp\left[-i\omega \left(t - \frac{x_1}{\alpha_0} \right) \right] \tag{2.10}$$

where,

$$\alpha_0 \;=\; \sqrt{\frac{\lambda_0 + 2\mu_0}{\rho_0}}$$

and ω is the angular frequency. The 3 components of the force vector F_i are found by substituting u_i^0 into equation 2.9:

$$F_1 = \left[\delta\rho\omega^2 - \frac{(\delta\lambda + 2\delta\mu)\,\omega^2}{\alpha_0^2} + i\frac{\omega}{\alpha_0}\frac{\partial\delta\lambda}{\partial x_1} + 2i\frac{\omega}{\alpha_0}\frac{\partial\,(\delta\mu)}{\partial x_1}\right] \exp\left[-i\omega\left(t - \frac{x_1}{\alpha_0}\right)\right], \tag{2.11}$$

$$F_2 = i\frac{\omega}{\alpha_0}\frac{\partial\delta\lambda}{\partial x_2} \exp\left[-i\omega\left(t - \frac{x_1}{\alpha_0}\right)\right], \tag{2.12}$$

$$F_3 = i\frac{\omega}{\alpha_0}\frac{\partial\delta\lambda}{\partial x_3} \exp\left[-i\omega\left(t - \frac{x_1}{\alpha_0}\right)\right]. \tag{2.13}$$

For the force in the x_1 direction, F_1, three types of local heterogeneities are extracted and are shown in Figure 2.2. The first inhomogeneity is defined by rewriting the first two terms of F_1 as a perturbation in P wave velocity:

$$\delta\rho\omega^2 - \frac{(\delta\lambda + 2\delta\mu)\,\omega^2}{\alpha_0^2} = -\omega^2\rho_0\left(-\frac{\delta\rho}{\rho_0} + \frac{\delta\lambda + 2\delta\mu}{\lambda_0 + 2\mu_0}\right)$$

$$= -2\omega^2\rho_0\frac{\delta\alpha}{\alpha_0}. \tag{2.14}$$

This inhomogeneity is known as δx type or "velocity perturbation" (Figure 2.2, *top*) and produces a scattered P wavefield in the x_1 direction only. The inhomogeneity in λ is derived from the 3^{rd} term in the expression for F_1:

$$\int_V x_i\,\frac{\partial\delta\lambda}{\partial x_k}\,dV = -\delta_{ik}\int_V \delta\lambda\,dV. \tag{2.15}$$

where $\delta\lambda$ is localised in a small region, V. The scattered wave perturbation occurs as 3 perpendicular dipoles resulting in scattered P wave energy in all directions but no scattered S waves.

Third, the $\delta\mu$ local heterogeneity is generated from a single dipole, if $\delta\mu$ is present only within a local small region V, and does not exist outside of V. Therefore, the moment tensor consists of M_{11} term only and will be proportional to $\int_V \delta\mu\,dV$. Scattered P waves are produced in the x_1 direction, though no S wave energy is produced in the x_1 direction, as is the case for all three local heterogeneities.

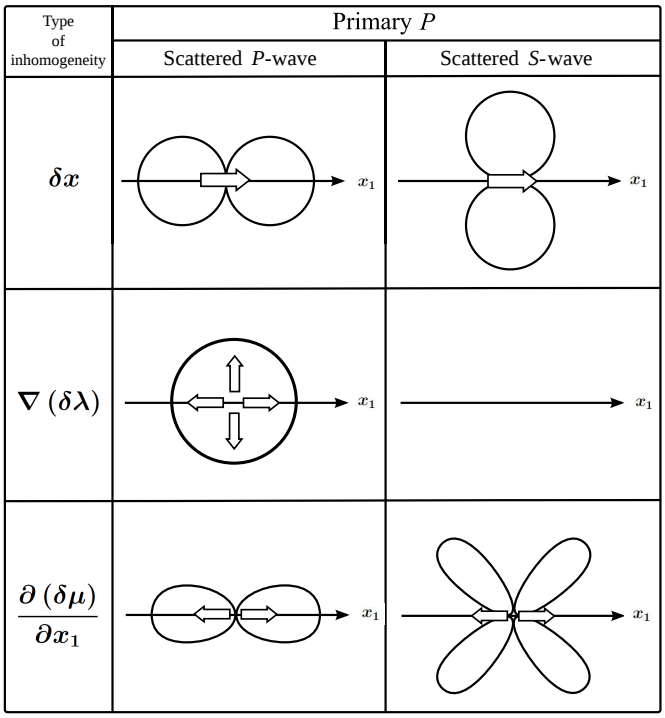

Figure 2.2: The radiation pattern of far-field P- and S-waves that are scattered from three types of localised inhomogeneity (heterogeneity) due to P-wave incident in the x_1 direction (redrawn from Aki and Richards (1980)).

Typically, the scale of crustal and mantle heterogeneities used in this study are velocity perturbation type inhomogeneities resulting in both P and S wave scattering. The following section will show how one can use this branch of theory to determine properties of the heterogeneities that produce such scattering.

2.2.2 Scattering Regimes

As expressed above the Born Approximation assumes that in the presence of weak scattering the combined wavefield is the sum of the scattered wavefield and the incident wavefield. The approximation also allows the scattered wave to be considered as a plane wave. The Born Approximation is useful in simplifying the solution to the scattered wave equation. For strong scattering the Born Approximation cannot be used and more advanced approaches are employed (see Section 2.4.2).

Aki and Richards (1980) found that the alterations and energy loss of a wavefield due to propagation through a scattered medium is dependent on the wavenumber k correlation length a and size of heterogeneous region L. Combinations of these parameters form different regimes of scattering, which have been useful when analysing scattering

of various strengths in the Earth. Figure 2.3 demonstrates some of the commonly used scattering regimes and how they relate to ka and kL. Scattering regimes that are often employed when analysing heterogeneities in the mantle are:

- Large-angle scattering: occurs when $0.1 < ka < 10$. The energy is scattered to wide angles and is responsible for high attenuation. An example of this type of scattering occurs in the crust and contributes to the generation of the P coda. With strong large angle scattering, the Born Approximation breaks down.

- Small-angle scattering: occurs when $ka >> 10$ and the scattering power is dependent on scattered angle, θ. Mostly forward scattering is produced within an angle of $(ka)^{-1}$ about the primary direction $\theta = 0$. Back scattering power (at $\theta = \pi$) is almost negligible. As scattering is weak, the Born Approximation can be applied.

For this study, the global observations of scattering in the teleseismic wavefield (large L) for small scale heterogeneities ($1 < a < 10$) with dominant frequencies of 1-1.5 Hz ($k < 10$), are most likely generated by small angle scattering creating a global signature of precursory energy.

The wave parameter D is related to ka and kL (Figure 2.3) and the value of D governs when ray theory ($D < 1$) and diffraction theory ($D > 1$) can be used. The wave parameter is defined as the ratio of the size of the first Fresnel zone and the inhomogeneity scale length:

$$D = \frac{4L}{ka^2}. \tag{2.16}$$

where L is the travel distance through the heterogeneous region. When $D << 1$, the amplitude fluctuation is also small and the phase fluctuation is approximately the fluctuation as expected from geometrical ray theory. For $D > 1$, strong scattering exists and numerical methods such as finite difference and finite element are required to solve these scattering problems.

2.2.3 Statistical description of heterogeneous media

It has been shown above that the scattered wavefield is affected by the change in velocity of heterogeneities across a region. The properties of heterogeneities can be explored

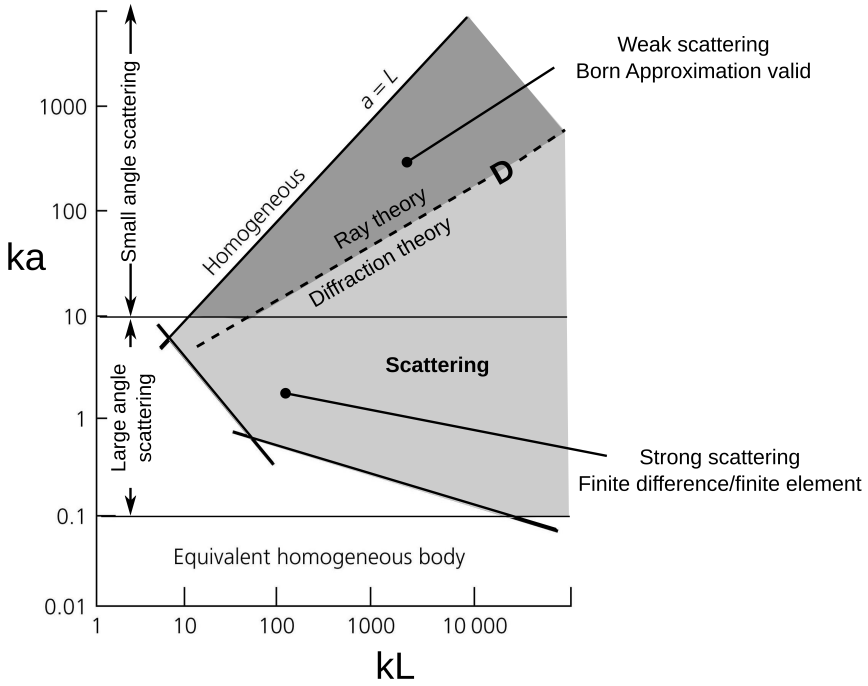

Figure 2.3: Classification of scattering problems with associated methods. k is the wavenumber, a is the correlation length, L is the length of the heterogeneous region and D (dashed line) is the wave parameter. After Stein and Wysession (2003) and Aki and Richards (1980).

using the scattered energy generated at heterogeneities and observed in array data for large epicentral distances.

For velocity perturbation scattering, the average of the spatial fluctuations of velocity in a media can be calculated statistically using a normalised autocorrelation function $N(\boldsymbol{r})$:

$$N(\boldsymbol{r}) \quad = \quad \frac{\langle\, \eta(\boldsymbol{r'})\eta(\boldsymbol{r'}+\boldsymbol{r})\,\rangle}{\langle\, \eta^2\,\rangle}. \tag{2.17}$$

Statistical models of inhomogeneities in a medium are used as it is not possible to characterise the properties discretely throughout a volume. It is assumed that the fluctuation of $\eta(\boldsymbol{r})$ has stationary statistical properties within the defined volume and as such the correlation function is an average of $\eta(\boldsymbol{r_1})\eta(\boldsymbol{r_1}+\boldsymbol{r})$ over the independent sample points $\boldsymbol{r_1}$. In order to find η, two autocorrelation functions (ACF) have been used previously: the exponential function,

$$N(\boldsymbol{r}) = e^{-|\boldsymbol{r}|/a}, \tag{2.18}$$

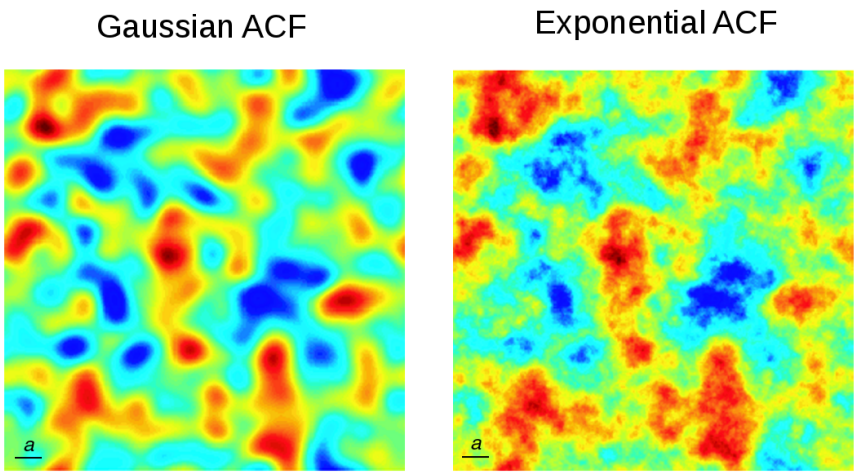

Figure 2.4: Random media examples which are defined by a Gaussian ACF (left) and an exponential ACF (right). The exponential medium has more short wavelength structure compared to the Gaussian medium. The correlation distance (a) is shown (bottom left corner). Reprinted from Shearer (2007), Copyright (2007).

and the Gaussian function,

$$N(\boldsymbol{r}) = e^{-|\boldsymbol{r}|^2/a^2}, \tag{2.19}$$

where a is the *correlation distance* aka the inhomogeneity scale length (Chernov, 1960). The two correlation functions produce different random media heterogeneous models with the exponential medium containing more structure at short wavelengths (Figure 2.4).

2.2.4 Off-azimuth reflections

Another possible mechanism of producing non-primary arrivals is through off-azimuth reflections, which are caused by heterogeneous features that lie outside of the direct path between source and receiver (Figure 2.5). The spherical wavefront of earthquake energy comes into contact with the heterogeneity and, with the right geometry and impedance contrast, the energy will be reflected towards the receiver. The azimuth of the reflected energy differs from the azimuth of global phases, which travel along a great circle path.

Off-azimuth or out-of-plane arrivals are unconventional phases and they are often labelled as scattered energy. As such I will refer to these arrivals as scattering, unless making a direct comparison between scattered arrivals and off-azimuth reflections. A key difference between the two phenomena is that true scattering follows the relation-

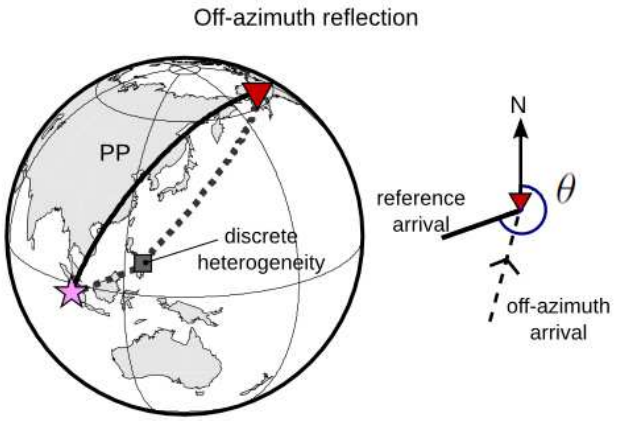

Figure 2.5: Schematic showing off-azimuth reflections observed at an array with difference in backazimuth $\delta\theta$.

ships derived from the wave equation in perturbed media (e.g. Born Approximation), whereas off-azimuth arrivals follow Snell's Law. Also, the deviation in backazimuth from a reference phase is not required for scattered energy but is essential in the description of out-of-plane arrivals. Theoretically energy maybe deemed as off-azimuth if the difference in backazimuth exceeds the width of the 1st Fresnel zone taking into account any error in the backazimuth calculation. Obviously, such quantitative limits are difficult to generalise as they depend on the frequency of waves and the array aperture.

As with scattering, heterogeneities cause off-azimuth reflections, but the arrivals are generated by strong impedance contrasts rather than considering a volume with average fluctuations of perturbed parameters. As the propagation of the wavefield is governed by Snell's Law, the feature generating the reflection would need to be a dipping plane, or topographic variations of a discontinuity, or the sharp edge of a discrete object in order to reflect the incident wave back to the receiver.

Different combinations of incident and reflected P and S wave combinations are possible when applying this law to seismic interfaces e.g. P-to-P, P-to-p, S-to-P (Figure 2.6). The type of body wave can be deduced by processing and analysing the directivity and travel time of anomalous energy recorded at the receivers.

Other analyses are performed to learn more about the properties of the heterogeneity. For example, the direction of the wave can be analysed as it is directly linked to the location of reflection. Also, the amplitude of the energy may be linked to the impedance contrast at the surface of the heterogeneity and the signal waveform may

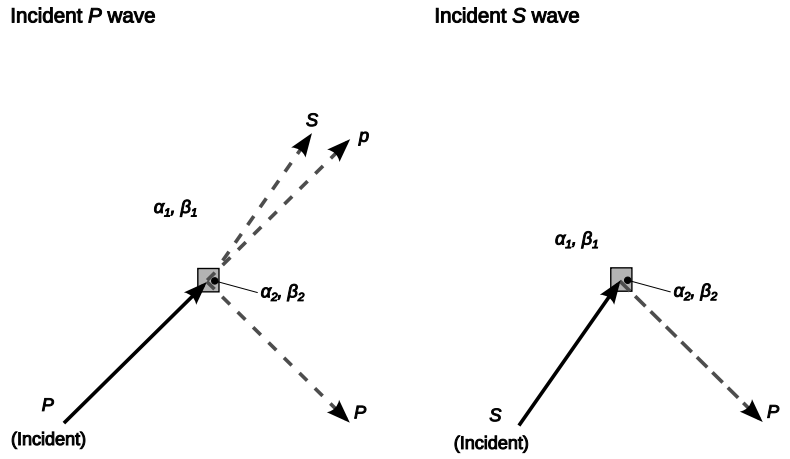

Figure 2.6: Possible reflection mechanisms for incident P wave (left) and incident S wave. Lower case p refer to up-going phases, where as upper case P and S refer to down going turning waves.

provide information as to the character of the interface.

2.3 Seismic Scattering Probes

It has been shown that properties of seismic scattering can be used to characterise heterogeneous media. Within the Earth, seismic scattering is mostly observed as precursory or coda energy to global seismic phases. Scattering in the mantle has been extensively studied using the scattered energy before and after many different P wave reference phases, including the P coda (Aki, 1973, Kaneshima and Helffrich, 1999, Shearer and Earle, 2004, Kito et al., 2008, Kaneshima and Helffrich, 2009), P_{diff} coda (Tono and Yomogida, 1996, Earle and Shearer, 2001), PP precursors (Weber and Wicks, 1996, Rost et al., 2008, Schmerr and Thomas, 2011), $P'P'$ precursors (King and Cleary, 1974, Vinnik, 1981), $PKiKP$ precursors (Vidale and Earle, 2000, Poupinet and Kennett, 2004, Koper et al., 2004), PKP precursors (Bataille and Flatt, 1988, Hedlin et al., 1997, Cormier, 1999) and $PKKP$ precursors (Earle and Shearer, 1998, Rost and Earle, 2010). The paths and travel time curves for such probes are shown in Figure 2.7 and Figure 2.8 respectively. Scattered energy can be incoherent across networks of receivers that have large station spacing and need to be studied by stacking of global datasets. However, some scattered energy is coherent across smaller networks and can be imaged using seismic array methods.

Scattering contained in the P coda has successfully been used to search for and locate P-to-P scattering (Weber and Wicks, 1996, Kito et al., 2007) and S-to-P con-

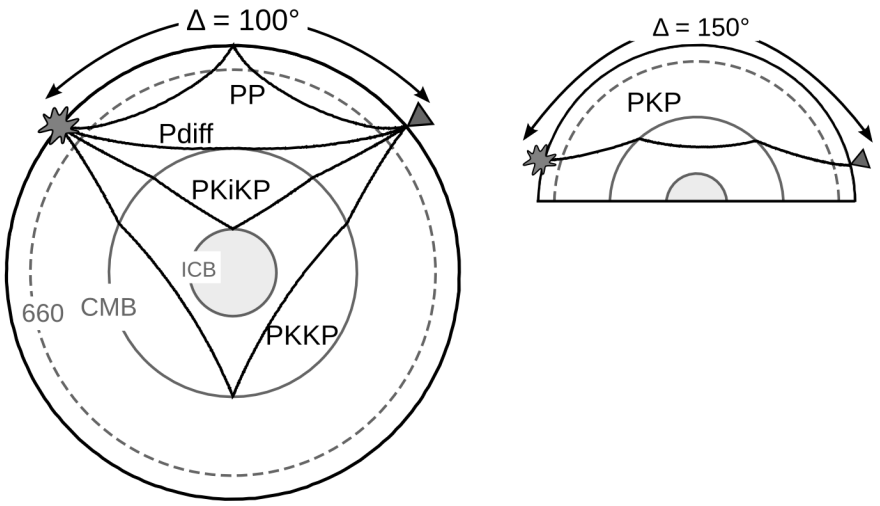

Figure 2.7: Probes that are used to study scattering from mantle heterogeneities for epicentral distances of 100° (*left*) and 150° (*right*).

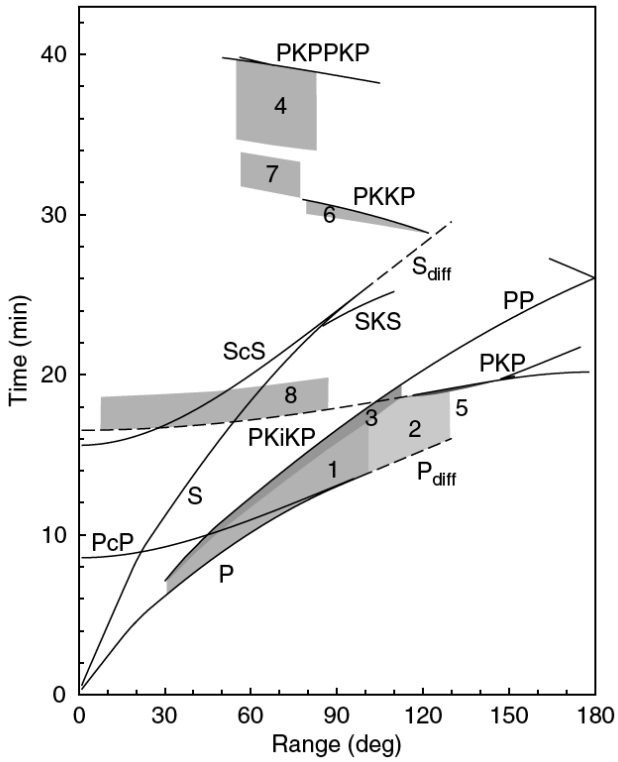

Figure 2.8: Traveltime curves for teleseismic body waves and regions in the wavefield that contain scattering from mantle heterogeneities. These include: 1) P coda, 2) P_{diff} coda, 3) *PP* precursors, 4) P'P' precursors, 5) PKP precursors, 6) PKKP precursors, 7) $PKKP_{\times}$, and 8) PKiKP coda; shown in grey with approximate boundaries (Shearer, 2007). The target phases used are shown in Figure 2.7. Reprinted from Shearer (2007), Copyright (2007).

verted phases (Castle and Creager, 1999, Kaneshima and Helffrich, 1999, Kito et al., 2007, Kaneshima and Helffrich, 2009) from mantle heterogeneities. However, often it is difficult to detect energy generated from mid-mantle scatterers due to the strong scattered arrivals from crustal heterogeneities. Typically, the P coda falls below the ambient noise level in the seismogram after ∼150 s, or ∼100 s before the PP arrival, depending on epicentral distance.

2.3.1 *PP* and *PP* precursors

In this study the scattered PP, the seismic phase that has reflected once midway between source and receivers, and the scattered wavefield are explored (Figure 2.7). PP is a minimum-maximum traveltime phase, which results in some out-of-plane or deep scattering to arriving as PP precursors. These PP precursors can often be weak (Rost et al., 2008) and so are difficult to detect in individual seismograms, however, the arrivals are noticeable in global stacks (e.g. Flanagan and Shearer, 1999, Rost et al., 2006) (Figures 2.9 and 2.10). PP precursors have been shown to have slowness similar to PP rather than P (Rost et al., 2006) suggesting the precursors are generated through a different mechanism to arrivals in the P coda.

PP precursors can be generated from many different structures in the crust and mantle. Many studies of PP precursors have found arrivals originating from underside P wave reflections off mantle discontinuities (e.g. Shearer, 1990, Flanagan and Shearer, 1998, Deuss et al., 2006). These arrivals, PdP phases (d corresponding to the depth of discontinuity) are observed across large distance ranges. In particular for distances 80-120°, $P^{410}P$ and $P^{660}P$ arrive more than 100 s before PP (Figure 2.9) leaving a quiet window for the 100 s before PP.

Additionally, some PP precursors have been shown to be generated by asymmetric reflections off the free surface at the crust (e.g. Wright, 1972). Similarly to PdP, Wright (1972) found that the precursors are generated from a global discontinuity rather than from small-scale 3D structure.

Conversely, some PP precursors detected have been shown to arrive with backazimuths that differ greatly from the backazimuth of PP (i.e. along great circle path). The origin of these off-azimuth arrivals have been linked to scattering not only in the crust and upper mantle (King et al., 1975, 1976, Kato and Hirahara, 1991, Weber and Wicks, 1996) but also in the mid and lower mantle (Rost et al., 2008). Rost et al. (2008)

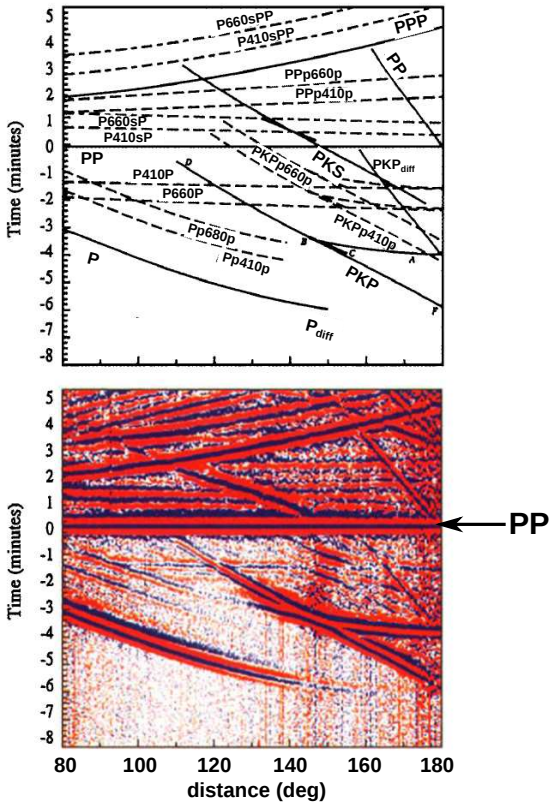

Figure 2.9: Long-period stacked seismograms showing *PP* and *PP* precursors. Stacks are relative to *PP* arrival time and are normalised to *PP* amplitude where positive amplitudes are blue and negative are red. The upper plot shows travel time curves for the primary phases (solid lines) and the reflections of mantle discontinuities (dashed). After Flanagan and Shearer (1999). Copyright © 1999 by the American Geophysical Union.

detected *PP* precursors using the Yellowknife Array (YKA), Canada and located the origin of scattering to Tonga and Mariana subduction zones. Through analysing precursor amplitudes they concluded that the scattered energy was produced from the paleo-Moho of subducted slabs. The study demonstrated that examining these particular precursors (*P*P*) can reveal important information about heterogeneities in the mid and lower mantle.

In summary, *PP* precursors in a time window up to 100 s before the *PP* arrival (Rost et al., 2006) are examined in this study as the probe has been successful but underutilised in revealing more about small-scale mantle heterogeneities. *PP* precursors are examined by two methods: a global stacking approach (Chapter 3) and application of array seismology techniques (Chapter 4), to characterise global averages of mantle heterogeneity and to image mantle heterogeneities associated with recently subducted slabs, as explained in the following sections.

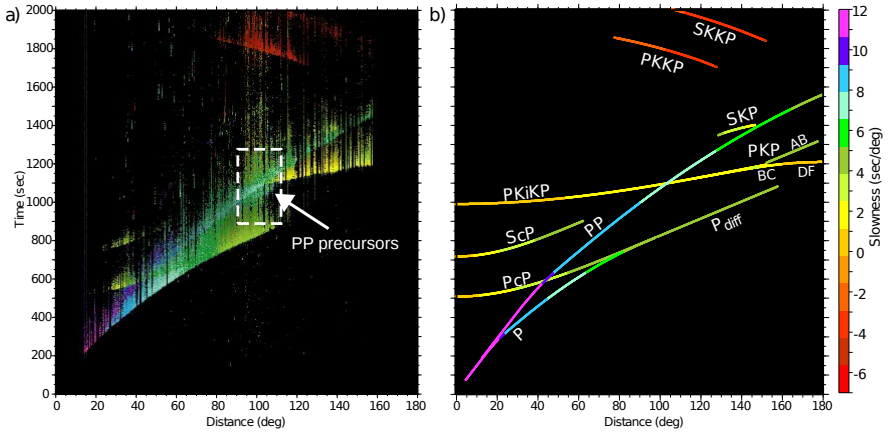

Figure 2.10: a). 10^{th} root vespa slowness stacks with colour of curves representative of theoretical slowness. White box highlights *PP* precursors for distances 90-110° which have slowness similar to *PP* and are not part of the *P* coda. b) Travel time curves with slowness of the arrivals colour coded as in a). After Rost et al. (2006).

2.4 Stacking and modelling of global seismic datasets

2.4.1 Global stacks

Stacking of global datasets is an extremely useful tool when searching for scattered energy generated within the Earth (e.g. Haddon and Cleary, 1974, Cleary et al., 1975, Hedlin et al., 1997, Earle and Shearer, 2001, Shearer and Earle, 2004). By using a wide-world distribution of earthquakes and stations, one can obtain an average of the amplitude of scattered energy that arrives in key parts of the seismogram. In contrast to array seismology (refer to Section 2.5), the station separation is too large on global networks for arrivals to be coherent so traditional array methods (e.g. Rost and Thomas, 2002) cannot be employed. The advantage of global stacks lie in their ability to obtain an average signature by combining the amplitudes of incoherent scattered energy. Spatially averaged fields have less bias on local features and noise, allowing weak arrivals to be studied. Furthermore, stacking reduces the volume of data, which enables modelling applications to be more manageable.

Global stacking has been applied to several phases that travel through the mantle (Figure 2.8). The most studied arrivals are *PKP* precursors (e.g. Hedlin et al., 1997, Hedlin and Shearer, 2000), which have been of interest since the proposal that these precursors are caused by scattering near the CMB (Cleary and Haddon, 1972). Theoretically, precursors arriving within 20 s of *PKP* for distance ranges 120-145°, can be generated in the lowermost 400 km of the mantle (Hedlin et al., 1997). *PKP* coda has

also been studied (Hedlin and Shearer, 2002) but is more sensitive to scattering in the crust and mid-mantle.

Other coda energy has been studied using global stacks, including the P coda (Shearer and Earle, 2004), which is mostly sensitive to scattering in the crust and upper mantle; and P_{diff} (Earle and Shearer, 2001), which is sensitive to whole mantle scattering, though structure in the lowermost mantle may have more influence on the wavefield.

A typical work flow for stacking global data is shown below, as adapted from Shearer and Earle (2008):

1. Collect data from global networks.

2. Filter traces - commonly filtered between 0.5 (or 0.7) and 2.5 Hz. This frequency range is chosen as it has low noise and provides greatest sensitivity to heterogeneity scale lengths of ∼10 km as found in the lower mantle.

3. Evaluate and construct envelope (Shearer, 1999) of each seismic trace.

4. Limit varying noise levels across stations by subtracting an average of pre-signal noise amplitude. Calculate and subtract the average on the envelope function squared because the recorded signal is the square root of the sum of the squared noise plus the squared signal, and take the square root.

5. Normalise each seismogram to the amplitude of the reference phase then align on the arrival time of the reference phase, before sorting into distance bins.

6. Finally, stack all the data in each distance bin by summing the traces and taking the mean.

2.4.2 Modelling

Several methods to model the scattered wavefield exist (Shearer and Earle, 2008). Solving the full wave equation is difficult, so approximations are often necessary to simplify the problem. Simplifications can be made through assumptions about scattering intensity and the scale length of the heterogeneity. Several reviews including Shearer (2007), Shearer and Earle (2008) explore the different modelling methods that can be applied to scattering. Since in this thesis, the PP precursory wavefield is the sole probe consid-

ered, the discussion is restricted to those modelling techniques that include scattering of the incident P wavefield.

If scattering is weak and if single scattering can be assumed, then scattering can be modelled by using the Born Approximation with correlation functions derived by Chernov (1960). The approach explores scattering power as a function of incident and scattered wavefields, through statistical averages of slowness fluctuation as described in Section 2.2.1. Previously, single scattering modelling has been used for studying PP (King et al., 1975) as well as P_{diff} coda (Earle and Shearer, 2001) and PKP precursors (Hedlin and Shearer, 2002). See the review by Shearer (2007) for comprehensive list of probes and studies.

As the Born Approximation does not adhere to the conservation of energy, the technique cannot be used to study strong multiple scattering. Instead the powerful finite difference (FD) or finite element (FE) techniques have been used to solve the wave equation for 2D and 3D heterogeneous media (e.g. Korn, 1997, Wagner and Langston, 1992, Thomas et al., 2000, Korn and Sato, 2005). Such techniques produce detailed patterns of scattering but are computationally expensive, especially for multiple scattering events. Therefore other approaches using additional assumptions have been developed to reduce the run time when solving for multiple scattering. Faster methods to model multiple scattering in random media solve the spatial distribution of energy (e.g. using the diffusion equation) through random walk algorithms and by assuming correlations in fluctuations of velocity and density. Such techniques were first used to study P coda in the 1960s (e.g. Wesley, 1965, Aki and Chouet, 1975) as they were faster than FD. The approach satisfies conservation of energy (essential for analysing strong scattering) however causality is violated as energy arrives before the direct P wave.

Recently, multiple scattering is more commonly explored using radiative transfer theory. First studied in the 1980s (e.g. Wu, 1985, Wu and Aki, 1988), such techniques model energy transport of particles throughout a volume, often including depth dependent and anisotropic 3D variations of heterogeneity. Combined with Monte Carlo approaches (Figure 2.11), the method simulates the random walk of millions of seismic energy phonons (conceptually analogous to light particles) that have been scattered with probabilities derived from random media theory (e.g. Shearer and Earle, 2004). This is an effective and powerful tool and successfully generates synthetic seismograms (Shearer, 2007). Particles are sprayed in all directions from the source in a 2D area of

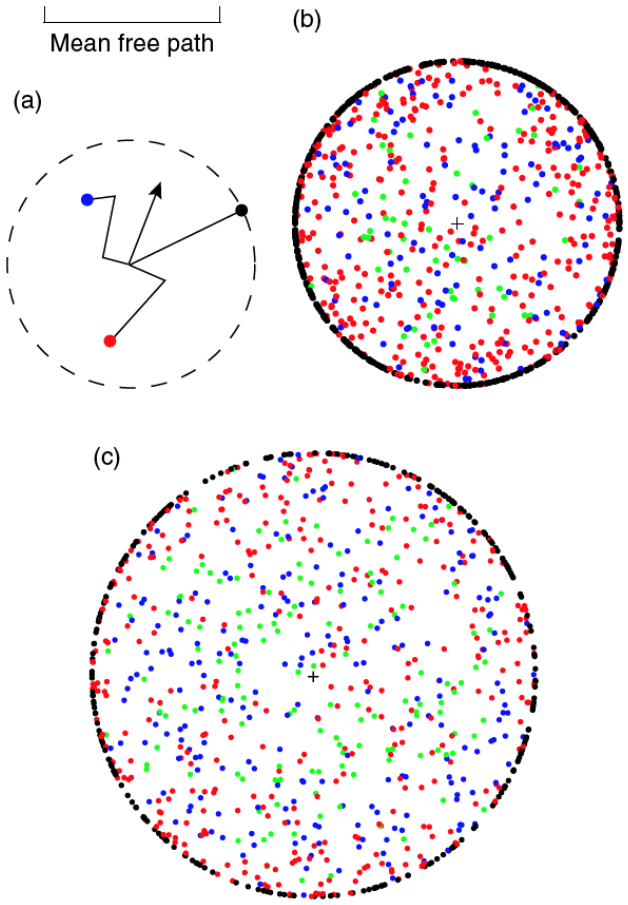

Figure 2.11: Example of a Monte Carlo computer simulation of random scattering of seismic energy particles. 2-D isotropic scattering in a uniform whole space is assumed. Particles are emitted in all directions from the source with constant scattering probability defined by the indicated mean free path length, l. a) Black dots show particles that have not not been scattered, red dots show particles that have scattered once, blue dots show particles that have scattered twice, and green dots show particles scattered three or more times. b) Results for 1000 particles after $t = \frac{l}{v}$, where v is velocity. c) Results for 1000 particles after $t = 1.25\frac{l}{v}$. Reprinted from Shearer (2007), Copyright (2007).

constant scattering probability (indicated as mean free length in the figure).

Several studies have developed Monte Carlo approaches to include P and S waves (Margerin et al., 1998, 2000, Margerin and Nolet, 2003a). Early work used a Monte Carlo approach for crustal and upper mantle scattering by converting the reflections and transmissions coefficients from the surface and moho boundaries, into probability functions (Margerin et al., 1998). Though this work was initially only for S wave scattering, the techniques were extended to study P-to-S conversions (Margerin et al., 2000), as well as whole mantle scattering and lower mantle scattering using PKP precursors (Margerin and Nolet, 2003a).

Shearer and Earle (2004) accurately modelled whole Earth scattering by using initial P and S waves and allowed mode conversions and intrinsic attenuation. Reflection and transmission coefficients can be included for most global discontinuities. Scattering probabilities and angles are calculated assuming random δv and $\delta \rho$ values derived from an exponential autocorrelation function (Section 2.2.3).

Since the scattered PP wavefield explored in this study is thought to contain weak small angle scattering, the Born Approximation is applicable and therefore a Monte Carlo phonon method by Shearer and Earle (2004) is used to calculate multiple scattering in random media. More detailed description of the approach and the application to PP precursors is described in Chapter 3.

2.5 Detecting scattered energy using seismic arrays

2.5.1 Array seismology theory

Individual coherent scattered arrivals are anomalous arrivals and are not predicted by Earth reference models. These scatterers are weak and detecting them amongst noise requires advance processing from array seismology.

For teleseismic distances with a minimum source-receiver separation of a few array apertures, the plane wave assumption is used to extract directional information from coherent arrivals (Rost and Thomas, 2009). The array is used as an antenna and so the direction of the incoming wave can be found. A wave arrives at each station with a different arrival time as the wavefront travels across the array (Figure 2.12). Using multiple stations in array formation two angles are calculated: backazimuth and vertical incident angle. The backazimuth θ is the orientation of the incident wavefront measured clockwise from north. The vertical incident angle i is most often converted to the observable slowness parameter u (or u_{hor}). Slowness is essentially the reciprocal of the apparent velocity of the wavefront (v_{app}) across the array and is dependent on the material velocity v_0:

$$u_{hor} = \frac{1}{v_{app}} = \frac{\sin i}{v_0}. \tag{2.20}$$

Using equation 2.20, the slowness vector in spherical geometry can be expressed as:

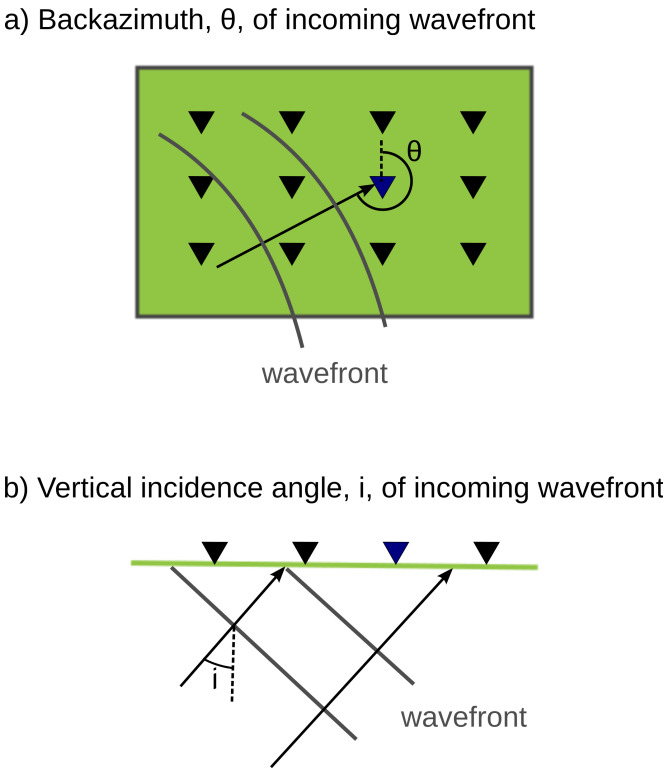

Figure 2.12: a) Map view of an array showing wavefront moving across the stations with horizontal angle, backazimuth (θ), measured from north. b) Cross section through subsurface beneath the array showing wavefront arriving at array with incident angle (i), measured from the vertical.

$$\begin{aligned} \boldsymbol{u} &= (u_x, u_y, u_z) \\ &= \Big(\frac{\sin\theta}{v_{app}}, \frac{\cos\theta}{v_{app}}, \frac{1}{v_{app}\tan i}\Big) \\ &= \frac{1}{v_0}\big(\sin i \sin\theta, \sin i \cos\theta, \cos i\big), \end{aligned} \tag{2.21}$$

where u_x is typically measured in the east-west direction, and u_y in the north-south direction. In most cases, the differences in station elevation are very small and so the vertical slowness component (u_z) cannot be measured.

For an incoming wavefront to the array, time differences would be observed at the stations and these depends on the slowness vector and the station location:

$$t_j = \boldsymbol{r}_j \cdot \boldsymbol{u}. \tag{2.22}$$

The signal to noise of weak scattered arrivals can be enhanced through beamforming.

The output of beamforming, the beamed trace is created by correcting for differences in arrival time (equation 2.22) i.e. shifting the time series, and summing the output of the individual array channels (Figure 2.13). The beamed trace $b(t)$ is defined as

$$b(t) = \frac{1}{M} \sum_{j=1}^{M} x_j(t + t_j). \tag{2.23}$$

where t_j is the delay time for the j^{th} station (relative to a reference station or point), x_j is the recording at the j^{th} station and M is the number of stations in an array. By stacking M seismograms where the noise is uncorrelated then the noise is reduced by a maximum of $\sqrt{M}$ (Rost and Thomas, 2002).

2.5.2 Calculating directivity

Slowness and backazimuth can be calculated through several established array techniques. A simple way to calculate slowness and backazimuth individually is to use velocity spectral analysis, otherwise called VESPA analysis (Davies et al., 1971). VESPA analysis computes vespagrams containing array beams for varying slowness with constant backazimuth or varying backazimuth with constant slowness. The VESPA process can be used to find the slowness of an arrival (Figure 2.14) through creating vespagram traces $v(t)$. Vespagrams are defined for the range of slowness, $u_{min} \leq u \leq u_{max}$, for constant backazimuth θ as:

$$v_u(t) = \frac{1}{M} \sum_{j=1}^{M} x_j(t + t_{j,u}) \tag{2.24}$$

where $t_{j,u}$ is the delay time at the j^{th} station for a slowness u (Rost and Thomas, 2009). A similar equation can also be utilised for forming backazimuth vespagrams.

For scattered arrivals, both the backazimuth and slowness are unknown. Slowness and backazimuth can be calculated simultaneously by performing a grid search of slowness and backazimuth in the time domain through process such as *Beaman* and *Beampack* (e.g. King et al., 1976, Rost and Thomas, 2009), and or a grid search of frequency and wavenumbers in the frequency domain using fk-analysis (Capon, 1969). The time and spectral domain methods produce very similar results, however computing directivity over a large grid is faster in the spectral domain (Rost and Thomas, 2002). To calculate the direction of an arrival using fk-analysis, a time window is se-

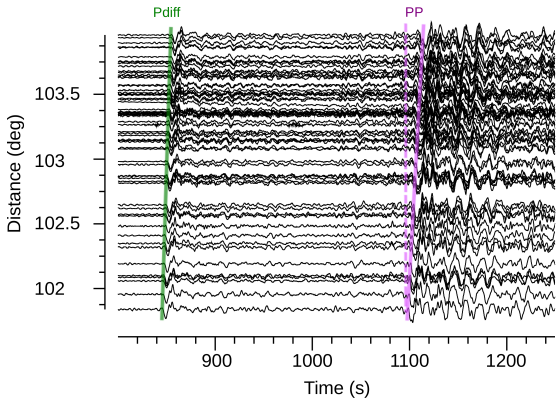

(a) Traces with no alignment

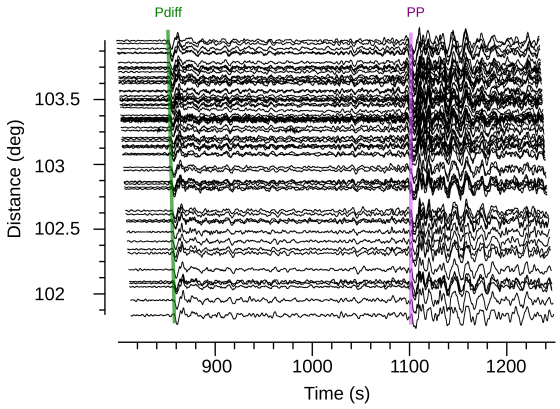

(b) Traces with traces alignment on *PP* arrival

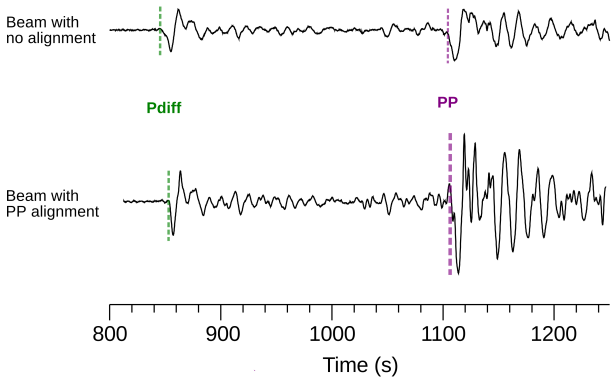

(c) Beamed traces without (top) and with (bottom) alignment on *PP*

Figure 2.13: An example of beamforming to correct for the moveout across an array. a) Seismograms are ordered by epicentral distance from earthquake. Coherent arrivals arrive at different times depending on distance. The main phases Pdiff (green) and *PP* (purple) show different moveouts across array as phases travel with different slowness. b) Seismograms are aligned on *PP* by correcting for differential travel times. Seismograms are taken from broadband stations at the High Lava Plains array, USA for earthquake on 3rd January 2009 at 19:43 (latitude, -0.41°; longitude, 132.88°; depth, 17 km; magnitude, 7.7).

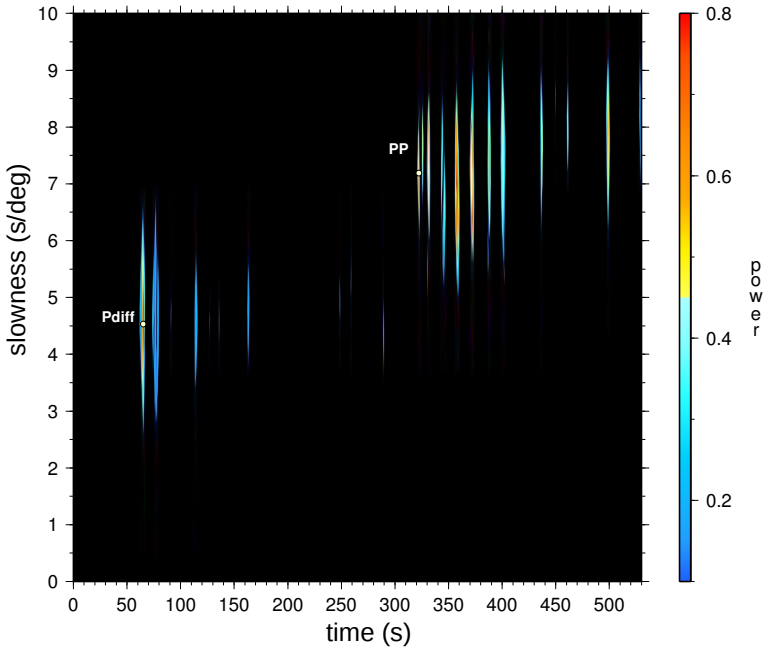

Figure 2.14: Vespagram generated for data in Figure 2.13. A range of slowness are used to correct for the time differences across the array for each time window and the amplitude of the resulting stack power is plotted in colour corresponding to the power scale. Seismograms are taken from broadband stations at the High Lava Plains array, USA for earthquake on 3$^{\text{rd}}$ January 2009 at 19:43 (latitude, -0.41°; longitude, 132.88°; depth, 17 km; magnitude, 7.7).

lected and transformed into the frequency-wavenumber domain. The tool uses trials of frequency and wavenumber, corrects for the moveout across the array, beamforms and calculates the total energy of that signal. The frequency-wavenumber pair that has the highest energy peak, corresponds to the slowness and backazimuth value which best aligns the signal. The key stages in the derivation of fk analysis are demonstrated below.

From Parseval's theorem, the energy recorded at an array is equal to the square of the amplitude of a wave. The energy in the frequency domain can be expressed as:

$$E(\boldsymbol{k} - \boldsymbol{k_0}) = \frac{1}{2\pi} \int |S(\omega)|^2 \, |A(\boldsymbol{k} - \boldsymbol{k_0})|^2 \, d\omega \tag{2.25}$$

where $S(\omega)$ is the Fourier transform of the time series (power spectral density), ω is the angular frequency, $\boldsymbol{k}$ is wave number vector, $\boldsymbol{k_0}$ is the wavenumber vector for slowness vector $\boldsymbol{u_0}$ and $|A(\boldsymbol{k} - \boldsymbol{k_0})|^2$ is the Array Response Function (ARF). The ARF is controlled by the number of stations (M) and the distribution of stations ($\boldsymbol{r_m}$) which affect the aperture size and inter-station spacing and is expressed as:

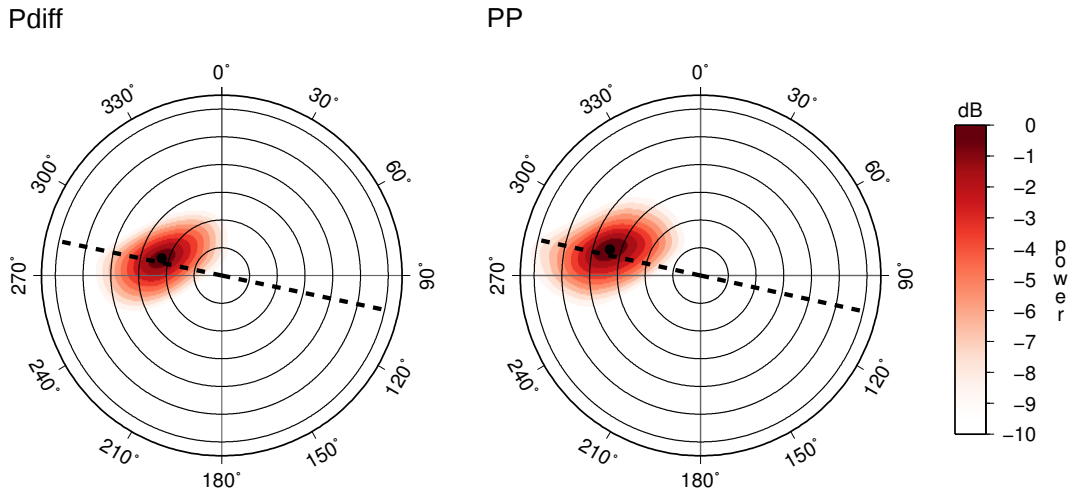

Figure 2.15: Results from fk-analysis shown as polar plots for P_{diff} and *PP*, with slowness varying on the radial. Contours on polar plots are centred around slowness and backazimuth found through fk-analysis. Circles on plots are slowness intervals of 2°/s. Analysis performed for data are taken from broadband stations at the High Lava Plains array, USA for earthquake on 3rd January 2009 at 19:43 (latitude, -0.41°; longitude, 132.88°; depth, 17 km; magnitude, 7.7).

$$|A(\boldsymbol{k}-\boldsymbol{k_0})|^2 = \left| \frac{1}{M} \sum_{m=1}^{M} e^{(2\pi i(\boldsymbol{k}-\boldsymbol{k_0})\cdot \boldsymbol{r_m})} \right|^2 \tag{2.26}$$

with

$$\boldsymbol{k} = (\mathrm{k_x}, \mathrm{k_y}) = \omega \cdot \boldsymbol{u}. \tag{2.27}$$

The wavenumber is directly related to slowness and backazimuth (equation 2.27) and by searching over a range of wavenumbers and evaluating the stacking power (equation 2.25), the optimum slowness and backazimuth can be identified for an arrival. The results of fk-analysis can be displayed as polar plots of beampower as a function of backazimuth and slowness (radial) (Figure 2.15).

As the frequency range has to be defined for the analysis, the frequency content of the signal should be known prior to fk analysis. Short time windows can be used so that only a single arrival is included in each analysis. The length of time window needed will vary between different signals and arrays and windows are chosen by considering the period of signal and the moveout (or time differences) of the arrival across receivers. The slowness and backazimuth derived from fk-analysis can be used along with traveltime to locate the origin of a scattered or reflected wave through migration.

2.5.3 Migration

Migration is a technique used in seismology to remove the effects of propagation (Stein and Wysession, 2003) by moving reflections to their true origin (Sheriff and Geldart, 1995). After the decades of success of using migrated seismics datasets from controlled sources, migration has started to play a prominent role in imaging small scale structures observed in teleseismic data (Lay, 1987, Lynnes and Lay, 1989, Scherbaum et al., 1997, Bostock and Rondenay, 1999, Thomas et al., 1999, Brana and Helffrich, 2004, Kito et al., 2007). Previously, migration has been difficult to implement in global seismology studies due to poor spatial coverage but with the recent installation of dense seismic arrays (e.g. USArray) migration can be powerful in revealing the 3D structure of Earth's interior.

There are many overlaps in applying migration procedures in global seismology studies to migration in exploration seismics, including Kirchhoff applications for simple geology, and wave equation algorithms for complex structures. Further details can be found in Yilmaz (2001) and reviews by Rost and Thomas (2002, 2009). Here, I will focus on describing some of the accessible techniques for studying small-scale structures in the mantle, namely Kirchhoff migration, simplified time migration, the generalised radon transform and the back projection (or steering) procedure.

Kirchoff migration applies Huygens principle to reflectors such that each point on the reflection surface is replaced by a secondary source resulting in closely placed diffraction points. In global seismology, 3D hyperbolae are created from 1D velocity models (Hutko et al., 2006) and the hyperbolae sum up coherently at the surface of the imaged feature and deconstructively elsewhere. The technique is not restricted to reflections, but can be used for imaging scatterers when assuming isotropic point scattering. When imaging deep reflectors or scatterers with low impedance contrast, weighted migrations have been used. For example Kito et al. (2007) use slowness and backazimuth weighted migration to effectively improve the migrated image of the scattering sources in subduction zones.

Simplified time migration is particularly useful in locating anomalous scattered energy in array data (e.g. Thomas et al., 2004). The method considers a grid of discrete cells (Figure 2.16) in a region that may contain 3D structure. The arrival time of an incoming wave from a cell is calculated at each station and the times are used to shift data (Figure 2.16). The amplitude at the arrival time is assigned to the cell resulting

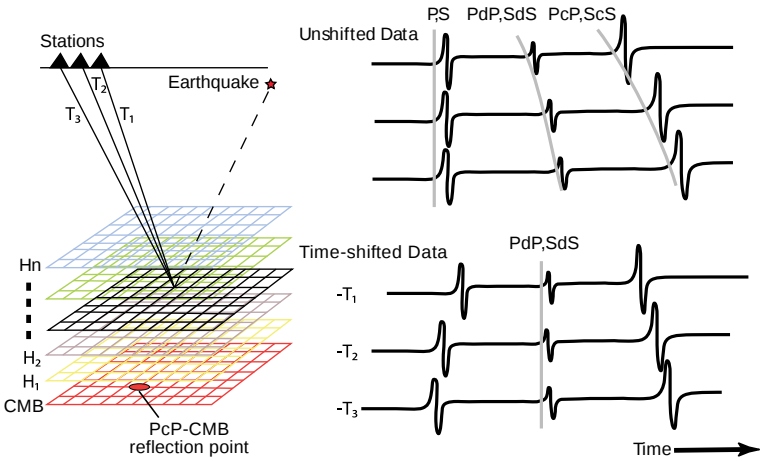

Figure 2.16: A schematic demonstrating the use of reverse time migration in imaging structure at the CMB using *PcP* or *ScS* waves. The mantle is split into a model of depth slices from H_1 to H_n containing a grid of cells. Travel times are calculated using the model from the earthquake to a chosen cell to each of the stations (T_1, T_2, T_3...). The travel times are used to shift the data and the seismograms are stacked. The amplitude at zero time is then placed at the cell. Reproduced with permission from Springer and Rost and Thomas (2009). With kind permission from © Springer Science and Business Media B.V. 2009.

in an amplitude density image of the study region. Simplified time migration requires many stations to ensure full data coverage and to increase signal-to-noise of the resultant image. This type of migration is is easy to implement and computation can be reduced by optimising cell size and the volume of the migration region.

Migration methods can also be applied in combination with radon transforms (e.g Wang et al., 2006, Ma et al., 2007, Kawakatsu and Watada, 2007). The radon transform (RT) is typically used in exploration seismology to attenuate unwanted events (Yilmaz, 2001). In recent years, RT has been explored in global seismology in an effort to suppress noise, enhance signal clarity and constrain travel times and slowness (Gu and Sacchi, 2009). The RT method is based on slowness slant stacking (or VESPA process) in the τ-p domain where slowness and travel times are derived for target arrivals (Figure 2.17).

The radon transform can be powerful for imaging crustal and mantle reflectivity structure. The generalised radon transform (GRT) is formed by incorporating Born scattering effects as was first applied in teleseismic imaging by Bostock et al. (2001). Since then the tool has been used to successfully map features in the D" and at the CMB (e.g Chambers and Woodhouse, 2006a,b, Wang et al., 2006, Van der Hilst et al., 2007, Cao et al., 2010). GRT is very powerful in generating images of structure from many different scattered phases and can reveal geometry and estimates of reflection

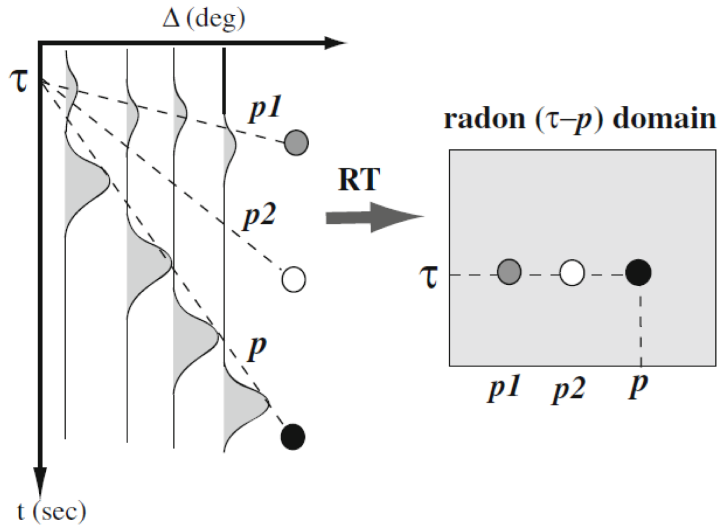

Figure 2.17: Radon transform procedure involves stacking along the ray parameter p. Ray parameter slopes of $p1$ and $p3$ map the strong time-domain peaks into sections of strong energy in the Radon domain (dark solid circle). In contrast, stacking along a ray parameter $p2$ results in negligible energy in the Radon domain. Reproduced with permission from Springer and Gu and Sacchi (2009). With kind permission from © Springer Science and Business Media B.V. 2009.

coefficients of heterogeneity bodies (Chambers and Woodhouse, 2006a, Wang et al., 2006).

Back projection (steering) techniques are similar in concept to simplified time migration, but exploit the slowness, backazimuth and traveltime of an arrival to identify the scattering point. The slowness and backazimuth of an arrival define a specific travel path through a 1D Earth model with the measured travel time defining a single point along this path. The back projection method is simple to implement and compute and has been useful in identifying regions of strong scattering prior to migrating with more sophisticated techniques (Chambers and Woodhouse, 2006a). As such, the back projection method is employed in this thesis in locating the scatterers detected at seismic arrays; details of the application of this method are found in Chapter 4.

Challenges that researchers face for imaging small-scale scatterers are centred around velocity models. Global seismology migration algorithms use travel times that are computed using ray-tracing of velocity profiles. As a good velocity model is crucial for the migration process, there will be relocation errors from using a 1D velocity model, especially for the deep mantle where the velocity structure is not well resolved. For the backprojection adopted, such errors are explored and explained in Chapter 4.

Chapter 3

Global patterns of heterogeneity derived from *PP* precursors

3.1 Overview

This Chapter describes an approach to obtain global averages of small-scale mantle heterogeneity from the stacking and modelling of *PP* and *PP* precursors. The main aim is to obtain global signatures of the high frequency *PP* precursory wavefield by stacking global seismic datasets. The heterogeneity that causes such precursory energy is analysed by forward modelling for scattering in the lithosphere and in the mantle using a Monte Carlo phonon based approach that incorporates ray theory (Shearer and Earle, 2004) and compares the resultant synthetic seismograms to the global average stacks. A key aim is to characterise and model global averages of the *PP* precursory wavefield for a large distance range in order to resolve the depth variation of the heterogeneity that cause this energy. Another aim is to produce average stacks of the *PP* wavefield in two hemispherical regions to assess regional variations of *PP* and *PP* precursors.

In this Chapter I describe the procedure I use for creating global and hemispherical average stacks of *PP* and *PP* precursors and highlight the key features of these stacks. Next, I summarise the key aspects of the modelling approach for studying the *PP* precursory wavefield and the main assumptions of the procedure. Then, I analyse the synthetics generated using published models and demonstrate that these models are not suitable to explain the features of *PP* precursors. Finally, I discuss a variety of new models that provide insight into the distribution and strength of mantle heterogeneity that contributes to the *PP* precursory wavefield.

3.2 Introduction

Most seismic investigations of the Earth's structure explore travel-times and waveforms of seismic phases that interact with the Earth's large-scale velocity structure. These observations are inverted for radially average velocity profiles and laterally varying 3D velocity models that are compared to large scale geodynamical processes. However, the short-period seismic record is dominated by scattered energy that is generated from small-scale heterogeneity. Scattered energy typically arrives as coda and precursory energy to main seismic phases. Most of the coda and some of the precursors are incoherent arrivals (see Chapter 2), which can be enhanced through envelope stacking and then modelled with statistical scattering theories (Shearer, 2007).

The first observations of the presence of seismic precursors were made by Gutenberg & Richter (1934) who found coherent arrivals prior to the onset of *PKP* and since then there has been a debate about their origin. The first attempt to calculate the strength of heterogeneity in the Earth from coda energy was described by Aki (1969) and Aki and Chouet (1975). Since these studies, a wide variety of scattering studies have observed and modelled coda and precursors to determine heterogeneity properties in the Earth. The majority of studies have explored P and S wave coda, as these mostly contain arrivals from strong scattering in the crust (or lithosphere) and upper mantle, but it is difficult to resolve the contribution of weaker scattering from deeper in the mantle in this coda energy (Shearer, 2007). Recently, many studies have explored precursors and coda of many P wave phases, and some of these arrivals are linked to scattering at a variety of depths in the mantle. Characterising scattering throughout the mantle is necessary for resolving the small-scale heterogeneity structure that cannot be imaged using seismic tomography. Detailed reviews of studies that analyse mantle scattering are contained in Sato and Fehler (1998) and Shearer (2007).

Scattering in the mantle has been explored using the coda to P (Shearer and Earle, 2004), P_{diff} (Bataille et al., 1990, Tono and Yomogida, 1996, Earle and Shearer, 2001) and $PKP(C)_{diff}$ (Nakanishi, 1990). Tono and Yomogida (1996) studied P_{diff} coda in the distance range 103-120° and compared the strength of P_{diff} coda to the strength of P coda. The differences in strength were linked to the lowermost mantle heterogeneities and a low velocity zone just above the CMB. Earle and Shearer (2001) also studied P_{diff} coda by stacking >900 seismograms from shallow events for distances 92.5-132.5°. They

found that the coda strength changes at 100°, a similar result as Tono and Yomogida (1996)), however they concluded that a whole mantle heterogeneity model presented the best fit to the data.

Shearer and Earle (2004) studied *P* coda with shallow (depth <50 km) and deep (depth >400 km) earthquakes to reduce the effect of lithospheric scattering. They created high density global envelope stacks for distances up to 100°, and modelled multiple scattering with a Monte Carlo phonon scheme. Scattering in the lithosphere and upper mantle was found (as expected for *P* coda) but they also concluded that lower mantle scattering was needed as well. Their preferred model contained 4% rms velocity heterogeneity at 4 km scale length for depths 0-200 km, 3% rms velocity heterogeneity at 4 km scale length for depths 200-600 km and 0.5% rms velocity heterogeneity at 8 km scale length for depths 600 km to the CMB.

Precursors to *P'P'* (Tkalcic et al., 2006), *PKKP(DF)* (Doornbos, 1974), *PKKP(BC)* Doornbos (1980), Earle and Shearer (1997), and *PKP* (e.g. Haddon and Cleary, 1974, Doornbos, 1978, Bataille and Flatt, 1988, Hedlin and Shearer, 2000, Hedlin et al., 1997, Margerin and Nolet, 2003b) have been shown to be produced by scattering in the different parts of the mantle. In particular *PKP* precursory energy has provided the most evidence for scattering in the deep mantle. *PKP* precursors were first used by Cleary and Haddon (1972) who correctly identified that the precursors arise by scattering from heterogeneities in the lowermost mantle. Other early studies explored scattering above the CMB as a source of precursors (e.g. Haddon and Cleary, 1974, Doornbos, 1978, Bataille and Flatt, 1988), whereas more recent studies have shown that whole-mantle scattering can explain the precursor amplitudes (Hedlin et al., 1997, Margerin and Nolet, 2003b) (Figure 3.1).

Doornbos (1974) analysed precursors to *PKKP(DF)* beneath the NORSAR array for earthquake data from the Solomon Islands and found that these are consistent with scattering in the mantle. Topography on the CMB has also been found to generate scattering that arrives as precursory energy, particularly to the BC branch of *PKKP*. Doornbos (1980), analysed *PKKP(BC)* precursors for distance range 80-110° and found a model of CMB topography of 100-200 m at 10-20 km horizontal scale length.

Precursors to *PKPPKP* (*P'P'*) have been shown to be linked to upper mantle scattering. Tkalcic et al. (2006) studied *P'P'* precursors for distances of <10°. Using precursor slowness and travel time they found that back scattering from small-scale

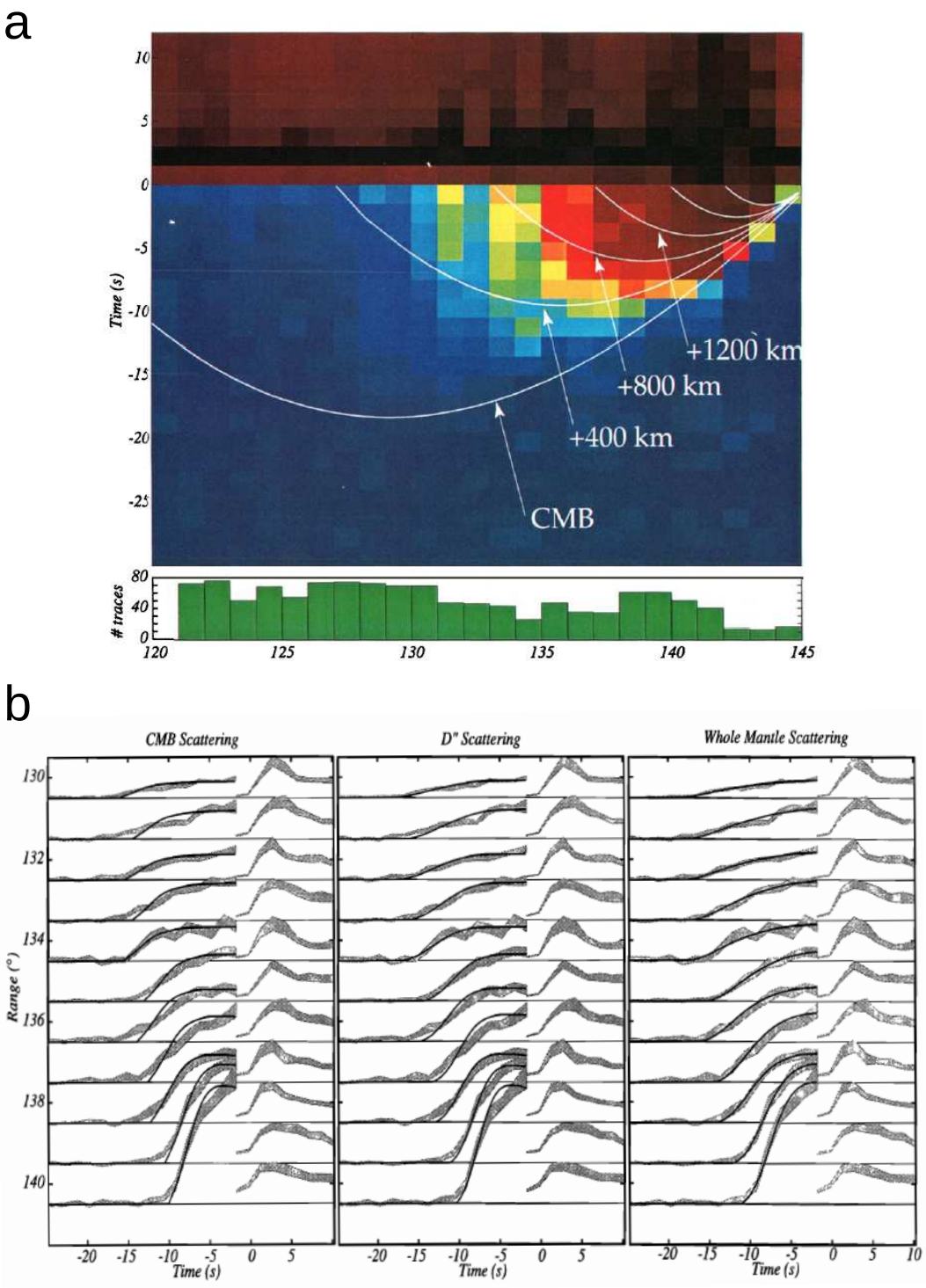

Figure 3.1: *PKP* precursors have been used to study heterogeneity in the mantle (Hedlin et al., 1997). a) For *PKP* data used in Hedlin et al. (1997), the sensitivity of the probe is restricted to <1600 km above CMB. Reproduced with permission from Hedlin and Shearer (2000) (http://onlinelibrary.wiley.com/doi/10.1029/2000JB900019/abstract). b) The *PKP* stacked data (grey bands) from Hedlin et al. (1997) are compared to synthetic data generated from different heterogeneity models (black): CMB scattering, *D"* scattering and scattering generated from the whole mantle. Models with scattering generated from whole mantle heterogeneity (right panel) are shown to fit the data best (Hedlin et al., 1997). However, this can only true for distances <139° (for depths <1200 km above the CMB). Reprinted by permission from Nature Publishing Group: Nature, Hedlin et al. (1997), copyright 1997

heterogeneities in the upper mantle (150-220 km depth) can explain the observations.

Scattering studies tend to focus on studying the lowermost mantle as this region is known to be highly heterogeneous and anisotropic. Even so, there remains a diverse collection of models that explain heterogeneity in the deep mantle with some models suggesting whole mantle scattering (Hedlin et al., 1997, Earle and Shearer, 2001, Hedlin and Shearer, 2002, Margerin and Nolet, 2003a), some suggesting reduced scattering in the lower mantle (Shearer and Earle, 2004) and some suggesting increased scattering in the lowermost mantle (Bataille and Flatt, 1988, Niu and Wen, 2001). Additionally, a problem seen across most studies is that whole mantle models and lower mantle scattering can explain the same observations (e.g. Hedlin and Shearer, 2000). As such, the ambiguity in the models arises from the lack of independent constraints from scattering in the upper and mid mantle.

This study attempts to characterise heterogeneity in the upper and mid-mantle by exploring precursors to *PP*. *PP* and its precursory energy have been used extensively for studying mantle structure (e.g. King et al., 1975, Kato and Hirahara, 1991, Revenaugh and Jordan, 1991, Estabrook and Kind, 1996, Weber and Wicks, 1996, Flanagan and Shearer, 1998, Deuss et al., 2006, Rost and Weber, 2002, Rost et al., 2008) but *PP* precursors have not been used previously for statistical modelling of small-scale heterogeneities in the mantle.

The aims of this Chapter are: a) to obtain global signatures of high frequency *PP* precursory wavefield through stacking of global datasets; b) to assess the hemispherical differences of the global stacks for any regional differences in *PP* precursory energy; c) to analyse the heterogeneity that causes the precursory energy by forward modelling of scattering in the lithosphere and mantle using a Monte Carlo phonon based method along side ray theory; d) to compare synthetic seismograms generated from forward modelling to the observed global stacks; e) to analyse and model the *PP* precursory wavefield for a variety of distances, attempting to resolve the depth dependence of the scattering that causes such precursory energy.

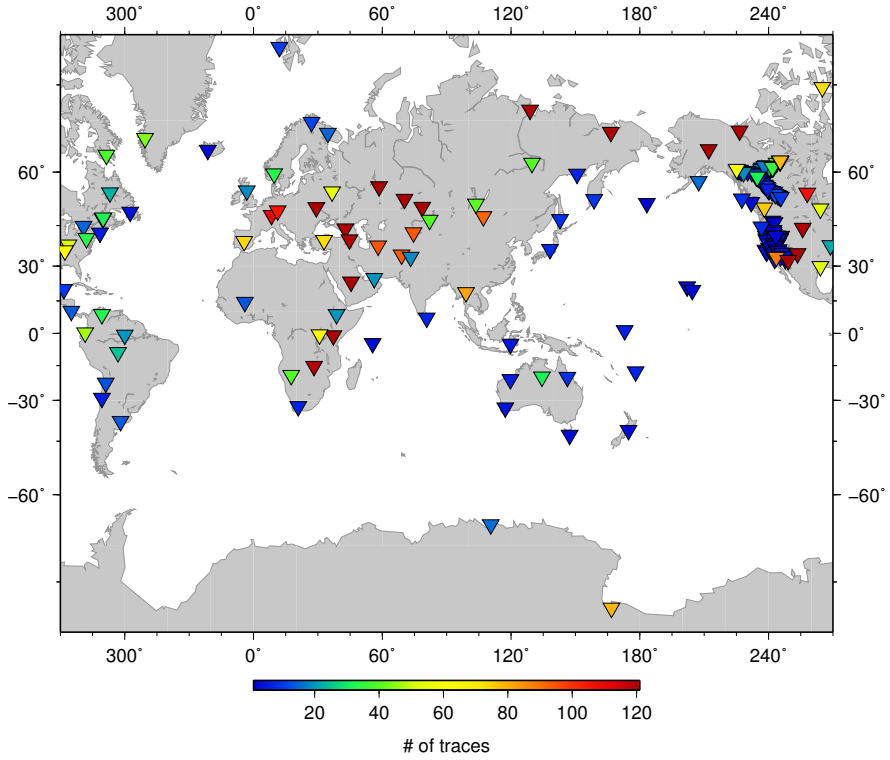

Figure 3.2: Stations used for global stacking of *PP* precursors (triangles), with symbol colour showing the number of traces used from each station in the stacks. Stations are well distributed across the globe. There is a high density of stations in North America and only a few stations from parts of Africa, Greenland and Russia. Only two stations are available for Antarctica. Eurasia stations contribute the most traces to the global stacks (≥120 traces).

3.3 Global stacking method

3.3.1 Networks and Data

Most of the stations used in this study are part of the Global Seismic Network (GSN). As GSN has >150 stations that are well distributed across all continents, this network is suitable for global seismic studies. Additional networks are included in the analysis to increase the overall coverage in the final stacked data. The extra networks used are North American arrays of USArray Temporary Array (TA); Canadian National network (CN), POLARIS network (POL) and Canadian Northwest Experiment (XN). These are selected as they are in a good distance range from regions of high earthquake activity. Data from 193 stations are used in the final stacks and their locations are shown in Figure 3.2. Time periods used for each array are listed in Appendix A.

Vertical broadband data are downloaded from the Incorporated Research Institutions for Seismology (IRIS) database (http://www.iris.edu) for earthquakes occurring from 2003 to 2012. Earthquakes are also selected based upon the following additional

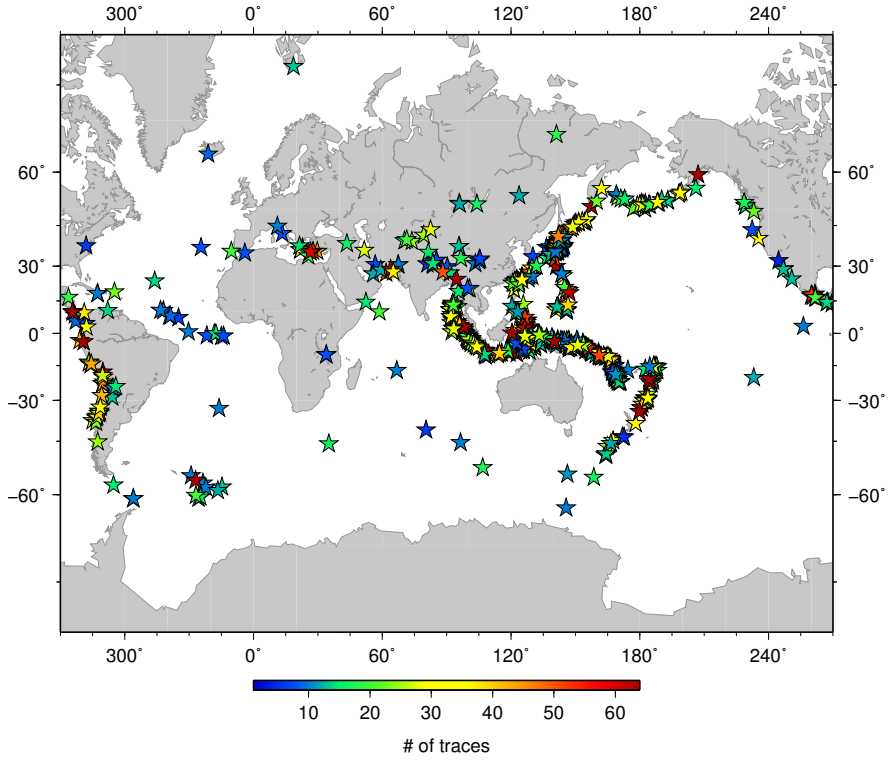

Figure 3.3: Earthquake locations used in global stacks with symbol (stars) colour showing the number of traces used from each earthquake in the stacks (max. 64 traces). Suitable earthquakes are generally located in subduction zones around the Pacific Ocean. Earthquakes that have >55 traces used in the stacks are distributed across all the earthquake centres.

criteria:

1. Earthquake depth, h: 0-100 km,

2. Earthquake magnitude, Mw >5.8,

3. Epicentral distance between source and station, Δ: 70-120°.

660 earthquakes are used in creating the stacks and these are shown in Figure 3.3. The distance ranges are chosen as *PP* precursors have been observed previously between 90° and 110° (Wright, 1972, Rost et al., 2008) and I attempt to extend this distance range (70-120°) in the search for further evidence of *PP* precursory energy. For a distance of 70° *PP* travels to 850 km depth and for 120° *PP* travels to 1550 km depth (Figure 3.4). Therefore variations in the character of *PP* in stacks across this distance range will be linked to properties of the mantle between 850 km to 1550 km. As *PP* precursors arrive with slowness similar to *PP* arrival (Rost et al., 2006), it is likely that the precursors travel to similar depths as *PP*. However, this is not necessarily

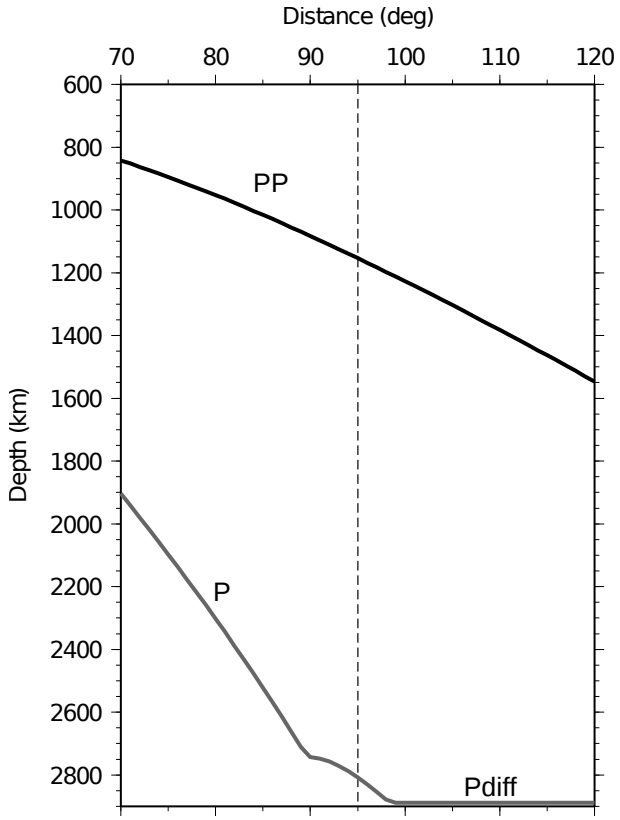

Figure 3.4: *PP* and *P* turning depths for the 70-120° distance range using in this study. Turning depths are calculated using IASP91 (Kennett and Engdahl, 1991). *PP* turning depth ranges from 850 km at 70° distance to 1550 km at 120° distance. For reference, the turning depth of *P* is shown and from 98° distance, the diffracted *P* wave P_{diff}) travels along the CMB.

the case since the scattered arrivals may have scattered multiple times (Shearer, 2007) and travelled out of plane, and therefore may travel to deeper depths than *PP*.

3.3.2 Pre-processing

Data are re-sampled to 100 samples per second and filtered using a two way bandpass filter with corner frequencies at 0.5 Hz and 2.5 Hz. This frequency band is chosen as high frequency noise is removed and this frequency range is sensitive to the small-scale (10 km) structure in lower mantle (Shearer and Earle, 2004). The envelope time function (Shearer, 1999) of each trace is calculated to obtain phase independent amplitude for stacking. The stacking of noise can be reduced by ensuring the mean of the noise is zero. An estimate of the mean noise level is found using the pre-signal noise, calculated in a small time window (25 s) starting 60 s before *P* (or P_{diff}), and this level is subtracted from the complete time series before stacking.

The data are aligned on the theoretical travel time of *PP* as calculated through

PREM (Dziewonski and Anderson, 1981). The actual *PP* arrival times in this dataset differ from the theoretical *PP* arrival times of PREM or other reference models, consistent with *PP* arrivals used in Chapter 4. Therefore *PP* was automatically picked using the following steps:

1. Using a low pass filter with cut off frequency of 0.05 Hz, a long period version of the dataset is created for each event. The time series for each record are cut at 5 s before and 30 s after theoretical *PP* time.

2. *PP* is picked by selecting the highest amplitude peak in this 35 s time window and this pick cannot coincide with the limits of the time window (at $t = -5$ s or $t = 30$ s). If *PP* cannot be identified, the trace is removed from further analysis.

3. Data are aligned on the picked *PP* and cut to the appropriate length.

4. Data are visually checked to ensure that *PP* has been picked correctly and to remove data where *PP* does not have a clear onset.

The signal to noise ratio (SNR) of *PP* to the noise level before *P* (or P_{diff}) is calculated and traces with SNR <5 are removed. The data are organised into 5° degree distance bins, centred at 72.5°, 77.5°, 82.5°, 87.5°, 92.5°, 97.5°, 102.5°, 107.5°, 112.5° and 117.5°.

3.3.3 Stacking of *PP*

Aligned data are stacked within each distance bin by summing the traces together, normalising by the number of traces and the absolute amplitude of *PP*. The stacks are shown in Figure 3.5 along with the number of traces used to create each distance stack. It is observed that *PP* is prominent and the shape is consistent across all distances. The *PP* precursory energy (100 s before *PP*) is clearly visible for distances >95° but *P* coda energy dominates within this time window for shorter distances. In contrast, for all distances the *PP* coda is visible and decays slowly, such that the amplitude is >30% of *PP* amplitude even at 100 s after *PP*.

The *P* coda is strong in the 100 s before *PP* for shorter distances (Δ <95°) and rapidly decreases in strength at 95° (Figure 3.5), coinciding with the direct *P* wave energy diffracting around the core P_{diff}. The IASP91 travel-time curves in Figure 3.5 show *PKiKP* becomes post-critical at cross over distance of 105°. For distances 70-107.5°, *PKiKP* is not visible, but can be seen in the stacks for distances 112.5° and 117.5° when *PKiKP* arrives >20 s before *PP*.

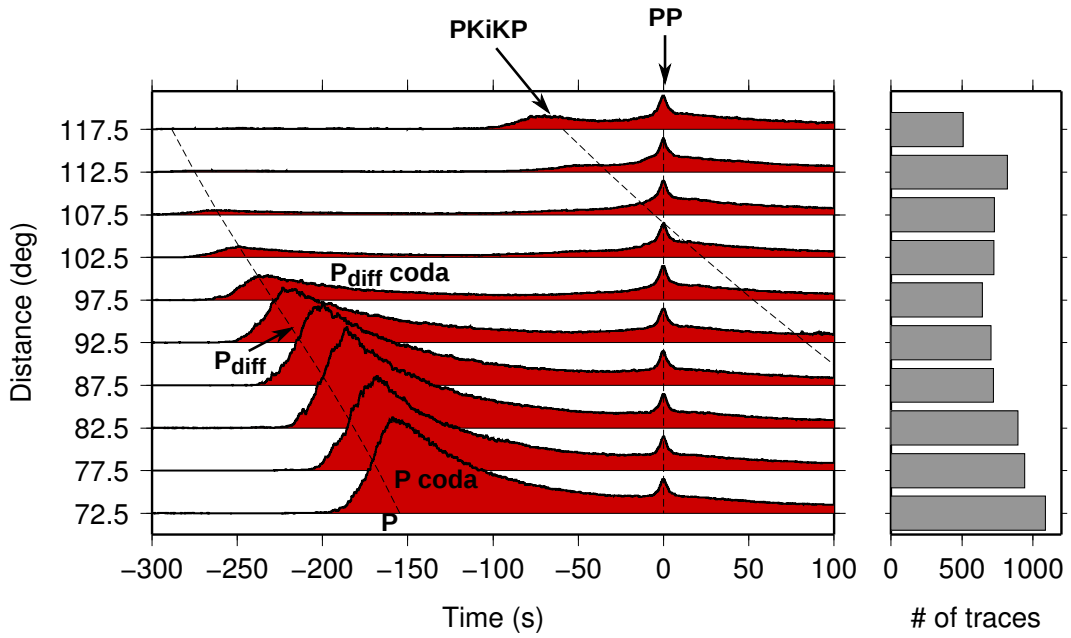

Figure 3.5: Global envelope-function stacks of 7905 traces organised and stacked in 5° distance bins. Time is relative to the *PP* arrival as indicated. *P*, P_{diff} and *PKiKP* travel times from IASP91 (Kennett and Engdahl, 1991) are marked as thin, black, dashed lines. *P* and P_{diff} are non-impulsive and the arrivals gradually increases with time due to aligning on *PP* and stacking in 5° distance bins. The number of seismograms stacked in each bin are shown on the right panel.

The number of traces in each distance bin generally decreases with distance, ranging from a minimum of ∼500 traces for 117.5° to a maximum of >1000 traces for 72.5° (Figure 3.5). The final stacked dataset provides good global coverage with the best sampled region beneath the Pacific Ocean and poorest sampling beneath Antarctica (Figure 3.6).

For the distances between 70° to 95°, it is difficult to separate the contributions from the *P* coda and *PP* precursory energy in the 100 s before *PP* target window, both in the single seismic traces and also in the stacked data (Figure 3.5). For distance bin 97.5° the *PP* precursory energy is visible but the onset of precursors is not clear due to interference from P_{diff} coda. For distances bins 102.5° and greater, the P_{diff} coda is weak and the onset of *PP* precursory energy is clear.

3.3.4 Removing the *P* coda

To remove interference of the *P* coda and P_{diff} coda, these codas are removed for each seismic trace (before stacking) by fitting and subtracting an exponential trend. An exponential trend is chosen because *P* coda have been shown to decay exponentially due

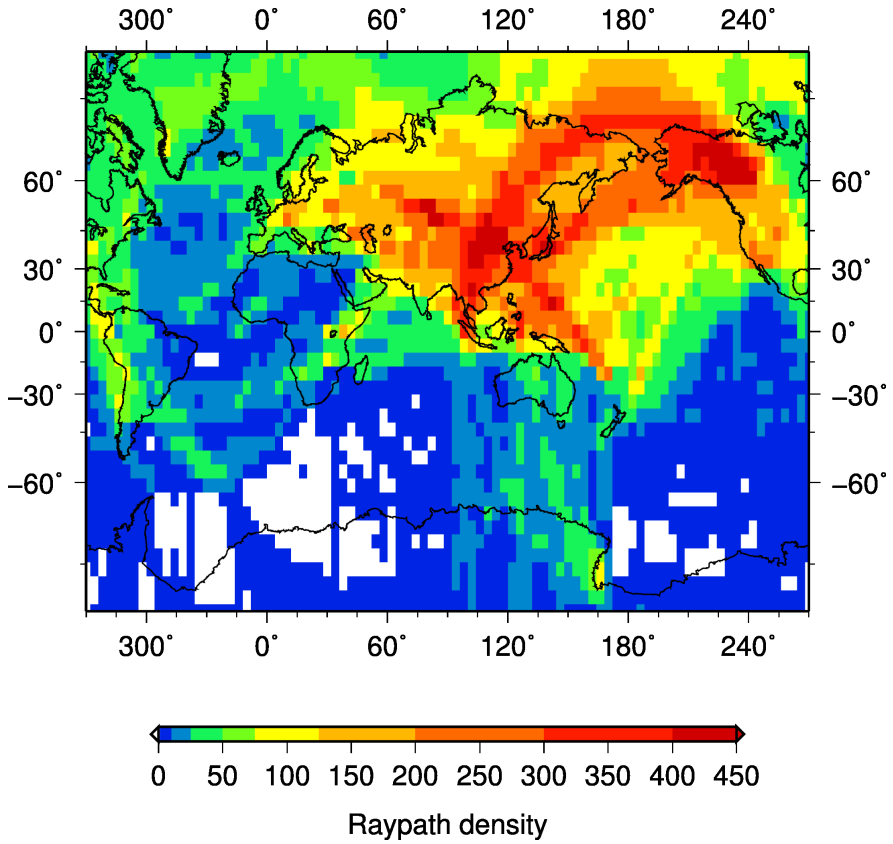

Figure 3.6: Spatial sampling of the seismic traces used in the global stacks. Raypath density in 4° bins is the found by summing the source-receiver great circle paths from every trace used in stacking. Most of the globe is sampled, with the greatest density observed in west North America, Japan and south-east Asia. There is poor sampling for Antarctica due to limited stations sited and earthquakes occurring in this region.

to intrinsic attenuation in the crust (Stein and Wysession, 2003). For the dataset used in this study, it is observed that the trend of complete P coda does deviate away from a single exponential function, possibly due to anelastic effects in the crust at the source and receiver side of the raypath. A solution to this issue is to fit an exponential decay to the later section of the P coda (Figure 3.7), using several different time windows and evaluating for goodness-of-fit. Other studies avoid this issue by using deep earthquakes (Shearer and Earle, 2004) but that was not possible for this study as the depth phase pPP would arrive in the PP precursory window.

The removal of the P coda is performed in 3 steps. First, the gap L is defined as the time difference between the highest peak of P (or P_{diff}) at time t_P, and the peak of PP at time t_{PP} (Figure 3.7). L is used to define the limits of the analysis time window (centred at t_i as shown in Figure 3.7) with the lower limit equal to $\frac{L}{8}$ and upper limit equal to $\frac{3L}{8}$. Second, the data are smoothed using 5 s moving average filter. Third, an exponential function is fit using a least-squares fitting approach which solves for non-linear least squares inverse solution using a trust-region-reflective-algorithm (MathWorks, 2013).

The goodness-of-fit (residual between input data and output model) of the exponential function and the stacked data are found to be dependent on the time window used, therefore steps 1-3 were repeated for varying time windows whose limits are defined by shifting t_i by -10 -5, 5, 10 and 15 s. The best exponential fit to the data is evaluated by finding the smallest residual and the optimum function is subtracted from the observed stacked data for the full time series.

After removing the P coda the data are stacked within each distance bin by summing the traces together, normalising by the number of traces and the amplitude of PP (Figure 3.8). PP is prominent with good waveform coherency and the PP precursory and PP coda energy are clearly visible for all distances. The PP precursory energy starts within 100 s prior to the onset of PP and increases in strength with time as can be seen in Figures 3.8 and 3.9). It is difficult to characterise the onset of PP precursors as the energy builds over time and the amplitude of the the base noise level is unclear.

The build up of energy can be characterised by looking at contours of equal amplitude (Figure 3.9). PP precursors that have amplitude of 10% PP amplitude (A_{PP}) arrive at earlier times for larger distance. For distance bin 72.5° the 10% contour is at $t = -50$ s at 72.5° and for distance bin 117.5° the 10% contour is at $t = -90$ s

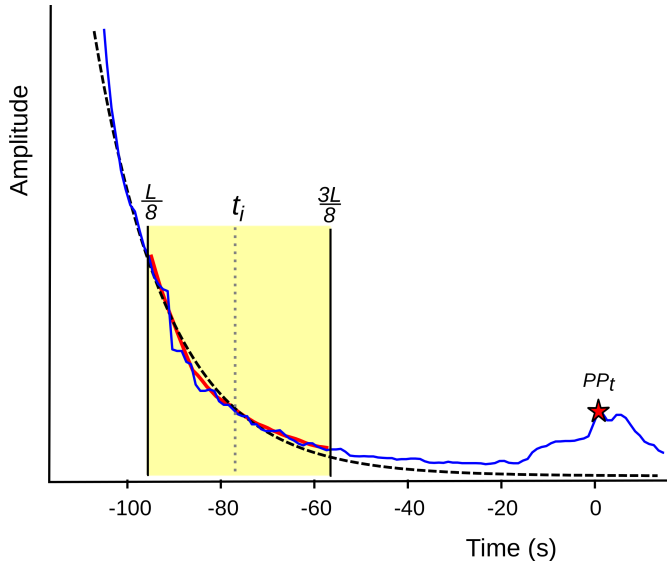

Figure 3.7: P coda removal approach for analysis window (yellow box) centred at t_i, bounded by limits of $\frac{L}{8}$ and $\frac{3L}{8}$, where L is the time lag between the maximum peak in P and the picked arrival time of PP (marked as red star). Original data (blue trace) is smoothed with 5000 point moving average filter for the analysis window. The smooth data (red) are fit with a least-squares exponential function model (black dashed line).

(Figure 3.9). Since 10% of A_{PP} is an arbitrary selected ratio, a contour of 20% of A_{PP} is also analysed and the arrival time of this energy has a similar trend with distance as the 10% contour. In summary, though the actual onset of PP precursory energy is unknown, constant amplitude contours of 10% and 20% show that the build up of precursory energy start earlier for larger distances and the strength of precursory energy increases with distance.

Few other phases appear coherently in the stacks. $PKiKP$ is visible for the 112.5° distance stack and is strong in the 117.5° stack. Conversely, coherent arrivals for the underside reflections from the 410 km and 660 km discontinuity are noticeably absent for all distances studied.

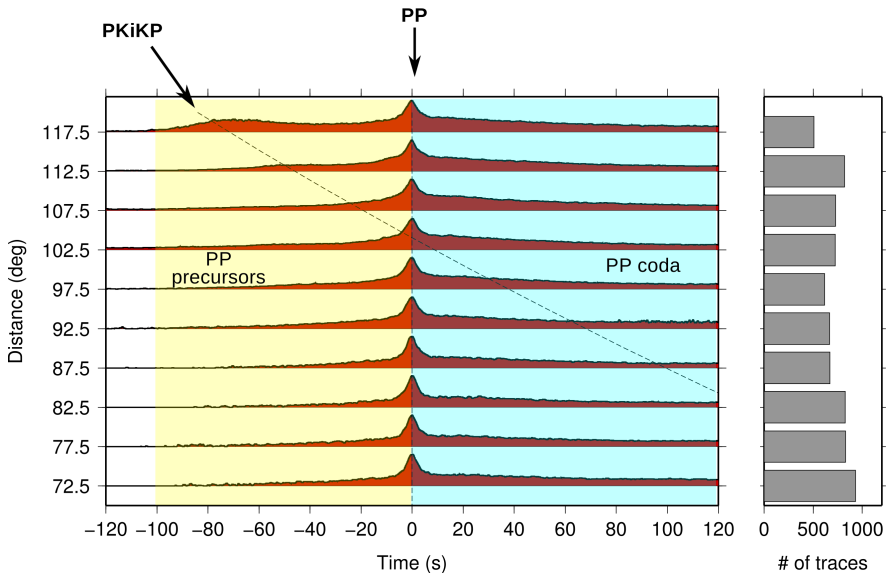

Figure 3.8: Envelope-function stacks for all data after processing and *P* coda removal. The number of seismograms that are summed within each 5° distance bin is shown on the right panel, for a total of 7320 traces. Time is relative to the *PP* arrival as indicated. *PP*, *PP* precursors (yellow box), *PP* coda (cyan box) and *PKiKP* are also identified.

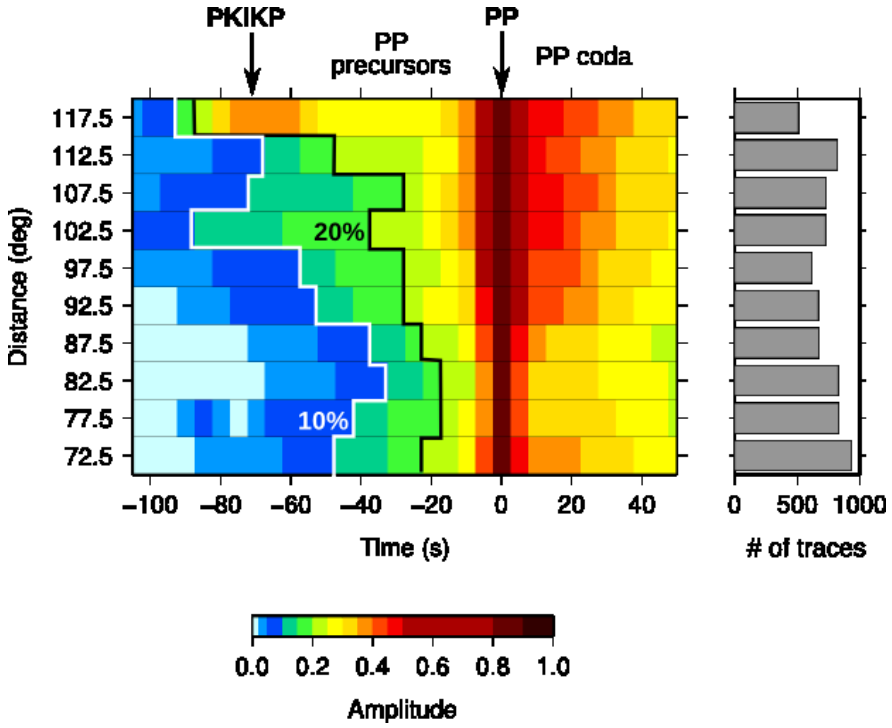

Figure 3.9: Power density representation of the stacks for all data after processing and *P* coda removal. The number of seismograms that are summed within each 5° distance bin is shown on the right panel, for a total of 7320 traces. Seismograms are aligned on *PP* and time is relative to the *PP*. The onset of *PP* precursors is difficult to pick. Variations in precursor strength can be found by comparing constant *PP* amplitude ratios, specifically contours of 10% (white) and 20% (grey) of amplitude of *PP*.

3.3.5 Regional stacks

To determine if there are hemispherical differences in the *PP* precursory energy, regional stacks are generated over two regions: the Pacific Ocean and the Atlantic Ocean. Regional differences amongst large scale stacks have been found previously by exploring variations in *PKP* precursors (Hedlin and Shearer, 2000). Weak scattering was found beneath South and Central America and Eastern Europe, whereas strong scattering was observed beneath Africa and the Tethyan margin. As *PKP* samples the lowermost 1000 km of the mantle, the scattering variations observed with this probe may not apply to *PP* precursors since these may be more sensitive to the mid-mantle (Shearer, 2007).

For this study regional variations in *PP* wavefield are analysed for two regions only as the source-receiver distances of 70-120° limit the regions that can be studied with high density stacking. The two regions selected are beneath the Atlantic Ocean and Pacific Ocean and these are chosen due to differences in tectonic processes between these regions and because each region is sampled by enough data for stacking (Figure 3.9). Data are selected for source-receiver paths between longitudes 60°E and 60°W for the Pacific region (4166 traces) and longitudes 150°W and 60°E for the Atlantic region (896 traces) (Figure 3.10). After stacking for each region without removing the *P* coda, the stacks are very similar for *PP* and *PP* precursory and coda energy (Figure 3.11). Some amplitude differences are observed in the *P* coda for distances 72.5-97.5°, which may exist due to variations in earthquake amplitudes.

The Pacific and Atlantic regional stacks are compared with the *P* coda removed in accordance with the method in Section 3.3.4 to highlight any variations in the *PP* wavefield. Figure 3.12 shows the regional stacks and the number of traces that are used in each distance stack. *PP*, *PP* precursors and *PP* coda are very similar in shape and amplitude between the stacks for each bin. Small variations are only observed in the precursory and coda energy for distance 87.5° (Figure 3.12). These amplitude differences are not observed in the stacks without removing *P* coda (Figure 3.11) and therefore the minor differences may arise from variations in the *P* coda removal that may be amplified when stacking with fewer traces (Figure 3.12).

To summarise, the regional stacks with and without *P* coda removal demonstrate that there are limited regional variations in the strength and shape of *PP* and *PP* precursors for almost all distances. As a result, the global stacks found in Section 3.3.3

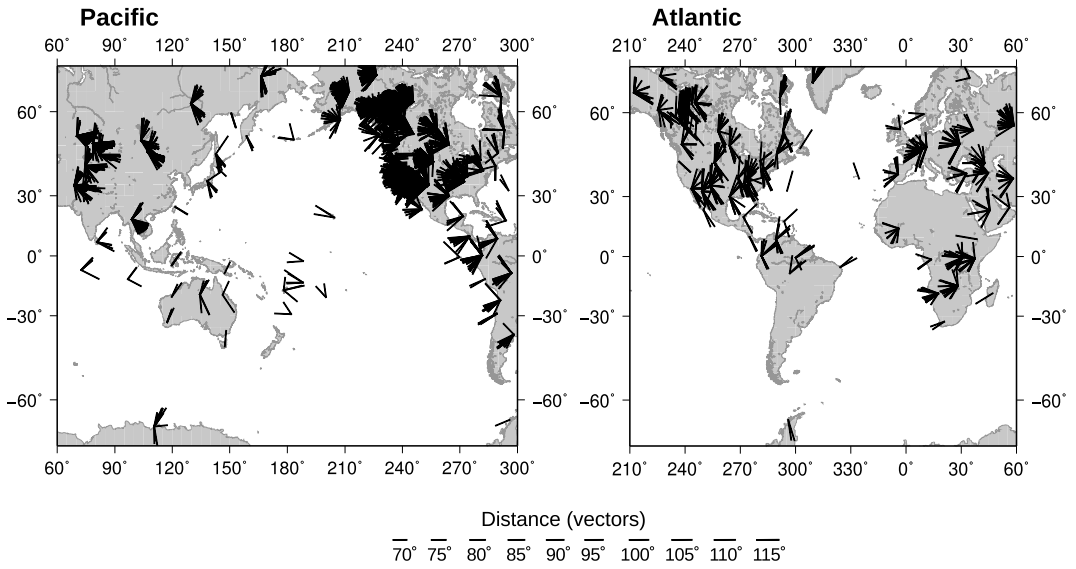

Figure 3.10: Map showing the locations of stations used for the comparison of two regional stacks. For the "Pacific" region, stations are selected in within longitude limits: 60°E and 300°E. For the "Atlantic" region, stations are selected in within longitude limits: 150°W and 60°E. At each station, data are used for the stacks are selected if the raypath crosses the relevant region. The azimuth of these data are shown at the station locations (black vectors) where length of vector is proportional to distance between earthquake source and station. The west coast of North America has a high density of stations that are for both Pacific and Atlantic stacks.

are suitable global and hemispherical averages of *PP* and *PP* precursors. Therefore the Monte Carlo models presented in the next Section are only compared to the global average stacks.

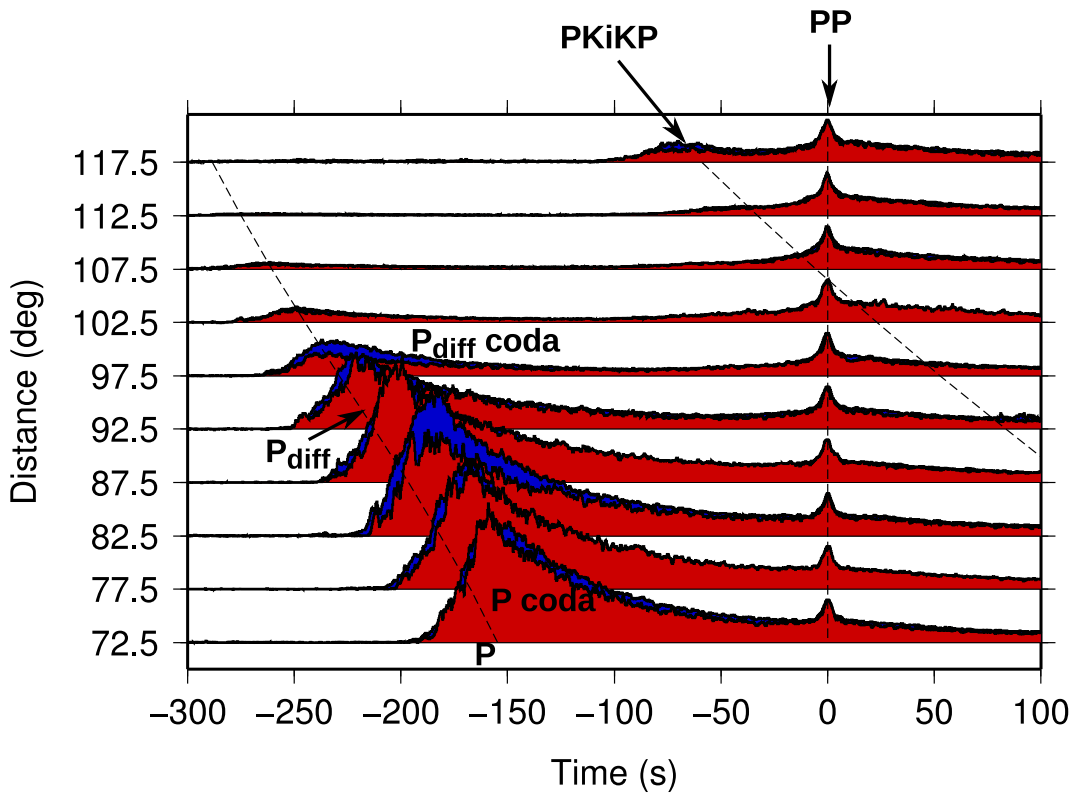

Figure 3.11: Comparison of the Pacific (blue) and Atlantic (red) regional envelope-function stacks. Time is relative to the *PP* arrival at $t = 0$. *P*, P_{diff} and *PKiKP* are marked as thin, black, dashed lines. *P* coda and P_{diff} coda are also identified.

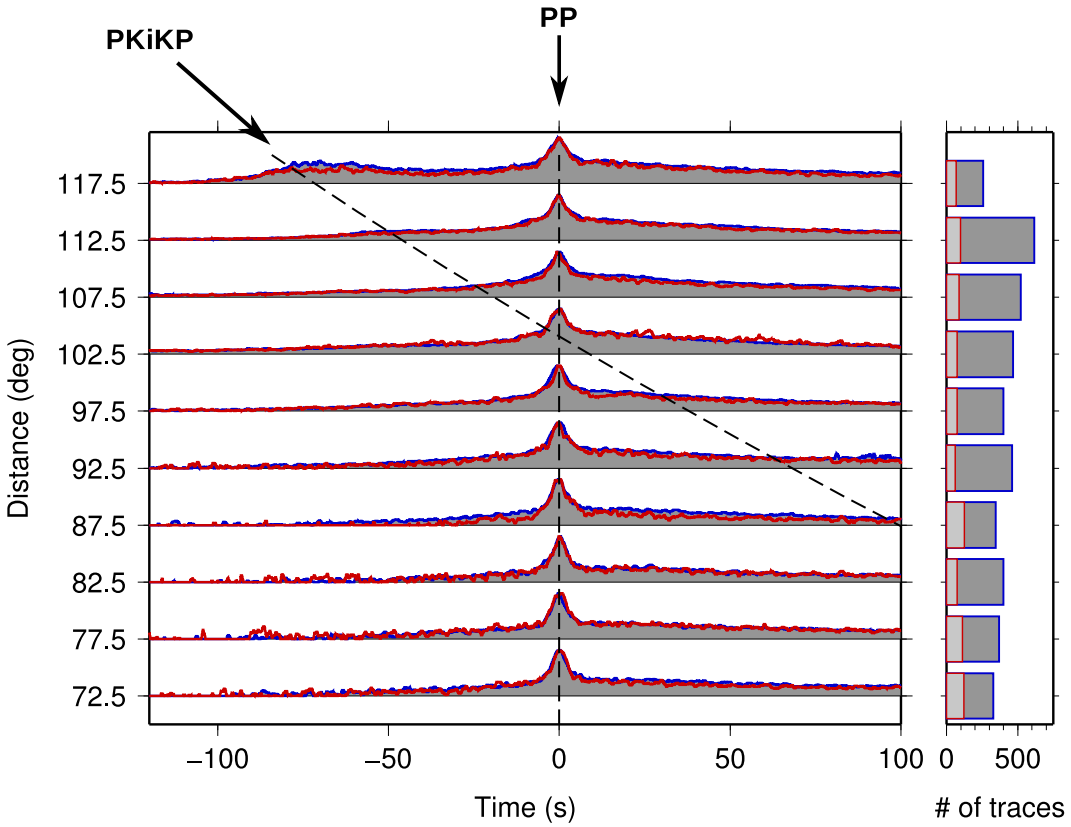

Figure 3.12: Comparison of the Pacific and Atlantic regional envelope-function stacks with P coda removed. Time is relative to the PP arrival as indicated. P, P_{diff} and $PKiKP$ are marked as thin, black, dashed lines. Number of traces in each distance bin (right) are: 4166 traces for Pacific stack (blue outline, dark grey fill) and 896 for Atlantic stack (red outline, no fill).

3.4 Monte Carlo modelling approach

As described in Chapter 2, there are various approaches to modelling scattering including single-scattering theory and the Born Approximation for weak scattering, and diffusion equation and radiative transfer theories for strong scattering. For modelling the *PP* precursory wavefield in this study, a Monte Carlo phonon based method by Shearer and Earle (2004) is used. The approach uses radiative transfer theory to model energy transport of phonons through whole Earth scattering models, taking into account the energy reduction in the primary wavefield and permitting multiple scattering events to occur. This method is chosen to model the *PP* precursors because it can simulate high frequency multiple scattering that is depth dependent. Multiple scattering has been shown to contribute a substantial amount of energy to the *P*coda (Frankel and Clayton, 1986) and therefore modelling of multiple scattering in the lithosphere, and potentially deeper in the mantle, is needed (Shearer, 2007). Additionally, the statistical phonon approach by Shearer and Earle (2004) provides information about the physical scattering process, without the intensive computing power that is required for finite difference models (Shearer, 2007).

In addition, intrinsic attenuation is incorporated into the modelling and can vary with depth. As the method is based on ray theory, the computation time for the completion of the models is manageable and each calculation is completed in ∼10 hours. There are limitations of using ray theory methods including the inability to model core diffracted waves such as P_{diff} (and this is noticeable in the synthetic seismograms produced, see Section 3.6).

In using the Monte Carlo method, one can vary the scattering properties of layers in the Earth by defining two key parameters that describe the scattering properties: root mean square (rms) fractional velocity fluctuation ϵ and the correlation (scale) length of the heterogeneity a. The following derivations show how these two parameters relate to the radiation pattern and amplitude of scattered waves, and demonstrate that by using energy transfer of phonons and scattering probabilities, one can produce synthetic seismograms that are representative of the *P*-to-*P* and *S*-to-*P* scattering produced in modelling a heterogeneous Earth, as described by Shearer and Earle (2004) and Shearer and Earle (2008). More extensive derivations and explanations on Born theory can be found in Sato and Fehler (1998), Wu (1985) and Wu and Aki (1985).

It is assumed that the fractional velocity variation ($\frac{\delta v}{v}$) for P wave velocity (α) and S wave velocity (β) are the same:

$$\xi(\boldsymbol{x}) = \frac{\delta\alpha(\boldsymbol{x})}{\alpha_0} = \frac{\delta\beta(\boldsymbol{x})}{\beta_0}, \tag{3.1}$$

where the mean P and S wave velocities of the medium are α_0 and β_0 respectively. The fractional density fluctuations are assumed to be proportional to the velocity variations:

$$\frac{\Delta\rho(\boldsymbol{x})}{\rho_0} = \nu\xi(\boldsymbol{x}), \tag{3.2}$$

with ν as a scaling factor between the velocity and density fluctuation. As the scattering is related to small-scale anomalies that are almost certainly compositional (Hedlin et al., 1997), an appropriate value for ν is 0.8 as obtained using Birch's Law (Sato and Fehler, 1998) as used in previous studies (Shearer and Earle, 2004).

Different scattering radiation patterns are produced depending on type of incident and scattered wave. The scattered wave components for varying incident and scattered waves in the r, ψ, ζ coordinate system (Figure 3.13) are given by the following equations:

$$\begin{aligned}
X_r^{PP}(\psi,\zeta) &= \frac{1}{\gamma_0^2}\left[\nu\left(-1+\cos\psi+\frac{2}{\gamma_0^2}\sin^2\psi\right)-2+\frac{4}{\gamma_0^2}\sin^2\psi\right],\\
X_\psi^{PS}(\psi,\zeta) &= -\sin\psi\left[\nu\left(1-\frac{2}{\gamma_0^2}\cos\psi\right)-\frac{4}{\gamma_0}\cos\psi\right],\\
X_r^{SP}(\psi,\zeta) &= \frac{1}{\gamma_0^2}\sin\psi\cos\zeta\left[\nu\left(1-\frac{2}{\gamma_0}\cos\psi\right)-\frac{4}{\gamma_0^2}\cos\psi\right],\\
X_\psi^{SS}(\psi,\zeta) &= \cos\zeta\left[\nu\left(\cos\psi-\cos 2\psi\right)-2\cos 2\psi\right],\\
X_\zeta^{SS}(\psi,\zeta) &= \sin\zeta\left[\nu\left(\cos\psi-1\right)+2\cos\psi\right],
\end{aligned} \tag{3.3}$$

where X_r^{PP} and X_r^{SP} are the radial components of P-to-P and S-to-P scattering respectively, X_ψ^{PS} and X_ψ^{SS} are the ψ component of P-to-S and S-to-S scattering respectively, and X_ζ^{SS} is the ζ component for S-to-S scattering. The angles ψ and ζ define the coordinate system of the scattered wave and coordinates X_ψ, X_ζ and X_r are shown in Figure 3.13. The velocity ratio γ_0 is defined as $\gamma_0 = \alpha_0/\beta_0$ and is approximated to a constant value within each scattering layer, calculated from the average velocity in that layer.

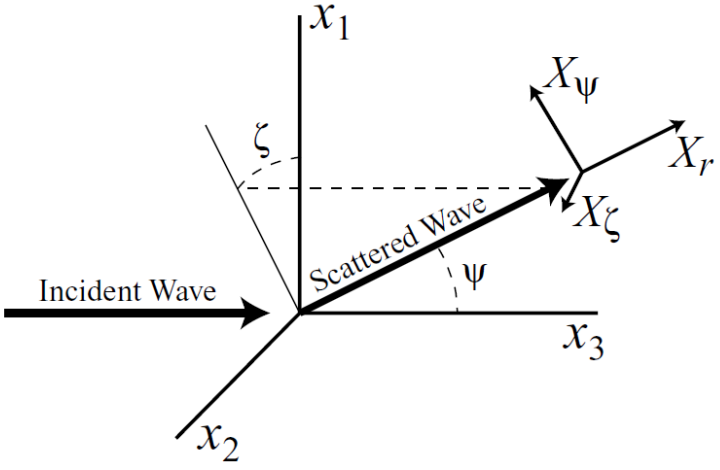

Figure 3.13: The coordinate axes for an incident wave are defined as x_1, x_2 and x_3. The incident ray is in the x_3 direction and for S waves, the initial polarisation is in the x_1 direction. The scattered ray direction is defined by the angles ψ and ζ, and the scattered ray polarisation is defined by coordinate axes X_r, X_ψ and X_ζ. Reproduced with permission from Shearer and Earle (2004), Figure 5.

The amount of power for each scattering component is required. The scattering power per unit volume (e.g. $g^{PP}(\psi, \zeta; \omega)$) is found by combining a random media model with the scattering coefficients (as obtained in Equation 3.3):

$$
\begin{aligned}
g^{PP}(\psi,\zeta;\omega) &= \frac{l^4}{4\pi}\left|X_r^{PP}(\psi,\zeta)\right|^2 P\left(\frac{2l}{\gamma_0}\sin\frac{\psi}{2}\right), \\
g^{PS}(\psi,\zeta;\omega) &= \frac{1}{\gamma_0}\frac{l^4}{4\pi}\left|X_\psi^{PS}(\psi,\zeta)\right|^2 P\left(\frac{l}{\gamma_0}\sqrt{1+\gamma_0^2-2\gamma_0\cos\zeta}\right), \\
g^{SP}(\psi,\zeta;\omega) &= \gamma_0\frac{l^4}{4\pi}\left|X_r^{SP}(\psi,\zeta)\right|^2 P\left(\frac{1}{\gamma_0}\sqrt{1+\gamma_0^2-2\gamma_0\cos\zeta}\right), \\
g^{SS}(\psi,\zeta;\omega) &= \frac{l^4}{4\pi}\left(\left|X_\psi^{SS}(\psi,\zeta)\right|^2+\left|X_\zeta^{SS}(\psi,\zeta)\right|^2\right) P\left(2l\sin\frac{\psi}{2}\right),
\end{aligned}
\tag{3.4}
$$

where the l is the S wavenumber for a given angular frequency (ω) is defined as $l = \omega/\beta_0$, and P is the power spectral density function (PSDF) for the random media model (Sato and Fehler, 1998). A exponential autocorrelation function is used to characterise scattering in random media (see Chapter 2) with associated PSDF defined as:

$$
P(m) = \frac{8\pi\epsilon^2 a^3}{(1+a^2m^2)^2}, \tag{3.5}
$$

where m is the wavenumber, a is the correlation length, ϵ is the rms of $\xi(\boldsymbol{x})$, the fractional velocity variation (equation 3.1) and ϵ is found from $\epsilon^2 = \langle \xi(\boldsymbol{x}) \rangle$.

The total scattering coefficients (e.g. g_0^{PP}) are found by taking the averages of the coefficients in equation 3.4 over a unit sphere. These are used to define the mean free path length ℓ (the average length the ray travels between scattering events) by calculating the reciprocals of the sum of the coefficients:

$$\begin{aligned} \ell^P &= \frac{1}{g_0^{PP} + g_0^{PS}}, \\ \ell^S &= \frac{1}{g_0^{SP} + g_0^{SS}}. \end{aligned} \tag{3.6}$$

P and S phonons are emitted from the source only in a specified direction only. For each phonon, the probability of a scattering occurrence is constant along its ray path. The length, r, to a point of scattering is related to the mean free path length ℓ and is found by:

$$\begin{aligned} r_P &= -\ell^P \ln x \\ r_S &= -\ell^S \ln x, \end{aligned} \tag{3.7}$$

where x is a random number between 0 and 1 and ℓ^P and ℓ^S are mean free paths for incident P and S waves respectively. A second random number is used to decide whether the scattered energy is P or S wave. A third random number is used to calculate the scattering angle (ψ and ζ) and if required, the S polarisation angle. The phonon then travels in the new direction until another scattering event. For each phonon, the calculation continues until a predefined time limit is reached and then a new phonon is emitted from the source.

The phonons are traced through the model and are counted at the free surface where they are observed and synthetic seismograms are produced. After only a few phonons are received, the seismograms appear noisy (or spikey) but over time as more phonons are computed, the seismogram will become more smooth. For isotropic sources and Earth models with bulk properties that are radially symmetric, the wavefield observed at the free surface is a function of distance as well as time and so the wavefield output is

used to construct synthetic seismograms for 0.5° distance increments. The seismograms are generated for all components of ground motion, however only the synthetics for the vertical component are used. Each phonon retains information about the travel path, which can be used to extract slowness information.

3.5 Application to global models of PP precursors

The phonon scattering modelling method is used to create synthetic seismograms, which are compared to the stacked *PP* arrival and *PP* precursory energy (as generated in Section 3.3.3). The modelling depends on several parameters and some of these parameters are fixed for all models including:

- Intrinsic attenuation - crust and mantle attenuation values were taken from Warren and Shearer (2000) at 1 Hz: $Q_\alpha = 227$ from 0 to 100 km and $Q_\alpha = 1383$ from 220 to 2889 km. S wave attenuation is computed by $Q_\beta = \frac{4Q_\alpha}{9}$; assuming a Poisson solid and that all attenuation is in shear. Inner core attenuation of 360 from Bhattacharyya et al. (1993) model is applied to both the inner and outer core to prevent strong *PKiKP* at distances >110° in the modelling (Figure 3.14).
- Take off azimuth - set to 90°.
- P/S energy ratio - chosen to be a constant value of 23.4 (Shearer and Earle, 2004).
- Velocity and density functions - P wave velocity, S wave velocity and density profiles calculated from IASP91 (Kennett and Engdahl, 1991) and shown in Figure 3.14.

In order to find the most appropriate mantle scattering models that fit the global stack data, the following parameters were tested:

- Number of scattering layers (n);
- Thickness of scattering layers (h);
- Scattering correlation length (a) in each scattering layer;
- Velocity fluctuation (ϵ) in each scattering layer.

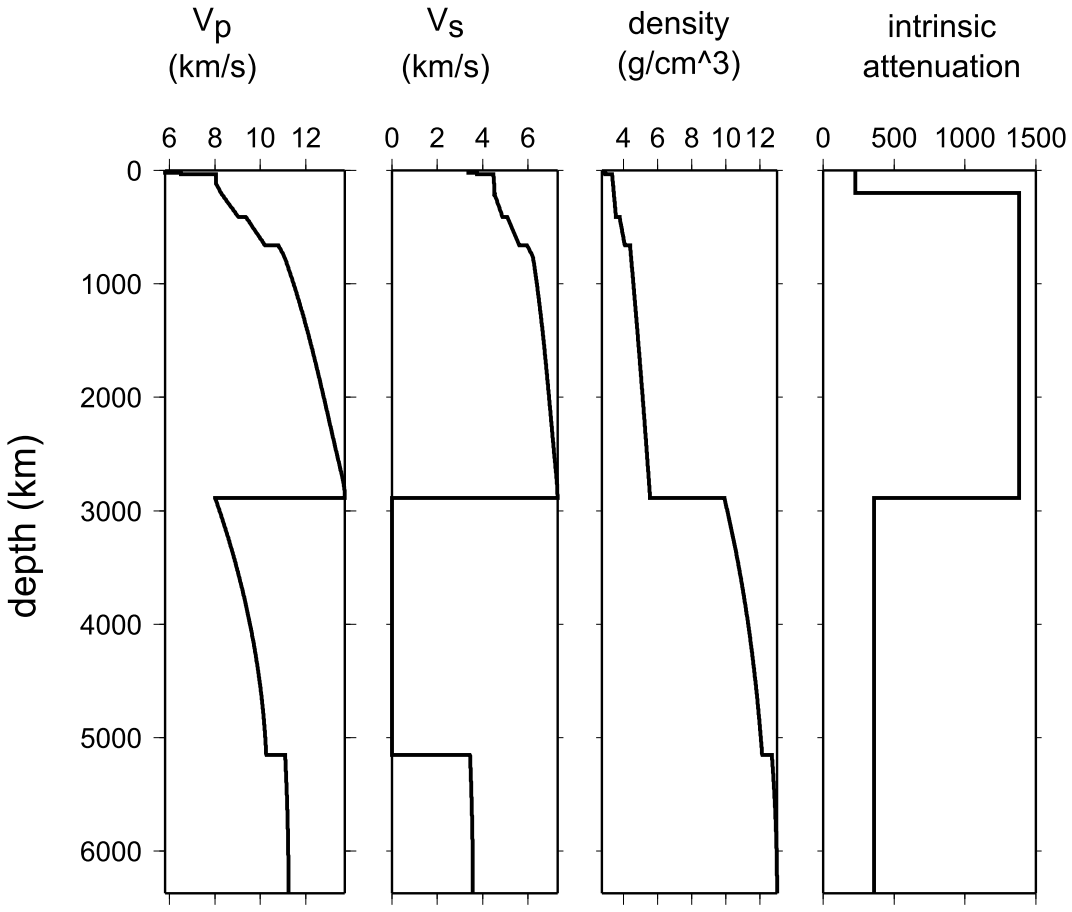

Figure 3.14: Velocity, density and attenuation profiles used in the Monte Carlo phonon modelling procedure. Variations of P wave velocity, S wave velocity and density with depth from reference model IASP91 (Kennett and Engdahl, 1991). Attenuation model for the mantle is from model by Warren and Shearer (2000) and attenuation for the (outer and inner) core is from model by Bhattacharyya et al. (1993).

Where possible, the models are compared to the global stacks that have the P coda removed. Therefore the P coda is also removed from the synthetic data by appling the same P coda removal method as described in Section 3.3.4.

3.6 Modelling Results

In this section the synthetics from different models are compared to the stacked data. Firstly, the results computed from models outlined in the studies by Hedlin et al. (1997), Earle and Shearer (2001) and Shearer and Earle (2004) are analysed. Then, three other types of models are evaluated (Figure 3.15) and are characterised by :

1. Lithospheric scattering only,
2. Lithospheric and single layer mantle scattering,
3. Lithospheric and multiple layer mantle scattering.

I evaluate the suitability of each model by assessing the fit of synthetic PP and PP precursors to the stacked seismograms for all distances. Some commentary regarding the PP coda fit is included but seeking models to represent this energy is beyond the scope of this study. Qualitative model comparisons and assessments are made following Hedlin et al. (1997) and Shearer and Earle (2004), as the focus is to find a suite of models that are appropriate for describing the global stack data. In addition, a misfit between the synthetic and stacked data is produced to quantitatively characterise the best fitting models and to analyse trends (Section 3.6.5). A full summary of all models considered is presented in Appendix B and comparisons of all synthetics and stacked data are shown in Appendix C.

3.6.1 Existing mantle scattering models

Several previous studies have analysed scattering properties within the mantle. Studies by Hedlin et al. (1997), Earle and Shearer (2001) and Shearer and Earle (2004) sample parts of the mantle using a variety of probes but have produced very different scattering models. The best fitting models in these studies have correlation length a ranging from 2 km to 6 km and rms velocity variation ϵ ranging from 0.5 to 4%.

As a starting point, I use the parameters from each of these models as parameters in the phonon method (Table 3.1). I use the parameters of two of these models: model by

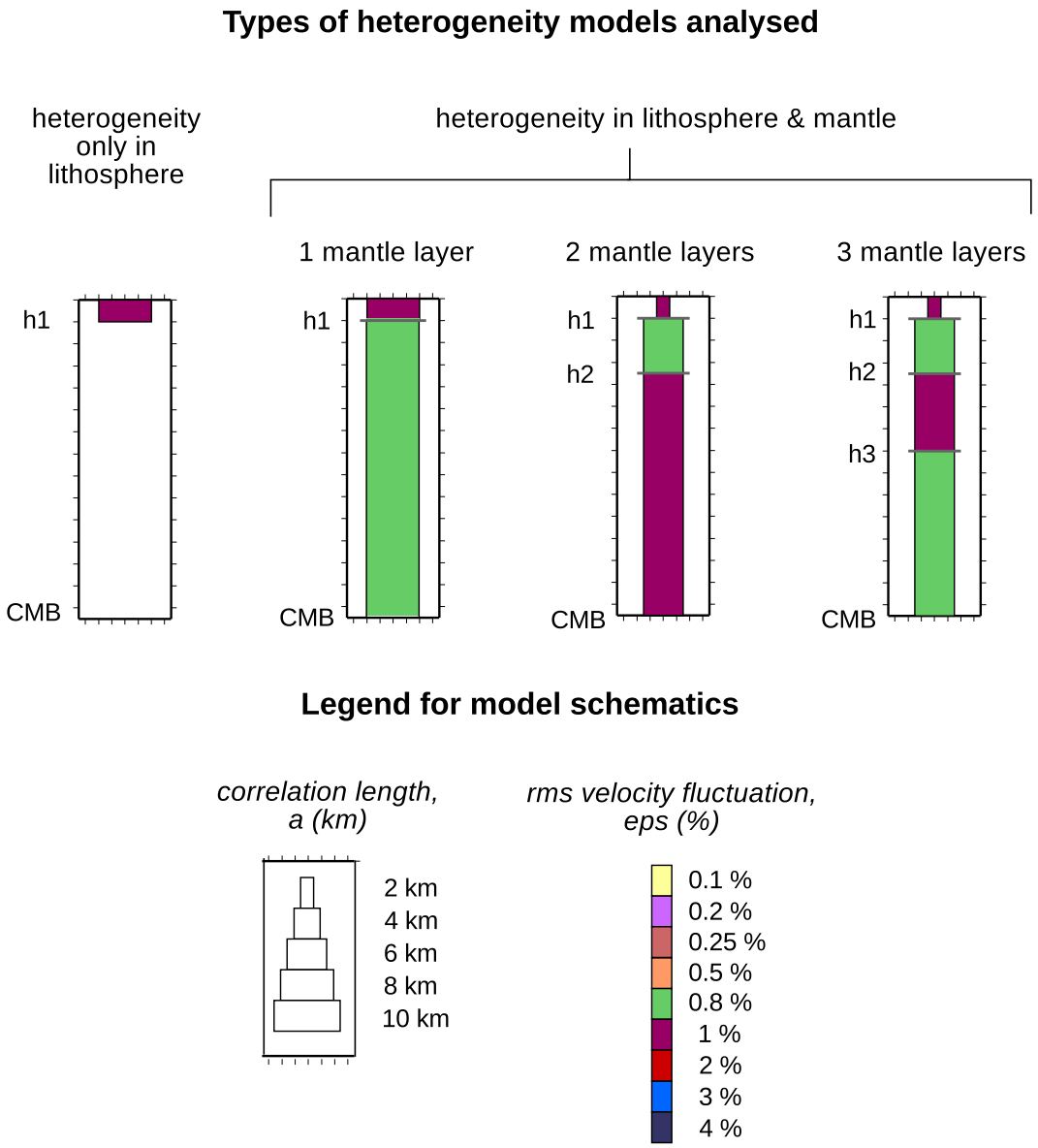

Figure 3.15: Schematic depicting the types of models considered in this study and legend for model schematics showing correlation length, a and rms velocity fluctuation, ϵ (or eps).

Depth (km)	H1997	ES2001	Depth (km)	SE2004
0-100	$a = 8$, $\epsilon = 1\%$	$a = 2$, $\epsilon = 1\%$	0-200	$a = 4$, $\epsilon = 4\%$
			200-600	$a = 4$, $\epsilon = 3\%$
100-2891	$a = 8$, $\epsilon = 1\%$	$a = 2$, $\epsilon = 1\%$	600-2891	$a = 8$, $\epsilon = 0.5\%$

Table 3.1: The parameters as input for models H1997 (Hedlin et al., 1997), ES2001(Earle and Shearer, 2001) and SE2004 (Shearer and Earle, 2004).

Hedlin et al. (1997) (H1997), which was generated by analysing *PKP* precursors; and the model by Earle and Shearer (2001) (ES2001), which was generated by analysing P_{diff} coda; with the attenuation profile from Warren and Shearer (2000) and Bhattacharyya et al. (1993) as described previously (Figure 3.14). The model by Shearer and Earle (2004) (SE2004) was produced by analysing *P* coda and was optimised using a different attenuation model for the crust and mantle: $Q_\alpha = 450$ for 0-200 km depth and $Q_\alpha =$ 2500 200-2891 km depth, and for consistency, I use this attenuation model for the SE2004 case.

The models are processed through the Monte Carlo modelling procedure and the resulting synthetic seismograms are stacked in 5° distance bins and are compared to the global stacked data from Section 3.3.3. The SE2004 model produces *P* coda amplitudes that are in disagreement with the data (Figure 3.16). The strong *P* coda energy masks the *PP* arrival and the *PP* precursory energy suggesting that the assumed levels of heterogeneity in the lithosphere ($\epsilon = 3\%$) and the upper mantle ($\epsilon = 4\%$) are too high.

The H1997 and ES2001 models use 1% rms velocity variation in the lithosphere and throughout the mantle and the resulting synthetic seismograms contain *P* coda energy in the *PP* precursory window that is more comparable to the observed stacked data for larger distances ($\Delta > 95°$) (Figure 3.16). For shorter distances ($70 - 95°$), the *P* coda is too strong, as with SE2004.

In order to evaluate the suitability of these models for the target window before *PP*, the *P* coda is removed for the H1997 and ES2001 models (Figure 3.17). H1997 synthetics show too much *PP* precursory energy in comparison to the global stacked data and this effect is greater for distances of 70-90°. Also, the *PP* arrivals in the modelled data are broader in comparison to those in the stacked data, for all distances. Likewise, the synthetic data that are generated for the ES2001 model contain too much *PP* precursory energy for shorter distances ($\Delta < 85°$) but the model generates

comparable energy for middle distances ($85 \leq \Delta \leq 95°$) and too little energy for the largest distances ($\Delta > 95°$). Though it is evident that the H1997 and ES2001 models are not a perfect fit, they provide good general background models that can be modified to fit the specific profile of the stacked dataset.

3.6.2 Effect of scattering in the lithosphere

In order to evaluate the effect of lithospheric scattering, the next set of models is generated with lithospheric scattering only i.e. with no mantle scattering. This allows one to evaluate the effect of lithospheric scattering on the *PP* waveform and if any of the energy from lithospheric scattering arrives as *PP* precursors.

Four models are discussed here: a model with the lithospheric heterogeneous layer from model ES2001 (a = 2 km, ϵ = 1%) labelled ES2001_C0; and three variations of this models: ES2001_C1 (a = 8 km, ϵ = 1%), ES2001_C2 (a = 2 km, ϵ = 2%) and ES2001_C3 (a = 2 km, ϵ = 4%). There are common characteristics amongst the synthetics from these four models (Figures 3.18 and 3.19). *PP* consists of a central peak with two smaller peaks, one either side. Further tests showed that the onset of these amplitude maxima are due to the onset of the heterogeneous lithosphere and that separation of these peaks is due to the thickness of the scattering layer. By increasing the thickness of the heterogeneous layer, the peaks are more spread out. Lithospheric scattering does produce *PP* precursors for the four models, starting about 40 s to 70 s before *PP* for distances of 70° to 95°. However, the precursory energy is absent after Δ = 95°. *PP* coda energy also is present but is very weak and reduces to noise level after ∼30 s.

The models ES2001_C1, ES2001_C2 and ES2001_C3 are compared to the ES2001 lithospheric scattering model. The rms velocity variation is increased from ϵ = 1% (model ES2001_C0) to ϵ = 2% (model ES2001_C2) to ϵ = 4% (model ES2001_C3), resulting in a small increase in *PP* precursory energy for shorter distances ($\Delta \leq 90°$). Increasing the correlation length from a = 1 km (ES2001_C0) to a = 8 km (ES2001_C1) broadens the waveform of *PP* and causes a delay in the start of *PP* precursors.

In summary, heterogeneity only in the lithosphere does not produce synthetic data that fit the *PP* and *PP* precursors observed in the stacked data. The rms velocity variation of ϵ = 1% provides the best fit for the amplitudes of *PP* and its precursors, however the correlation length is unresolved. As shown in the next section, the heterogeneity

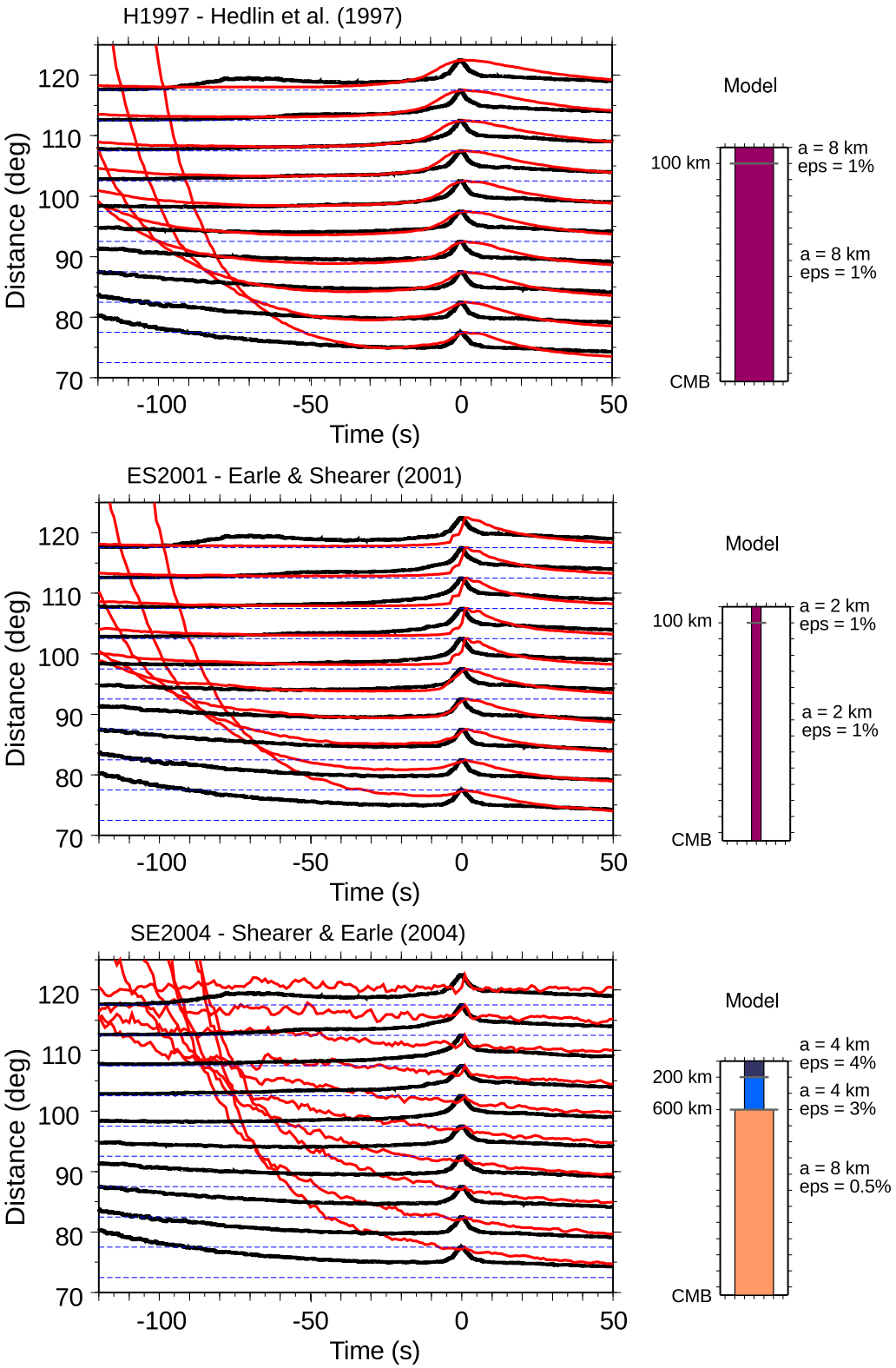

Figure 3.16: Comparison of global stacks (black) to synthetic seismograms (red) from published models: H1997 (Hedlin et al., 1997), ES2001 (Earle and Shearer, 2001) and SE2004 (Shearer and Earle, 2004). The parameters that are used in the modelling are shown in the legend (right). To characterise the amount of P coda energy, the synthetic seismograms are stacked without removing the P coda.

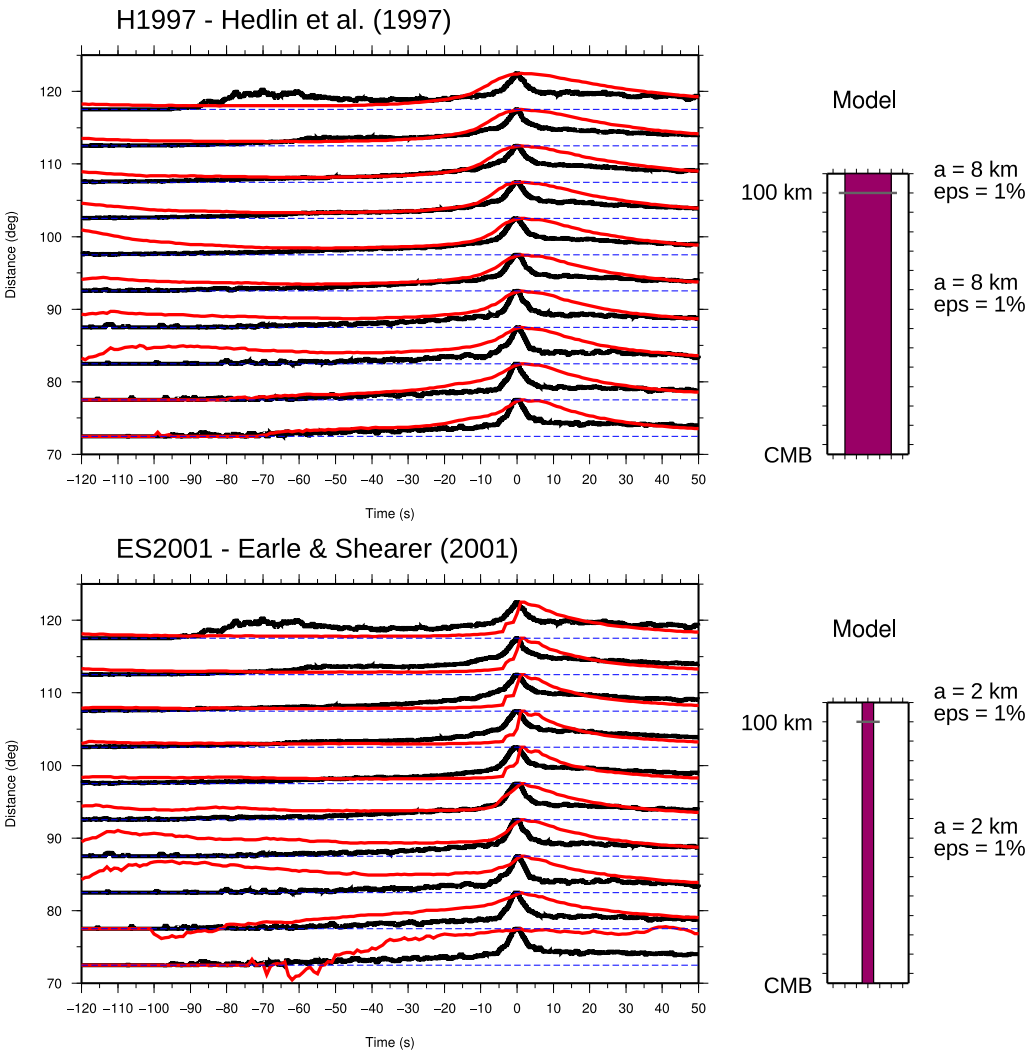

Figure 3.17: Comparison of global stacks (black) to synthetic seismograms (red) from H1997 and ES2001. The *P* coda has been removed from the global stacks and model stacks. The parameters used in the modelling are shown in the legend (right).

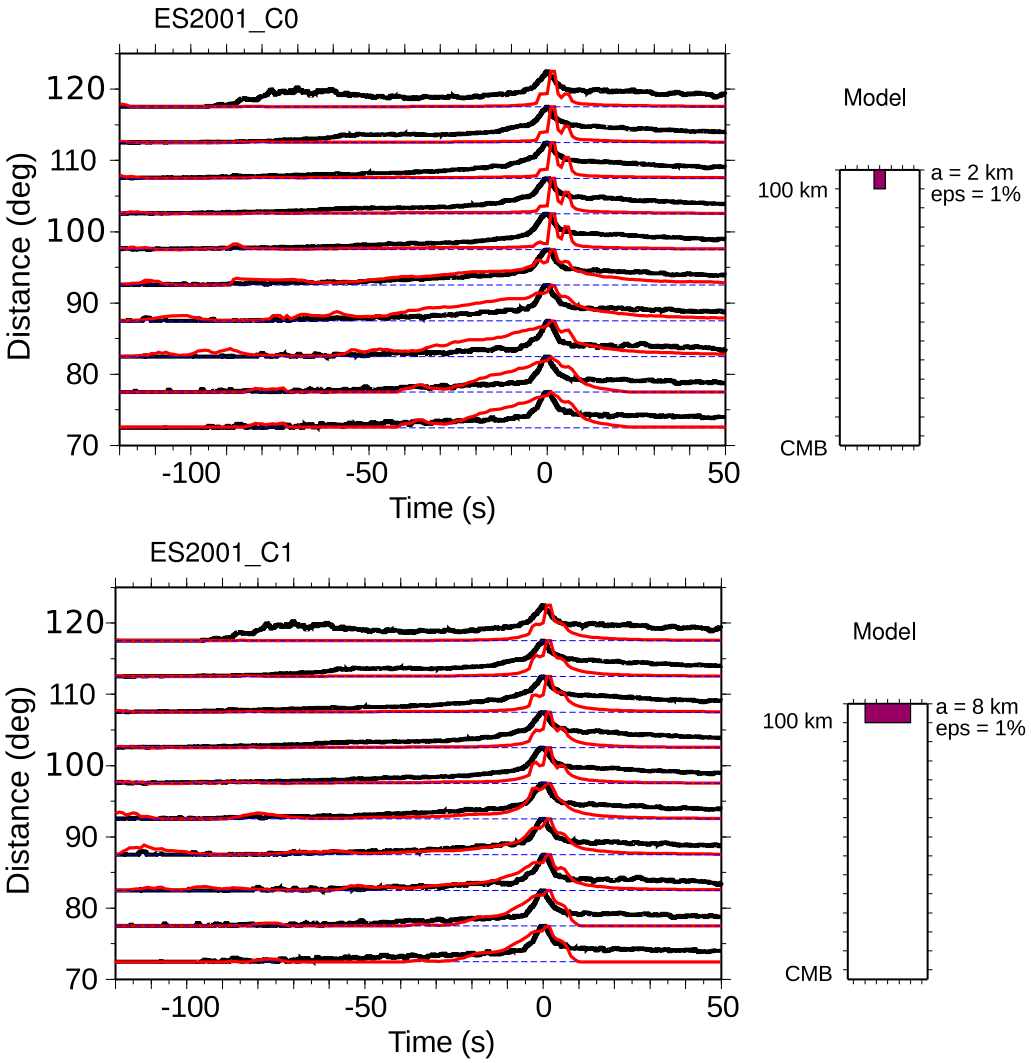

Figure 3.18: Comparison of global stacks (black) to synthetic seismograms (red) for two lithospheric models ES2001_C0 and ES2001_C1. The *P* coda has been removed from the global stacks and model stacks. The parameters that are used in the modelling are shown in the legend (right).

in the lithosphere has a trade off with the heterogeneity in the mantle.

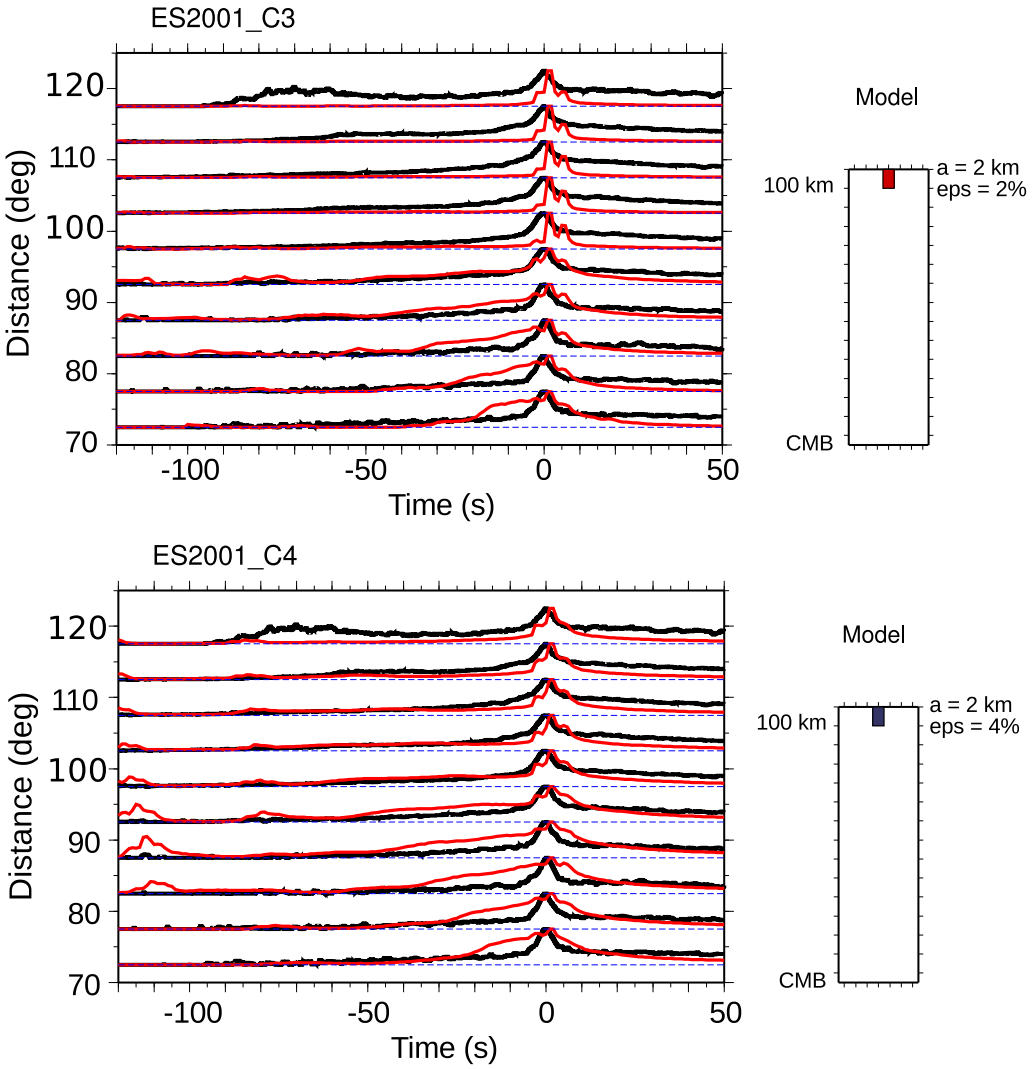

Figure 3.19: Comparison of global stacks (black) to synthetic seismograms (red) for two lithospheric models ES2001_C2 and ES2001_C3 The *P* coda has been removed from the global stacks and model stacks. The parameters that are used in the modelling are shown in the legend (right).

3.6.3 Models with lithospheric and uniform whole mantle scattering

Using the lithospheric heterogeneity parameters from models H1997 and ES2001, 33 models with a uniform scattering parameters in the mantle are analysed. Significant models are selected from this collection: 3 are variants of the ES2001 models and 4 are variants of the H1997 model from Section 3.6.1. These seven models were chosen either because model synthetics are similar to the global distance stacks or because the model synthetics are very different from the stacked data. Both cases are useful in determining what heterogeneity properties exist in the mantle. The scattering parameters and synthetic seismograms for these models are shown in Figures 3.20, 3.21 and 3.22. Figures and scattering parameters for all other models can be found in Appendices B and C.

Models ES2001_M11, ES2001_M17 and ES2001_M20 (Figure 3.20) are based on model ES2001 and use a 100 km thick scattering layer for the lithosphere with $a = 2$ km (ϵ in the lithosphere varies between the models). These three models have a mantle heterogeneity layer with $\epsilon = 0.5\%$, a reduction of 50% from the rms velocity fluctuation compared to base model ES2001. The main difference between the models is that the correlation length in the mantle is varied: 2 km (ES2001_M20) to 6 km (ES2001_M17) and 8 km (ES2001_M11).

The shape of *PP* scattering is analysed across the models (Figure 3.20). The *PP* waveform consists of a central peak with two smaller peaks, one either side, and the amplitude and separation of the peaks is related to scattering in the lithosphere (as observed in Section 3.6.2). For models ES2001_M11, ES2001_M17 and ES2001_M20, *PP* shape varies, such that *PP* is smoother and the side peaks are suppressed for models with larger correlation length (ES2001_11 and ES2001_17) (Figure 3.20). For smaller correlation length (ES2001_20) the central and side peaks within the *PP* waveform are more defined and less smooth (Figure 3.20). This suggests that the shape of *PP* is affected by correlation length in both the lithosphere and the mantle, with larger correlation lengths producing a broader and smoother shape.

PP precursors are visible in all models but the strength of the precursors are only a good match for distances less than 95°. For larger distances ($\Delta > 95°$), the precursory energy is too weak (Figure 3.20). Even though the differences in correlation length are significant, only small differences in the precursory energy are observed at larger distances for mantle velocity variations $\epsilon = 0.5\%$. Regarding the coda energy of *PP*,

generally the models under-predict the amplitude of the coda, though model ES2001_20 produces a coda that matches the data for distances less than 90° (Figure 3.20).

Models H1997_M04, H1997_M05, H1997_M07 and H1997_M08 (Figures 3.21 and 3.22) are based on H1997 and use a 100 km thick lithospheric scattering layer with $a = 8$ km and rms velocity variation ranging from $\epsilon = 1\%$ to $\epsilon = 2\%$ between the models. All these models have an 8 km correlation length in the mantle with rms velocity variation ranging from $\epsilon = 0.1\%$ (H1997_M04) to $\epsilon = 0.5\%$ (H1997_M05, H1997_M07) to $\epsilon = 0.8\%$ (H1997_M08) as shown in Figures 3.21 and 3.22.

The shape of *PP* is influenced by a combination of ϵ in the lithosphere and ϵ in the mantle; by increasing ϵ in either the lithosphere or mantle, the width of *PP* waveform increases. With a mantle rms velocity fluctuation $\epsilon = 0.1\%$, the model H1997_M04 has the worst fitting *PP* (Figure 3.22).

The rms velocity variation in the mantle also influences the amount of *PP* precursory energy. Model H1997_M04 with lowest mantle rms velocity variation ($\epsilon = 0.1\%$), has the poorest match to *PP* precursory energy (Figure 3.21). Model H1997_M05 (with $\epsilon = 0.5\%$) has *PP* precursory energy that is a reasonable match to the stacked data for shorter distances (up to 87.5°) and for precursory window 20-90 s before *PP* (Figure 3.21). Model H1997_M07 also has $\epsilon = 0.5\%$ in the mantle but has stronger rms velocity variation in the lithosphere ($\epsilon = 2\%$), and this combination of lithospheric and mantle heterogeneity provides a better fit of precursory energy for distances 70-110° (Figure 3.22). Model H1997_M08 uses the lithospheric heterogeneity parameters from H1997 and H1997_C1 (and H1997_M04 and H1997_M05) in combination with a rms velocity variation of 0.8% in the mantle, which results in a good fit for *PP* precursory energy for distances 90-110° like H1997_M07 (Figure 3.22). However, H1997_M08 has *PP* coda energy that matches the stacked data better than model H1997_M07.

In summary, models with a single characteristic layer of heterogeneity spanning across the whole mantle do not produce synthetics that are sufficiently similar to the global stack data for all distances, indicating that more complicated models are required to fit the data. Nonetheless, the models do show that correlation length plays an important role in governing the amplitude of *PP* precursors. The correlation length of the scattering in the mantle is likely to be more than 2 km i.e. the mantle has larger dominant heterogeneities than heterogeneities in the lithosphere. Further analysis of the influence of correlation length, in addition to the general suitability of uniform

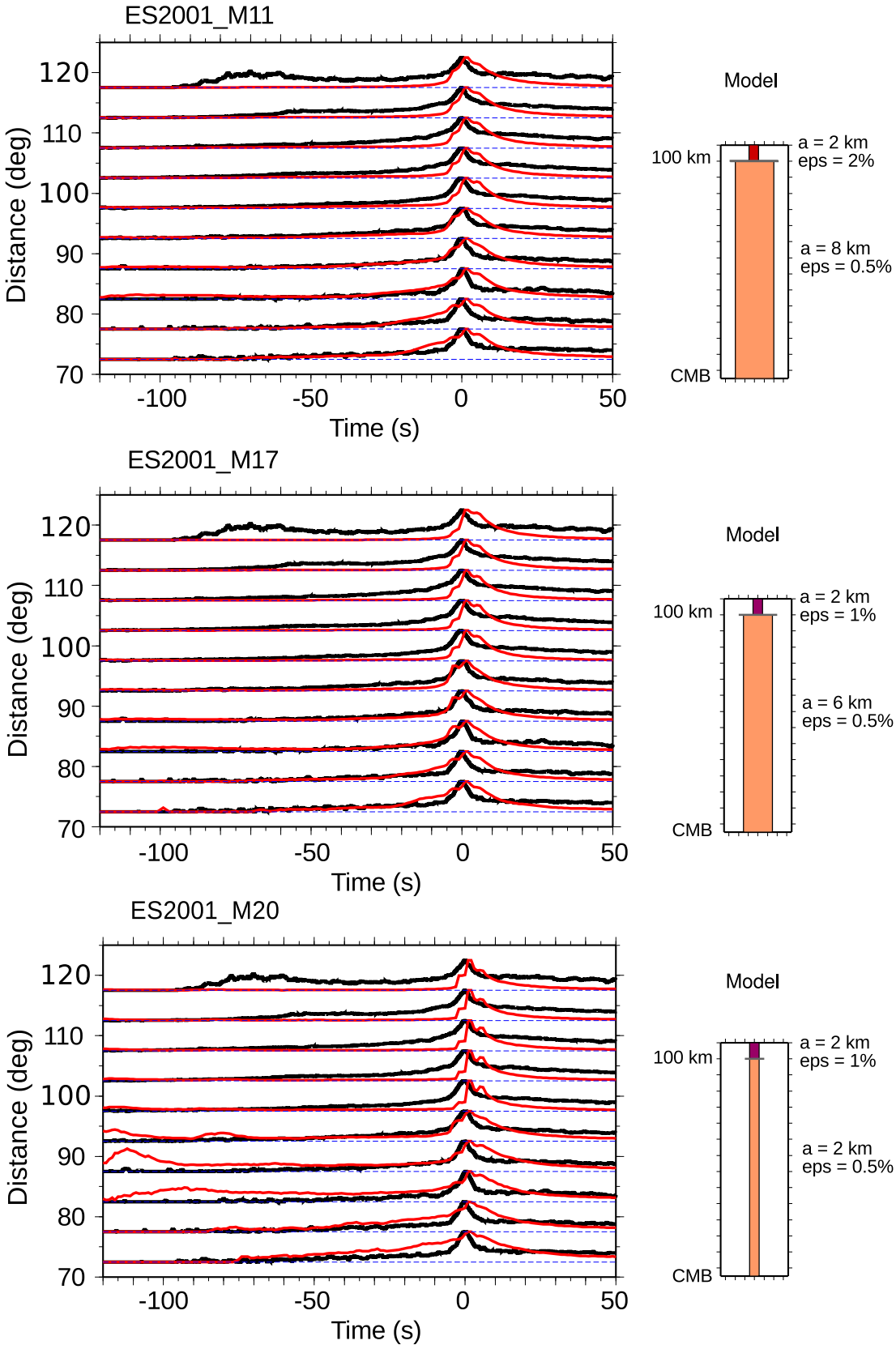

Figure 3.20: Comparison of global stacks (black) to synthetic seismograms (red) for three whole mantle models ES2001_M11, ES2001_M17 and ES2001_M20, based on model ES2001. The *P* coda has been removed from the global stacks and model stacks. The parameters that are used in the modelling are shown in the legend (right). The correlation length of the heterogeneous mantle differs and this results in variations in *PP* waveform, amount of *PP* precursory and coda energy.

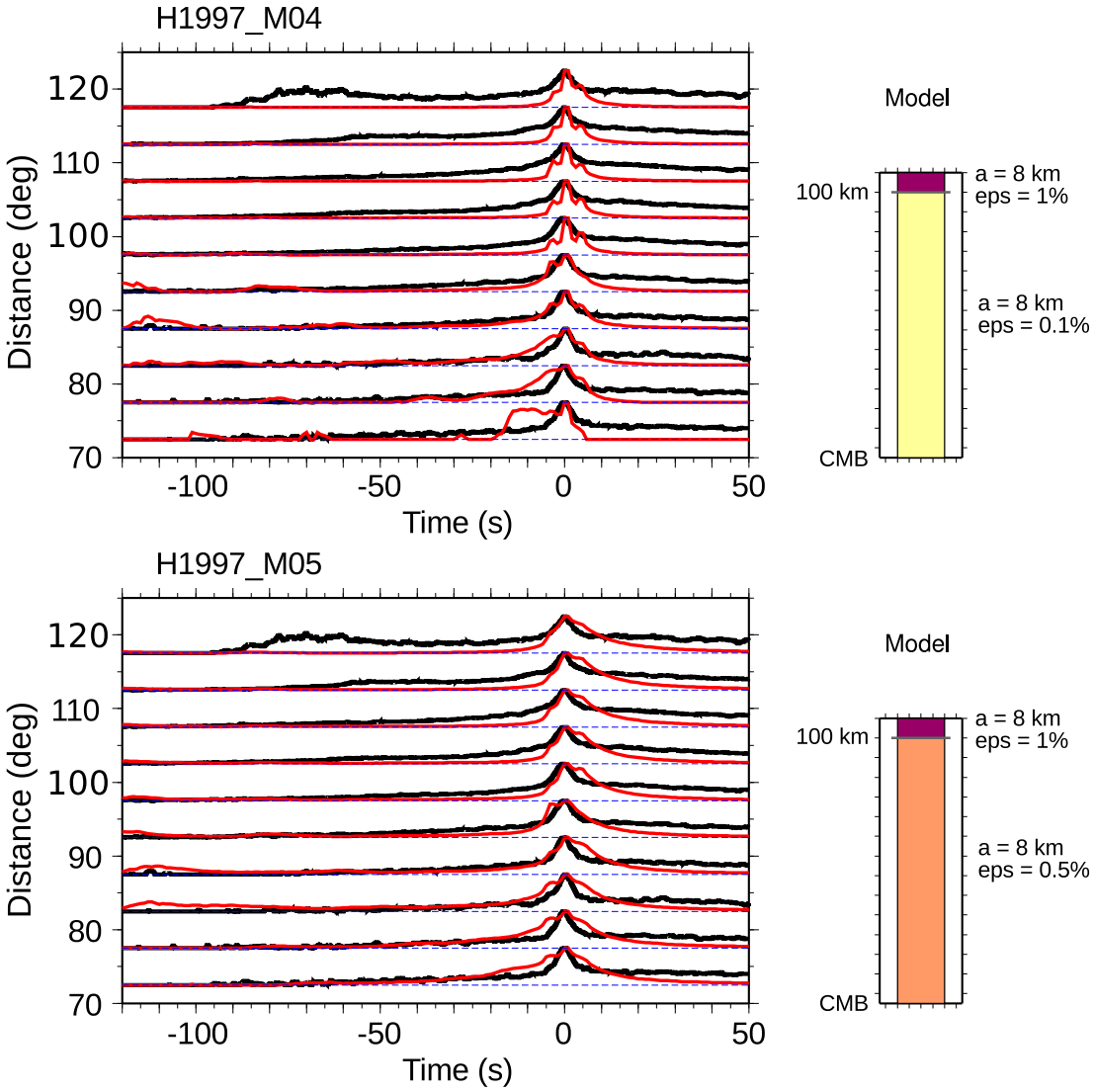

Figure 3.21: Comparison of global stacks (black) to synthetic seismograms (red) for two whole mantle models H1997_M04 and H1997_M05, based on H1997. The *P* coda has been removed from the global stacks and model stacks. The parameters that are used in the modelling are shown in the legend (right). The rms velocity variation of the heterogeneous mantle differs and this results in variations in *PP* waveform, amount of *PP* precursory and coda energy.

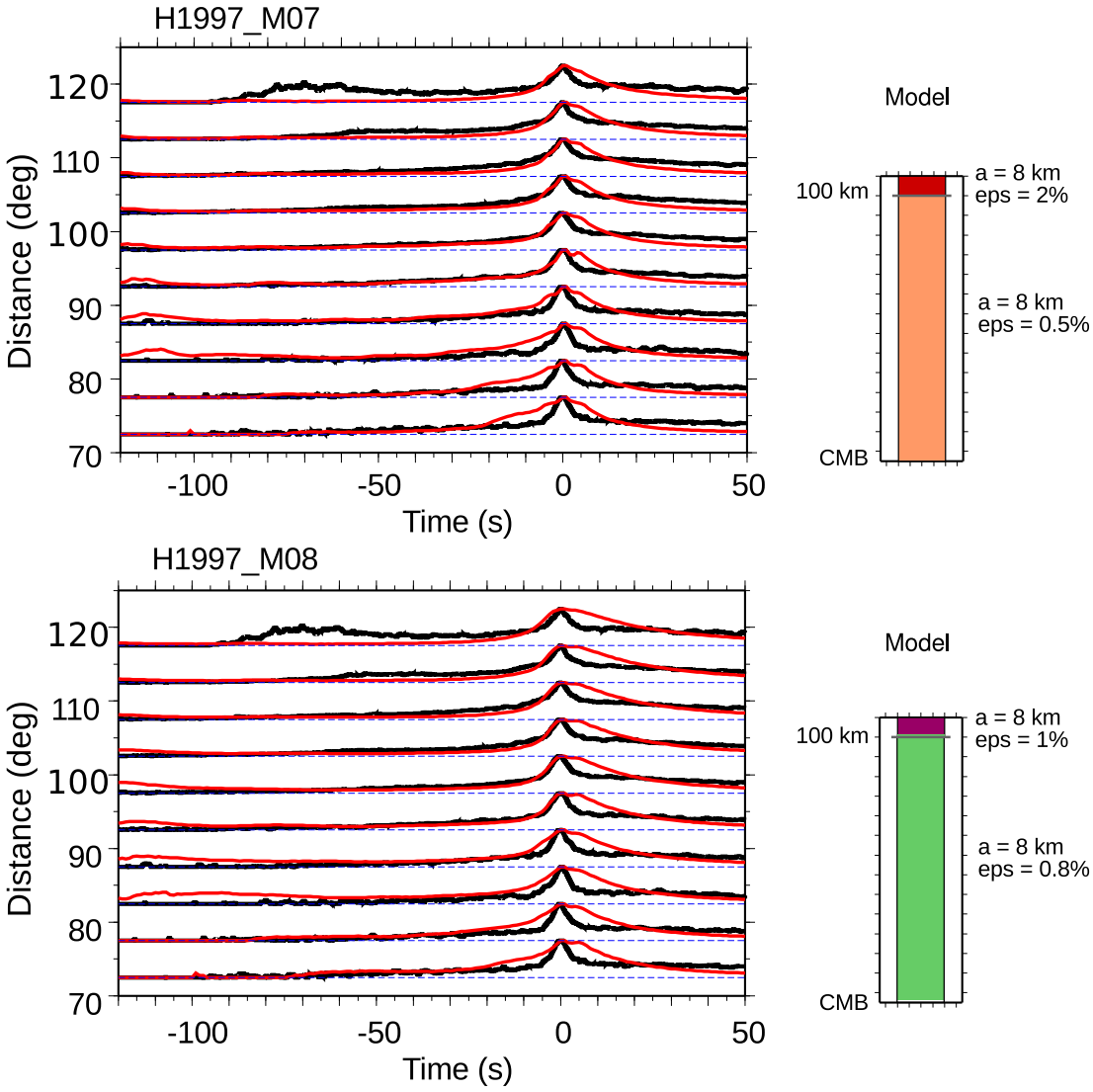

Figure 3.22: Comparison of global stacks (black) to synthetic seismograms (red) for two whole mantle models H1997_M07 and H1997_M08, based on H1997. The *P* coda has been removed from the global stacks and model stacks. The parameters that are used in the modelling are shown in the legend (right). The rms velocity variation of the heterogeneous mantle differs and this results in variations in *PP* waveform, amount of *PP* precursory and coda energy.

mantle scattering models, can be achieved through a quantitative measure of misfit, as outlined in Section 3.6.5. In addition, from the mantle models discussed it has been found that a combination of both lithospheric and mantle rms velocity variations can produce reasonable fitting *PP* precursors for shorter distances, but evaluating the fit in *PP* coda energy may help in discriminating between the models.

3.6.4 Models with layered mantle scattering

Since the single layer mantle heterogeneity models are not providing a good fit to the data, a further 46 models with 2 or more layers of mantle scattering were analysed. Four better fitting models were selected and the scattering parameters and synthetic seismograms for these models are shown in Figures 3.23 and 3.24. All other models can be found in Appendix C.

These four models use a correlation length of 6 km for all mantle layers, and use ϵ ranging from 0.5% to 1%. Two models have two mantle scattering layers with depth extents 100-700 km and 700 km to the CMB. Model LAYM_01 has $\epsilon = 0.5\%$ for depth 100-700 km and $\epsilon = 1\%$ for depth 700-2891 km; and model LAYM_44 has $\epsilon = 0.8\%$ for depth 100-700 km and $\epsilon = 1\%$ for depth 700-2891 km. Models LAYM_01 and LAYM_44 produce *PP* precursory energy that correctly represents the shape and magnitude of the precursory energy in the global stacked data. Model LAYM_44 does generate synthetics with a better match in precursor amplitude, without increasing the *PP* coda length, and this may be due to the slight increase in ϵ of the upper mantle layer.

Model LAYM_45 is similar to model LAYM_44, but differs by including a third scattering layer at depths 1400-2891 km and has $\epsilon = 0.8\%$ and $a = 6$ km. The synthetic seismograms contain *PP* precursors that are similar to the shape and amplitude of the precursors in the stacked data. The fit is best for distances $\Delta > 85°$ and for the 50 s before *PP*. However, the *PP* coda is much stronger in the synthetics than in the real data.

Model LAYM_46 is also adapted from model LAYM_44, retaining the two scattering layers but defining the boundary between the two layers at 400 km. The synthetic seismograms contain *PP* precursors that are similar to the amplitude of the precursors in the stacked data but the shape of the precursory energy and *PP* are noticeably different. The fit is best for distances $85° < \Delta < 105°$ and for the 50 s before *PP*. Model LAYM_46 contains the largest amount of *PP* coda in the synthetics across all

the models and this energy is far stronger than the coda in the real data.

In summary, models LAYM_44, LAYM_45 and LAYM_46 fit the *PP* precursory energy for most distances, though for larger distances ($\Delta > 105°$) the fit could be improved. In the layered mantle models the synthetic *PP* is 3× broader than the *PP* in the data ($T \approx 10$ s). The broader *PP* results in a poor fit of the *PP* coda until ∼30 s after *PP*. It should be noted that there are minor variations between the synthetics of models LAYM_44, LAYM_45 and LAYM_46, suggesting the layers of heterogeneity that are common between these models are the layers in the mantle that cause the *PP* precursors, or that the modelling process is non-unique.

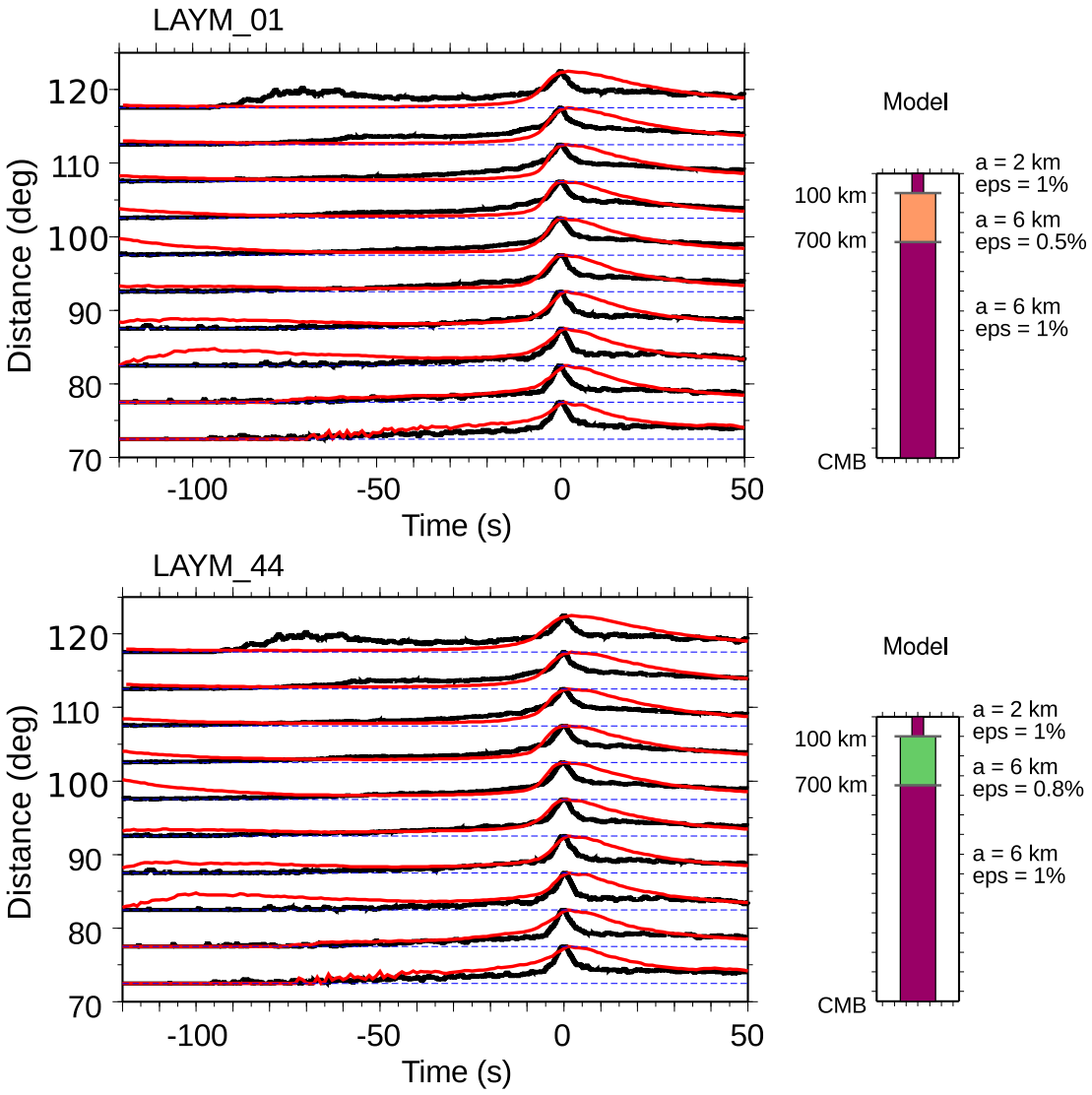

Figure 3.23: Comparison of global stacks (black) to synthetic seismograms (red) for two whole mantle models LAYM_01 and LAYM_44. The *P* coda has been removed from the global stacks and model stacks. The parameters that are used in the modelling are shown in the legend (right). The rms velocity variation of the heterogeneous region from 100-700 km in the mantle differs between the models and this results in variations in *PP* waveform, amount of *PP* precursory and coda energy in the synthetic seismograms.

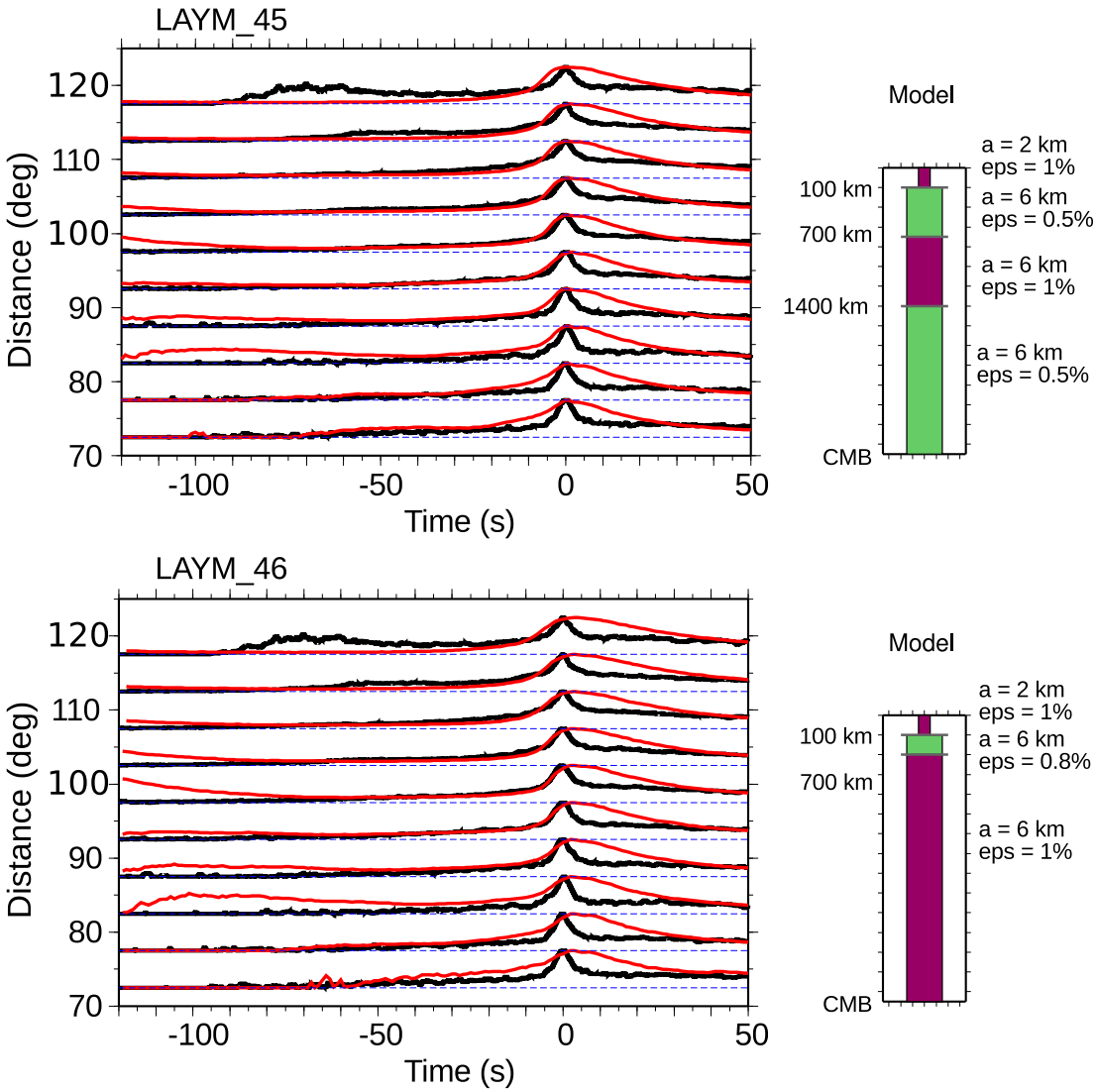

Figure 3.24: Comparison of global stacks (black) to synthetic seismograms (red) for two whole mantle models LAYM_45 and LAYM_46. The *P* coda has been removed from the global stacks and model stacks. The parameters that are used in the modelling are shown in the legend (right). The heterogeneity models apart from LAYM_45 has three mantle layers and LAYM_46 model has two mantle layers. The differences in the models results in variations in *PP* waveform, amount of *PP* precursory and coda energy in the synthetic seismograms.

3.6.5 Quantitative analysis

Quantitative assessments of the fit of heterogeneity models derived in Section 3.6 are analysed by calculating the RMS misfit between the observed stacked data (D) and the synthetic data (M) for each distance bin (d), to yield the RMS misfit $F_{mis}(d)$:

$$F_{mis}(d) = \sqrt{\frac{\sum_{i=1}^{N} (D_i - M_i)^2}{N}}. \tag{3.8}$$

where N samples in the chosen time window. The values of $F_{mis}(d)$ for distances 72.5° to 117.5° (every 5°) are summed to find the total misfit, T_{mis}:

$$T_{mis} = \sum_{d=72.5}^{117.5} F_{mis}(d). \tag{3.9}$$

The misfit is only calculated for the 40 s window before PP (with sample spacing of 1 s) because this window contains the clearest precursor information for all distances. In addition, the misfit is only calculated for the models with mantle heterogeneity, since the models with heterogeneity confined to the lithosphere are not realistic and are a poor fit to the data (Section 3.6.2).

The total misfit ranges from 7.23 to 32.48, with a mean of 11.26 and standard deviation of 4.43. The five lowest misfits (i.e. the best models found from quantitative analysis) and the misfits for the best qualitative models (as discussed in Sections 3.6.3 and 3.6.4) are summarised in Table 3.2 and shown in Figure 3.25. The total misfits for all the models are tabulated in Appendix D.

Model LAYM_47 is the best fitting model with constant correlation length (a = 8 km) and velocity variation $\epsilon = 1\%$ in the lithosphere, $\epsilon = 0.5\%$ in the upper mantle (100-700 km) and $\epsilon = 1\%$ in the mid-mantle (700-1400 km). The difference in misfit between the three best models (LAYM_43, LAYM_49, LAYM_33) is quite small (0.38) compared to the total misfit range (7.23-32.48), probably due to the similarities of the heterogeneity profiles.

Comparing model fit with mantle correlation length, *a*

Comparisons are made between the misfit and mantle correlation length for whole mantle heterogeneity models with $a = 2$ km and $\epsilon = 2\%$ in the lithosphere. These models are organised into three groups with $\epsilon = 0.1\%$, $\epsilon = 0.5\%$ and $\epsilon = 1\%$. For each

Model	T_{mis}
H1997_M04	10.26
ES2001_M20	9.71
ES2001_M17	9.35
LAYM_49	8.99
H1997_M05	8.93
LAYM_01	8.57
ES2001_M11	8.49
H1997_M07	8.47
LAYM_44	8.36
ES2001_M23	7.95
LAYM_45	7.92
H1997_M08	7.85
LAYM_33	7.61
LAYM_49	7.25
LAYM_47	7.23

Table 3.2: Total RMS misfit between real and synthetic data for the five models with the lowest misfit and for the models discussed in Sections 3.6.3 and 3.6.4.

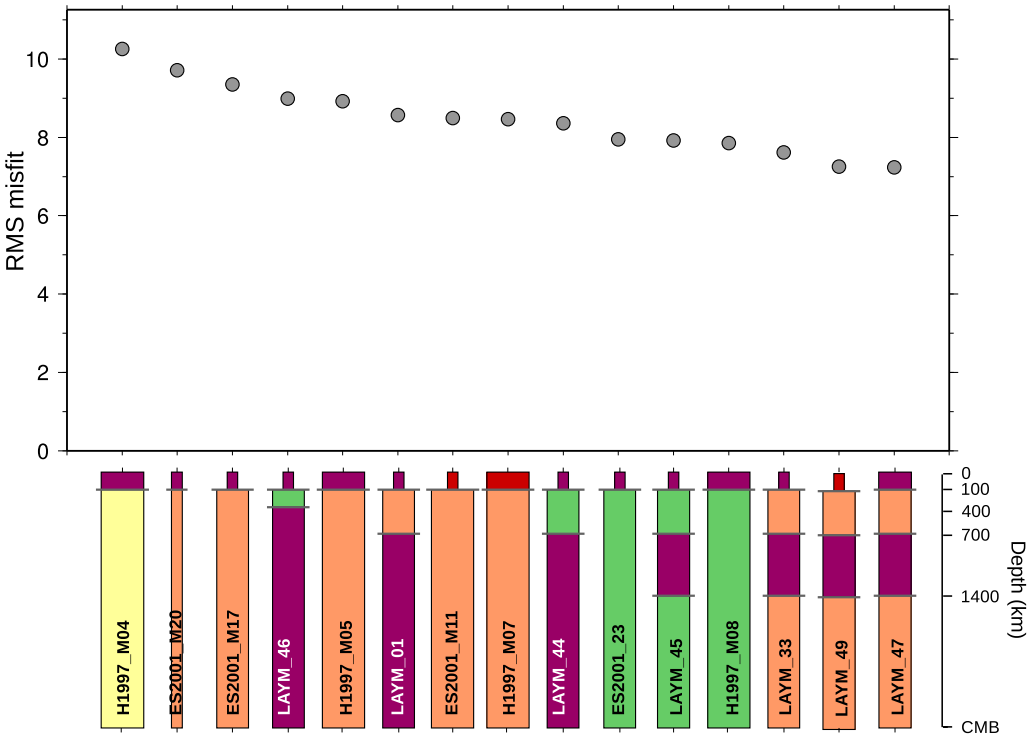

Figure 3.25: Total RMS misfit (grey circle) between real and synthetic data for the five models with the lowest misfit and for the models discussed in Sections 3.6.3 and 3.6.4. Models are ordered from highest misfit (left) to lowest misfit (right).

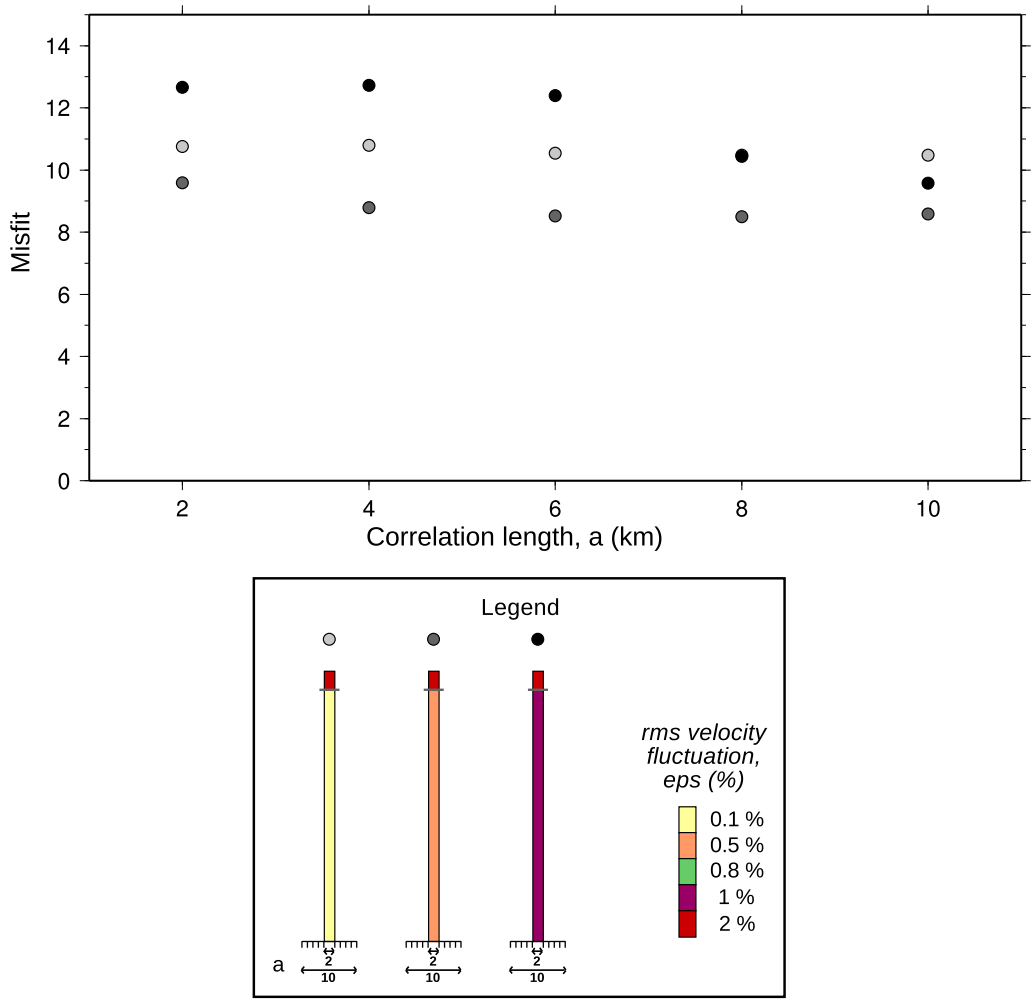

Figure 3.26: Correlation for total RMS misfits for models with increasing correlation length in the mantle, for three groups with different rms velocity variation in the mantle: 0.1% (light grey circles), 0.2% (dark grey circles) and 1% (black circles). The correlation length ($a = 2$ km) and rms velocity variation ($\epsilon = 2\%$) for the lithosphere remain constant for all models.

of these groups, the misfit with increasing mantle correlation length has a different trend (Figure 3.26). The misfits for models with mantle $\epsilon = 0.1\%$ are similar misfits for all the mantle correlation lengths considered (i.e. 2-10 km). In contrast, for models with $\epsilon = 0.5\%$, the misfits decrease with increasing correlation lengths until $a = 6$ km, but then stay almost constant. Likewise, for models with $\epsilon = 1\%$, the misfits decrease with increasing correlation lengths but do not reach a local minima.

To summarise, models generated using $\epsilon = 0.5\%$ but using a different correlation length, have similar fit to the stacked data i.e. similar total misfit (Figure 3.26). Furthermore, the model with heterogeneity parameters of $\epsilon = 0.5\%$ and $a = 6$ km in the mantle has the smallest misfit and is the best model in this series.

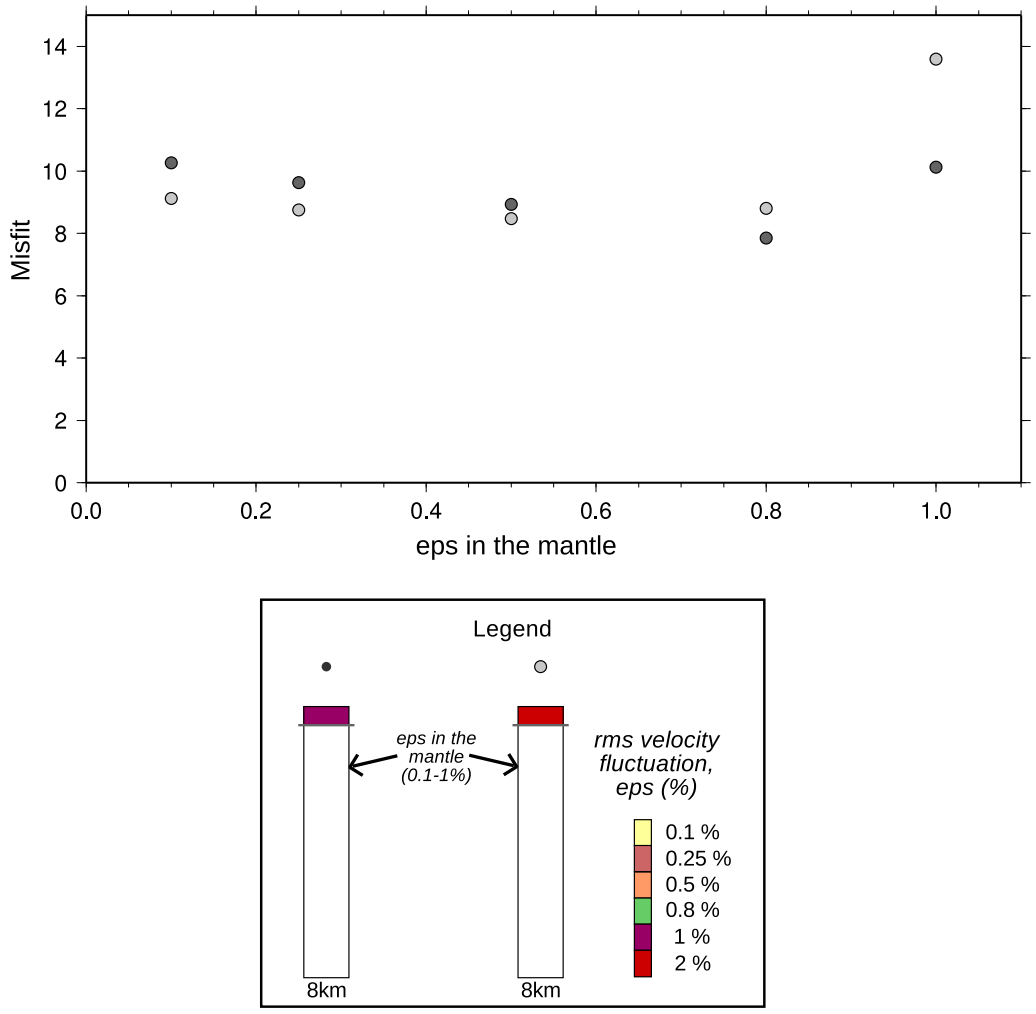

Figure 3.27: Correlation of total RMS misfits for models with increasing rms velocity variation in the mantle, for two groups with different rms velocity variations: 1% (light grey circles) and 2% (dark grey circles). The correlation length for the lithosphere and mantle are constant ($a = 8$ km) for all models.

Comparing model fit with mantle velocity fluctuation, ϵ

A comparison is made between the misfit and velocity fluctuation for whole mantle heterogeneity models with a constant correlation length of $a = 6$ km in the lithosphere and mantle. These models are organised into two groups with $\epsilon = 1\%$ and $\epsilon = 2\%$ in the lithosphere. The velocity fluctuation in the mantle is varied between 0.1% to 1% and the misfits are found (Figure 3.27).

For both groups, the misfit decreases using ϵ from 0.1% to 0.5%, and increase using ϵ from 0.8% to 1%. However, for a lithosphere with $\epsilon = 2\%$, the smallest misfit is found for a model with $\epsilon = 0.5\%$ in the mantle; whereas for a lithosphere with $\epsilon = 1\%$, the smallest misfit is found for a model with $\epsilon = 0.8\%$ in the mantle.

Comparing model fit for different three layer models

A comparison is made between the misfit and the depth of the second mantle heterogeneity layer for three layered heterogeneity models. These models are organised into four groups, all with $a = 2$ km and $\epsilon = 1\%$ in the lithosphere. For the mantle, the models have either $a = 2$ km or $a = 6$ km, with velocity fluctuation that varies between 0.5% to 2% for the two mantle layers (Figure 3.28). The first mantle layer can extend into the lower mantle, to the maximum depth of 2900 km (core-mantle boundary) which is equivalent to a whole mantle heterogeneity model (Figure 3.28).

It is observed in Figure 3.28 that there is not a simple relationship between increasing the depth of the second mantle heterogeneity layer and the misfit between model and data. The worst fitting models have a constant correlation length of $a = 2$ km in the lithosphere and mantle. The best models have $a = 6$ km in the mantle with $\epsilon = 0.8\%$ in the top (or only) mantle layer.

Comparing model fit for different four layer models

A comparison is made between the misfit and velocity fluctuation for the upper and lower mantle within four layer heterogeneity models. These models are organised into three groups with $\epsilon = 1\%$ and either $a = 2$ km or $a = 6$ km in the lithosphere, and constant correlation length of $a = 6$ km in the mantle (Figure 3.29). The models also have three heterogeneity layers in the mantle bounded by 700 km and 1400 km with $\epsilon = 1\%$ in the mid-mantle layer (700-1400 km).

Figure 3.29 shows that the misfits for these four layer models do not vary greatly, suggesting that the correlation length in the lithosphere does not contribute greatly to the precursory energy. In addition, the similar misfits suggest that the common features between the models (for instance the mid-mantle layer with heterogeneity parameters of $\epsilon = 1\%$ and $a = 6$ km) may be constrained. The models with upper and lower mantle velocity fluctuation of $\epsilon = 0.5\%$ fit better than those with $\epsilon = 0.8\%$ (Figure 3.29).

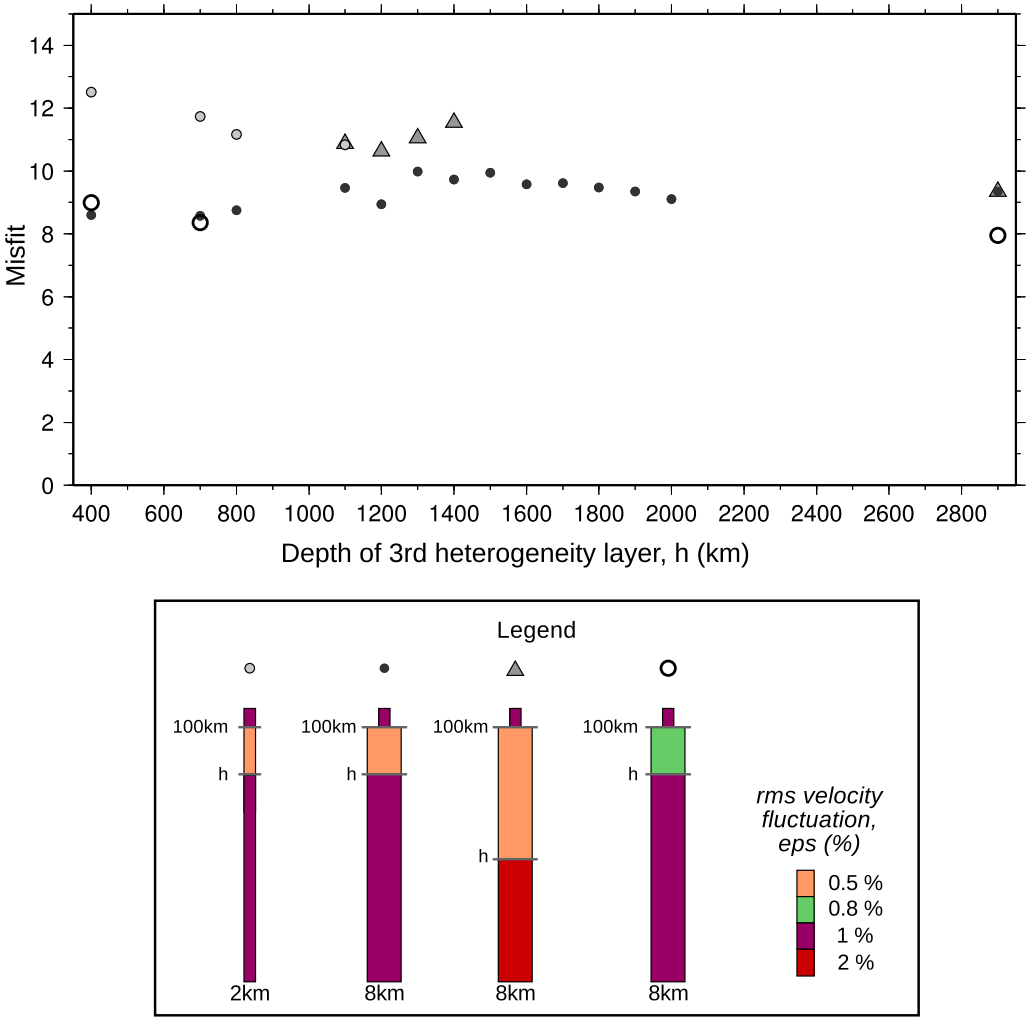

Figure 3.28: Correlation of the total RMS misfits for models with increasing depth of the third layer. The models used are separated into four groups with different mantle correlation length and different rms velocity variation in the upper and lower mantle: $a = 2$ km, $\epsilon = 0.5\%$ and $\epsilon = 1\%$ (light grey circles); $a = 6$ km, $\epsilon = 0.5\%$ and $\epsilon = 1\%$ (dark grey circles); $a = 6$ km, $\epsilon = 0.5\%$ and $\epsilon = 2\%$ (light grey triangles); and $a = 6$ km, $\epsilon = 0.8\%$ and $\epsilon = 1\%$ (black open circles). The correlation length ($a = 2$ km) and rms velocity variation ($\epsilon = 1\%$) for the lithosphere remain constant for all models.

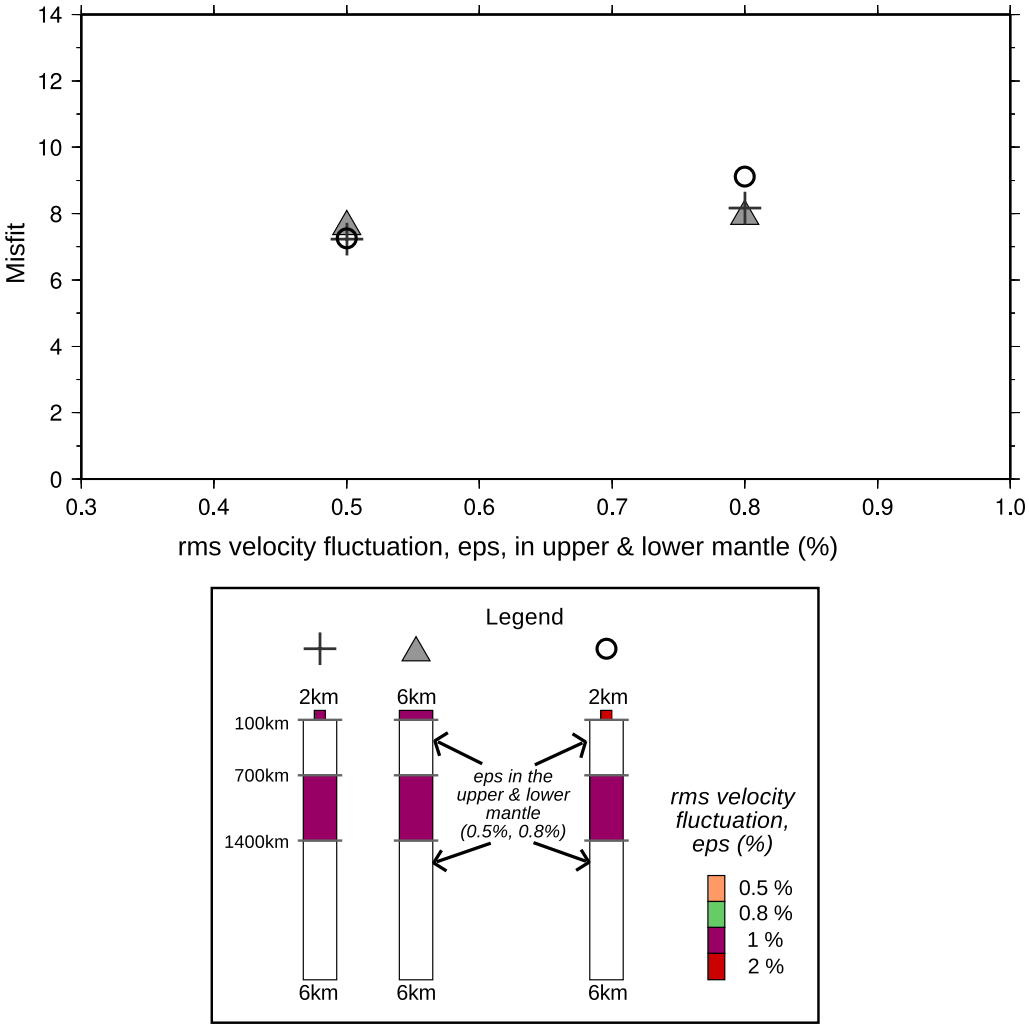

Figure 3.29: Correlation of the total RMS misfits for models with increasing rms velocity fluctuation (ϵ or eps) in the upper and lower mantle for models with four heterogeneity layers. The models used are separated into two groups with different lithospheric correlation length and rms velocity variation: $a = 2$ km and $\epsilon = 1\%$ (black cross); $a = 6$ km and $\epsilon = 1\%$ (light grey triangles); and $a = 2$ km and $\epsilon = 2\%$ (open black circles). The correlation length in the mantle ($a = 6$ km) and the rms velocity variation in the mid-mantle, for depths 700-1400 km, ($\epsilon = 1\%$) remain constant for all models.

3.7 Limitations

In applying the Monte Carlo modelling procedure to *PP* precursors, several parameters are assumed to be constant as outlined in Section 3.5. As a result there a few limitions to the method:

1. The modelling procedure is limited to radially symmetric shells of heterogeneity and does not consider the effect of lateral variations in scattering properties, especially crustal structure and topography of the moho and mantle discontinuities. The 3D variations of the crust are especially important as *PP* bounce points are mostly within the Pacific where the basaltic crust is ∼8 km thick. All models discussed have a constant lithospheric thickness of 100 km and do not take into account heterogeneity variations between the crust and underlying lithosphere. A surface heterogeneity layer that is too thick may result in a broader *PP* in the synthetics than in the data. Ideally, models should have laterally variations of the thickness of the surface layer to correspond to the variation of heterogeneity in continental and ocean regions, but this is not possible with the existing method.

2. No station corrections are applied to modelled data. The effect of this should be minimal for the stacked data as the effect of station elevation or near receiver velocity variations are suppressed when creating global averages. The effect on modelled data is unclear but as *PP* precursors properties (amplitude and time) are relative to *PP* properties then near receiver effects are probably reduced.

3. All models are created using an earthquake at the surface. For completeness, multiple versions of the same model should be run for different earthquake depths. Through tests it was found that varying the earthquake depth between surface and 100 km only caused small variations in the *PP* waveform. Shallow (0-50 km) and very deep (>400 km) earthquakes have been shown to effect the characteristics of the *P* coda (Shearer and Earle, 2004) but in this study for studying *PP* precursors, only shallow (0-100 km) earthquakes are used.

4. There may be other properties of the Earth that affect the amount of *PP* precursory energy. Directional scattering from anisotropy in the crust and upper mantle, or upper mantle waveguides are not considered, and are beyond the scope of this study.

5. The earthquake source mechanism was not analysed, and there may be variations in the amount of shear wave energy between earthquakes. The P/S energy ratio is selected to be a constant value of 23.4 for this study as consistent with previous studies that study upper and mid-mantle structure (Shearer and Earle, 2004). Variations in this ratio may result in different amounts and type of scattering but the impact on PP precursors is unknown and beyond the scope of this study.

6. The modelling process is non-unique and there are trade-offs between correlation length and rms velocity variation. The number of suitable models can be reduced by evaluating model fit to separate segments of the global stacked seismograms.

3.8 Discussion

3.8.1 Global average stacks

It is observed that the PP arrival is sharp (width of ∼10 s in the stacked data) and has a consistent shape across all distances. Analysis of the PP ray path distribution of the global dataset shows that there is good global coverage (Figure 3.6). Although the Pacific Ocean is better sampled due to the distribution of earthquakes and stations, two regional stacks formed from raypaths across the Pacific Ocean and the Atlantic Ocean show that there are few differences in the stacks between the regions. Therefore PP in the stacks likely represents a global signature of the underside reflection at the free surface, and the high frequency PP precursory and coda energy do represent a global signature of scattering.

As expected, the P coda energy is strong in the stacks, even when aligning on PP. Surprisingly, the PP underside reflections from the mantle discontinuities, particularly at 410 km and 660 km depth, are noticeably absent, even though these have slowness similar more similar to PP slowness than the P coda. These mantle discontinuities precursors may have different arrivals times due to regional topography on the discontinuities, which can be up to 40 km over 100 km in some regions (Shearer and Masters, 1992, Flanagan and Shearer, 1998, Rost and Weber, 2001, Cornwell et al., 2011). $PKiKP$ is prominent for distance 117.5° and visible in 112.5° but the phase is spread out in time, due to aligning on PP slowness.

PP precursory energy is clearly visible in global stacks, demonstrating that scattering is a global feature and is suitable for modelling of spherical shells of heterogeneous

media. It is apparent that *PP* precursors have a maximum amplitude of ∼50% of *PP*. The strength of the precursory energy does generally increase with distance. This may be expected at larger distances, as the travel path of *PP* increases and so the chance of scattering may increase. Alternatively, an increase in *PP* precursors may be an indication of scattering increasing with depth, as seismic energy with larger epicentral distances travel deeper into Earth (Figure 3.4). An additional consideration is that the precursory amplitude is relative to *PP* and it is assumed that this relationship is the same for all distances. As a result, variations in *PP* precursory energy maybe due to variations in *PP* strength rather than changes in heterogeneity. However, *PP* amplitude varying over distance is not an observed phenomenon here or in other studies.

3.8.2 Monte Carlo modelling applied to *PP* precursors

I have explored a number of models to find synthetic seismograms that match data including models that have been produced from analysis of other phases. Global stacks of *P* coda were modelled by Shearer and Earle (2004) and their best model (SE2004) predicts high levels of scattering in lithosphere and upper mantle. These levels of scattering cause the modelled *P* coda to completely saturate *PP* and mask the *PP* precursory energy. It is very difficult for this model to explain the observations in this study. Earle and Shearer (2001) analyse of the P_{diff} for distances 85-135° to produce a model with a simple lithospheric and mantle heterogeneity model of $a = 2$ km and $\epsilon = 1\%$ (ES2001). Their model produces *PP* precurors that are comparable to data for some distances (90-100°) but are over-predicted for shorter distances and under-predicted for larger distances. Modelling of *PKP* by Hedlin et al. (1997) produces a scattering model with constant $a = 6$ km and $\epsilon = 1\%$ (model H1997) that over-predict the amplitudes of *PP* precursors and produces *PP* that are too broad.

However, recent results show that ϵ in the mantle is 0.1% rather than the published 1% due to modelling errors in the work by Hedlin et al. (1997) (Shearer, pers. comm. 2013). Even with this adjustment, the model does not provide synthetics that fit the data in this study. H1997, ES2001 and SE2004 and others (e.g. Hedlin and Shearer, 2002, Margerin and Nolet, 2003b) all infer different models of heterogeneity in the mantle from different approaches, demonstrating that there is a significant trade off between the model parameters.

Crustal scattering does have a large effect on the shape of *PP* and precursory

energy. From the selection of models that best represent the global stack data, the most appropriate rms fluctuation in the lithosphere is consistently 1% but the lithospheric correlation length can vary from 2-8 km . As *PP* samples the lithosphere at the source, the receiver and the *PP* bounce point, then the scattering may occur at many locations in the lithosphere.

Though the main focus is to analyse the scattering effect on the *PP* precursory energy, the coda of *PP* also provides some important information and can be used in discriminating the fit of the models. From the models containing a single mantle scattering layer in addition to the lithospheric layer, model H1997_M08 (constant $a =$ 6 km with $\epsilon = 1\%$ in the lithosphere and $\epsilon = 0.8\%$ in the mantle) produces synthetic energy that best fits the *PP* precursors. However, this model underpredicts the *PP* coda energy. As *PP* is a min-max phase, *PP* coda most likely contains energy that has been scattered from heterogeneities that are deeper than the precursors to *PP*. By reducing the correlation length in the lithosphere (to a =2 km) and inserting an additional layer of scattering at 700 km ($\epsilon = 1\%$), model LAYM_44 also fits the precursory energy and provides a better match for the *PP* coda.

A few models with multiple scattering layers in the mantle provide synthetics that are a reasonable fit to the data. Models LAYM_44, LAYM_45 and LAYM_46 are all multi-layered scattering models with $\epsilon = 0.8\%$ in an upper mantle layer and a deeper layer of $\epsilon = 1\%$ starting at 700 km (for LAYM_44 and LAYM_45) or 400 km (LAYM_46) and extending to the CMB, or to 1400 km and the CMB, respectively. There are limited differences between the synthetics of these models, suggesting that the *PP* precursors are sensitive to the uppermost mantle and the mid-mantle (700-1400 km). The models under-predict *PP* precursors for the furthest distances (112.5-117.5°) in this study. For these distances *PP* samples deeper in the mantle (turning point of up to 1550 km), and so a model with an additional layer, for example between 1000-1400 km, with increased scattering may provide a better fit.

In addition to qualitative assessment of the model fit, the total RMS misfit is calculated to select the best fitting quantitatively (Section 3.6.5). The best misfits ($\approx$ 7.2) are found for models LAYM_47 and LAYM_49 (Table 3.2), which have four layers of heterogeneity within the lithosphere and mantle. These models are similar to the best fitting models found through qualitative assessment, such that they all have a mid-mantle with $\epsilon = 1\%$ and $a = 6\ km$. One of these models, LAYM_45, also has

a very low misfit (7.92), possibly due to similar upper and lower mantle rms velocity fluctuation in LAYM_45 (0.8%) to the rms velocity fluctuation in models LAYM_47 and LAYM_49 (0.5%).

The best fitting models selected by qualitative and quantitative assessments do not match and such differences probably arise from a subjective bias to certain distance stacks. In particular, models with better fit in the mid distances (92.5-107.5°) are preferred than those with a good fit for short (<92.5°) or large (>107.5°) distances, because the *P*coda removal and contamination from *PKiKP* may influence the amplitudes respectively. In contrast, the quantitative analysis is performed with no weighting applied to any particular distance bin.

Though it is difficult to know exactly what depths the *PP* precursors analysed in this study are mostly sensitive to, the models show that the precursory energy is unlikely to be sensitive to heterogeneity at depths > 1400 km. Models derived from *PKP* precursors and *PKP* coda reveal whole mantle scattering (Hedlin et al., 1997, Hedlin and Shearer, 2002, Margerin and Nolet, 2003b). *PKP* precursors are generally sensitive to lower mantle features but also sample other shallower parts of the mantle by increasing the epicentral distance. The single-layer mantle scattering model preferred from the research listed above only fit the stacked data up to a distance of 139° which is only sensitive to depths of below 1700 km (Figure 3.1) and thus do not sample the same portion of the mantle as *PP* precursors. Unfortunately the distance range in this study is not sensitive to lower mantle scattering so lower mantle heterogeneities and the discrepancies between previously published models cannot be resolved (e.g. Margerin and Nolet, 2003b, Shearer and Earle, 2004).

3.9 Summary

Global stacks of *PP* have revealed *PP* precursory and coda energy for distances 70-120°. The *PP* precursory energy increases in time and with distance, and the onset of precursors (with amplitude ∼10% of *PP* amplitude) occurs between 30 and 90 s before *PP* depending on distance. Similarly, the *PP* coda also slightly increases with distance, but, since the coda is stronger than the precursory energy, the precursors and coda probably have different sources of heterogeneity.

Forward modelling of heterogeneity in the lithosphere and mantle has been applied to analyse the high frequency *PP* precursory wavefield. More than 100 simple models

have been examined with varying correlation length and rms velocity fractional fluctuation in up to 4 layers of heterogeneity through the lithosphere and mantle. The modelled precursory wavefield provides a good fit to the data for models with 1% scattering in the lithosphere, $0.5-0.8\%$ scattering in an upper mantle layer and 1% scattering at depths greater than $\sim$700 km. The extent of this deeper mantle layer has not been resolved and could only be determined using larger epicentral distances. For distances $>102.5^{\circ}$, accurate modelling of the *PKiKP* arrival would have to be considered. Nonetheless, these results suggest that there is certainly some variation between scattering strengths between lithosphere and mantle, and that scattering probably varies in strength and correlation length between the upper and lower mantle.

Chapter 4

Regional patterns of heterogeneity derived from *PP* precursors

4.1 Overview

The Chapter describes an approach to detect and locate high frequency coherent scattering that is associated with small-scale heterogeneity in the mantle. The approach focuses on detecting regional patterns of heterogeneity using array seismology methods, in contrast to the global stacking method undertaken in Chapter 3.

The main aim is to detect coherent *PP* precursors that arrive off great circle path from a scatterer that lies out of plane. Such precursors are analysed for directivity and arrival time and the origin of scattering is located using ray-tracing. The located scatterers are compared to tomography, slab topography, and present day and ancient surface tectonic features to reveal deformation of subducted slabs to infer the dynamics of mantle flow.

4.2 Introduction

In the last few decades, seismic tomography has been very successful in imaging the large scale structure of the interior of the Earth (e.g. Dziewonski and Woodhouse, 1987, Engdahl et al., 1995, Hilst et al., 1991, Ritsema et al., 1999, Grand, 2002, Huang and Zhao, 2006, Ritsema et al., 2011). Dominant features in these studies are bands of fast seismic velocities that correlate well with the locations of past and current subduction

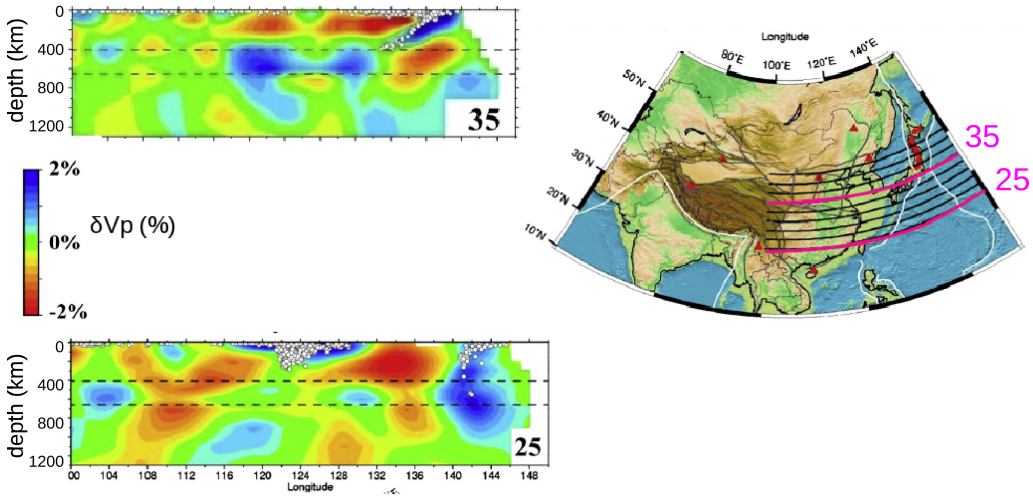

Figure 4.1: *P* wave tomography beneath SE Asia showing horizontal fast velocity feature in the transition zone (cross section at latitude 25°) and a steep linear fast velocity anomaly that is present from the surface until depths of 1000 km (cross section at latitude 35°) (Huang and Zhao, 2006). Reprinted from Zhao and Ohtani (2009). Copyright 2009, with permission from Elsevier and International Association for Gondwana Research.

zones and are interpreted as subducted oceanic plates or slabs in the Earth's mantle (van der Hilst and Seno, 1993). High resolution regional tomography has shown that some steeply subducting slabs penetrate into the lower mantle while other slabs stagnate in the transition zone and lie horizontally on the 660 km seismic discontinuity (Figure 4.1). The resolution of tomography is reduced with depth so currently the structure of slabs in the lower mantle is uncertain. Also, tomography is sensitive to the long wavelength features and cannot resolve the small-scale crustal component of the slab. As summarised in Chapter 1, the subducted crust introduces chemical heterogeneities in the mantle and knowledge of the distribution of subducted crust can give important supplementary information on large-scale flows.

Subducted slabs are the major driver to transport chemical heterogeneity through the upper mantle and sometimes into the lower mantle (Hofmann, 1997, van Keken et al., 2002, Helffrich, 2006, Rapp et al., 2008). Resolving the structure and dynamics of the compositional heterogeneity represented by these slabs is an important piece of our understanding of the chemical evolution of the mantle. Generally, the subducted slab consists of two large components: the harzburgite lithospheric base and the basaltic upper crustal component, with a thin (∼1 km) layer of hydrous sediments deposited on the oceanic crust before subduction. Though some of this material might be transported into the mantle, most of the sediments are likely to be removed during the subduction

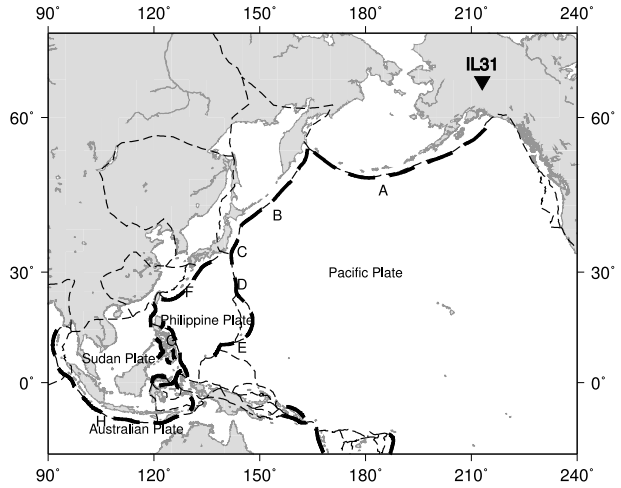

Figure 4.2: Map showing western Pacific subduction zones (thick dashed lines) in relation to the ILAR array. Key subduction zones are labelled. A - Aleutians; B - Kurile; C - Japan; D - Izu-Bonin; E - Mariana; F - Ryukyu; G - area containing Philippine, North Sulawesi, Sangihe, Manila and Halmahera; H - Sudan Arc (Java Trench). Plate boundaries are shown as thin dashed lines (Bird, 2003).

process and are not important for the overall chemical heterogeneity of the subducted slab deeper in the mantle.

The western Pacific region has >11 subduction zones (Figure 4.2) and has a history of subduction for more than 100 Ma. The region has been extensively studied using subduction zone seismicity and tomography (van der Hilst et al., 1999, Huang and Zhao, 2006, Zhao and Ohtani, 2009) but recently, studies of the short-period, scattered seismic wavefield have detected small-scale elastic heterogeneities beneath circum-Pacific subduction zones (Weber and Wicks, 1996, Kaneshima and Helffrich, 1999, Krüger et al., 2001, Rost et al., 2008, Kaneshima, 2009). These heterogeneities are commonly interpreted as the remnants of the subducted oceanic crust that are now located in the mid and lower mantle. The elastic properties of these heterogeneities agree well with the expected properties of mid-oceanic ridge basalt under high pressure and temperature (Rost et al., 2008) as determined by theoretical and experimental studies (Irifune and Tsuchiya, 2007). The scale-length of the detected heterogeneities is typically on the order of 10 km, partly due to the dominantly 1 Hz seismic energy used in the analysis. This scale agrees well with the expected thickness of subducted crust.

Most seismological studies imaging these heterogeneities use P-to-P or P-to-S scattered energy arriving in the P coda. They often use some form of simplified time migration of the P *coda* energy to locate, and study the heterogeneities. Kaneshima

(2009) and Kaneshima and Helffrich (2009) use semblance analysis of S-to-P scattering to detect heterogeneities in the uppermost lower mantle in close proximity to slabs beneath several Pacific subduction zones. They conclude that the seismic data reveal the early stages of a mechanical mixing process of the subducted MORB into the mantle and that the density of the subducted material does not prevent it from being entrained into the lower mantle, i.e. the basaltic crust does not de-laminate from the harzburgitic slab and does not remain in the upper mantle. Rost et al. (2008) detect scatterers down to depths of about 1000 km mainly beneath the steeply dipping Mariana and Tonga/Fiji subduction zones. The locations of the scatterers detected by Rost et al. (2008) also agree well with fast velocities commonly observed in tomographic images. They conclude that they likely detect the subducted paleo-Moho in the lower mantle.

The seismological detection of subducted crust is important for our understanding of the chemical evolution of the lower mantle especially since several studies indicate that some lower mantle structures such as Large Low-Shear Velocity Provinces (LLSVPs) might contain ancient subducted MORB material (Christensen and Hofmann, 1994, Tackley, 2000, Deschamps et al., 2010). Further seismological studies targeting the very fine scale structure of the mantle will allow us to estimate the material flux from the surface to the lower mantle due to the subduction process. The material flux will depend on the slab descent speed, the density contrast of the subducted material and the mantle viscosity (Quinteros et al., 2010). Therefore the seismic imaging of the subducted oceanic crust will provide constraints on these properties that are essential for mantle convection modelling.

In this Chapter I present results of a novel approach exploiting a probe and a seismic array that have been under-utilised in detecting fine-scale mantle structure. Energy arriving as precursors to PP is recorded and analysed at the small-aperture Eielson Array (ILAR) in Alaska. Such precursory energy is scattered off the great circle path between source and receiver (Rost et al., 2008). A weighted semblance analysis similar to Kaneshima (2009) and Kito et al. (2008), is employed to detect the source of scattering (scatterers), and directivity and travel-time are used to located the scattering. As the PP probe has not been used greatly for studying off azimuth arrivals, the spatial sensitivity and relocation accuracy of the approach is explored. Located scatterers are compared to tomography, slab topography, paleo-subducted trenches and scatterers found in other studies, in order to draw more informed conclusions.

4.3 Data

4.3.1 Eielson Array

In this study data is used from the Eielson Array (ILAR), Alaska (Figure 4.3). ILAR is located approximately 90° to 110° away from several western Pacific subduction zones, a distance ideal for the study of scattered *PP* precursory energy (Rost et al., 2008). ILAR is a small (10 km) aperture seismic array and is designed to detect high frequency signals from underground nuclear explosions (Figure 4.3a).

ILAR consists of 19 vertical component short-period (SHZ) Geotech 23900 seismometers (IL01 - IL19) with a sample rate of 20 samples a second; and a single three-component broadband Geotech KS54000 seismometer (IL31) with a sample rate of 40 samples a second. The short-period stations have used the Geotech 23900 model since the original installation in April 1995, even though the instruments have been replaced in July 2006. The broadband instrumentation was changed from the Geotech KS36000 (BHE and BHZ components) and R00231 (BHN) models, which were installed in April 1995, to the Geotech KS54000 seismometers that are used presently.

The stations are quasi-randomly distributed over a circular area with stations IL01 and IL31 located at the centre of the array with coordinates (64.77, -146.89) (see Appendix E for a full list of stations, coordinates and elevations). The circular, quasi-random distribution of the seismic stations ensures little spatial aliasing and suppression of sidelobes in the array response function (ARF) (Figure 4.3b). Slowness-wavenumber resolution of the array is not optimal due to the small aperture, but advanced array processing (described in Section 4.4) results in precise determination of the directivity of the incoming seismic wavefield.

The high frequency instruments and low spatial aliasing allow ILAR to be well suited to studying the high frequency *PP* wavefield. ILAR has been used previously to study small-scale structure in the Earth, for example characterising lower mantle features using core-reflected phases (Idehara et al., 2007) and analysing the properties of the inner core boundary using *PKiKP* (Koper and Dombrovskaya, 2005). As ILAR is a small aperture array, the variations in topography and geology can affect directivity measurements (Koper and Dombrovskaya, 2005) and as such Lindquist et al. (2007) studied the slowness and backazimuth variations at ILAR for key seismic phases including *PcP, PKiKP, PKP* and *PKKP* and succeeded in developing a semiautomatic

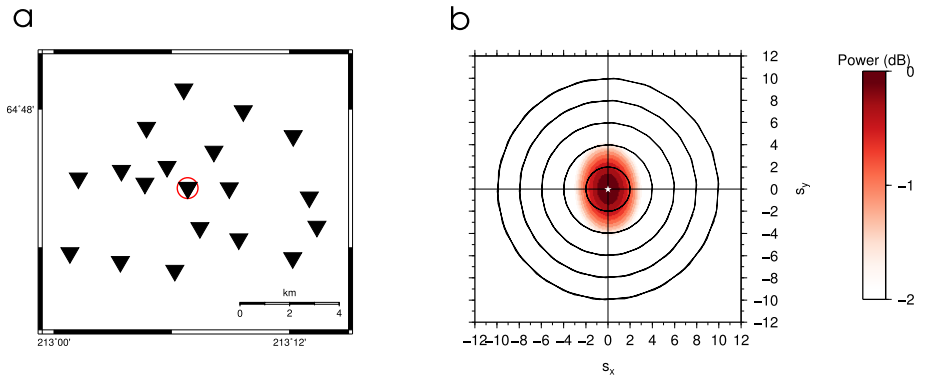

Figure 4.3: a) ILAR array consists of 19 short period stations (black triangles) and 1 broadband station, IL31 (red circle) that are centred around the short period station IL01, co-located with IL31 (lat: 64.77, lon: -146.89) . b) Array Response Function (horizontal slowness components, S_x and S_y) for the ILAR array.

calibration method to be applied to further studies at ILAR.

4.3.2 Probe - *PP* and *PP* precursors

As outlined in Chapter 2.3.1, the probe used for studies in this thesis is *PP* and *PP* precursors. *PP* is a seismic phase that has reflected once midway between source and receivers (Figure 4.4). *PP* is a minimum-maximum travel time phase with respect to variations along and perpendicular to the source-receiver plane and energy scattered from interfaces at depth arrive as *PP* precursors.

Such anomalous energy arriving prior to *PP* has been associated to seismic reflections and scattering from small-scale heterogeneities in the mantle (e.g. King et al., 1975, Kato and Hirahara, 1991, Revenaugh and Jordan, 1991, Estabrook and Kind, 1996, Weber and Wicks, 1996, Flanagan and Shearer, 1998, Deuss et al., 2006, Rost and Weber, 2002, Rost et al., 2008).

Many studies of *PP* precursors have found the arrivals to originate from underside reflections off mantle discontinuities (e.g. Shearer, 1990, Flanagan and Shearer, 1998, Deuss et al., 2006). *PP* precursors can also be generated by asymmetric reflections off the free surface (e.g. Wright, 1972). For such mantle discontinuity reflections or asymmetric reflections *PP* precursors arrive approximately along the great circle path.

For this study, only *PP* precursors that arrive off great circle path with backazimuth deviation of $\delta\theta$ are required (Figure 4.4). These off azimuth arrivals (denoted *P*P*) have been successful previously in detecting and mapping scatterers in the mantle (Rost et al., 2008). The off azimuth reflected or scattered *PP* wavefield is best observed in

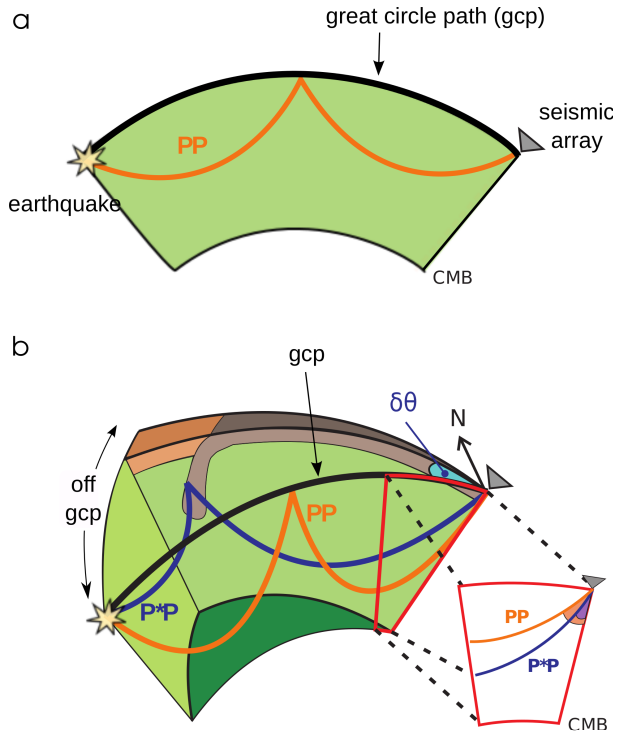

Figure 4.4: a) *PP* (orange path) travels along great circle path (black line) between earthquake and array. b) A precursory arrival to *PP*, denoted *P*P* (purple path) may arrive at the array due to scattered energy from a subducted slab that lies off the great circle path. The two arrivals have different backazimuth (difference in backazimuth labelled as $\delta\theta$) and different incident angles (shown in the insert). After Rost et al. (2008).

the distance range of 90° to 110° (Wright, 1972, Rost et al., 2006, 2008) and arrives in a time window up to 100 s before the *PP* arrival (Rost et al., 2006). As *P*P* arrive off azimuth, they can be differentiated from other precursors e.g. underside reflections off mantle discontinuities which arrive along great circle path.

4.3.3 Earthquakes

As required for studying *PP* precursors, earthquakes are selected within the distance range 90°-110° from ILAR array. Earthquakes occurring in SE Asia are suitable to study mantle structure associated with subduction in the western Pacific as the seismic energy travels through many present day subduction zones (Figure 4.5a). Therefore, earthquakes that arrive at ILAR with backazimuth between 180° and 345° are selected (Figure 4.5a).

As the *PP* precursors are weak, larger earthquakes with magnitude Mw $>$ 6 are required to increase detection likelihood. The focal depth of the earthquakes used is limited to less than 100 km because deeper earthquakes produce other arrivals, such

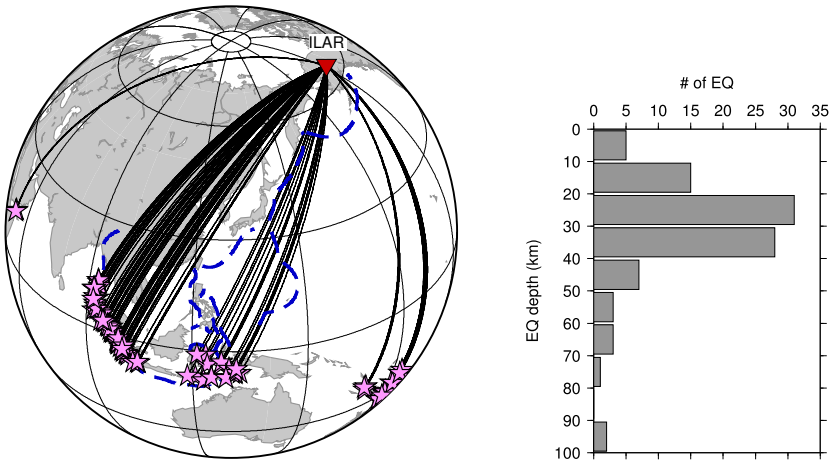

(a) (b)

Figure 4.5: a) Earthquake locations (pink stars) of seismic data that contain *PP* precursors. Great circle paths of *PP* (black arcs) travel close to western Pacific subduction zones (blue dashed lines) (Gudmundsson and Sambridge, 1998) before arriving at ILAR (red triangle). b) Depth distribution of the 95 earthquakes used in this study.

as depth phases and scattering from depth phases, and these phases arrive in the same window as *PP* precursors. In total, 239 earthquakes occurring from year 2000 to 2012 fit the selection criteria with only 95 of these earthquakes contain *PP* precursors (Figure 4.5, Table F.1).

4.4 Method

4.4.1 Pre-processing

Global stacks of teleseismic data between 90°-110° show scattered energy arriving ∼100 s before *PP* (Rost et al., 2006). This time window is well suited to study the scattered energy because it is free from *P*-coda energy (Figure 4.6), other main phases (e.g. *PKiKP*, *PcP*) and depth phases (and their codas) for shallow to intermediate depth earthquakes (Rost et al., 2008).

Data are bandpass filtered with corner frequencies of 0.5 Hz and 1.4 Hz; the frequency band that has been found to be most appropriate for the targeted scattered energy (Figure 4.7). Obvious data errors (e.g. spikes) and trends are removed from the seismograms. Only events with strong *PP* arrival are selected to aid precise traveltime measurements and discard traces with a signal-to-noise ratio (SNR) of less than 4 (SNR calculated as *PP* amplitude relative to the noise prior to the P/P_{diff} arrival, i.e. the P-wave diffraction along the CMB). Events are retained for further analysis if more

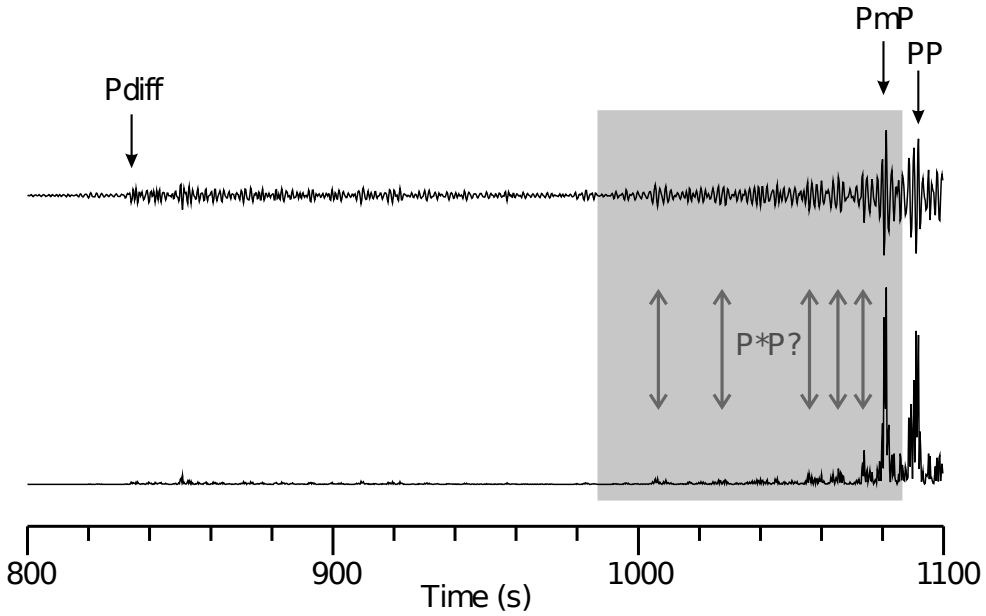

Figure 4.6: *PP* beamed seismogram (top) and *PP* beamed and squared seismogram (bottom) for earthquake on 15th April 2009, 20:01 (lat: -3.12, lon: 100.47, dep: 22 km, epicentral distance 102.33°, Mw: 6.3). Beam was formed from aligning traces from all 19 short period stations using theoretical *PP* slowness and backazimuth. Phases Pdiff and *PP* are marked, as well as the 100 s window before *PP*, which contains weak energy that may be *P*P* arrivals.

than 10 traces are suitable.

Due to the low energy of P_{diff} in the short-period recordings *PP* is used as the reference phase for the determination of the relative travel time of the precursors. It is known that all 1D Earth models struggle to correctly predict *PP* traveltimes (Kennett et al., 1995), but for this dataset ak135 shows the smallest error between picked and predicted traveltimes for *PP*. Differences in *PP* travel time may arise from local velocity variations and these are described in Section 4.4.3.

Traveltimes calculated for the 1D Earth model ak135 (Kennett et al., 1995) are used as a reference to pick the *PP* arrival time from the data of the central broadband station within ±50 s of this traveltime. *PP* is first identified in broadband (Figure 4.8) data since the additional passes of *PP* through the crust further attenuate the higher frequencies of *PP*, therefore the phase is detected more easily at longer periods (T>5 s). Using the broadband pick of *PP* as a guide is also useful in avoiding the picking the strong Moho reflection (*PmP*) in error, as *PmP* can be dominant in the short-period records in this time window (Figure 4.7). A a time window of ± 2 s is defined around the *PP* broadband pick and the best *PP* arrival is chosen as the highest amplitude arrival within the window, for each short-period station seismogram (Figure

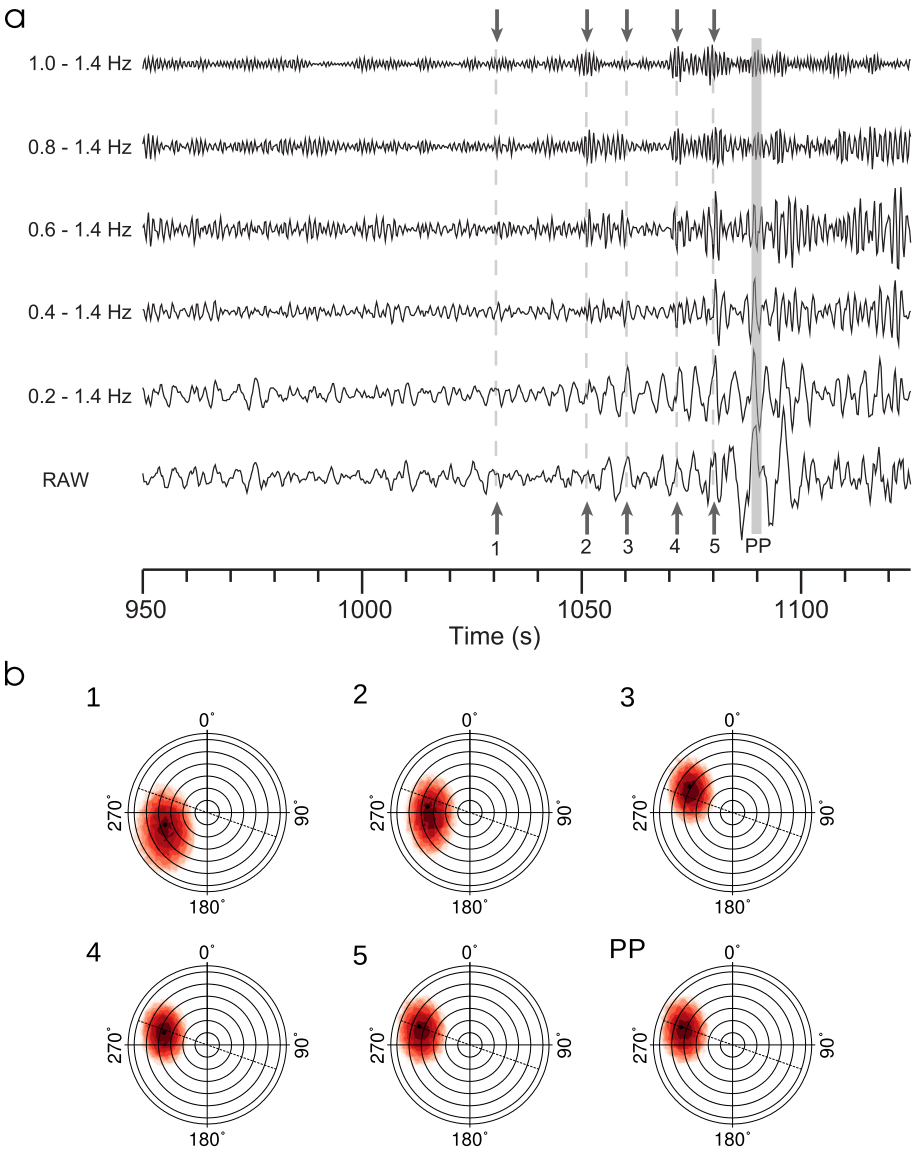

Figure 4.7: a) *PP* beam data from earthquake on 15th April 2009, 20:01 (see Figure 4.6) for different frequency bands. Data were filtered with 5 different bandpass filters. Observed *PP* arrives at 1090 s and is identified until the 0.8-1.4 Hz band (*PP* highlighted in grey). At least 5 coherent arrivals as precursors to *PP* are noticeable in most frequency bands. Precursors are marked by the arrows and dashed lines. b) Polar plots showing the optimum slowness (radial axis) and backazimuth (angular axis) found using fk analysis for precursors marked 1-5 and for *PP*. Dashed line marks the backazimuth for the great circle path. Radial circles mark every 2 s/° of slowness and power scale is the same as for Figure 4.3b.

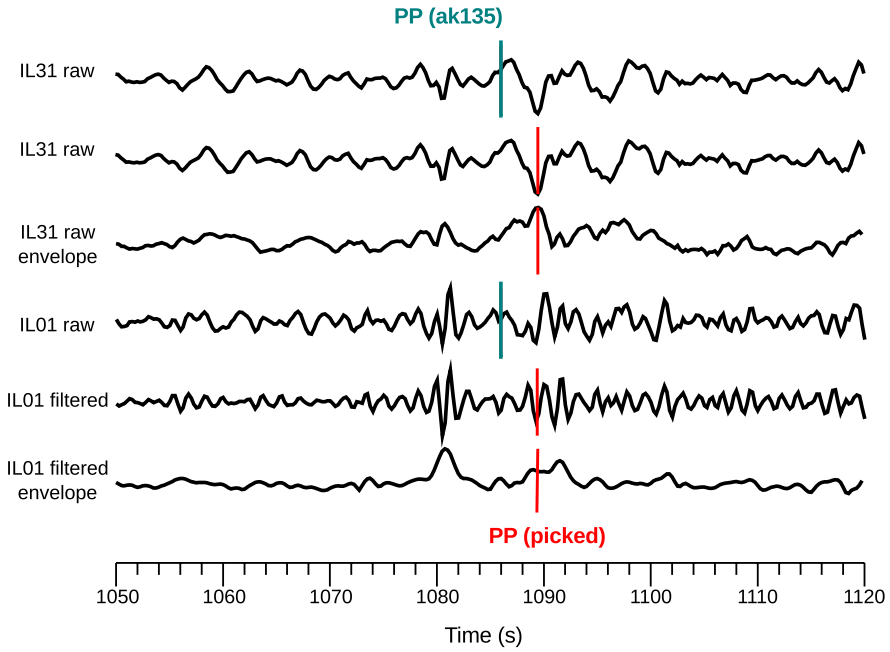

Figure 4.8: Picking procedure for *PP*. *PP* arrival time varies from those predicted by reference models.

4.8). Despite this careful picking procedure, there remains a *PP* traveltime uncertainty of 1 s, since the short-period *PP* waveform is complicated due to the interaction with the layered crust at the reflection point (Rost and Weber, 2001). As expected, the picking error will add to the uncertainty in scatterer relocation (see 4.4.3 Corrections and Errors).

The energy related to the *PP* scattered wavefield can be observed in individual seismic traces and in array beam traces (Figure 4.6 and 4.7). To maximise the detection of weak arrivals amongst the noise level, arrivals are selected based on the semblance and directivity properties of the *PP* precursors as described in the next section.

4.4.2 Automatic detection of *PP* precursors

To avoid a bias of selecting higher amplitude scattered arrivals that are visually more prominent in the seismic data, an automatic approach (TOPCAT: Toolkit for Out-of-Plane Coherent Arrivals Tracking) is developed, which exploits waveform coherence in detecting and extracting information from the scattered energy. Explicitly, a semblance weighted beampower is used as a measure of the coherence and amplitude of the pre-*PP* energy. The semblance of the signal f is calculated (Neidell and Tanner, 1971) for M stations through the equation:

$$S_c = \frac{\sum_{j=k-(\frac{N}{2})}^{k+(\frac{N}{2})} \left\{ \sum_{i=1}^{M} f_{i,j(i)} \right\}^2}{M \sum_{j=k-(\frac{N}{2})}^{k+(\frac{N}{2})} \sum_{i=1}^{M} f_{i,j(i)}^2} \tag{4.1}$$

where N is the number of samples in the time window and k indicates the sample at the centre of the semblance time window. A sliding-window approach (Rost and Weber, 2002) is employed to calculate semblance in a short (3 s) time window, shifting it across the 100 s time window before *PP* energy with a 0.2 s overlap between windows. A time window of 3 s allows the inclusion of the dominant period of the scattered energy and overlapping windows allow centring of the energy limiting any truncation of the waveforms. The slowness vector (slowness and backazimuth) in each time window is determined using frequency-wavenumber (fk) analysis (Capon, 1969).

The slowness and backazimuth derived from the fk-analysis is used to correct for moveout of the signal in each analysis window, and a beamtrace (sum of traces from each station) is produced and its amplitude (A) is measured. The semblance coefficient S_c for each time window is used to weight the beampower by ${S_c}^2 * A$. A normalised semblance weighted beampower (NSWB) time series is formed by dividing the spectrum by the weighted beampower of *PP*.

Variations in slowness, backazimuth, semblance, beampower and NSWB across the 100 s time window of an example event are shown in Figure 4.9. A precursor is defined as energy arriving with a NSWB > 0.1 (Figure 4.9), a threshold that is found through testing the detection of precursors in synthetic data. Four synthetic datasets are created for *PP* and five precursors under four different noise conditions (SNR = 5, 9, 18, 89). An extracted *PP* waveform (from real data) is used for synthetic *PP* and *PP* precursors, and extracted pre-signal noise is used as the synthetic noise signal. Resultant synthetics with SNR= 18 are spectrally and visually similar to the real data (Figure 4.10). Synthetics are then processed through TOPCAT and the number of precursors detected are shown in Figure 4.11. A NSWB threshold of 0.1 is chosen as the 5 precursors are detected for most noise levels and no spurious arrivals are picked (Figure 4.11).

Another condition for selection is that a precursor must be at least 3 s from another selected precursor to avoid multiple detection of a single arrival in the analysis window. A scattered arrival is defined as a precursor with a backazimuth that is $\pm 5^\circ$ from

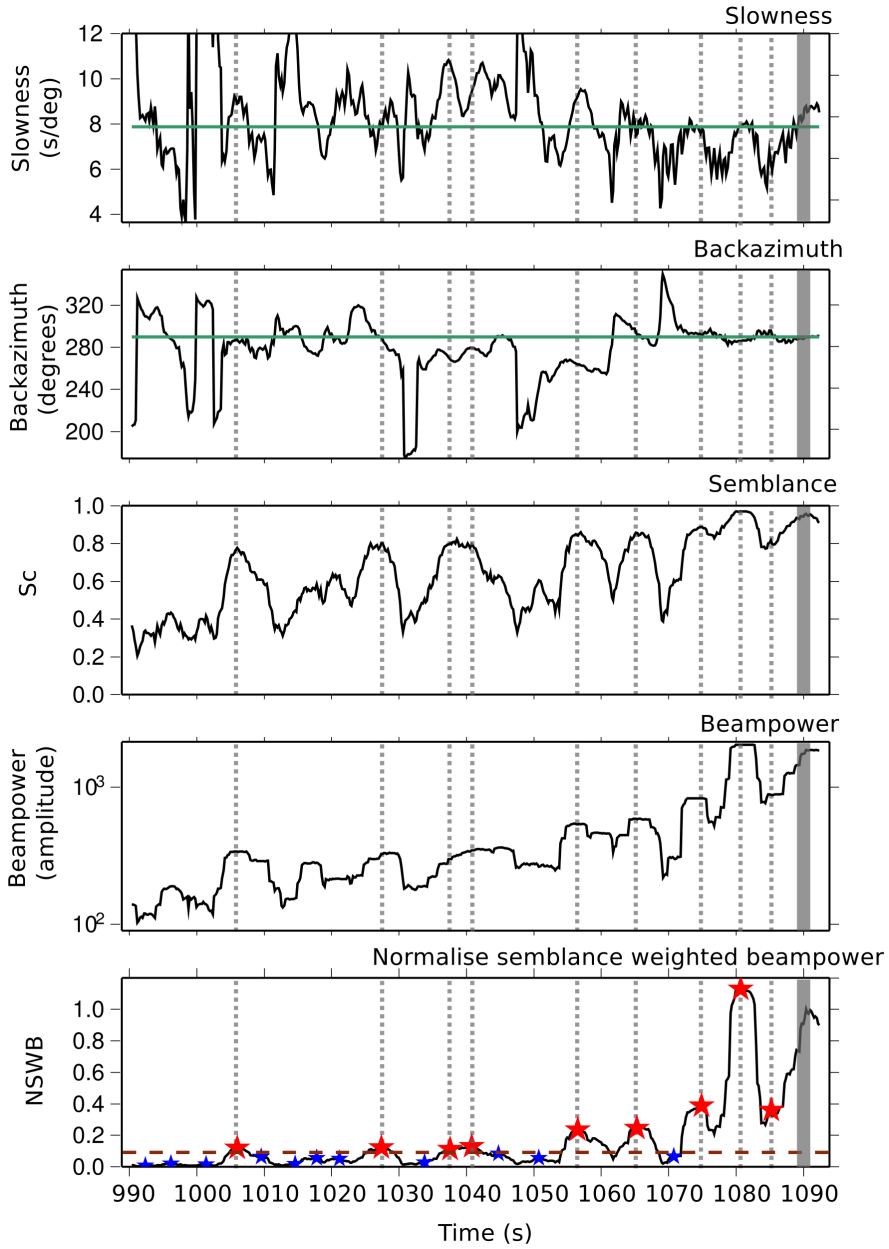

Figure 4.9: An example of the results from TOPCAT for event 15th April 2009, 20:01 (see Figure 4.6). From top to bottom: plots show variations in time of slowness, backazimuth, semblance coefficient, Beampower and normalised semblance weighted beampower (NSWB). Theoretical PP slowness (7.515 s/°) and backazimuth (289.38°) marked by green horizontal lines. Peaks in the NSWB spectrum that are below the 0.1 threshold are marked with blue stars and those above the 0.1 threshold and classified as precursors are marked with red stars and grey dashed lines.

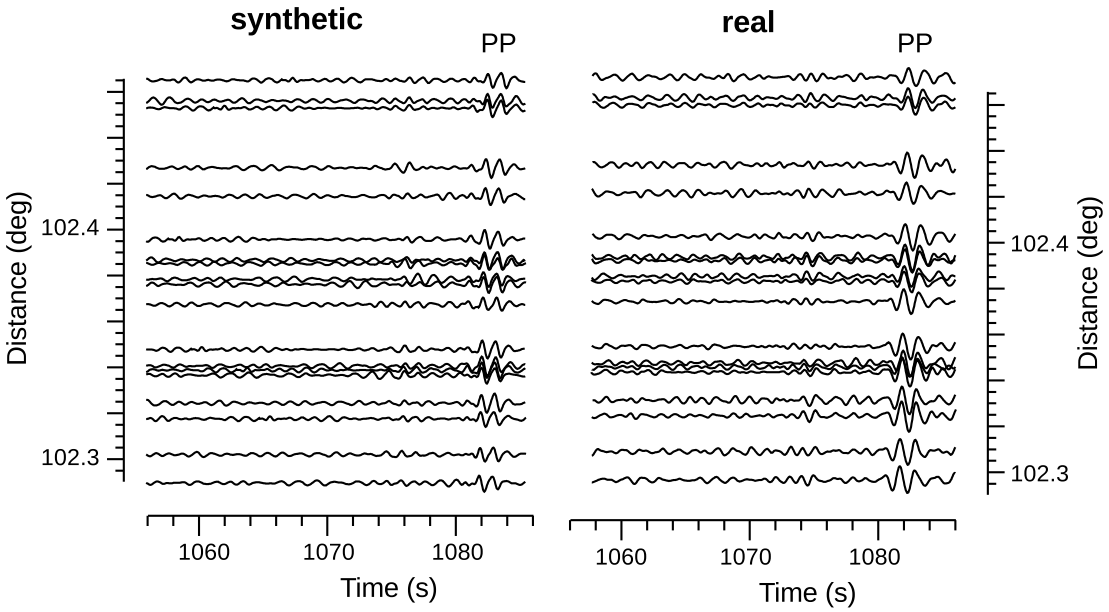

Figure 4.10: Synthetic data (left) generated with SNR= 18 using extracted *PP* waveform from real data (right) to produce modelled *PP* and *PP* precursory arrivals. *PP* precursor amplitudes range between 15% and 30% of *PP* amplitude. Synthetic and real data have same spectral content.

the observed *PP* backazimuth to avoid the detection of in-plane underside reflections. Scatterer travel-time is selected as the time of the maximum beampower within the analysis window.

4.4.3 Corrections

It is observed that there are differences between the *PP* slowness and backazimuth as measured at the array and the *PP* slowness and backazimuth derived from 1D reference models for the same source-receiver geometry. Since scatterer locations are found by ray-tracing through a 1D model, corrections should be applied for any observed slowness and backazimuth deviations that are due to velocity variations in the vicinity of the receivers. Though corrections for ILAR have been previously explored (Lindquist et al., 2007), these corrections can not be used for this dataset due to the different distance (i.e. slowness) and backazimuth ranges that are covered. Instead, slowness/backazimuth deviations are derived from the data by collating slowness and backazimuth that are measured for *PP* for each event and compare these to the theoretical values for ak135. The measured uncertainties are displayed as mislocation vectors between expected and measured slowness and backazimuth values (Figure 4.12). It is found that the mean of the observed slowness is less than the mean of the calculated

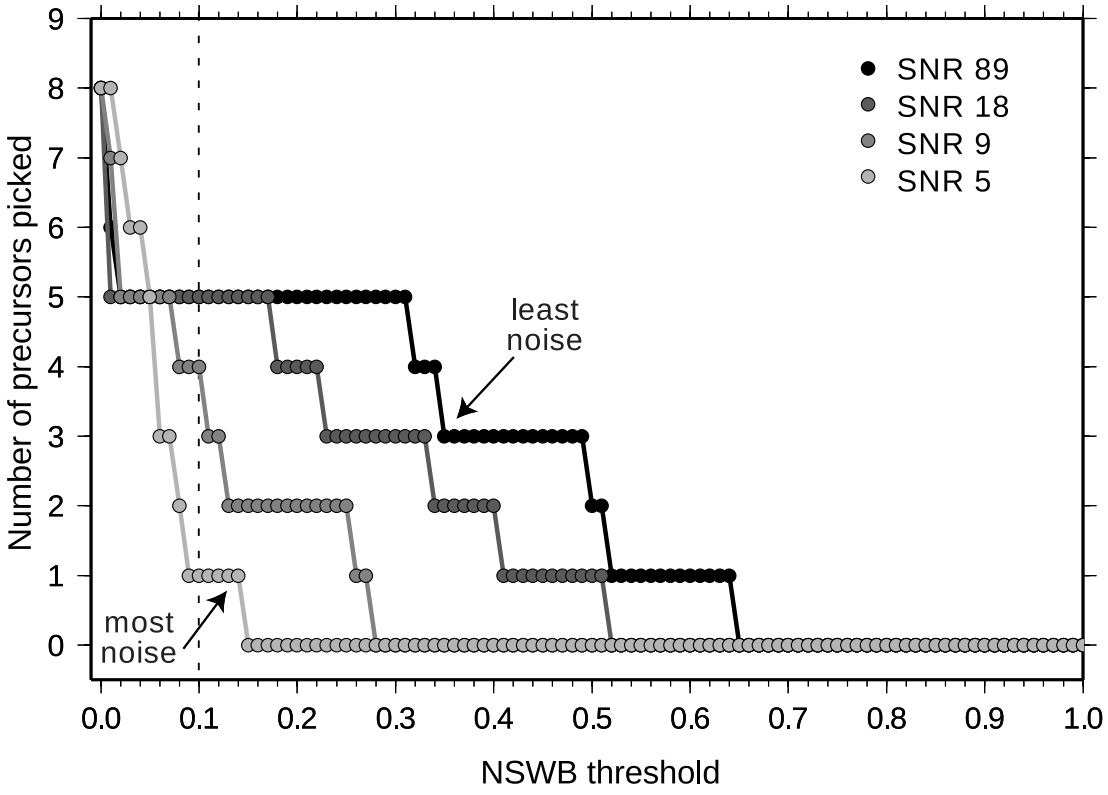

Figure 4.11: To select the Normalised Semblance Weighted Beampower (NSWB) threshold for the automatic picking of precursors, synthetic datasets with coherent signals of known slowness, backazimuth and travel time are generated and processed through TOPCAT. We vary the threshold in the resultant NSWB spectrum and calculate the number of peaks that exceed each of those thresholds (i.e. criteria of a PP precursor). We use four synthetic datasets with various levels of PP amplitude to pre-signal noise (SNR of 5, 9, 18 and 89) with the SNR defined after beamforming. The synthetics contain six precursors of variable amplitude in addition to PP. For synthetics seismograms with SNR$\geq$18, all six precursors are found when using NSWB threshold = 0.1. For the synthetic seismograms with the most noise (SNR=5 and SNR=9), one precursor is not detected when applying the 0.1 threshold, but this is not considered problematic as a majority of beamformed seismograms used in this study have SNR>20.

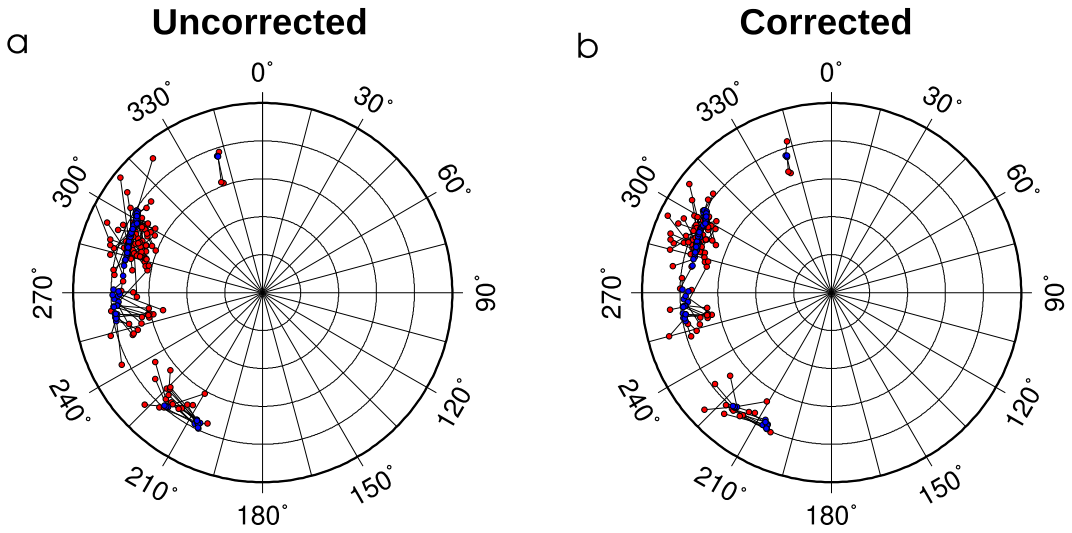

Figure 4.12: a) Polar plots in slowness (radial) and backazimuth space, showing vectors of theoretical (blue) and observed (red) directivity (slowness and backazimuth) for *PP* observed within the dataset for this study. b) Polar plots in slowness (radial) and backazimuth space, showing vectors of theoretical *PP* directivity (blue) and observed *PP* directivity after the slowness correction has been applied. For both figures, ak135 (Kennett et al., 1995) is used to derive the theoretical directivity.

slowness, with difference of 0.46 s/°. Since the average observed slowness is less than the average theoretical slowness, the *PP* waves are arriving steeper than expected, which could be caused by the higher velocity layer of the Aleutian subducted slab (Lindquist et al., 2007). As little variation of slowness deviation with distance or backazimuth is observed, a bulk shift of 0.46 s/° is applied to the *PP* precursors to correct for 3D structural variations beneath the array. The difference in the means of the observed and theoretic backazimuth is small ($\Delta\theta \approx 0.83°$) but individual differences between observed and theoretical backazimuth varies greatly with backazimuth. The lack of azimuthal coverage in our dataset limits a comprehensive analysis of azimuthal correction and therefore no corrections for backazimuth deviations are made (Figure 4.12).

4.4.4 Locating scatterers that generate the *PP* precursors

The origin of scatterer is located using the backprojection method as introduced in Section 2. The calculated slowness, backazimuth and travel-time (relative to *PP*) for each scatterer are used to raytrace through the 1D Earth model ak135 (Kennett et al., 1995). Slowness and backazimuth define a ray from receiver to scatterer origin (Figure 4.13) and travel-time is used to locate the exact location (in latitude, longitude and depth) along this ray by minimising the misfit between measured traveltime and the-

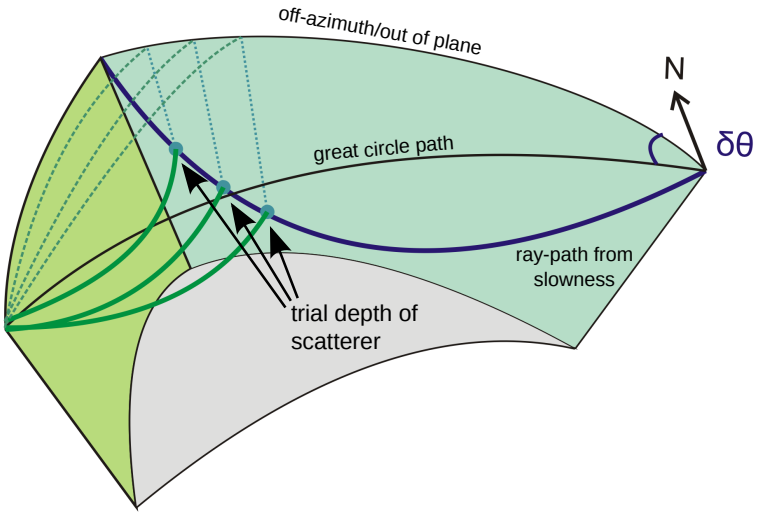

Figure 4.13: Procedure for locating *P*-to-*P* scatterers observed in the *PP* precursory wavefield. Slowness and backazimuth define a ray (blue path) from receiver to scatterer origin. Depth and source-scatterer path are unknown. These are found by ray-tracing from source to trial depths at every 20 km from surface to turning point (green paths). True scatterer depth is found by calculating total traveltime and minimising the misfit between measured traveltime and theoretical traveltime.

oretical traveltime for a vertical grid spacing of 20 km (Figure 4.13). Scatterers with traveltime misfit of more than 1 s are discarded from the analysis. Tests with the data show that only *P*-to-*P* scattering gives reasonable results in the relocation and solutions for *S*-to-*P* or *P*-to-*S* scattering have not been found. Therefore it is assumed that only *P*-to-*P* scattered energy is observed on the vertical instruments at ILAR.

4.4.5 Errors

Several errors will contribute to the mislocation of the scatterer origin as determined in the approach in this study. These are either related to the array measurement or the uncertainty in ray tracing through a 1D Earth model as used in the relocation procedure.

Errors in calculating directivity and travel-time

The uncertainties in the determination of slowness, backazimuth and travel time at the array are evaluated. These errors are then used to derive errors in latitude, longitude and depth of the scatterer locations. The slowness/backazimuth measurements obtained using the fk-analysis are dependent on the noise conditions in the time window.

	Slowness (s/°)	Backazimuth (°)	Travel time (s)
PP (input)	7.5	285	-
PP (TOPCAT result)	7.51	285.7	-
Precursor (input)	7.0	270	6.0
Precursors (TOPCAT result)	7.19	268.8	5.5
Detection errors	0.19	1.2	0.5

Table 4.1: Input directivity and travel times for *PP* and 1 precursor (with amplitude ratio of *PP* to precursor of 5), and output directivity and travel times (relative to *PP*) from TOPCAT.

Therefore errors determined from the main phase *PP* might underestimate the errors that apply to the precursors.

Using simple synthetic timeseries generated at each station in array (similar those in Figure 4.10) that simulate arrivals for varying slowness and backazimuth, estimates of the accuracy of the slowness and backazimuth measurements are generated. Synthetics are created using extracted waveform from real data (see Section 4.4.2) for SNR of 18 and are processed identically to recorded data. The results for these tests are shown in Table 4.1. Overall it is found that for good data noise levels (amplitude ratio of *PP* to precursor of 4 or more), the accuracy of the measurements for slowness, backazimuth and travel time are ±0.19 s/°, ±1.2° and ±0.5 s, respectively.

Errors in relocating origin of scattering

The detection uncertainties are used to find the errors in the backprojection procedure, using two test scatterers: one at 300 km depth and one at 1000 km, to evaluate if errors vary with depth. The calculated slowness, backazimuth and traveltime for each scatterer are altered by the errors of each of these parameters: ±0.19 s/° for slowness, ±1.2° for backazimuth and ±0.5 s for traveltime. Therefore for each scatterer six relocation cases are considered (Table 4.2) and results are listed in Table and shown in Figure 4.14. Errors in latitude, longitude and depth are derived for each scatterer by taking the largest differences between input and output parameters from the cases within each group.

Figure 4.14 shows that the smallest errors for latitude, longitude and depth are found to be generated with the errors in travel time (0.2°, 0.6° and 5 km, respectively), whereas the largest errors are due to errors in slowness (3°, 1.8° and 40 km). Errors in depth are slightly greater for a scatterer at $h = 1000$ km, but errors in coordinates do not greatly increase with depth.

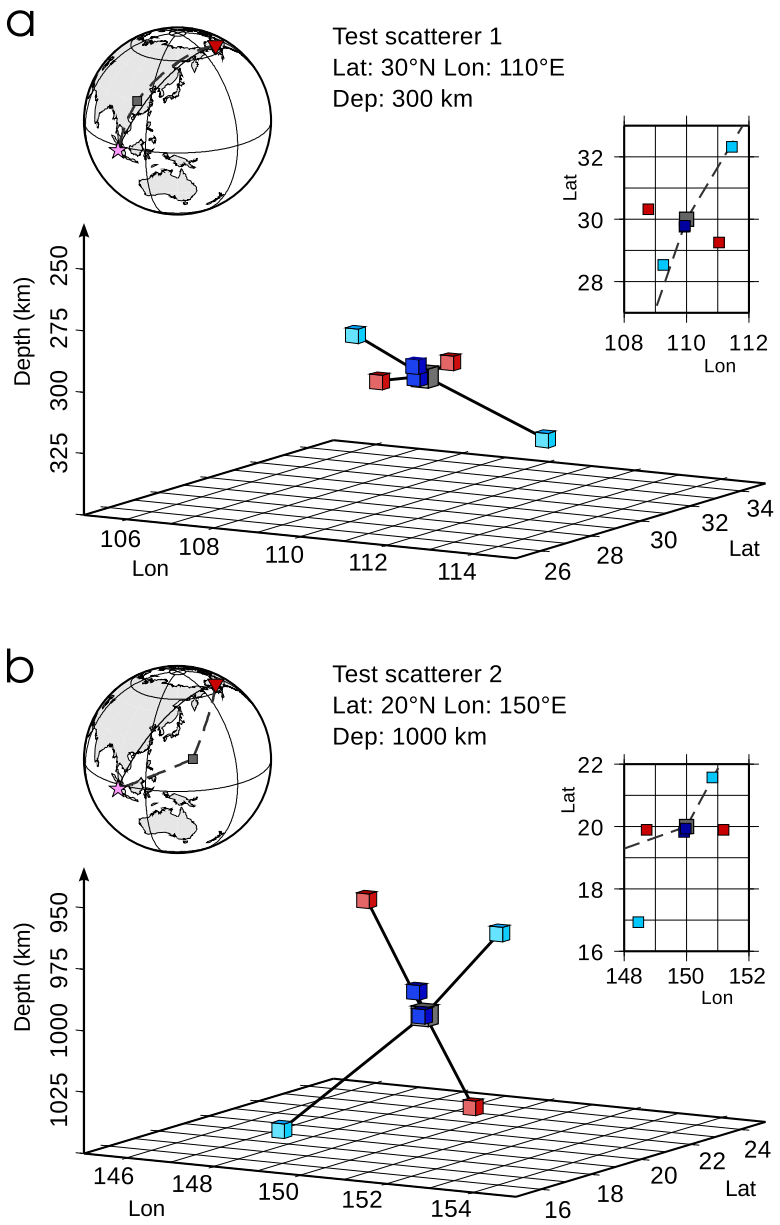

Figure 4.14: Relocation errors for two test scatterers each with six relocation cases for a) Shallow scatterer at: 30°N, lon: 110°E and dep: 300 km, b) Deep scatterer at: 20°N, lon: 150°E and dep: 1000 km. Grey cubes show the true location of scatterer. Red cubes are the scatterer locations after ray-tracing with backazimuth errors. Cyan cubes are the scatterer locations after ray-tracing with slowness errors. Blue cubes are the scatterer locations after ray-tracing with travel time errors.

	u (s/°)	θ (°)	time (s)	lat (°N)	lon (°E)	h (km)
Scatterer 1	6.187	294.84	80.402	30.00	110.00	300
θ error (+1.2°)	6.187	296.04	80.402	30.32	108.77	305
θ error (-1.2°)	6.187	293.64	80.402	29.25	111.03	290
u error (+0.19 s/°)	6.377	294.84	80.402	32.32	111.45	330
u error (-0.19 s/°)	5.997	294.84	80.402	28.54	109.25	280
δt error (+0.5 s)	6.187	294.84	79.902	29.76	109.94	295
δt error (-0.5 s)	6.187	294.84	80.902	29.78	109.95	300
Errors (max)				1.80	2.32	30
Scatterer 2	6.241	254.10	74.807	20	150	1000
θ error (+1.2°)	6.241	255.30	74.807	19.90	148.71	955
θ error (-1.2°)	6.241	252.90	74.807	19.89	151.18	995
u error (+0.19 s/°)	6.431	254.10	74.807	21.57	150.83	970
u error (-0.19 s/°)	6.051	254.10	74.807	16.94	148.46	1040
δt error (+0.5 s)	6.241	254.10	74.307	19.82	149.92	990
δt error (-0.5 s)	6.241	254.10	75.307	19.94	149.98	1000
Errors (max)				1.54	3.06	45

Table 4.2: Relocation cases used for error analysis of relocation procedure. There are 6 cases for two test scatterers. Errors in latitude, longitude and depth are derived for each scatterer by taking the largest differences between input and output parameters from the cases within each group.

As the relocation approach involves ray-tracing through a 1D model, errors will exist due to 3D velocity variations. These errors can be calculated by ray-tracing along scatterer paths through a 3D tomographic model. An average error of ±0.5 s is found, which is similar to the travel time picking error and translates to an additional ∼50 km and 5 km of mislocation in the lateral plane and in depth respectively.

Combining all the potential errors, the relocations in this study are accurate to ±300 km laterally and 65 km in depth for realistic slowness, backazimuth and traveltime errors, providing a good localisation of heterogeneities using this method.

4.5 Method sensitivity

As *PP* is a min-max phase, *P*-to-*P* scatterers can be generated at a range of depths and arrive in the *PP* precursory wavefield. However, there are limits to the spatial sensitivity of the method. The sensitivity can be derived for each earthquake by considering precursors that arrive within a limited backazimuth range ($-60 \leq \delta\theta \leq 60$) and within the 100 s time window before *PP*. For each backazimuth within this range, a distance is chosen for the receiver side path and the slowness and turning depth are calculated

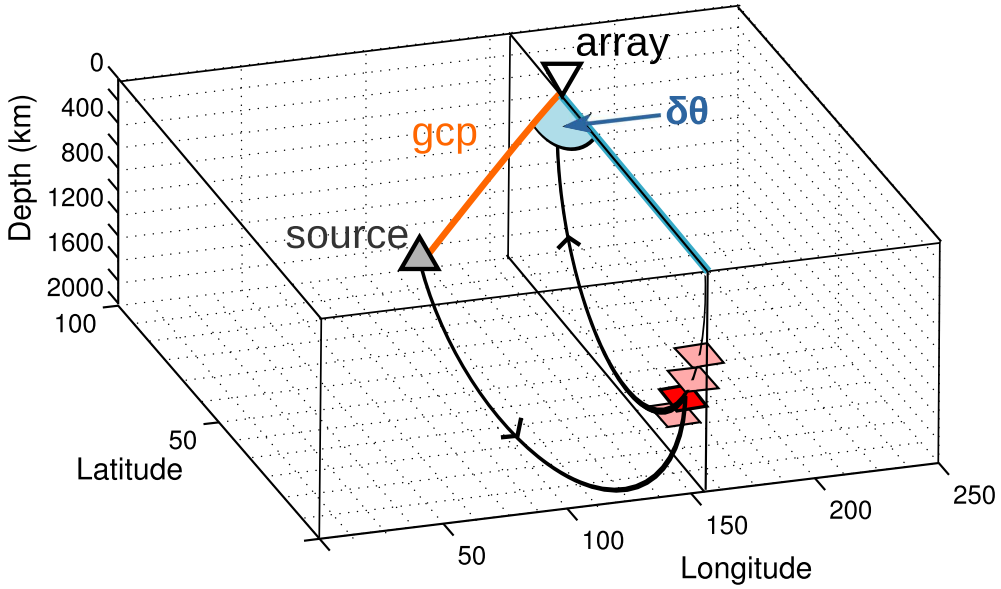

Figure 4.15: The sensitivity of P-to-P scattering is derived for each source-receiver combination by considering precursors that arrive within a limited backazimuth range of $-60 \leq \delta\theta \leq 60$ (and within the 100 s time window before PP). For an arrival with a backazimuth, the slowness and turning depth are calculated using ray-tracing. From the surface to the turning depth, the raypath is split into cells at every 20 km and the total travel-time is calculated from the earthquake source to the cell and the cell to the array.

using ray-tracing. From the surface to the turning depth, the raypath is split into cells at every 20 km and by ray-tracing from the source to the cell and from the cell to the array (Figure 4.15), the total travel time is calculated. If the travel-time arrives within the 100 s window before PP then the cell can be detected using the method and has the value of 1. If the cell has a travel time that is out of the 100 s window, the cell has a value of zero. The procedure is repeated for every 4° in distance and then repeated for every 4° in backazimuth.

Since P-to-P scattering is considered only, both branches of the path must have a turning P wave. The cells between the turning depth of the receiver-side branch and the receiver would generated an up-going p phase and therefore are excluded. In addition, there are limits in distance as to where scattering can occur. The distance travelled must be restricted to 95° for each source and receiver branch of the travel path because for distances greater than 95° the P wave starts to diffract around the outer core.

The resultant sensitivity volume for one earthquake is shown in Figure 4.16. In both map and side view one can see that the precursors can be generated at shallow depths but the side view shows that these surface scatterers are generated close to the receiver. Cells are detectable at all depths from surface to the core-mantle boundary, but the

number of cells that can be detected decreases with depth. For depths >1000 km, cells along the great circle path cannot be detected, but cells either side of the great circle path are suitable for detection. The deepest scatterers are found on the source side of the total travel path and are confined to a limited backazimuth range that is off great circle path by at least 10° (Figure 4.16). Overall the solution shows that for one earthquake, the number of cells that can be imaged are the greatest for depths 0-1000 km but for depths >1000 km (mid to lower mantle depths) the detection of cells is confined to small regions that are governed by the source-receiver geometry.

The procedure is repeated for 10 earthquakes that are selected (from all earthquakes) to ensure an even representation of the wide distribution of earthquake locations. Once the suitable cells are found and are assigned the value of 1, the results are weighted by the number of earthquakes that are closest to each of the 10 earthquakes. The weighed hits are then binned into $4 \times 4°$ cells and then the 10 sets of data are summed, resulting in total method sensitivity of the source-receiver geometries that are used in this study.

The total method sensitivity shows that there is good coverage beneath Asia, western Pacific and central Pacific for depths to ∼1400 km (Figure 4.17). Below 1400 km, gaps in the sensitivity are present beneath China and central Pacific, but the western Pacific subduction zones remain in coverage to depths of 2600 km. In particular the mantle beneath Philippine Sea retains high sensitivity to depths of at least 2200 km (Figure 4.18).

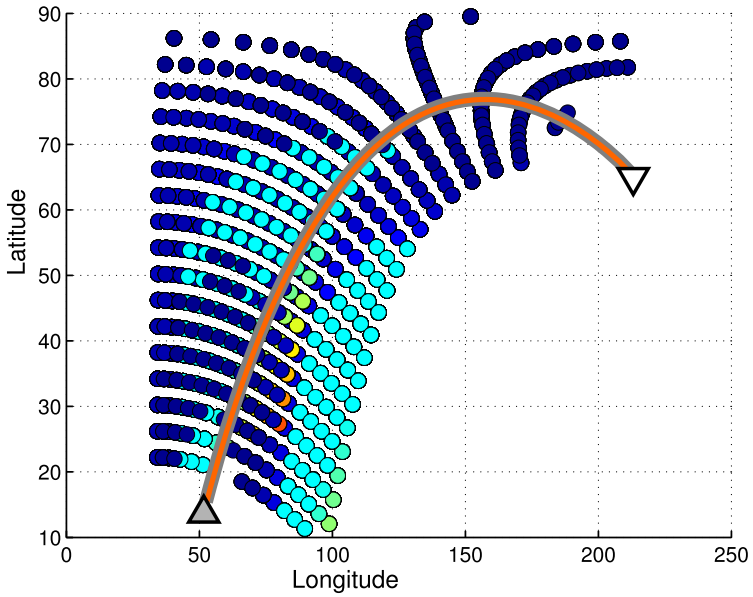

(a) Map view

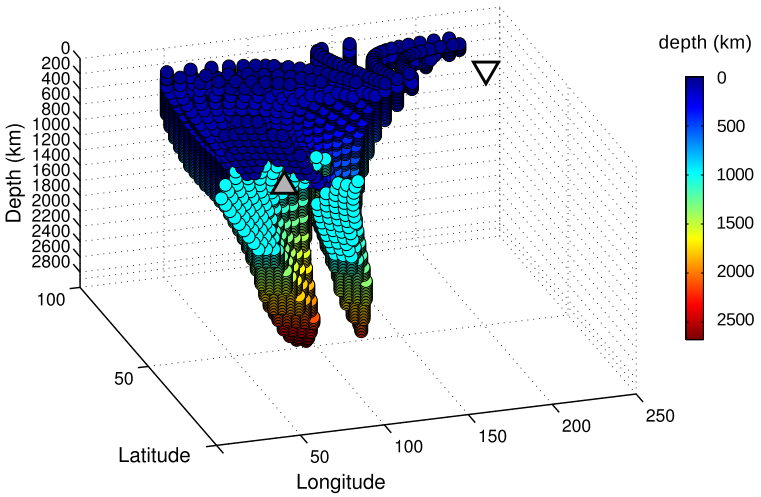

(b) Side view

Figure 4.16: Scatterers (circles) that can be detected for one earthquake (lat: -3.12, lon: 100.47, dep: 22 km, epicentral distance: 102.33°) in a) map view and b) side view (colour codes by depth, see scale in b)). Close to the array, the scatterers are restricted to the crust and upper mantle (depths <400 km). Scatterers for depths >800 km are located between the source and halfway along the great circle path.

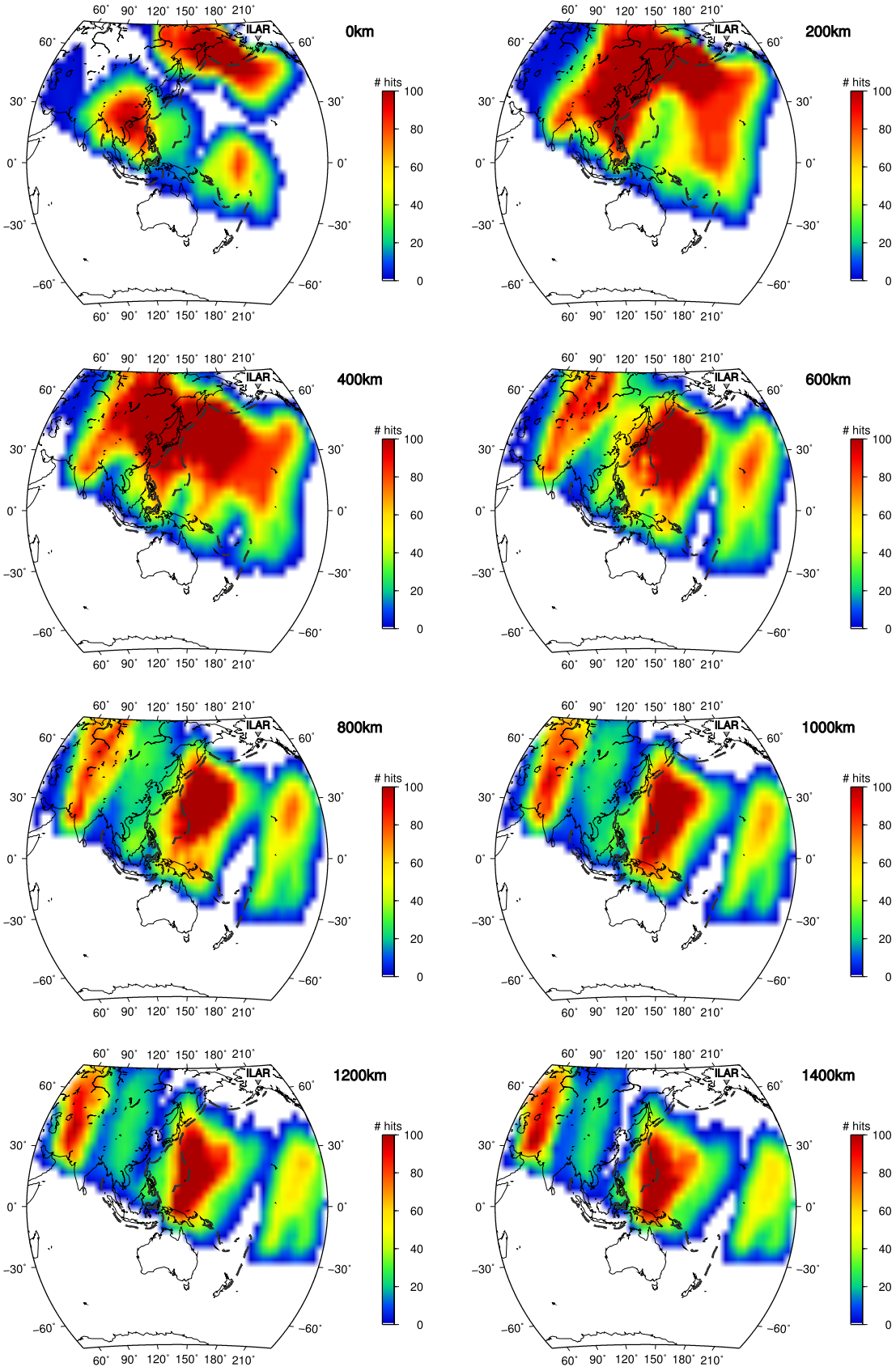

Figure 4.17: Method sensitivity for 200 km depth slices from 0 to 1400 km.

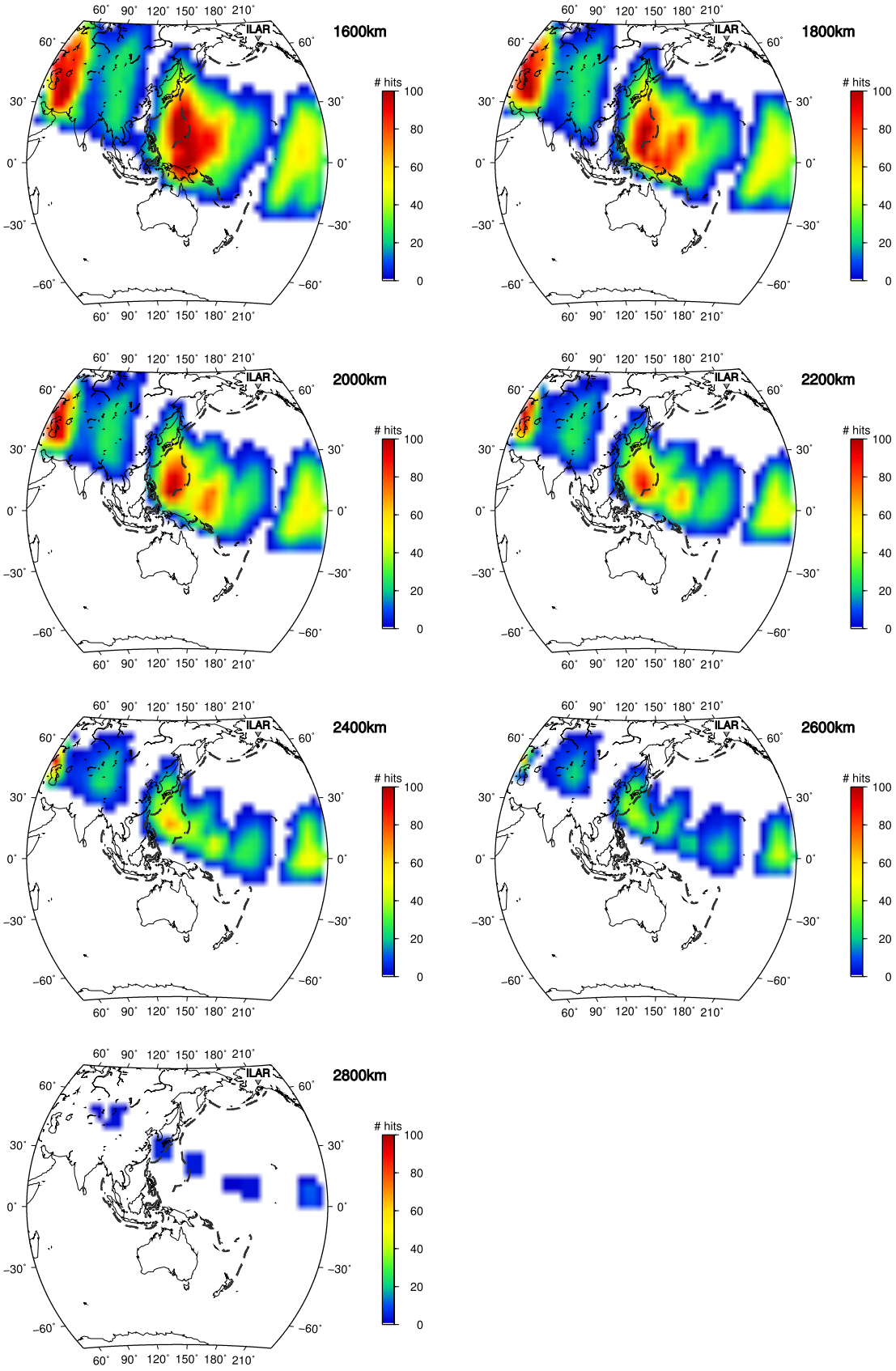

Figure 4.18: Method sensitivity for 200 km depth slices from 1600 to 2800 km.

4.6 Results

Altogether 670 precursors from 95 events with detectable energy in the NSWB time series are found. The total can be separated into those that arrive along and off great circle path: 201 arrive along great circle path ($\delta\theta \leq 5°$) and 469 arrive off circle path ($\delta\theta > 5°$). The precursors that arrive along circle path are not used in the relocation procedure and are beyond the scope of this study.

The scattering locations for the off azimuth precursors are distributed beneath the Pacific Ocean and across coastal China (Figures 4.19 and 4.20). Majority of the scatterers are found in the crust (70%) and the upper mantle (19%) and for these depths, it is observed that the number of scatterers decrease exponentially with depth (Figure 4.19). Only 10% of scatterers are found deeper than 400 km. A full list of the locations of the off azimuth precursors, along with event information, can be found in Appendix G, Table G.1.

The largest group of off azimuth precursors (282 scatterers, 68%) are found amongst the subduction zones in the western Pacific (region bounded by latitudes of 5°N and 60°N, and longitudes of 90°E and 160°E) and these results are discussed collectively. These scatterers are the primary focus of this part of the study due to their abundance in a confined region. In addition interpretation of these scatterers is more straight forward as subduction is a known mechanism of introducing crustal heterogeneities into the mantle.

Additionally, 187 scatterers are found outside of the western Pacific region indicated in Figure 4.20. In the crust and upper mantle (0-400 km) groups of scatterers are found beneath the central Pacific Plate and at the junction between the Japan and the Aleutian subduction zones (Figure 4.19). At greater depths (Figure 4.20), the scatterers are mostly located beneath the central Pacific plate (400-600 km) and clusters are observed beneath the Hawaiian-Emperor seamount chain and beneath the Solomon double subduction zone (between longitudes 140° and 170° on the equator). Further analysis of these scatterers is beyond the scope of this study, though the presence of these scatterers is briefly discussed in Section 5 of this Chapter.

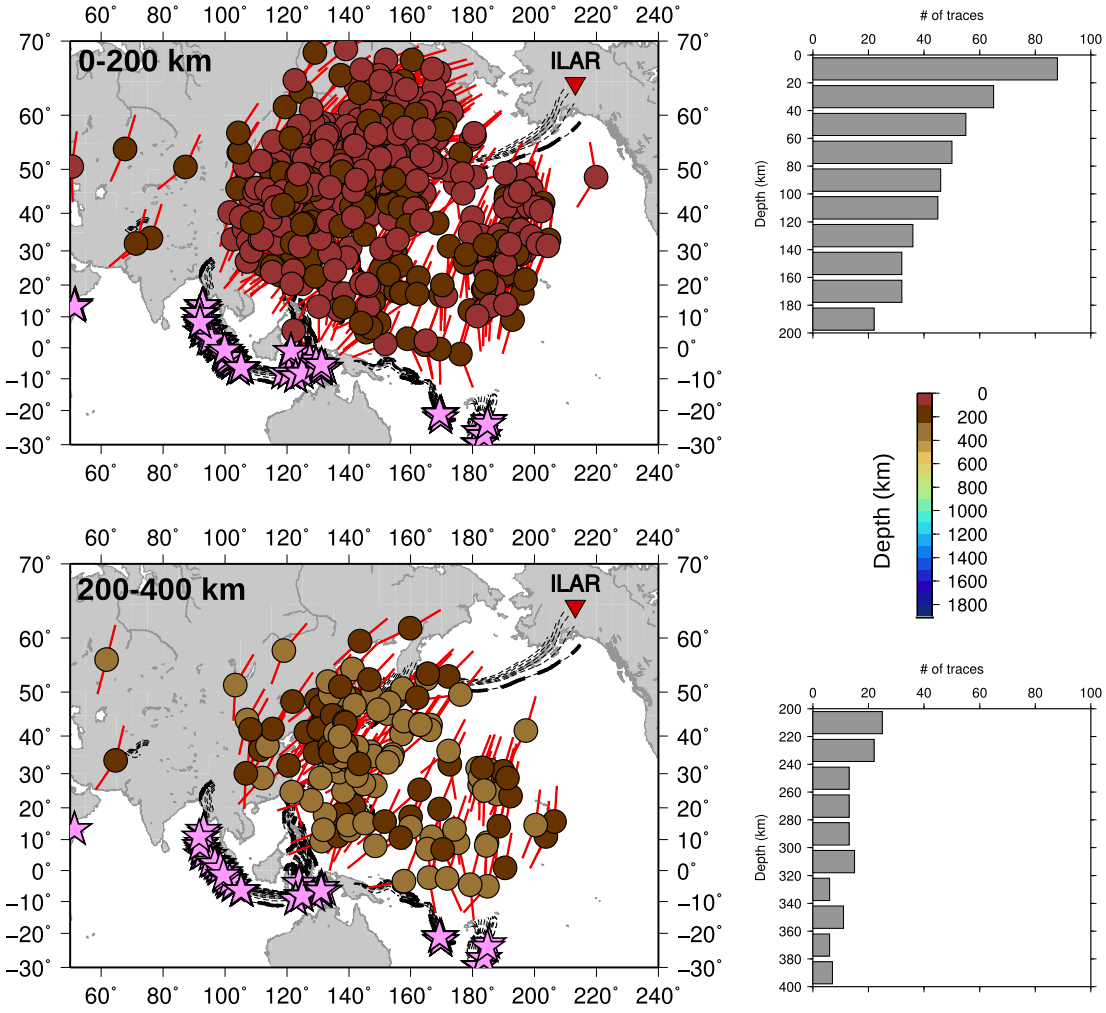

Figure 4.19: Locations of all scatterers that generate *P*P* recorded at ILAR for depths 0-200 km (top) and 200-400 km (bottom).

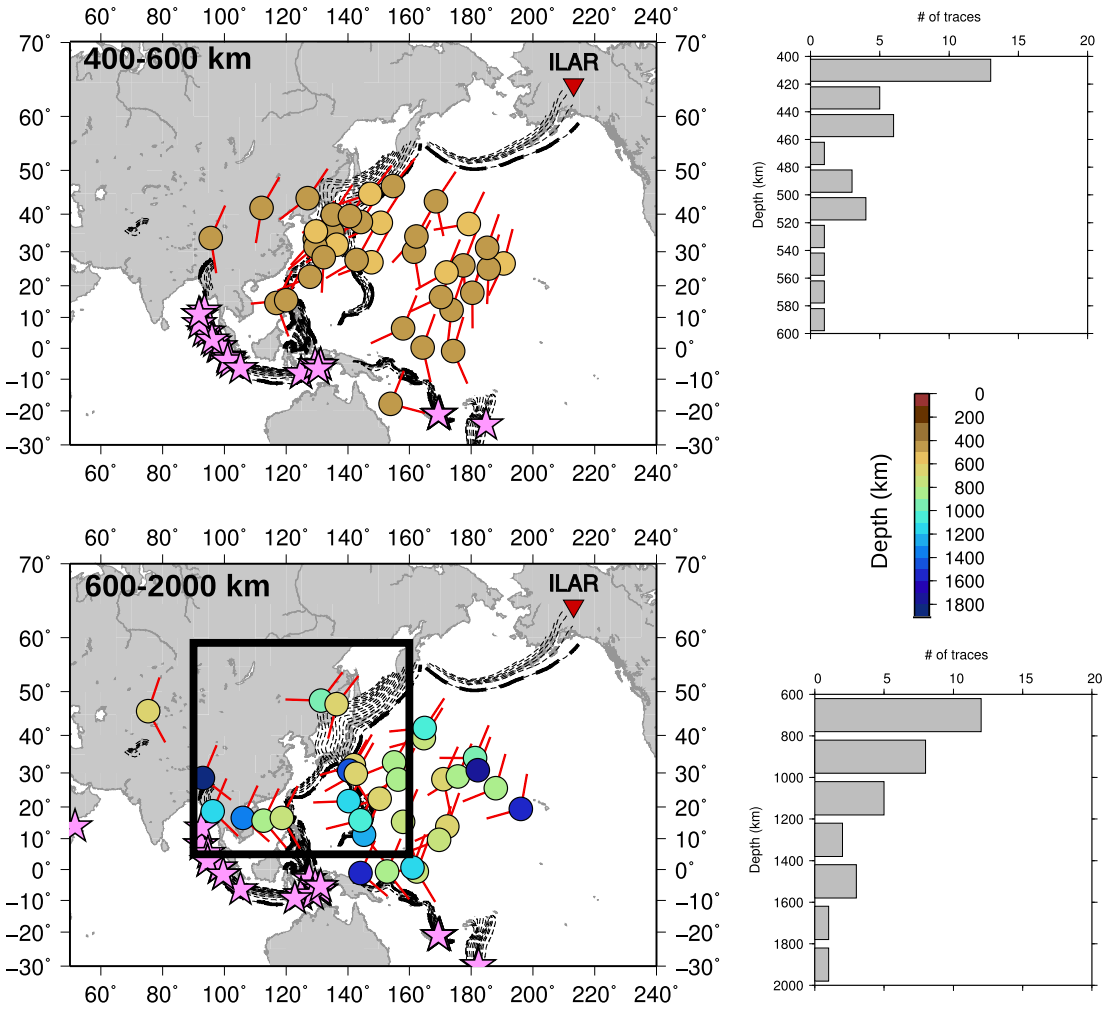

Figure 4.20: Locations of all scatterers that generate *P*P* recorded at ILAR for depths 400-600 km (top) and 600-2891 km (bottom). The western Pacific region (black box) is bounded by latitudes of 5°N and 60°N, and longitudes of 90°E and 160°E.

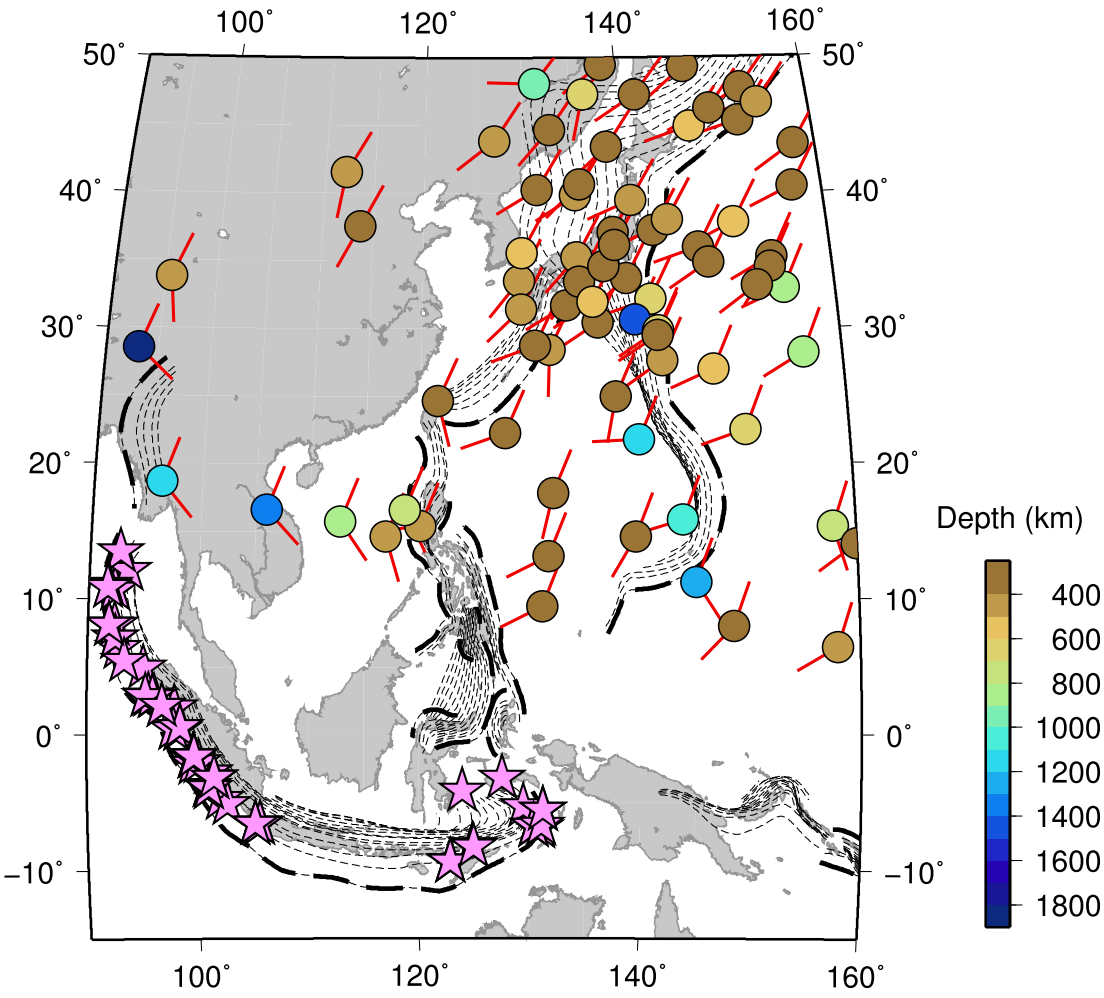

Figure 4.21: Locations of scatterers in the western Pacific (range from 250-1900 km; see colour scale) mapped with the angles of approach and reflection of the *P*-to-*P* precursor (red vectors). Ocean trenches are shown in thick dashed blacked lines. RUM model subduction zone contours (Gudmundsson and Sambridge, 1998) are shown as thin black dashed lines (contour interval of 50 km). Events processed through TOPCAT that show scattering are shown as pink stars.

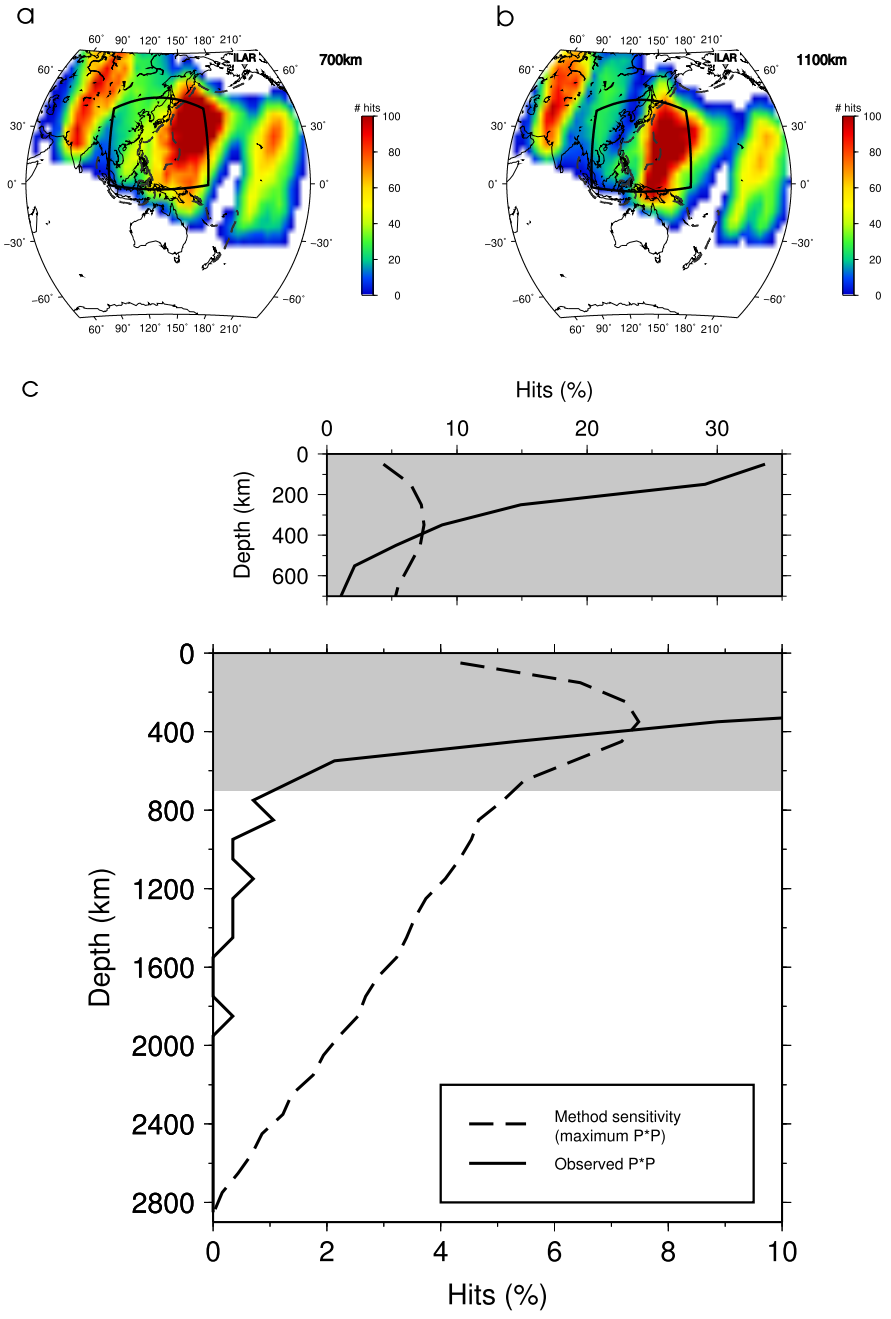

Figure 4.22: For each source-receiver combination, the sensitivity of *PP* precursor scattering detection method is found by creating a grid in longitude and latitude (for every 20km in depth) and for each cell evaluating if it is possible for a precursor to be detected. By combining all the contributions from each event for each cell, the total sensitivity is observed for every cell for each depth slice and such sensitivity maps are shown for depths 700 km (a) and 1100 km (b) (most sampled regions are in red and regions with no detectability in white). The best sampled region is bounded by the black box, and position of ocean trenches are shown in dark grey dashed line. c) Graph showing total number of observed precursors (solid black lines) for each depth and the sensitivity as a function of depth (based on source-receiver geometry, velocity model and relocation method used; shown in dashed black lines), are plotted against depth. Insert: upper mantle and transition zone scatterers in more detail.

4.6.1 Results: Scatterers beneath western Pacific subduction zones

In total 282 off-azimuth precursors are found from 70 events with detectable energy in the NSWB time series (Figure 4.21). An additional 137 precursors arrive along great circle path (±5°) and likely represent underside reflections. For the off-azimuth precursors, 34% are found in the shallow subsurface (surface to 100 km), 53% occur in the uppermost mantle (100 to 400 km), 7% occur in the transition zone (400-600 km) and 6% are found in the mid and lower mantle (deeper than 600 km). It is observed that there is a decrease in the number of scatterers with depth (Figure 4.22) as expected from the detection capability of the method (as derived in Section 4.5). A general decrease in amplitude strength of NSWB with depth is also observed. However, detections deeper than the transition zone show constant but weak amplitude in NSWB (NSWB less than 0.3). As the precursors are weak and generally below the noise level of individual traces, it is difficult to study the waveforms of the precursors. However, it is observed that many of the precursor beams have a spindle-shape form (symmetrical waveform with gradual onset and slow decay) for high frequencies, similar to the spindle-shape of *PP* (Figure 4.7). Unfortunately, the low amplitude of the precursors prevents any further analysis of the waveform of the scattered energy.

Figure 4.23 shows detected scatterer locations at depths from 300 to 600 km in 100 km intervals. The scatterer locations in these 4 depth intervals correlate well with slab contours from the RUM model (Gudmundsson and Sambridge, 1998) and clusters of scatterers are correlated with the triple junction between the Marianas, Japan and Western Philippine slabs. The comparison of scatterer locations with tomographic images (Ritsema et al., 2011) shows a good correlation of scatterer location with the edges of fast anomalies (Figure 4.23a); in particular scatterers correlate with velocity variations of -0.5% to 0.5%.

The best correlation of scatterer locations with structures in the S40RTS tomographic models is determined by calculating the distances between scatterers and intervals of velocity variation (dV_s/V_s). The mean distances between the scatterers and intervals of dV_s/V_s (denoted $\delta\bar{d}$) are evaluated to establish if there is a range of values that are preferentially closer to the scatterer locations (Figure 4.23b). Comparing $\delta\bar{d}$ to the mean distances calculated for 100 random scatterer datasets (with the same number of scatterers and depth distribution statistics) and establishing the mean and standard deviation (σ) of the random datasets, the preferred dV_s/V_s range is 0 to 0.17%. This

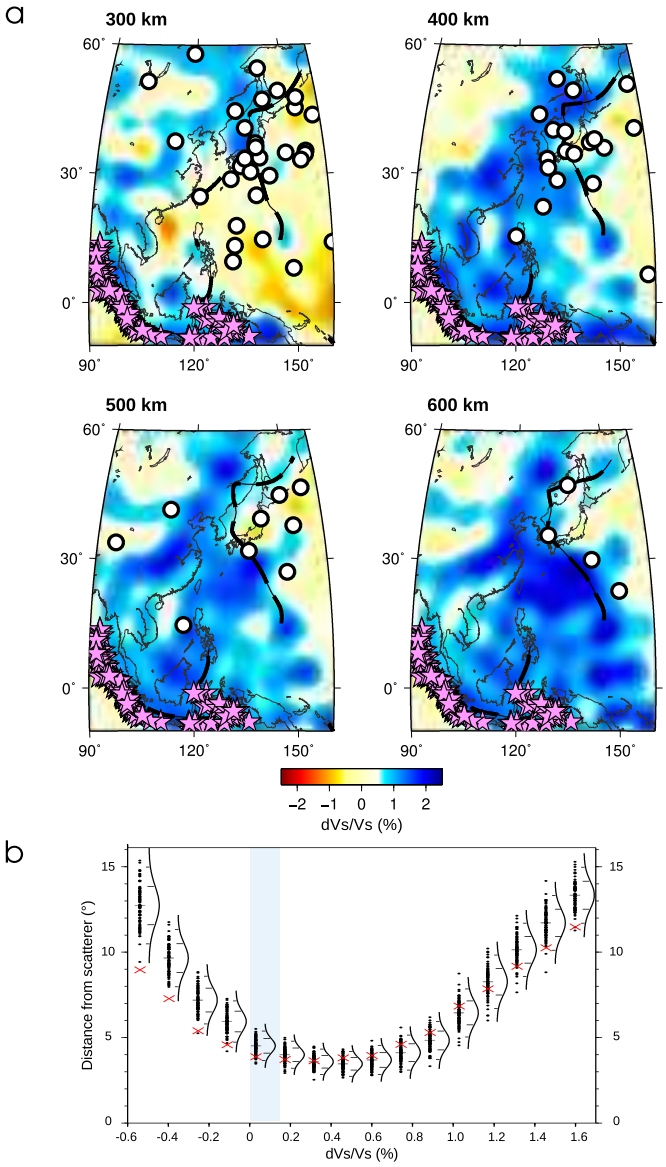

Figure 4.23: a) Depth slices for 300-600 km (100 km interval) of S40RTS tomography model (Ritsema et al., 2011), scatterer locations in intervals defined as ±50 km of each depth (black circles), RUM model subduction contours (dashed black lines) (Gudmundsson and Sambridge, 1998) and locations of earthquakes that show scattering (pink stars). b) Method of quantitatively assessing the correlation between scatterer locations and S40RTS tomography model. The mean distance between the scatterer locations and intervals of velocity variation are evaluated (red crosses). In addition, the mean distance between 100 random dataset of scatterer locations and intervals of velocity variation are calculated (black dots), and are used to generate the mean (grey horizontal lines), standard deviation 1σ (inner black lines on Gaussian curves) and 2σ (outer black lines on Gaussian curves). The best correlation is chosen for the velocity variation interval of 0 to 0.17% (blue box) as this interval has the lowest mean distance and lies outside at least 1σ.

range lies outside 1σ, demonstrating there is 66% confidence that the correlation has not occurred by chance.

The tomography gradient of S40RTS is calculated for depth slices 300-600 km (Figure 4.24a) as the gradient of tomographic velocity structures has been useful in the interpretation of smaller scale structure (Thorne et al., 2004). The contours of low gradients (< 0.30 %/°) correlate with the edge of the fast velocity features in S40RTS and are likely to be the edge of the slab. In addition, scatterers show good visual correlations with the tomography gradient of 0.14-0.23 %/° (Figure 4.24a). Producing mean distance calculations for the tomography gradient (Figure 4.24b), the preferred gradient ranges are 0.14-0.19 %/° and 0.19-0.23 %/°, which lie outside 1σ and 2σ respectively. While the range 0.14-0.19 %/° has the lowest $\delta\bar{d}$ (1.33°), the $\delta\bar{d}$ for 0.19-0.23 %/° is close to this minimum (1.51°) and this latter range shows a better correlation of 2σ, equating to 95% confidence that the correlation has not occurred by chance. Therefore, it is likely that the gradient that best represents the scatterer locations is within the range 0.14-0.23 %/°.

In contrast, the relocated scattered energy shows a poor correlation with the largest gradients of 0.40-0.76 %/°, which at some depths corresponds to the core of the slab (e.g. for depths 500 km and 600 km). Therefore, in agreement with previous studies (e.g. Rost et al., 2008, Kito et al., 2008), we likely observe scattering from the top or bottom of the subducted crust. However, considering scattering angles and subduction contours as well (Figure 4.21), the energy detected could be from underside reflections (Kito et al., 2008) and also from top-side reflections off the slab.

Considering deeper scatterers, 17 scatterers are found to be deeper than 600 km (from here on referred to as deep scatterers). A reduction of scatterer detection is expected at this depth as shown in the sensitivity analysis (see Figure 4.22 and Section 4.7). Deep scatterers are located north of the Indonesian slab; underneath the current position of the Mariana/Izu-Bonin trenches; and to the east of the Mariana/Izu-Bonin trenches. The deepest scatterer found in this study (at 1880 km deep) is located in the first region, ∼200 km northeast of the Assam subduction zone (Figure 4.25). Four other scatterers in this area are located at depths of 790 to 1385 km. Each of these scatterers are generated off great circle path by more than 20° but are found in seismograms from different earthquakes. The scatterers form an arc tracing the present day shape of the Sunda arc subduction system (Indonesia) offset northward by ∼15°. These scatterers

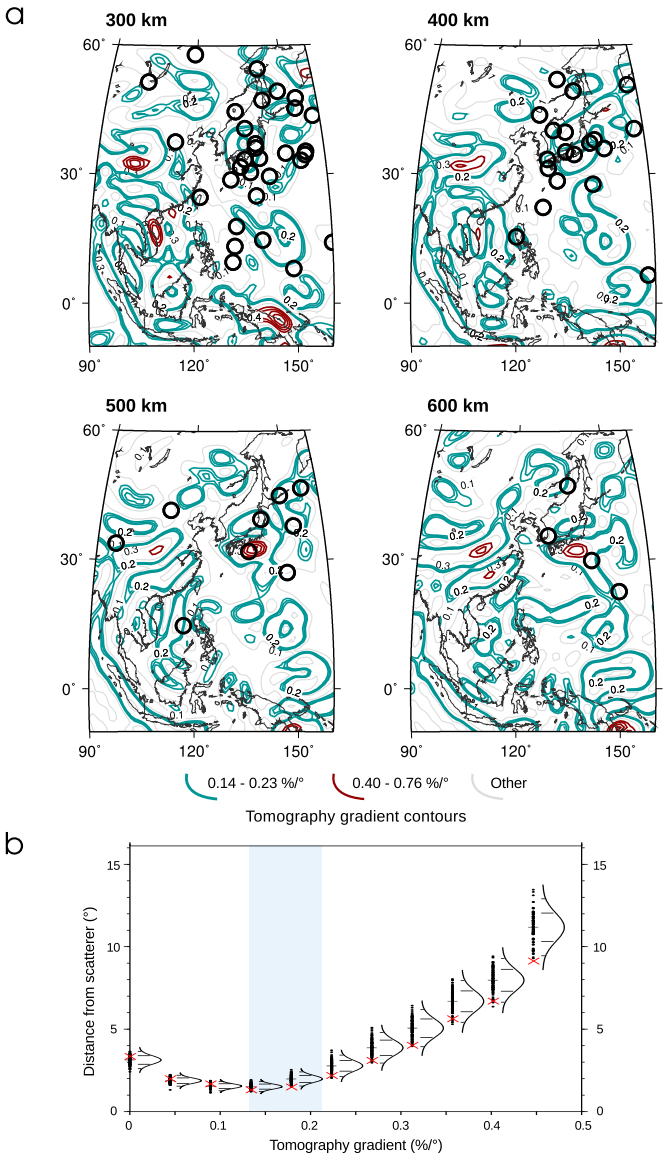

Figure 4.24: a) Depth slices for 300-600 km (100 km interval) showing the gradient of S40RTS tomography model and scatterer locations in intervals defined as ±50 km of each depth (black circles). b) Method of quantitatively assessing the correlation between scatterer locations and the gradient of the S40RTS tomography model. The mean distance between the scatterer locations and intervals of gradient are evaluated (red crosses). In addition, the mean distance between 100 random dataset of scatterer locations and intervals of gradient are calculated (black dots), and are used to generate the mean (grey horizontal lines), standard deviation 1σ (inner black lines on Gaussian curves) and 2σ (outer black lines on Gaussian curves). The best correlations are chosen for the gradient intervals of 0.14-0.23%/° (blue box) as these intervals generally have the lowest mean distances and lies outside at least 1σ.

correspond to a region of known lithospheric graveyards (Engebretson et al., 1992) and particularly coincide with the location of the Indonesian trench ∼100 Ma ago (e.g. Richards and Engebretson, 1992, Wen and Anderson, 1995, Hall, 2012). Figure 4.25b shows the location of these scatterers in side view (azimuth of sight is 341°). Using a tetrahedral interpolation of the scatterer locations in this sub-region it is found that the scatterers do not outline a planar shape as would be expected from an unaltered subducted slab.

The second region (Mariana/Izu-Bonin subduction zones; Figure 4.25) contains 8 scatterers ranging in depth from 600 km to 1480 km and these correlate well with the position of the Marianas trench over the last 17 Ma (Seno and Maruyama, 1984), as shown in Figure 4.26a. The tetrahedral interpolation of these scatterer locations shows an almost planar feature with a strike of ∼330° (Figure 4.25b). This result agrees well with a dipping reflector found by Castle and Creager (1999) (Figure 4.25), to depths of ∼1600 km. Several other studies have also imaged scatterers in this region in the mid mantle (Krüger et al., 2001) and to deeper depths in the mantle (∼1900 km) (e.g. Kaneshima and Helffrich, 1999, 2009) and are in good agreement with our results.

The remaining 4 deep scatterers are found between 730 km and 885 km depth and lie more than 7° to the east of the most easterly position of the past Izu-Bonin and Mariana trenches, which is larger than the maximum error associated with locating scatterers in this study (recall errors of 3° and 1.5° for latitude and longitude respectively). Other scatterers have been found in the region previously by Rost et al. (2008), especially beneath the Philippine Sea down to depths of ∼1000 km. There is an absence of scattering observed beneath the Philippine Sea in this study as this dataset and method are sensitive to other parts of the western Pacific subduction region (due to the different source-receiver combinations). However this study agree with Rost et al. (2008) who found scattering from a region east of Izu-Bonin. Since there are few scattering points at these depths, it is difficult to come to a conclusion on the structure underlying the heterogeneities at this stage.

4.7 Discussion

This study gives further evidence for the existence of small-scale mantle heterogeneities that might be caused by the subduction process. The data analysed has a dominant period of about 1 s, indicating that the heterogeneities leading to scattered energy have

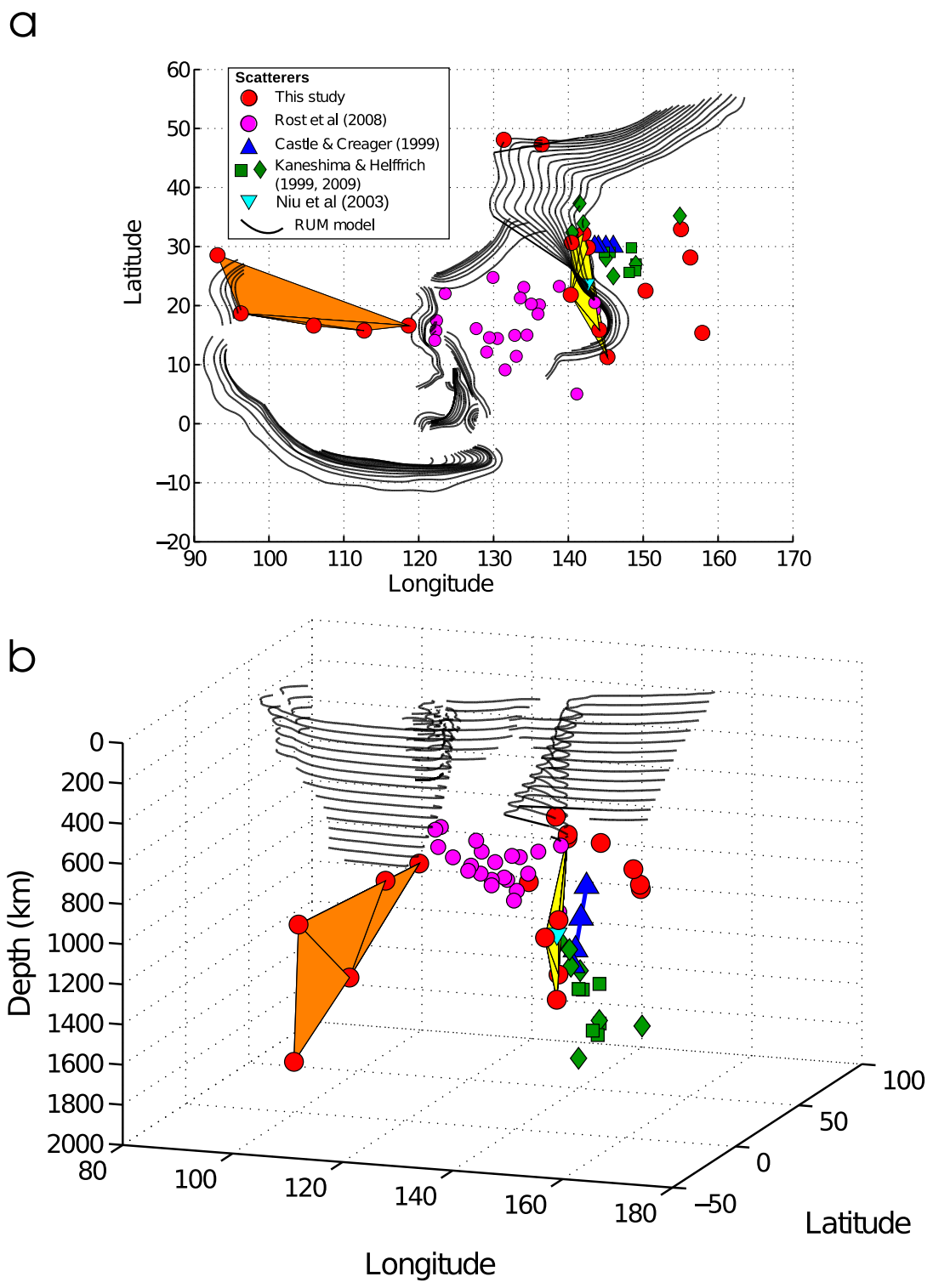

Figure 4.25: a) Map and b) side view with azimuth 341°, of the location of the 17 deep scatterers found in this study and scatterers found in previous studies (see legend). Tetrahedral objects are created for the scatterers beneath SE Asia (orange) and beneath the Izu-Bonin and Mariana trenches (yellow). Contours of the slab topography (solid black lines) are from the RUM model (Gudmundsson and Sambridge, 1998).

a spatial extent of about 10 km. The high thermal diffusivity of mantle materials would allow thermal anomalies to dissipate within a few million years (van Keken et al., 2002) and therefore it seems likely that the scattered energy is generated from compositional heterogeneities. Although the energy is treated as a scattered wavefield from small-scale heterogeneities, the detected energy might be related to dipping, sharp reflectors in the mantle (Castle and Creager, 1999). An obvious candidate for this reflector is the subducted paleo-Moho (Rost et al., 2008). Therefore, scattered energy is related to the subduction process since the study region is heavily influenced by past and present subduction.

Tomographic models (Widiyantoro et al., 1999, Grand, 2002, Huang and Zhao, 2006, Ritsema et al., 2011) and studies of the seismicity of subduction zones in the western Pacific have shown that subducted slabs in this region are roughly planar and continuous in the upper mantle to the base of the transition zone. Depth slices through the tomography model S40RTS (Ritsema et al., 2011) in the study region for depths 300 to 600 km (Figure 4.23) show that scatterer locations correlate well with the edges of fast velocity features at these depths and support the suggestion that the scatterers reflect or scatter off the edge of the slab. Such a correlation does not extend past 600 km depth (scatterer depths 550-650 km), although a clear correlation is difficult to make due to the reduction in the number of scatterers in the mid and lower mantle.

It is also found that the locations of shallow and transition zone scatterers show a correlation with the 0.14-0.23 %/° gradient interal of S40RTS (Figure 4.24a). While one might expect the largest tomography gradient to coincide with the strongest compositional gradient, this is not observed here likely due to the long period nature of the tomographic image which is likely more sensitive to the broader thermal signal of the slab. The scatterers located in this study are correlated with the smaller tomography gradients (Figure 4.24b) corresponding to the edge of fast velocity features in the tomography model. The highest S40RTS gradients of about 0.76 %/° are observed in the centre of slabs (Figure 4.24a) where compositional gradients are small and where previous studies have shown that thermal gradients are strong due to an insulated cold core of the slab (e.g. Helffrich et al., 1989, Davies and Richards, 1992). As tomography is sensitive to long wavelength structures, it may well be dominated by the temperature signature and only weakly influenced by the short wavelength compositional variation.

Additional information on slab structure can be extracted from slab reconstructions

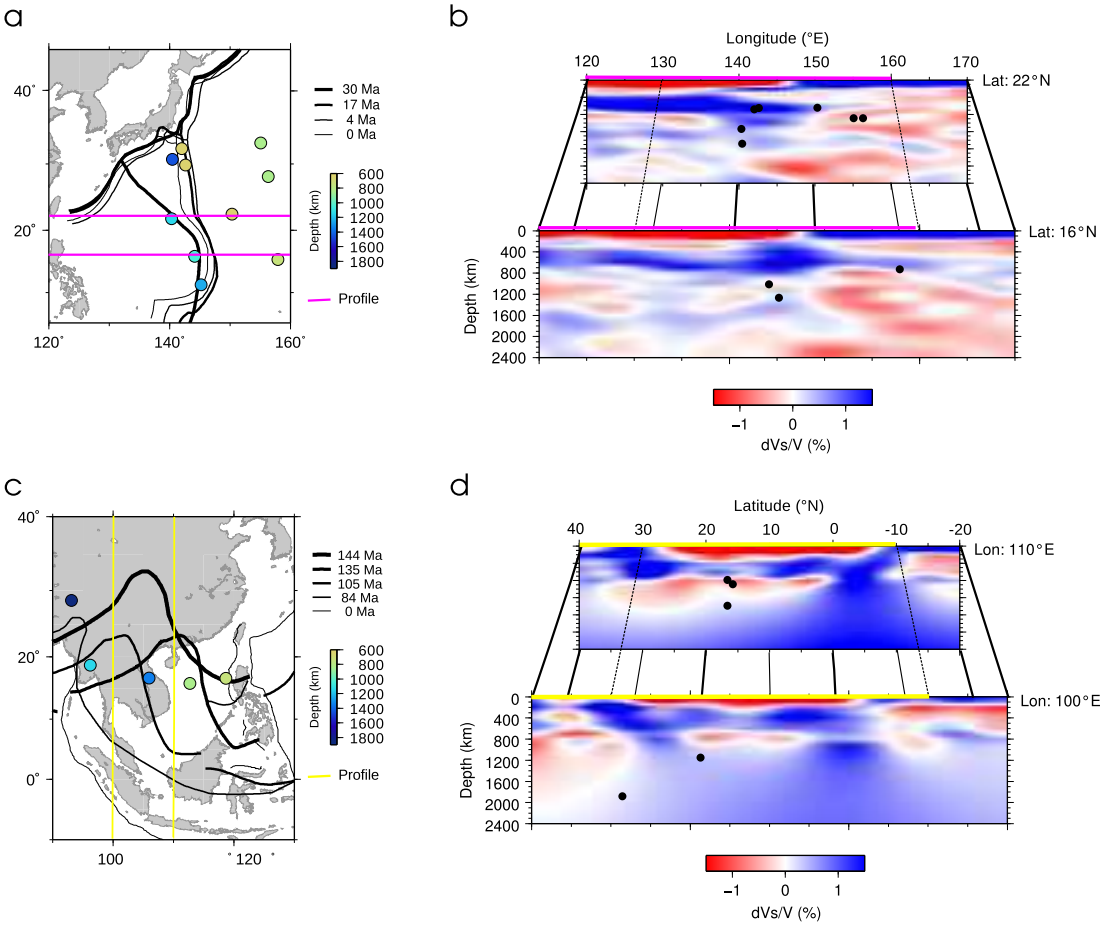

Figure 4.26: a) Location of deep scatterers (circles, coloured by depth) in Izu-Bonin/Mariana subduction region with location of ancient subduction trenches (Seno and Maruyama, 1984) where thickness of line represents year. b) Two E-W cross sections through S40RTS (Ritsema et al., 2011) tomography model in the Izu-Bonin and Mariana subduction region with location of scatterers (black circles). c) As a) but location deep scatterers (circles, coloured by depth) beneath SE Asia with location of ancient Indonesian subduction trench (Getech 2012, personal communication) where thickness of line represents year. d) Two N-S cross sections through S40RTS tomography model in Indonesia and SE Asia subduction regions.

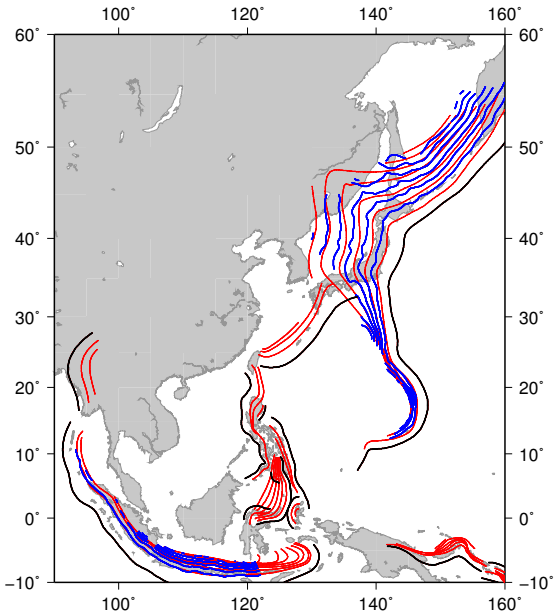

Figure 4.27: Subduction contours for western Pacific in 100 km intervals for the RUM model are shown in red (Gudmundsson and Sambridge, 1998) and the Slab 1.0 model (where available) are shown in blue Hayes et al. (2012). Subduction trenches are from the RUM model and are shown in black.

such as RUM (Gudmundsson and Sambridge, 1998) or Slab 1.0 (Hayes et al., 2012) (Figure 4.27), which show that the southern Izu-Bonin slab and the Mariana slabs are steeply dipping down to 700 km depth (Figure 4.25). The slab reconstructions agree well with regional tomographic models which indicate fast seismic velocities continuing into the lower mantle (e.g. Huang and Zhao, 2006). Both of the slab models show that there is a gradual change in dip angle of the northern part of the Izu-Bonin slab, north of latitude 33°. The Slab 1.0 model shows a gap in the slab beneath a slab tear at ∼35°N, 350 km depth, as highlighted in regional tomography (Obayashi et al., 2009). This gap is important in explaining the differences in subduction dip angle between the connected Japan and Izu-Bonin slabs. Deeper into the mantle (below 600 km) where slab models are absent and tomographic models are less well constrained (Figure 4.26), interpretation of the scatterer distribution is not straightforward. Scatterers beneath the Izu-Bonin and Mariana subduction zones align to form a near-planar shape oriented ∼330°, sub-parallel to the general profile of this subduction system in the present day (Figure 4.25) and for the location of the paleo Izu-Bonin/Mariana subduction trenches of 17 Ma (Seno and Maruyama, 1984) (Figure 4.26 a). Such a feature suggests that the steeply dipping Mariana slab is continuous and penetrates into the lower mantle, to depths of at least ∼1450 km, and contains a detectable crustal component. The

inferred slab location in this study is consistent with previous observations of a dipping feature in the lower mantle (Castle and Creager, 1999) and is in close proximity to other scatterers at a similar depth (Kaneshima and Helffrich, 1999, Niu et al., 2003, Kaneshima and Helffrich, 2009).

Seno and Maruyama (1984) suggested that the Pacific plate started to subduct under the Philippine Sea at least 43 Ma ago generating the Izu-Bonin/Mariana subduction zones and tomography shows that these slabs are steeply dipping (Huang and Zhao, 2006, Ritsema et al., 2011). Though the subduction angle and style has probably changed during the lifetime of these subduction zones (Seno and Maruyama, 1984, Miller et al., 2006), a first order calculation of the expected depth that the slabs have descended to can be made. The expected depth calculated can be compared to the depth of the scatterers to infer if the scatterers could be connected to the present day subduction system. Assuming a steeply dipping slab (constant subduction angle of 90°), subduction rate of 4.84 cm yr^{-1} as an average from rates over the last 0-8 Ma (Miller et al., 2006) and continuous subduction for the past 43 Ma, the Mariana slab could be present at depths of 2081 km. The deepest scattering associated with this slab has been observed by Kaneshima and Helffrich (2009) at depths of 1900 km, consistent with the above calculation. Overall, this suggests that the Mariana slab, steeply subducting without any inhibitors to flow, likely reaches the lower mantle but not the lowermost mantle or the CMB, explaining the absence of scatterers in this region at greater depths.

Though the Mariana slab is steeply dipping in the present day and is connected to an advancing trench at the surface, both Seno and Maruyama (1984) and Miller et al. (2006) agree that in the past the slab was stagnant and horizontal at the base of the transition zone whilst experiencing a period of trench retreat. Trench retreat would have caused the trench to move eastwards but after the trench switched to migrating westwards, the slab may have penetrated into the lower mantle where it may have anchored (Seno and Maruyama, 1984, van der Hilst and Seno, 1993, Miller et al., 2006) resulting in strain within the slab and possibly causing the proposed slab tear that separates the steeply dipping Mariana slab and the shallower dipping Izu-Bonin slab (Hilst et al., 1991, Castle and Creager, 1999). However, the time period in which the trench motion changed is still debated, with suggestions of 17 Ma ago (Seno and Maruyama, 1984) and 8 Ma ago (Miller et al., 2006). If the scatterers are

indeed subducted crust in the lower mantle, we can use their presence to constrain the subduction style and temporal changes in style at this trench. As scatterers related to the Mariana slab are observed down to depths of 1480 km, the minimum time that the slab has been in the lower mantle can be estimated. To travel these 820 km vertically at 4.84 cm yr^{-1}, the slab must have been steeply penetrating the 660 km discontinuity 16.9 Ma ago (Figure 4.28), agreeing with the trench retreat and advance model proposed by Seno and Maruyama (1984). The scatterers could be explained by the model proposed by Miller et al. (2006) if subduction rates were a lot faster in the past (>10%), but these are not reported in the literature. Moreover if the deepest scatterers found from Kaneshima and Helffrich (2009) are also part of the Mariana slab, the subducted slab must have started penetrating into the lower mantle by ∼26 Ma or possibly later if the subducted rates were significantly greater in the past.

The deep scatterers in the west of this study region trace the shape of the present day Indonesian trench at depth. The scatterers are correlated with the locations of the paleo-Indonesian subduction trenches between 82 and 144 Ma (Getech, 2012, personal communication). It is plausible for the slab to have entered the lower mantle by 144 Ma since subduction was initiated 180 Ma and descended to 1880 km depth. Although the scatterers are consistent with the present day shape of the slab in map view, a planar slab is not supported by the shape of the ancient subduction trenches shown in Figure 4.26c. Geodynamic models show significant amount of buckling and thickening of subducted slabs as they travel into and through the lower mantle (Lee and King, 2011), though such models are generated with simple linear trench styles and do not take realistic trench geometries into account (Figure 4.26). Nonetheless, the scatterers possibly image the subducted crust of this ancient slab in the lower mantle.

The dataset used here does not have high sensitivity for the whole of the western Pacific region for all depths. For example, model sensitivity in the area between the present day Indonesian trench and the observed scatterers of the inferred deep paleo-Indonesian slab is relatively low at 1000 km depth (Figure 4.22). However, tomographic images indicate that the Indonesian slab is horizontal at ∼900 km at 15°N and scattering has been previously detected at depths of 930 to 1070 km using S-to-P conversions (Vanacore et al., 2006). In contrast, it is possible that our method can detect scattering beneath the Philippine Sea for depths >1000 km but no scatterers are observed in the region (Figure 4.22). The absence of scattering may suggest that slab material

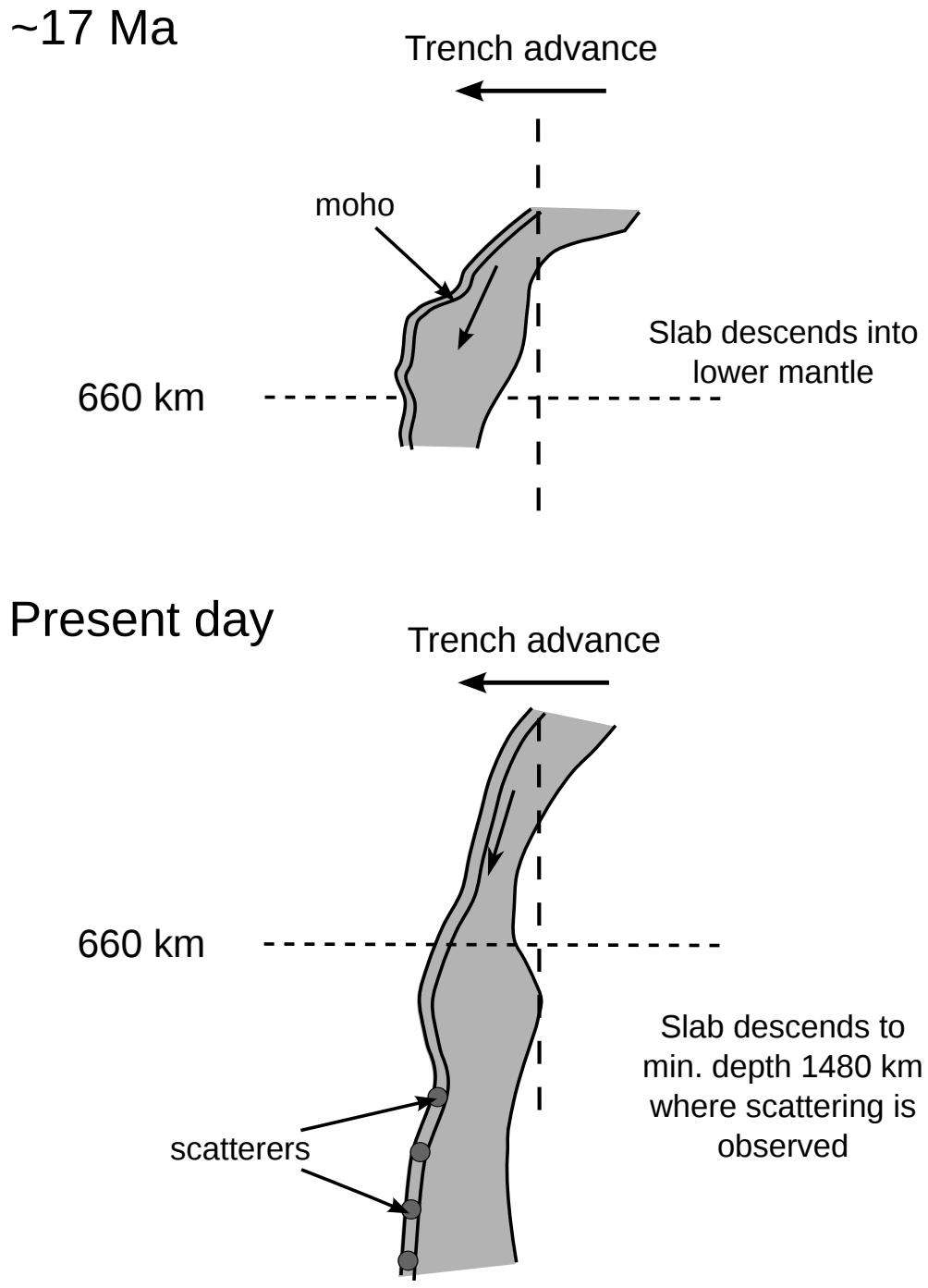

Figure 4.28: Schematic of the evolution of the Mariana subducted slab over last 17 Ma. The minimum depth extent of the present day slab (bottom) can be inferred from the presence of scatterers (dark grey circles) to depths of 1480 km. After Miller et al. (2006).

does not cross the 660 km discontinuity in this region. This conclusion is supported by tomographic images showing a fast anomaly at the base of the transition zone that is disconnected to other fast anomalies that have been interpreted as subducted slabs (Huang and Zhao, 2006). Rost et al. (2008) have observed some scattering under the Philippine Sea, to depths of ∼900 km, with the depth of scattering increases towards the eastern region of the Philippine sea, close to the scatterers found in this study. It is possible that the ancient Mariana slab crossing the 660 km discontinuity has provided a preferred route for subducted slab material trapped in the transition zone (from Japan and other trenches) to descend into the lower mantle. Such a complex scenario may require subducted material to be deformed in the transition zone (Schellart, 2011) and cease to be a rigid structure. Scatterers are also observed to the east of Izu-Bonin and Mariana trenches. It is not clear how these would fit into the history of subduction of this region and it is possible that they are from older paleo-subduction systems.

Scatterers have also been observed beneath the central Pacific region, with 12 scatterers found below 600 km. The scatterers are found in very different tectonic settings with some found beneath the seamounts along the Hawaiian-Emperor hotspot track, the Micronesia islands and seamounts in the central Pacific and the Kapingamarangi Rise north of the Solomon double subduction zone (Figure 4.29). With few scatterers across a large area it is difficult to interpret the cause of these heterogeneities. However, some observations can be made. The deep scatterers connected to the Solomon subducted slabs may be unexpected since the slabs have been mapped to a maximum depth of only ∼550 km in the RUM model (Gudmundsson and Sambridge, 1998). However, the scatterers found along both the Hawaiian and Emperor seamount branches may indicate that heterogeneities of ∼10 km scale (i.e. recycled crust) are entrained into the mantle upwelling that produces the surface volcanism. Although, the Hawaiian plume is reported to be have a stationary source in the deep mantle (Wolfe et al., 2009) and there is no obvious reason why heterogeneities associated with the plume should correlate with the plume track, the correlation of scatterers with the Hawaiian-Emperor seamount chain should be further investigated using more data.

The detected scatterers are all located shallower than 1900 km although it is possible to detect at larger depths despite decreasing likelihood (Figure 4.22). However, far fewer scatterers are detected in the mid and lower mantle (deeper than 600 km) than is expected from the detection capabilities of the method, suggesting that structural

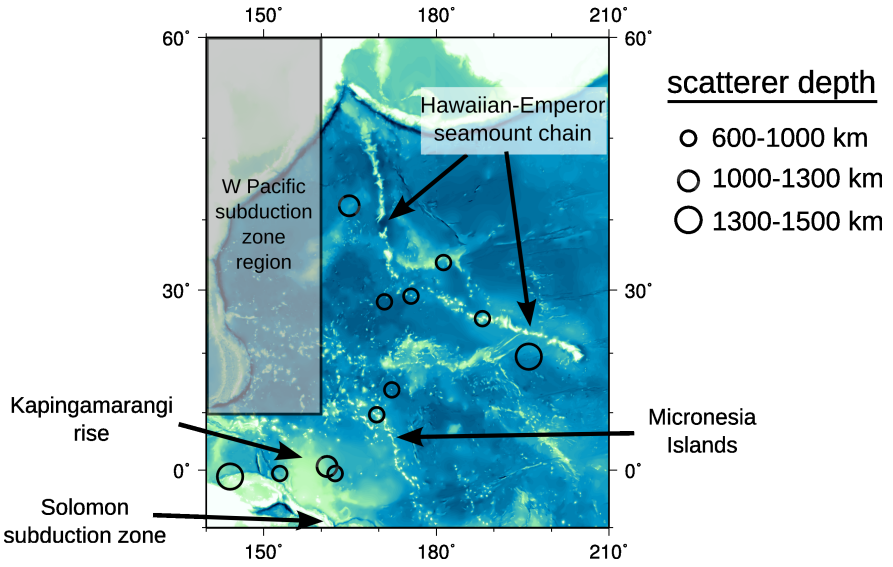

Figure 4.29: Twelve scatterers with depth >600 km (black circle with size proportional to depth) are located beneath the central Pacific with Pacific Ocean bathymetry from the GEBCO One Minute Grid, Version 2.0, http://www.gebco.net. Scatterers correlate with surface features, in particular the Hawaiian-Emperor seamount chain and the Solomon subduction zone. The shaded box to the west of the map corresponds to part of the western Pacific subduction region that contains other scattering found in this study.

changes are responsible for the decrease of scattering at these depths. The geometry of source-receiver locations and the orientation of the slab could have a strong influence on whether the scattered or reflected energy arrives at the array. Also, impedance contrasts could be a major influence as both basalt-pyrolite and basalt-harzburgite impedance contrasts sharply decrease at 1500 km depth (Rost et al., 2008), confirmed by the weak scattering observed in this study.

Currently, it cannot be determined if the oceanic crust remains connected to the underlying lithosphere as it descends into the lower mantle due to the different uncertainties in tomographic and scattering imaging. Dynamical numerical modelling studies have shown that slabs are deformed greatly as the viscosity increases at the 660 km discontinuity (e.g. Stegman et al., 2010, Lee and King, 2011) and calculations demonstrate that mechanical stirring may attenuate the crustal component by stretching and shearing during 100 Myr of mixing (Stixrude and Lithgow-Bertelloni, 2012). Some dynamical models show small-scale convection in the mid-mantle, which could more rapidly attenuate the subducted crust, leading to very small-scale (2 km) heterogeneity distributed throughout the mantle as observed in modelling of global mantle heterogeneity (Earle and Shearer, 2001). However, it has been suggested that the crust

does not detach from the slab until it descends into the lower mantle (e.g. Christensen and Hofmann, 1994, Miller and Niu, 2008) and it has been shown that it is possible to accumulate crust at the base of the mantle (Christensen and Hofmann, 1994).

An alternative explanation for the generation of scattering could be caused by subduction related anisotropy in the mid-mantle (Kito et al., 2008). Highly localised strain can be generated by slab flow, resulting in lattice preferred orientation (LPO) when combined with dislocation creep. This is dominant over diffusion creep in the upper mantle and the transition zone (McNamara et al., 2002). Recent studies have attributed shear wave splitting in the mid-mantle to the presence of LPO (e.g. Wookey et al., 2002, Long and Silver, 2008, Foley and Long, 2011, Faccenda and Capitanio, 2012). However, it is unclear, if the anisotropy could produce a velocity contrast that is strong enough to generate scattered or reflected arrivals (Kito et al., 2008). (Wookey et al., 2002) report an average 3% velocity fractional difference between slow and fast shear wave velocity for anisotropy in the Tonga-Fiji subduction system. Though, this velocity difference is comparable to impedance contrasts found previously for P-to-P scattering (Rost et al., 2008), it is difficult to predict how the variations in S-wave velocity would affect P-wave scattering. If the velocities are sufficient to cause scattering, the presence of a fairly wide anisotropy region (McNamara et al., 2003) could explain the presence of scatterers on top of and beneath the slab topography contours.

4.8 Summary

PP precursors that are related to scattering from small-scale mantle heterogeneities in western Pacific subduction zones and the central Pacific have been detected using novel array methods. For the western Pacific subduction zone region >200 scatterers in the lithosphere and upper mantle and 17 scatterers deeper than 600 km have been relocated. In the upper mantle, scatterer locations correlate well with subducted slabs inferred from tomography and subduction contours, thus there is strong support that the *PP* are generated from the heterogeneous subducted crust. Extrapolating this interpretation to scatterers in the mid and lower mantle where the resolution of tomography is reduced, it is likely that the crustal component of the subducted slab is still present beneath the Izu-Bonin and Mariana trenches and beneath the location of an Indonesian paleo subduction trench active during the period from 80-144 Ma.

In addition, deep scatterers have been found beneath the Hawaiian-Emperor seamount

chain and north of the Solomon subduction zone, but with few scatterers the distribution of these heterogeneities is difficult to explain. Across the whole region, scatterer locations are not dependent on the detection and relocation methods applied here but scatterer detections do depend on the elastic properties and the orientation of the heterogeneities.

Chapter 5

Discussion

5.1 Overview

Analysis of *PP* precursors in global average stacks for distances 70° to 120° has been successful in creating heterogeneity models for the upper and mid-mantle. Additionally, the processing of individual coherent *PP* precursors for distances 90° to 110° using array seismology approaches has revealed regional signatures of mantle heterogeneity particularly in active subduction regions.

In this Chapter I will discuss how *PP* precursors have been used to image mantle heterogeneities and how global and regional patterns of heterogeneities may be useful for understanding mixing process in the mid-mantle.

5.2 Using *PP* precursors to image mantle heterogeneities

In this study weak high frequency *PP* precursors generated from small scale mantle heterogeneities are analysed using two methods that examine different precursory signatures. The first method examines the stacked envelope of *PP* precursors for different distances to reveal global averages of the energy and then generate models of mantle heterogeneity. The second method uses array seismology to enhance *PP* precursors that arrive coherently at a small seismic array and to locate the origin of these individual arrivals.

Amplitude, travel time and directivity information are important in characterising the heterogeneities that generate *PP* precursors. The amplitudes of *PP* precursors are used in the global stacking method and analysis of amplitude variations with time and distance reveals the variation of heterogeneity properties with depth. Directivity and

travel time information are extracted from coherent *PP* precursors found using the array method. Such parameters are used to locate scatterers, demonstrating that scattering is generated from the crustal component of slabs from present day and ancient subduction zones.

Though using *PP* precursors to detect heterogeneities has been successful, the scattered *PP* wavefield is complicated to analyse. As *PP* is a minimum-maximum phase, *PP* precursors can arrive from all azimuths and from many depths thus targeting specific tectonic regions for analysis can be challenging. *PP* precursors arriving off great circle path (out of plane) can be generated by *P*-to-*P* single scattering from all depths in the mantle while precursors arriving on great circle path are limited to single scattering occurring at depths less than 1000 km (Section 4.5, Figure 4.16).

Nonetheless under the assumptions discussed in Sections 3.4 and 4.4 I have located mantle heterogeneities using these two different approaches to analyse *PP* precursors. Although the methods have some connected uncertainties (Sections 3.7 and 4.4.5) I make some progress in characterising the small-scale structure in the mantle.

5.3 Summary of heterogeneities found from *PP* precursors

5.3.1 Global patterns of heterogeneity

Global stacking observations

Global stacks of *PP* and *PP* precursors are created for distances of 70° to 120° in 5° bins (Section 3.3.3). Across all distances the *PP* waveform has a width of ∼10 s and has a similar waveform envelope shape. The *PP* onset is sharp while the onset of the precursory energy is emergent. *PP* precursors start within ∼100 s before *PP* and gradually increase with time until reaching a maximum amplitude of ∼50% of the *PP* amplitude. Precursor amplitudes generally increase with distance, a trend that is not evident in spite of the arrival of *PKiKP* in the precursory window from cross-over distances ∼105°. *PKiKP* is strong at distance ∼117.5° and as a result the energy in the precursory window may be stronger than expected (about 50% stronger) for these distances.

The global average stacks are created with a minimum of 500 traces in each distance bin and the data show a good sampling across most of the globe (Figure 3.6). Two

regional stacks are also created across the Pacific Ocean and Atlantic Ocean (Section 3.3.5). These regional stacks are very similar for most distance bins, which is not necessarily expected for such different geodynamical settings at different depths in the mantle. The Pacific region contains a large plume feeding Hawaiian volcanism with lower mantle material, and the Atlantic region contains a mid-ocean ridge fed by an upper mantle source. In addition, these regions are affected differently by past subduction.

Monte Carlo modelling observations

A Monte Carlo phonon scattering modelling approach is used to model the mechanism by where the mantle heterogeneity produces the observed scattered energy. The synthetic seismograms thus produced are compared to the global stacks to find the best fitting heterogeneity model (Section 3.6). Models of mantle heterogeneity created in previous studies are analysed with model parameters generated by Hedlin et al. (1997), Earle and Shearer (2001) and Shearer and Earle (2004) are used to create models H1997, ES2001 and SE2004 respectively (see Table 5.1).

Comparing the SE2004 model with the global stacked data shows that the model produces too much energy in the *P* coda, which masks any *PP* and *PP* precursory energy. Too much *P* coda is probably due to the relatively high rms velocity variations in the lithosphere and upper mantle (3-4%) and lower attenuation (Section 3.6.1) specified for this model. Therefore these parameters are not suitable to describe the *PP* precursor signatures that are observed from the global stacks.

ES2001 and H1997 models produce *PP* and *PP* precursors amplitude closer to those observed in the stacked data (Figure 3.17). However, in both models, *PP* precursors are under-predicted and/or over-predicted for certain distances and the model *PP* has the wrong envelope shape. These results indicate that scattering is too strong within the crust and mantle for ES2001 and H1997 parameters.

Both rms velocity fluctuations ϵ and correlation lengths a at various depths could be changed to achieve an improved fit between synthetics and data. Unfortunately, the parameter space is large and by implementing forward modelling approaches, it might be difficult to find a unique set of parameters that describe the data.

Models with heterogeneity only in the lithosphere (depths 0-100 km) are explored (Section 3.6.2) but none of the models correctly predict the amplitude and shape of

	H1997	ES2001		SE2004
Depth (km)	*PKP pre*	P_{diff}	Depth (km)	*P* coda
0-100	$a = 8$, $\epsilon = 1\%$	$a = 2$, $\epsilon = 1\%$	0-200	$a = 4$, $\epsilon = 4\%$
			200-600	$a = 4$, $\epsilon = 3\%$
100-2891	$a = 8$, $\epsilon = 1\%$	$a = 2$, $\epsilon = 1\%$	600-2891	$a = 8$, $\epsilon = 0.5\%$

Table 5.1: The parameters as input for models H1997 (Hedlin et al., 1997), ES2001(Earle and Shearer, 2001) and SE2004 (Shearer and Earle, 2004).

PP precursors in the global stacks. However, the lithospheric models do reveal how scattering affects the *PP* waveform. The modelled *PP* waveform may be more complex than *PP* in the stacked data depending on the choice of correlation length and thickness of the layer. The models that best fit the data in terms of amplitude and width have rms velocity fluctuation $\epsilon = 1\%$ but correlation length a is uncontrained and can vary between 2 and 8 km for similar fitting models. None of the purely lithospheric heterogeneity models fit the envelope shape of *PP* though, indicating that *PP* is also influenced by scattering in the mantle.

Models with whole mantle heterogeneity are considered based on models ES2001 and H1997. Models ES2001_M11, ES2001_M17 and ES2001_M20 are the best fitting models based on ES2001 (Section 3.6.3). These models all have a correlation length of 2 km in the lithosphere and mantle rms velocity fluctuation of 0.5%, rather than 1% rms velocity fluctuation used in ES2001. Various correlation lengths in the mantle (8 km, 6 km and 2 km) are tested but the *PP* and *PP* precursors energy in the synthetics have similar characteristics. The three models produce *PP* with a width that is a good fit but over-predict the amplitude of *PP* precursors for distances <85° and under-predict *PP* precursors for distances >95° (Figure 3.20).

Modifying model H1997 by increasing mantle rms velocity fluctuation from 0.1% to 0.5% (model H1997_M07) and to 0.8% (model H1997_M08) while keeping the 8 km correlation length produces precursors that are a good fit for distances >90° but over-predicts *PP* precursors for distances <90° (Figures 3.21 and 3.22), and produces *PP* envelopes that are too broad. It is difficult to find a model based on H1997 with correlation length of 8 km in the lithosphere that fits for *PP* shape and *PP* precursory amplitude for all distances.

The ES2001 whole mantle models match the observed *PP* relatively well due to the

small correlation length of 2 km assumed throughout the crust and mantle. Though the *PP* precursors are under-predicted at large distances ($\Delta > 95°$), additional layers of increased heterogeneity can be included to produce more scattering that arrives in this time window. Reduction in rms velocity variation in the upper mantle could reduce the amount of *PP* precursory energy at shorter distances ($\Delta < 85°$).

As no model with uniform mantle heterogeneity provide a good fit for *PP* and *PP* precursors, models with several mantle layers of different heterogeneity properties are considered through trial and error (Section 3.6.4). After analysing qualitative and quantitative, it is found that the best layered models are LAYM_45, LAYM_33, LAYM_47 and LAYM_49 (Table 5.2). These models differ in lithospheric correlation length (a from 2 to 6 km) and rms velocity variation (ϵ from 1% to 2%), suggesting the lithospheric parameters have not been well constrained using *PP* precursors. These models have a consistent mantle correlation length of $a = 6$ km and a mid-mantle with rms velocity variation of $\epsilon = 1\%$, however rms velocity variation ranges between 0.5% and 0.8% in the upper and lower mantle (Table 5.2). Despite differences in the model parameters, *PP* precursors in the synthetic seismograms produced by these models are very similar. The similarities may be due to common features in the model, including a reduction in rms velocity variation in the upper mantle and a higher rms velocity variation of 1% between 700 km and 1400 km. The heterogeneity parameters in the lithosphere and for depths greater than 1400 km are less constrained and are may be beyond the sensitivity of *PP* precursors for the distances studied.

Some models provide a good fit for *PP* precursors for most distances but fit poorly for the largest distances. The models tend to under-predict *PP* precursors at distance 112.5° and 117.5°, which could indicate the need for a deeper heterogeneity layer with an increase in heterogeneity properties (strength or scalelength) to produce more scattering. However, the global stack *PP* precursory energy at these distances may be not only due to scattering in the mantle but may be influenced by the *PKiKP* arrival. The 20 s before *PP* which includes the transition between precursors and *PP* onset fits the data well, though the width of *PP* is too broad. This may indicate that a thinner lithospheric heterogeneity layer is needed. Further investigation into the trade-off between heterogeneity properties of the lithosphere and mantle is required. In addition, knowing the scattering mechanisms could produce *PP* precursors (e.g. *P*-to-*P*-to-*P*, *P*-to-*p*) for each phonon in the model would help constrain what depths the precursors

h (km)	LAYM_45	h (km)	LAYM_33
0-100	$a = 2$,	0-100	$a = 2$,
	$\epsilon = 1\%$		$\epsilon = 1\%$
100-700	$a = 6$,	100-700	$a = 6$,
	$\epsilon = 0.8\%$		$\epsilon = 0.5\%$
700-1400	$a = 6$,	700-1400	$a = 6$,
	$\epsilon = 1\%$		$\epsilon = 1\%$
1400-2900	$a = 6$	1400-2900	$a = 6$,
	$\epsilon = 0.8\%$		$\epsilon = 0.5\%$
misfit	7.92	misfit	7.61

h (km)	LAYM_49	h (km)	LAYM_47
0-100	$a = 2$,	0-100	$a = 6$,
	$\epsilon = 2\%$		$\epsilon = 1\%$
100-700	$a = 6$,	100-700	$a = 6$,
	$\epsilon = 0.5\%$		$\epsilon = 0.5\%$
700-1400	$a = 6$,	700-1400	$a = 6$,
	$\epsilon = 1\%$		$\epsilon = 1\%$
1400-2900	$a = 6$,	1400-2900	$a = 6$,
	$\epsilon = 0.5\%$		$\epsilon = 0.5\%$
misfit	7.25	misfit	7.23

Table 5.2: The input parameters and misfit for layered mantle heterogeneity models LAYM_45, LAYM_33, LAYM_47 and LAYM_49.

sample and therefore would assist interpretation of the modelling results.

5.3.2 Regional patterns of heterogeneity

As demonstrated in Chapter 4, out-of-plane precursors to *PP* are detected and, in total, 471 scatterers are located. 407 scatterers (86%) are found in the crust and upper mantle, 31 scatterers (7%) are found in the transition zone and 33 (7%) found deeper than 650 km. More than two-thirds of the scatterers are beneath western Pacific subduction zones (region bounded by latitudes of 5°N and 50°N, and longitudes of 90°E and 1600°E) with 87% found in the lithosphere and uppermost mantle (100 to 400 km), 7% occur in the transition zone (400-600 km) and 6% are found in the mid and lower mantle (deeper than 600 km).

For the western Pacific subduction zone region, the scatterers generated by heterogeneities in the upper mantle correlate well with subducted slabs as inferred from tomography and subduction contours in the western Pacific subduction region (Section 4.6.1). Heterogeneity locations are aligned with the edges of fast velocity features evident in tomography model S40RTS (Ritsema et al., 2011) for depths of 300 to 600 km and slab reconstructions such as RUM (Gudmundsson and Sambridge, 1998) or Slab 1.0 (Hayes et al., 2012). These findings suggest that the scatterers are reflected/scattered energy of the edge of the slab (Figure 4.23). The scatterer locations also correlate with the 0.14-0.23 %/° gradient interval of S40RTS that may correspond to the compositional component at the edge of the fast velocity features in the tomographic model (Section 4.7). Therefore, there is strong support that the scatterers are related to the subducted crust, which possibly represents the main source of heterogeneity in the mantle.

Other scatterers are observed in the transition zone but are located away from the present day subduction slab and also correspond to the range of tomography gradient of 0.14-0.23 %/°. These may be the crustal component of ancient subducted slabs that have been preventing from subducting past 660 km discontinuity.

Correlating scatterers with tomographic images and subduction contours past 600 km depth (scatterer depths 550-650 km) is difficult due to the reduction in the number of scatterers, reduction in resolution of tomography and the absence of subducted slab contours for the mid and lower mantle. Nonetheless, extrapolating this conclusion to deeper scatterers where the resolution of tomography is reduced, it is possible that the

scatterers are the crustal component of the subducted slab in the lower mantle beneath the Izu-Bonin and Mariana trenches and beneath the location of an Indonesian paleo subduction trench that was active from 80-144 Ma. Comparing scatterer locations to paleo subduction zones thus can be useful in resolving past subducted slab styles and subduction velocities (Section 4.7).

Scatterers observed outside of the western Pacific subduction zones are found beneath various tectonic settings (Section 4.6). Shallow scatterers are found under the central Pacific Plate and at the junction between the Japan and the Aleutian subduction zones (Figure 4.19). For deeper depths (Figure 4.20), the scatterers are mostly located beneath the central Pacific plate (400-600 km) and tend to be organised in clusters beneath the Hawaii-Emperor seamount chain and beneath the Solomon subduction zones (between longitudes 140° and 170° on the equator). Though there are too few scatterers in each of those regions to generate a comprehensive analysis, the scatterers beneath the Hawaiian-Emperor seamount chain are interesting and may indicate that chemical heterogeneity is entrained by upwelling mantle flow.

The number of scatterers relocated in this study is found to decrease with depth with the deepest scatterer observed at 1880 km. The cause of the reduction and the absence of scatterers for depths of 1900 km and deeper, could be due to a variety of factors. Scatterer detections probably depend on the elastic properties as both basalt-pyrolite and basalt-harzburgite impedance contrasts sharply decrease at 1500 km depth (Rost et al., 2008). Orientation and position of the heterogeneities could be a strong factor as the relocation procedure has geometrical limits (Section 4.5). In contrast, the detection and relocation methods can be ruled out as a factor since the sensitivity analysis of the method shows that if they were more uniformly distributed, many more scatterers would be found than are actually detected (see Section 4.6.1, Figure 4.22).

5.4 Combined mantle heterogeneity discussion

5.4.1 Spatial variations of heterogeneity

The main difference between the results of the global stacking study and the ILAR array study is where they detect heterogeneities. For the global stacks, density plots created from earthquake and station distribution show that the method has good global sampling, though with a slight bias to the northern hemisphere (Figure 5.1). The lack of

variation of *PP* precursor signatures between different tectonic and geodynamic regions suggests that the global heterogeneity models produced can be applied to the regional scale. In contrast, the mantle scatterers found by studying scattering using ILAR array are only found in the western Pacific subduction zone and central Pacific Ocean. In this case, the heterogeneities are clearly associated with the subduction process.

5.4.2 Heterogeneity scale length variations

The heterogeneities found in the two studies in this thesis have different lengthscales: 6 km lengthscale heterogeneities work best in the global stacking study and 10 km scale heterogeneities using the array method. For mantle lengthscales, 6 km may not appear significantly different from 10 km, however, from the comparison of global stacks with modelling results, models with correlation length $a = 10$ km do not fit the data well, suggesting the 6 km correlation length may be an upper estimate of a. This difference in lengthscale of the heterogeneities may be explained in terms of crustal thinning.

The ∼10 km scatterers found beneath Izu Bonin and Mariana subduction zones are probably connected to the crustal component of subducted slabs that have been subducted within the last 20 Ma. From the analysis in Section 4.7, the scatterers likely image the subducted moho of crust that is still attached to the slab. As such, the subducted crust imaged here is probably within the initial stages of the mixing cycle. In contrast, the heterogeneities derived from modelling the global stacks are of a smaller correlation length of 6 km within a global layer (shell) of depths 700-1400 km (Section 5.4.1). As there are no regional variations evident the heterogeneities may be well mixed within this layer and are probably later in the mixing cycle than the scatterers observed using discrete *PP* precursors.

If the smaller (6 km) lengthscale heterogeneities are further along the mixing process, these heterogeneities would be produced by the attenuation of recycled crust rather than accumulation. Attenuation of crust of lengthscales of 1-10 km occurs through stretching and folding and depends on the vigour of convection (Stixrude and Lithgow-Bertelloni, 2012). The change in thickness of crust over time can be quantified through:

$$h = h_0 \exp(-\dot{\varepsilon}\tau) \tag{5.1}$$

where $\dot{\varepsilon}$ is the strain rate in the crust, h_0 is the initial thickness and h is the deformed thickness at time τ (Spence et al., 1988). Typical values of the strain rate are derived

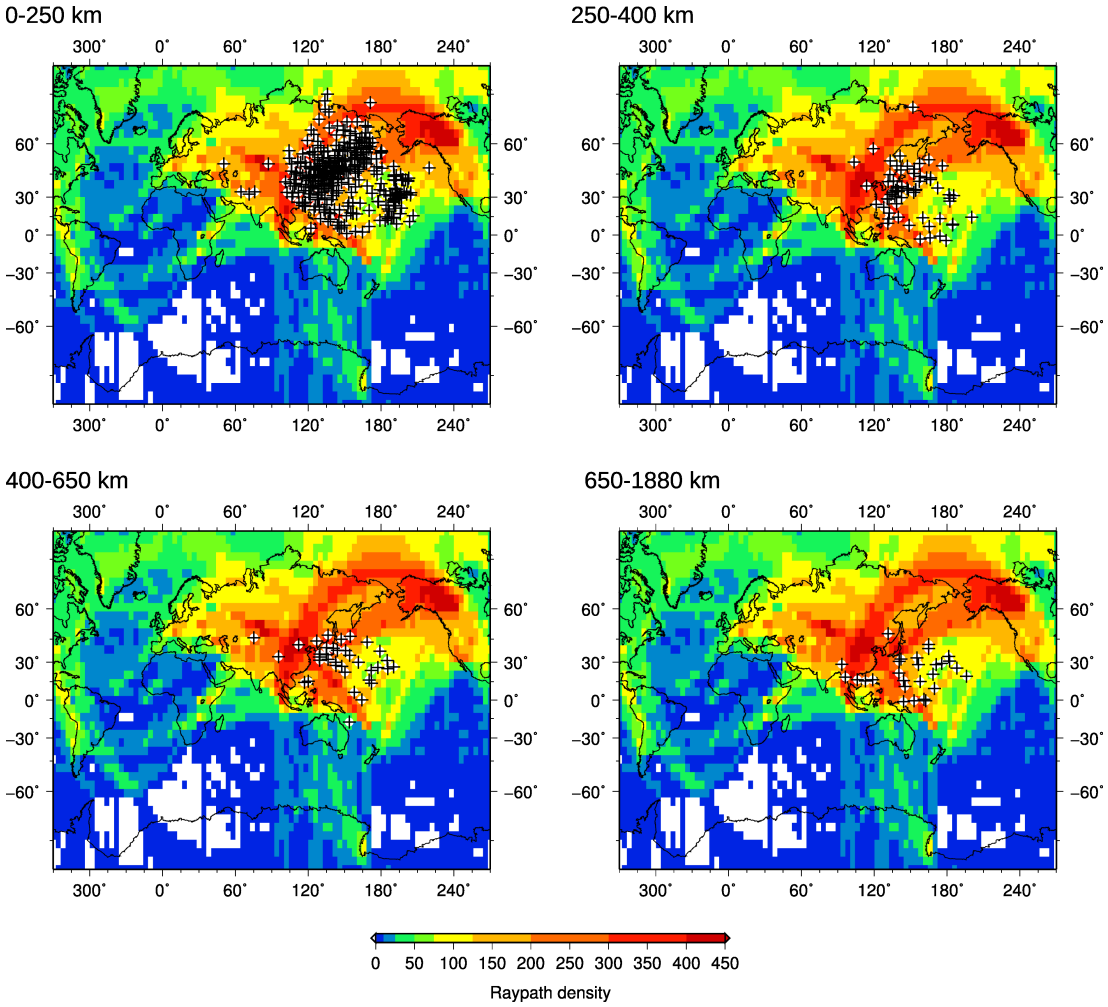

Figure 5.1: Variable density of the spatial sampling of the seismic traces used in the global stacks from Chapter 3 (all four maps are identical) in comparison to the locations of the scatterers (black cross with white circle) detected using the ILAR array in Chapter 4. The global stacking method is sensitive to most of the globe with the greatest density observed in west North America, Japan and south-east Asia and least sensitivity under Antarctica. The locations of scatterers detected using ILAR are limited to the Asian continental crust and upper mantle, and are mostly present in Western Pacific subduction zones and beneath the mid Pacific.

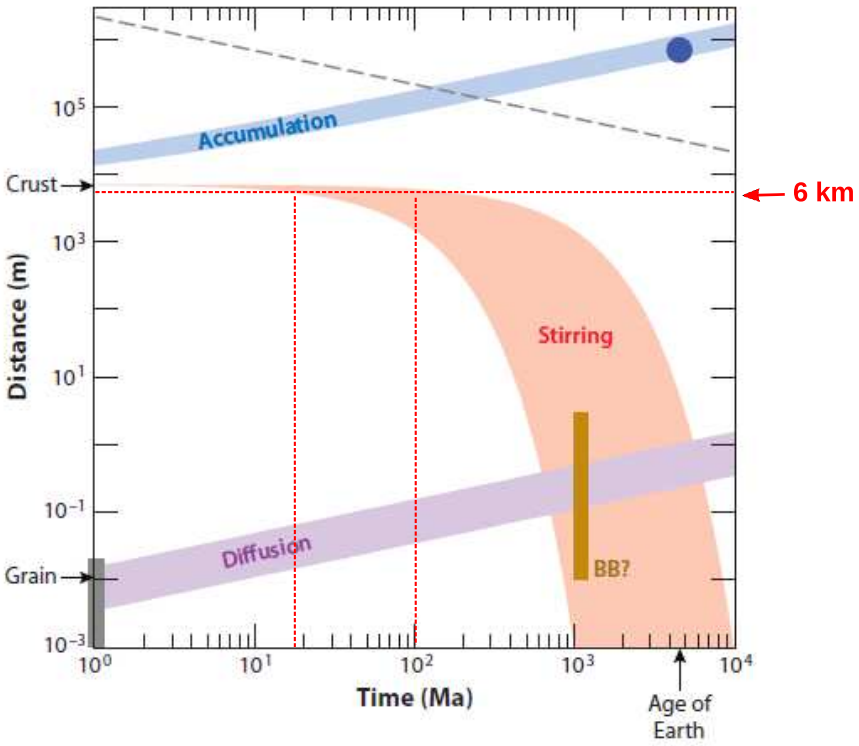

Figure 5.2: Evolution of lengthscales relevant to the survival of heterogeneity in the mantle. Mechanical stirring (orange band) reduces the lengthscale of oceanic crust (according to equation 5.1) to 6 km lengthscales within 15 Ma to 100 Ma. Stirring dominates the mixing process until 1 Ga when the crust is thinned to grain size (cm scale) and diffusion (purple band) becomes effective. Accumulation of heterogeneity (blue band) increases from 10 km to nearly 1000 km over the age of the Earth. Republished with permission of Annual Reviews, from Stixrude and Lithgow-Bertelloni (2012); permission conveyed through Copyright Clearance Center, Inc.

through present day average plate speed $u = 5.5$ cm yr^{-1} and the depth of the mantle $L = 2891$ km in the expression $\dot{\varepsilon} = u/L = 6 \times 10^{-16}$ s^{-1}. Uncertainties in convective vigour are taken into account by assuming 10% of the present day value (Stixrude and Lithgow-Bertelloni, 2012). For an initial thickness of crust of 7 km (Stixrude and Lithgow-Bertelloni, 2012) a range of crustal thicknesses develops (Figure 5.2). Using these parameters, subducted crust deforms to 6 km lengthscale over a time period that may vary in the range of 15 Myr to 100 Myr.

5.4.3 Heterogeneity variations with depth

As discussed above, a few models developed from the Monte Carlo modelling have a good fit to the *PP* precursors in the global stacks. The models do not fit well for all the larger distances (i.e. 112.5-117.5°) indicating that the heterogeneity properties assumed at depth are not well resolved in the models. Nonetheless, inferences about

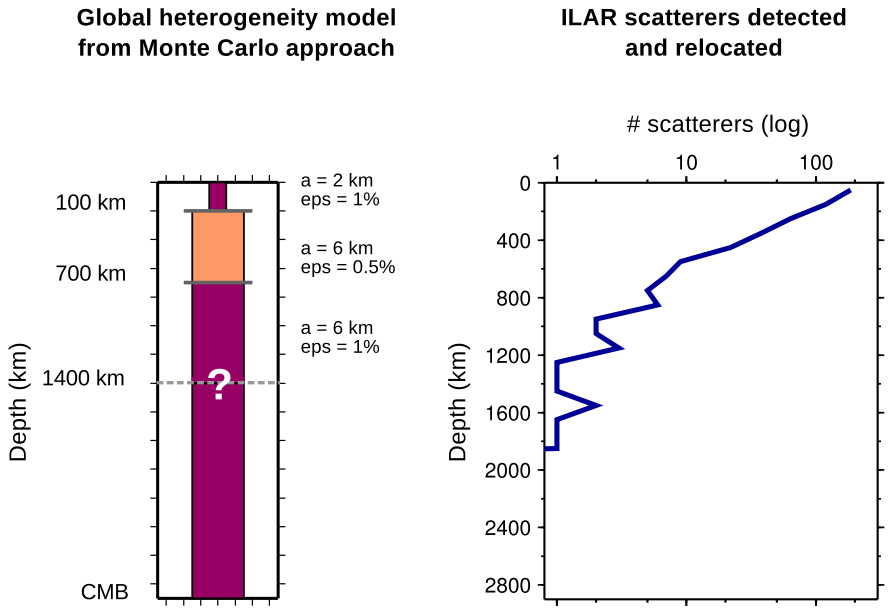

Figure 5.3: From the Monte Carlo phonon modelling, the properties of heterogeneity change with depth (left). The scalelength of heterogeneity (a) increases from 2 km in the crust to 6 km throughout the mantle. Rms velocity variation (ϵ or eps) is 1% in the crust. Rms velocity variation increases in the mantle from 0.8% in the upper mantle to 1% at 700 km. The depth extent of these heterogeneity properties of $\epsilon = 1\%$ and $a = 6\ km$ is a minimum of 1400 km depth but could be deeper. The number of coherent scatterers observed using the ILAR array decrease with depth (right) with no scatterers observed deeper than 1900 km.

the similarities between the models can be made. The common parts of the models include a lithosphere (0-100 km) with rms velocity variation $\epsilon = 1\%$ and correlation length $a = 2$ km, an upper mantle (100-400 km) with $\epsilon = 0.8\%$ and $a = 6$ km and a mid-mantle (700-1400 km) with $\epsilon = 1\%$ and $a = 6$ km (Figure 5.3). In these models, the strength of heterogeneity decreases in the upper mantle, then increases in strength at 700 km.

Figure 5.3 shows that the majority of scatterers found using the ILAR array are located in the crust and upper mantle (407 scatterers) and the number of scatterers found decreases with depth to the deepest scatterer observed at 1900 km. However, the strength of heterogeneity increases with depth in the preferred Monte Carlo models. The opposing trends of heterogeneity with depth may be important in establishing how the subducted crust is mixed into the mantle.

5.4.4 Geodynamical Interpretation

Figure 5.4 shows a combined interpretation of the mantle heterogeneity observations and scalelength, and how these vary spatially and with depth. Oceanic crust with

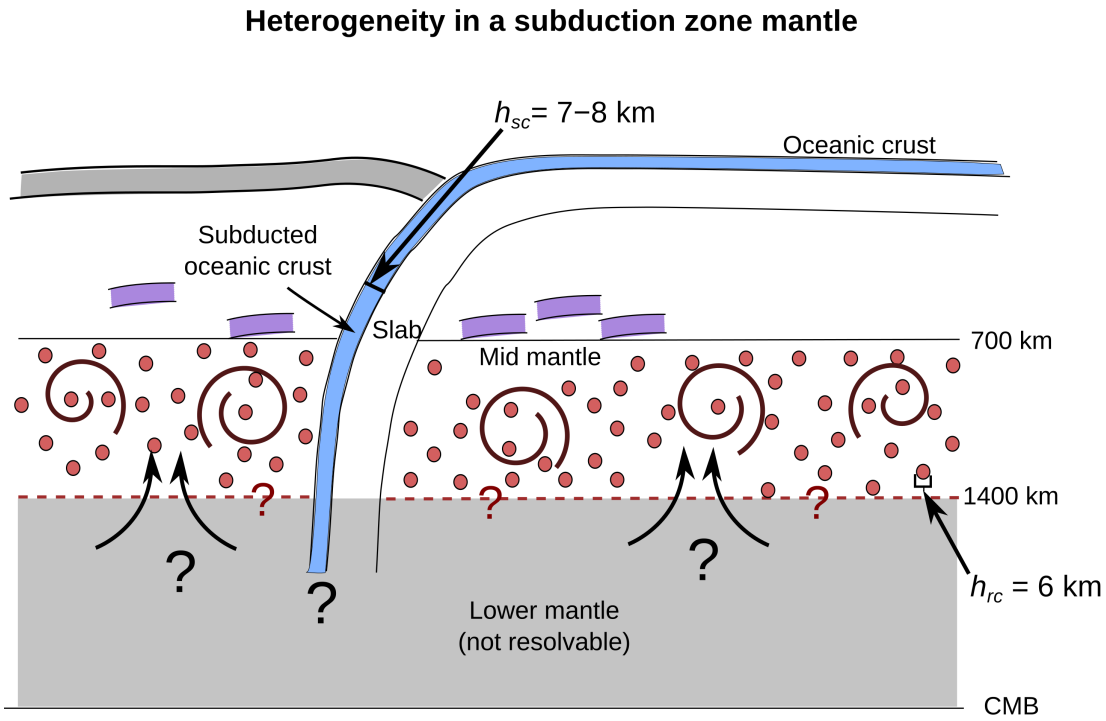

Figure 5.4: Interpretation of the mantle heterogeneity observed in this study applicable to a subduction zone region with a steeply dipping slab (e.g. Marianas). The subducted crust remains attached to the lithospheric part of the slab and is detectable to depth of 1900 km. Some crustal remnants are detected in the transition zone and may be the remnant of previous shallow dipping subduction, which was inhibited from entering the mid-mantle. The mid-mantle contains 6 km scale heterogeneities that may be recycled MORB that has been entrained upwards by flow from the lower mantle. The layer may be well mixed by small scale convective currents. Average heterogeneity properties in the transition zone are not well resolved but the strength of heterogeneity in the uppermost mantle is probably less than the strength of heterogeneity in the crust and mid-mantle. In this study, global heterogeneity averages are not resolvable for depths $\geq$1400 km, and the subducted crust is not resolvable for depths $\geq$1900 km due to decrease in impedance contrast. Lower mantle processes that recycle and deform the crust are not resolvable in this study.

thickness $h_{sc} = 7$ km to 8 km enters the mantle at subduction zone (Figure 5.4), and is detected to depths of 1900 km (Figure 5.1) where the impedance contrast and/or geometry limit further detection. If slabs descend steeply they would take 12 Ma to reach 700 km, at the present day average subduction rate of 5.5 cm yr^{-1}, which is not long enough to thin the crust significantly (Figure 5.2). Using the same descent rate, the slab would reach 1400 km by 24 Ma, by which time, some portion of subducted crust may have thinned to 6 km, though most of the crust will probably continue deeper into the mantle.

In contrast, smaller heterogeneities with correlation length $a = 6$ km randomly distributed within the mid-mantle explain the global stacks (Figure 5.4) and may be caused by recycled crust that has been entrained into the mid-mantle after the subducted slab has reached the lower mantle (Figure 5.4). The crust becomes well mixed by small scale convection between 700-1400 km (Davies, 1984), though the lower limit at 1400 km is not well constrained and should not be interpreted as a physical or chemical boundary. Other lengthscales have not been detected with *PP* precursors but models with layers containing multiple heterogeneity lengthscales are not considered in this study.

Information in the lower mantle is limited from this study of *PP* precursors. Subducted crust below 1900 km depth may not detectable with *P*-to-*P* scattering due to decrease in impedance contrast (Rost et al., 2008). In addition, modelling of global averages of *PP* precursors may not be sensitive to depths deeper than 1400 km though this is difficult to characterise without knowing all scattering mechanisms that can produce *PP* precursory energy. Other studies have modelled the average properties of lower mantle heterogeneities (Hedlin et al., 1997, Earle and Shearer, 2001, Shearer and Earle, 2004) but there is little agreement amongst these results.

Heterogeneity from different parts of the mantle mixing process have been found here and these results can be compared to features found in thermo-chemical convection models. The Monte Carlo modelling results in this study suggest that the mid-mantle contains heterogeneities with ∼6 km scalelength (Figure 5.4) . Though MORB is denser than the ambient perovskite in the mid-mantle (Irifune and Tsuchiya, 2007) some models show that crust becomes entrained into upwellings and then mixes with the mid-mantle (Brandenburg and van Keken, 2007) (Figure 5.5, region D). Other studies shows that some recycled crust remains in the lower mantle (Hirose et al., 2005) due

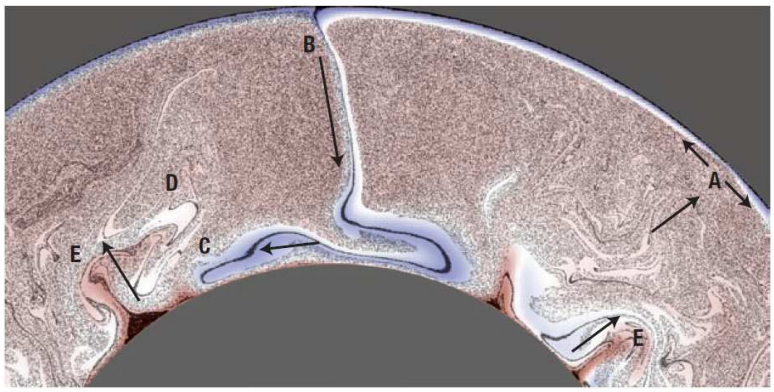

Figure 5.5: Numerical thermo-chemical modelling of mantle convection with chemically distinct oceanic crust (black lines). Basaltic crust is formed at the mid-ocean ridge (A) and is introduced into the mantle at subduction zones (B). The crust is present in the lower mantle (C) and is recycled to the rest of the mantle (D). Crust is brought up by plumes to ocean island hotspots (E) or passively at mid-ocean ridges (B - again). Image reprinted by permission from Nature Publishing Group: Nature Geoscience, Plank and van Keken (2008), copyright 2008, using models from Brandenburg and van Keken (2007).

to MORB density increase (Christensen and Hofmann, 1994) and is accumulated in piles at the CMB (point E in Figure 5.5). Though the approach in this study is not sensitive to the lowermost mantle, accumulated piles of crust with assumed lengthscale of >10 km, have not been detected in the upper or mid-mantle.

However, locating scatterers using array seismology methods in this study show that some heterogeneity of 10 km scale remains in the transition zone. This is in contrary to many studies, which suggest that stirring alone could not delaminate the crust on such rapid timescales in the transition zone (Jin et al., 2001, van Keken et al., 1996). However, Lee and Chen (2007) showed that a weak serpentinite layer between crust and underlying lithosphere could result in basalt delamination within the transition zone.

Chapter 6

Conclusions and Future Work

Novel methods has been developed for studying global averages of the *PP* wavefield. The approach has been optimised for epicentral distances of 70-120° including a tool to remove the interference of the *P* coda. The resultant global stacks of *PP* have revealed that *PP* precursors exist for all distances in the range 70 to 120° with the amplitudes increasing with distance and time, and with a maximum amplitude of 50% of *PP* amplitude. In addition, subsets of the data are used to produce regional stacks for the Pacific and Atlantic Oceans to assess regional variations in *PP* precursors. Despite the large discrepancy in the number of traces stacked between the regions, the regional stacks are very similar for most distances, suggesting the heterogeneities that generate *PP* precursors do not vary with tectonic region.

PP precursors are modelled using a Monte Carlo phonon method that generates statistical scattering models for random media. Modelling results show that heterogeneities in the crust and mantle contribute to the scattered *PP* wavefield, and heterogeneity strength and scale length vary with depth. The modelled precursory wavefield has a good fit to the data for models with 1% scattering in a lithospheric layer, reduced scattering of 0.8% in the uppermost mantle and an increase in scattering to 1% at ∼700 km. The extent of this deeper mantle layer is not well resolved and may be determined using larger epicentral distances.

PP precursors that are caused by scattering at small-scale mantle heterogeneities in western Pacific subduction zones and beneath the central Pacific have been detected using novel array methods. An automatic tool for detecting weak precursors has found 469 off-azimuth arrivals ($\delta\theta > 5°$) and the origins of scattering are located using a backprojection scheme. Though a majority of scatterers are located in the crust and

upper mantle, scatterers in the transition zone, mid- and lower mantle have been found in western Pacific subduction zones. These scatters correlate with subducted slabs as inferred from tomography, tomography gradients and subduction contours. Scatterers deeper than 600 km likely image the crustal component of the subducted slab to depths of 1900 km and are consistent with scatterers found in other studies (Castle and Creager, 1999, Kaneshima and Helffrich, 1999, Niu et al., 2003, Kaneshima and Helffrich, 2009). Such lower mantle scatterers are found beneath the location of an Indonesian paleo subduction trench that was active from 80-144 Ma and these scatterers further constrain recent subduction history for the Izu-Bonin and Mariana slabs. In addition, some deep scatterers have been found beneath the Hawaiian-Emperor seamount chain and north of the Solomon subduction zone. Unfortunately the heterogeneities producing such scattering are difficult to interpret with so few scattering points located. Analysis of the method sensitivity shows that the locations of scatterers are not dependent on the detection and relocation methods applied in this study but most likely depend on the elastic properties and the orientation of the heterogeneities.

Results from the global stacking and regional array studies of heterogeneity have been combined into a mantle heterogeneity interpretation that is applicable to the Mariana subduction zone. I interpret that a steeply dipping slab with the crustal component attached is a mechanism of introducing crustal heterogeneities into the lower mantle. I also suggest it is unlikely that the heterogeneities in the mid-mantle (as imaged through statistical scattering modelling) are derived from recently subducted crust since the heterogeneity layer appears well mixed. Furthermore, I interpret the averaged properties of heterogeneities in the mid mantle (700-1400 km) as representative of recycled crust that has been subducted to the lower mantle and entrained into up-going mantle flow over time periods that are consistent with mechanical mixing rates.

6.1 Future Work

Based on these conclusions this research topic can be extended through the following suggestions of future studies:

- Further progress in the global stacking of *PP* in Chapter 3 can be explored by extending the present dataset to include more seismic arrays. This will increase

the data sampling and may allow a more detailed analysis of regional variations. If the sampling is high across most of the globe then average stacks could be generated for a sliding region that is, for example, shifted in longitude.

- In addition, backazimuth stacks could be generated from the existing dataset to examine variations in precursory energy in backazimuth.

- Additional models can be explored to better constrain the heterogeneities that generate the *PP* precursors. Models with a thinner lithosphere(less than 100 km) may produce synthetics that are a better fit for *PP*, i.e. have *PP* envelope width of ∼10 s. Whereas models with additional layers of heterogeneity may be useful in providing better fit for the largest epicentral distances (102.7-105.7°). Furthermore, models using lower attenuation levels than the Warren and Shearer (2000) could be explored.

- The ILAR array dataset could be extended with more recent earthquakes and combined with other North American arrays (e.g. Yellowknife, USArray) to perform a migration of the Izu-Bonin and Marianas subduction zones.

- The automatic detection tool (TOPCAT) developed for ILAR can be applied to a larger array to study the central Pacific and western Pacific and Indonesia subduction zones. An example dataset could be obtained from High Lava Plains (HLP) Project array and initial data collection suggests that 240 events are suitable. These events fit the criteria of: earthquake source depth of 0-100 km, magnitude greater than 6 and epicentral distances of 90-110° (Figure 6.1).

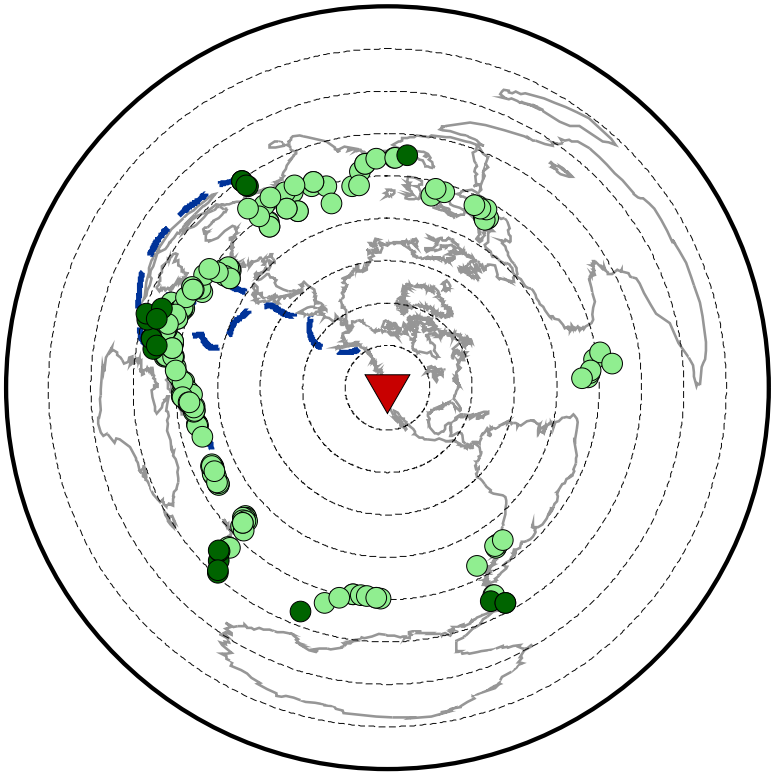

Figure 6.1: Earthquake locations within distances of 90-100° (light green) and 100-110° (dark green) of High Lava Plains (HLP) Project Array, with western Pacific subduction zones (blue dashed lines) from Gudmundsson and Sambridge (1998).

References

Aki, K. (1969), Analysis of the seismic coda of local earthquakes as scattered waves, *Journal of Geophysical Research*, *74*(2), 615–631. 3.2

Aki, K. (1973), Scattering of P waves under the Montana Lasa, *Journal of Geophysical Research*, *78*(8), 1334–1346, doi:10.1029/JB078i008p01334. 2.3

Aki, K., and B. Chouet (1975), Origin of coda waves: Source, attenuation, and scattering effects, *Journal of Geophysical Research*, *80*(23), 33223342, doi:10.1029/JB080i023p03322. 2.4.2, 3.2

Aki, K., and P. G. Richards (1980), *Quantitative Seismology - Theory and Methods*, 1st ed., W. H. Freeman and Company. 2.2.1, 2.2.1, 2.2, 2.2.2, 2.3

Allegre, C. J., and D. L. Turcotte (1986), Implications of a two-component marble-cake mantle, *Nature (London)*, *323*(6084), 123–127. 1.5

Ammann, M. W., J. P. Brodholt, J. Wookey, and D. P. Dobson (2010), First-principles constraints on diffusion in lower-mantle minerals and a weak D" layer, *Nature*, *465*(7297), 462–465, doi:10.1038/nature09052. 1.5, 1.5

Bataille, K., and S. M. Flatt (1988), Inhomogeneities near the core-mantle boundary inferred from short-period scattered PKP waves recorded at the global digital seismograph network, *Journal of Geophysical Research: Solid Earth*, *93*(B12), 15,05715,064, doi:10.1029/JB093iB12p15057. 2.3, 3.2

Bataille, K., R. S. Wu, and S. M. Flatte (1990), Inhomogeneities near the core-mantle boundary evidenced from scattered waves; a review, *Pure and Applied Geophysics*, *132*(1-2), 151–173. 3.2

Becker, T. W., J. B. Kellogg, and R. J. O'Connell (1999), Thermal constraints on the survival of primitive blobs in the lower mantle, *Earth and Planetary Science Letters*, *171*(3), 351–365, doi:10.1016/S0012-821X(99)00160-0. 1.4, 1.6, 1.5

Bhattacharyya, J., P. Shearer, and G. Masters (1993), Inner core attenuation from short-period PKPbc versus PKPdf waveforms, *Geophysical Journal International*, *114*(1), 1–11, doi:10.1111/j.1365-246X.1993.tb01461.x. 3.5, 3.14, 3.6.1

Bird, P. (2003), An updated digital model of plate boundaries, *Geochemistry, Geophysics, Geosystems*, *4*(3), doi:10.1029/2001GC000252. 4.2

Bostock, M. G., and S. Rondenay (1999), Migration of scattered teleseismic body waves, *Geophysical Journal International*, *137*(3), 732746, doi:10.1046/j.1365-246x.1999.00813.x. 2.5.3

Bostock, M. G., S. Rondenay, and J. Shragge (2001), Multiparameter two-dimensional inversion of scattered teleseismic body waves 1. theory for oblique incidence, *Journal of Geophysical Research: Solid Earth*, *106*(B12), 30,77130,782, doi:10.1029/2001JB000330. 2.5.3

Brana, L., and G. Helffrich (2004), A scattering region near the core-mantle boundary under the North Atlantic, *Geophysical Journal International [Geophys. J. Int.]*, *158*(2), 625–636. 2.5.3

Brandenburg, J. P., and P. E. van Keken (2007), Deep storage of oceanic crust in a vigorously convecting mantle, *Journal of Geophysical Research: Solid Earth*, *112*(B6), doi:10.1029/2006JB004813. 1.7, 1.5, 5.4.4, 5.5

Cao, Q., P. Wang, R. D. van der Hilst, M. V. de Hoop, and S.-H. Shim (2010), Imaging the upper mantle transition zone with a generalized radon transform of SS precursors, *Physics of the Earth and Planetary Interiors*, *180*(1-2), 80–91, doi:10.1016/j.pepi.2010.02.006. 2.5.3

Capon, J. (1969), High-resolution frequency-wavenumber spectrum analysis, *Proceedings of the IEEE*, *57*(8), 1408–1418. 2.5.2, 4.4.2

Castle, J. C., and K. C. Creager (1999), A steeply dipping discontinuity in the lower mantle beneath Izu-Bonin, *Journal of Geophysical Research*, *104*(B4), 7279–7292, includes appendix. 2.3, 4.6.1, 4.7, 4.7, 6

Chambers, K., and J. H. Woodhouse (2006a), Investigating the lowermost mantle using migrations of long-period S-ScS data, *Geophysical Journal International*, *166*(2), 667678, doi:10.1111/j.1365-246X.2006.03002.x. 2.5.3, 2.5.3

Chambers, K., and J. H. Woodhouse (2006b), Transient D" discontinuity revealed by seismic migration, *Geophysical Research Letters*, *33*(17), doi:10.1029/2006GL027043. 2.5.3

Chernov, L. A. (1960), *Wave propagation in random medium*, McGraw-Hill, New York, translated from Russian by R. A. Silverman. 2.2.3, 2.4.2

Christensen, U. R., and A. W. Hofmann (1994), Segregation of subducted oceanic crust in the convecting mantle, *Journal of Geophysical Research*, *99*(B10), 19,867–19,884, doi:10.1029/93JB03403. 1.5, 4.2, 4.7, 5.4.4

Christensen, U. R., and D. A. Yuen (1984), The interaction of a subducting lithospheric slab with a chemical or phase boundary, *Journal of Geophysical Research*, *89*(B6), 4389–4402, doi:10.1029/JB089iB06p04389. 1.3

Cleary, J. R., and R. a. W. Haddon (1972), Seismic wave scattering near the core-mantle boundary: a new interpretation of precursors to PKP, *Nature*, *240*(5383), 549–551, doi:10.1038/240549a0. 2.4.1, 3.2

Cleary, J. R., D. W. King, and R. A. W. Haddon (1975), P-wave scattering in the Earth's crust and upper mantle, *Geophysical Journal International*, *43*(3), 861–872, doi:10.1111/j.1365-246X.1975.tb06200.x. 2.4.1

Coltice, N., and Y. Ricard (1999), Geochemical observations and one layer mantle convection, *Earth and Planetary Science Letters*, *174*(1-2), 125–137, doi:http://0-dx.doi.org.wam.leeds.ac.uk/10.1016/S0012-821X(99)00258-7. 1.4, 1.6

Cormier, V. F. (1999), Anisotropy of heterogeneity scale lengths in the lower mantle from PKIKP precursors, *Geophysical Journal International*, *136*(2), 373384, doi:10.1046/j.1365-246X.1999.00736.x. 2.3

Cornwell, D. G., G. Hetényi, and T. D. Blanchard (2011), Mantle transition zone variations beneath the ethiopian rift and afar: Chemical heterogeneity within a hot mantle?, *Geophysical Research Letters*, *38*(16), doi:10.1029/2011GL047575. 3.8.1

Davies, D., J. Kelly, and J. R. Filson (1971), Vespa process for analysis of seismic signals, *Nature Physical Science*, *232*(27), 8–13. 2.5.2

Davies, G., and M. Richards (1992), Mantle convection, *Journal of Geology*, *100*(2), 151–206. 1.3, 4.7

Davies, G. F. (1984), Geophysical and isotopic constraints on mantle convection; an interim synthesis, *Journal of Geophysical Research*, *89*(B7), 6017–6040, doi:http://0-dx.doi.org.wam.leeds.ac.uk/10.1029/JB089iB07p06017. 1.4, 5.4.4

Davies, G. F., and M. Gurnis (1986), Interaction of mantle dregs with convection; lateral heterogeneity at the core-mantle boundary, *Geophysical Research Letters*, *13*(13), 1517–1520, doi:http://0-dx.doi.org.wam.leeds.ac.uk/10.1029/GL013i013p01517. 1.4

Day, J. M. D., D. G. Pearson, C. G. Macpherson, D. Lowry, and J.-C. Carracedo (2009), Pyroxenite-rich mantle formed by recycled oceanic lithosphere: Oxygen-osmium isotope evidence from Canary Island lavas, *Geology*, *37*(6), 555–558, doi:10.1130/G25613A.1. 1.3

Deschamps, F., P. J. Tackley, and T. Nakagawa (2010), Temperature and heat flux scalings for isoviscous thermal convection in spherical geometry, *Geophysical Journal International [Geophys. J. Int.]*, *182*(1), 137–154. 4.2

Deschamps, F., E. Kaminski, and P. J. Tackley (2011), A deep mantle origin for the primitive signature of ocean island basalt, *Nature Geoscience*, *4*(12), 879–882, doi:10.1038/ngeo1295. 1.4

Deuss, A., S. A. T. Redfern, K. Chambers, and J. H. Woodhouse (2006), The nature of the 660-Kilometer discontinuity in Earth's mantle from global seismic observations of PP precursors, *Science*, *311*(5758), 198–201, doi:10.1126/science.1120020. 2.3.1, 3.2, 4.3.2

Doornbos, D. (1978), Seismic-wave scattering by a rough core-mantle boundary, *Geophysical Journal of the Royal Astronomical Society*, *53*(3), 643–662, doi:10.1111/j.1365-246X.1978.tb03765.x, WOS:A1978FA65400015. 3.2

Doornbos, D. J. (1974), Seismic wave scattering near caustics: Observations of PKKP precursors, *Nature (London)*, *247*(5440), 352–353. 3.2

Doornbos, D. J. (1980), The effect of a rough core-mantle boundary on PKKP, *Physics of the Earth and Planetary Interiors*, *21*(4), 351–358. 3.2

Dziewonski, A. M., and D. L. Anderson (1981), Preliminary reference earth model (Prem), *Eos*, *62*(17), 332. 1.1, 1.2, 3.3.2

Dziewonski, A. M., and J. H. Woodhouse (1987), Global images of the earth's interior, *Science*, *236*, 37–48, doi:10.1126/science.236.4797.37. 1.2, 4.2

Earle, P., and P. Shearer (2001), Distribution of fine-scale mantle heterogeneity from observations of Pdiff coda, *Bulletin of the Seismological Society of America*, *91*(6), 1875–1881. 2.3, 2.4.1, 2.4.2, 3.2, 3.2, 3.6, 3.6.1, 3.1, 3.16, 3.8.2, 4.7, 5.3.1, 5.1, 5.4.4

Earle, P. S., and P. M. Shearer (1997), Observations of PKKP precursors used to estimate small-scale topography on the core-mantle boundary, *Science*, *277*(5326), 667–670. 3.2

Earle, P. S., and P. M. Shearer (1998), Observations of highfrequency scattered energy associated with the core phase PKKP, *Geophysical Research Letters*, *25*(3), 405408, doi:10.1029/97GL53365. 2.3

Engdahl, E. R., R. D. van der Hilst, and J. Berrocal (1995), Imaging of subducted lithosphere beneath south america, *Geophysical Research Letters*, *22*(16), 2317–2320, doi:10.1029/95GL02013. 1.2, 4.2

Engebretson, D., K. Kelley, H. Cashman, and M. Richards (1992), 180 million years of subduction, *GSA today*, *2*(5), 93–100. 4.6.1

Estabrook, C. H., and R. Kind (1996), The nature of the 660-kilometer upper-mantle seismic discontinuity from precursors to the PP phase, *Science*, *274*(5290), 1179–1182, doi:10.1126/science.274.5290.1179. 3.2, 4.3.2

Faccenda, M., and F. A. Capitanio (2012), Development of mantle seismic anisotropy during subduction-induced 3-d flow, *Geophysical Research Letters*, *39*(11), doi:10.1029/2012GL051988. 4.7

Flanagan, M. P., and P. M. Shearer (1998), Global mapping of topography on transition zone velocity discontinuities by stacking SS precursors, *Journal of Geophysical Research-Solid Earth*, *103*(B2), 2673–2692, doi:10.1029/97JB03212. 2.3.1, 3.2, 3.8.1, 4.3.2

Flanagan, M. P., and P. M. Shearer (1999), A map of topography on the 410-km discontinuity from PP precursors, *Geophysical Research Letters*, *26*(5), 549–552, doi:http://0-dx.doi.org.wam.leeds.ac.uk/10.1029/1999GL900036. 2.3.1, 2.9

Foley, B. J., and M. D. Long (2011), Upper and mid-mantle anisotropy beneath the tonga slab, *Geophysical Research Letters*, *38*(2), doi:10.1029/2010GL046021. 4.7

Frankel, A., and R. W. Clayton (1986), Finite difference simulations of seismic scattering: Implications for the propagation of short-period seismic waves in the crust and models of crustal heterogeneity, *Journal of Geophysical Research: Solid Earth*, *91*(B6), 64656489, doi:10.1029/JB091iB06p06465. 3.4

Grand, S. P. (2002), Mantle shear-wave tomography and the fate of subducted slabs, *Philosophical Transactions of the Royal Society of London. Series A: Mathematical, Physical and Engineering Sciences*, *360*(1800), 2475–2491, doi:10.1098/rsta.2002.1077. 1.2, 4.2, 4.7

Gu, Y., and M. Sacchi (2009), Radon transform methods and their applications in mapping mantle reflectivity structure, *Surveys in Geophysics*, *30*(4), 327–354, doi:10.1007/s10712-009-9076-0. 2.5.3, 2.17

Gudmundsson, O., and M. Sambridge (1998), A regionalized upper mantle (RUM) seismic model, *Journal of Geophysical Research*, *103*(B4), 7121– 7136, doi:10.1029/97JB02488. 4.5, 4.21, 4.6.1, 4.23, 4.25, 4.27, 4.7, 4.7, 5.3.2, 6.1

Haddon, R., and J. Cleary (1974), Evidence for scattering of seismic PKP waves near the mantle-core boundary, *Physics of the Earth and Planetary Interiors*, *8*(3), 211–234, doi:10.1016/0031-9201(74)90088-0. 2.4.1, 3.2

Hall, R. (2012), Late Jurassic-Cenozoic reconstructions of the Indonesian region and the indian ocean, *Tectonophysics*, *570-571*, 1–41. 4.6.1

Hart, S. R., J.-G. Schilling, and J. L. Powell (1973), Basalts from iceland and along the reykjanes ridge: Sr isotope geochemistry, *Nature*, *246*(155), 104–107, doi:10.1038/10.1038/physci246104a0. 1.3

Hauri, E. H., and S. R. Hart (1993), ReOs isotope systematics of HIMU and EMII oceanic island basalts from the south pacific ocean, *Earth and Planetary Science Letters*, *114*(2-3), 353–371, doi:10.1016/0012-821X(93)90036-9. 1.3

Hayes, G. P., D. J. Wald, and R. L. Johnson (2012), Slab1.0: A three-dimensional model of global subduction zone geometries, *Journal of Geophysical Research*, *117*(B1), doi:10.1029/2011JB008524. 4.27, 4.7, 5.3.2

Hedlin, M. A., and P. M. Shearer (2002), Probing mid-mantle heterogeneity using PKP coda waves, *Physics of the Earth and Planetary Interiors*, *130*(34), 195–208, doi:10.1016/S0031-9201(02)00007-9. 2.4.1, 2.4.2, 3.2, 3.8.2

Hedlin, M. A. H., and P. M. Shearer (2000), An analysis of large-scale variations in small-scale mantle heterogeneity using global seismographic network recordings of precursors to PKP, *Journal of Geophysical Research*, *105*, 13–13,673. 2.4.1, 3.2, 3.1, 3.3.5

Hedlin, M. A. H., P. M. Shearer, and P. S. Earle (1997), Seismic evidence for small-scale heterogeneity throughout the earth's mantle, *Nature*, *387*(6629), 145–150, doi:10.1038/387145a0. 2.3, 2.4.1, 3.2, 3.1, 3.4, 3.6, 3.6, 3.6.1, 3.1, 3.16, 3.8.2, 5.3.1, 5.1, 5.4.4

Helffrich, G. (2006), Heterogeneity in the mantle; its creation, evolution and destruction, *Tectonophysics*, *416*(1-4), 23–31. 1.1, 4.2

Helffrich, G. R., S. Stein, and B. J. Wood (1989), Subduction zone thermal structure and mineralogy and their relationship to seismic wave reflections and conversions at the Slab/Mantle interface, *Journal of Geophysical Research*, *94*(B1), 753–763, doi:10.1029/JB094iB01p00753. 4.7

Hilst, R. D. v. d., E. R. Engdahl, W. Spakman, and G. Nolet (1991), Tomographic imaging of subducted lithosphere below northwest pacific island arcs, *Nature*, *353*, 37–42. 4.2, 4.7

Hirose, K., N. Takafuji, N. Sata, and Y. Ohishi (2005), Phase transition and density of subducted MORB crust in the lower mantle, *Earth and Planetary Science Letters*, *237*(1-2), 239–251, doi:http://0-dx.doi.org.wam.leeds.ac.uk/10.1016/j.epsl.2005.06.035. 1.4, 5.4.4

Hofmann, A. W. (1997), Mantle geochemistry: the message from oceanic volcanism, *Nature*, *385*(6613), 219–229, doi:10.1038/385219a0. 1.1, 4.2

Hofmann, A. W., and S. R. Hart (1978), An assessment of local and regional isotopic equilibrium in the mantle, *Earth and Planetary Science Letters*, *38*(1), 44–62. 1.5

Honda, M., I. McDougall, D. B. Patterson, A. Doulgeris, and D. A. Clague (1991), Possible solar noble-gas component in hawaiian basalts, *, Published online: 10 January 1991; | doi:10.1038/349149a0*, *349*(6305), 149–151, doi:10.1038/349149a0. 1.3

Huang, J., and D. Zhao (2006), High-resolution mantle tomography of China and surrounding regions, *Journal of Geophysical Research*, *111*(B9), doi:10.1029/2005JB004066. 1.2, 1.4, 4.2, 4.1, 4.2, 4.7, 4.7, 4.7

Hutko, A. R., T. Lay, E. J. Garnero, and J. Revenaugh (2006), Seismic detection of folded, subducted lithosphere at the core-mantle boundary, *Nature*, *441*(7091), 333–336, doi:10.1038/nature04757. 2.5.3

Idehara, K., A. Yamada, and D. Zhao (2007), Seismological constraints on the ultralow velocity zones in the lowermost mantle from core-reflected waves, *Physics of the Earth and Planetary Interiors*, *165*(1-2), 25–46. 4.3.1

Irifune, T., and T. Tsuchiya (2007), Mineralogy of the Earth - phase transitions and mineralogy of the lower mantle, in *Treatise on Geophysics*, edited by G. Schubert, pp. 33–62, Elsevier, Amsterdam. 1.9, 4.2, 5.4.4

IRIS (2010), USArray, A continental-scale seismic obersevatory. 2010. transportable array. 1.2

Ishii, M., and J. Tromp (1999), Normal-mode and free-air gravity constraints on lateral variations in velocity and density of earth's mantle, *Science*, *285*(5431), 1231–1236, doi:10.1126/science.285.5431.1231, PMID: 10455043. 1.2

Jin, Z.-M., J. Zhang, H. W. Green, and S. Jin (2001), Eclogite rheology: Implications for subducted lithosphere, *Geology*, *29*(8), 667–670, doi:10.1130/0091-7613(2001)029¡0667:ERIFSL¿2.0.CO;2. 1.5, 5.4.4

Kaneshima, S. (2009), Seismic scatterers at the shallowest lower mantle beneath subducted slabs, *Earth and Planetary Science Letters*, *286*(1-2), 304–315, doi:10.1016/j.epsl.2009.06.044. 1.6, 4.2, 4.2

Kaneshima, S., and G. Helffrich (1999), Dipping low-velocity layer in the mid-lower mantle; evidence for geochemical heterogeneity, *Science*, *283*(5409), 1888–1891. 1.6, 2.3, 2.3, 4.2, 4.6.1, 4.7, 6

Kaneshima, S., and G. Helffrich (2009), Lower mantle scattering profiles and fabric below pacific subduction zones, *Earth and Planetary Science Letters [Earth Planet. Sci. Lett.]*, *282*(1), 234–239. 2.3, 2.3, 4.2, 4.6.1, 4.7, 6

Kárason, H., and R. D. van der Hilst (2001), Tomographic imaging of the lowermost mantle with differential times of refracted and diffracted core phases (pkp, pdiff), *Journal of Geophysical Research: Solid Earth (1978–2012)*, *106*(B4), 6569–6587. 1.2

Kato, M., and K. Hirahara (1991), Precursory arrivals to PP, *Geophysical Journal International*, *106*(3), 551–557, doi:10.1111/j.1365-246X.1991.tb06329.x. 2.3.1, 3.2, 4.3.2

Kawakatsu, H., and S. Watada (2007), Seismic evidence for deep-water transportation in the mantle, *Science*, *316*(5830), 1468–1471. 2.5.3

Kellogg, L. H., and D. L. Turcotte (1990), Mixing and the distribution of heterogeneities in a chaotically convecting mantle, *Journal of Geophysical Research: Solid Earth*, *95*(B1), 421432, doi:10.1029/JB095iB01p00421. 1.5

Kellogg, L. H., B. H. Hager, and R. D. van der Hilst (1999), Compositional stratification in the deep mantle, *Science*, *283*(5409), 1881–1884, doi:10.1126/science.283.5409.1881. 1.6, 1.4

Kennett, B. L. N., and E. R. Engdahl (1991), Traveltimes for global earthquake location and phase identification, *Geophysical Journal International*, *105*(2), 429–465, doi:10.1111/j.1365-246X.1991.tb06724.x. 1.2, 1.2, 3.4, 3.5, 3.5, 3.14

Kennett, B. L. N., E. R. Engdahl, and R. Buland (1995), Constraints on seismic velocities in the earth from traveltimes, *Geophysical Journal International*, *122*(1), 108–124, doi:10.1111/j.1365-246X.1995.tb03540.x. 1.2, 4.4.1, 4.12, 4.4.4

King, D. W., and J. R. Cleary (1974), A note on the interpretation of precursors to PKPPKP, *Bulletin of the Seismological Society of America*, *64*(3-1), 721–723. 2.3

King, D. W., R. A. W. Haddon, and E. S. Husebye (1975), Precursors to PP, *Physics of the Earth and Planetary Interiors*, *10*(2), 103127. 2.3.1, 2.4.2, 3.2, 4.3.2

King, D. W., E. S. Husebye, and R. A. W. Haddon (1976), Processing of seismic precursor data, *Physics of The Earth and Planetary Interiors*, *12*(2-3), 128–134, doi:10.1016/0031-9201(76)90042-X. 2.3.1, 2.5.2

Kito, T., A. Rietbrock, and C. Thomas (2007), Slowness-backazimuth weighted migration: A new array approach to a high-resolution image, *Geophysical Journal International*, *169*(3), 1201–1209, doi:10.1111/j.1365-246X.2007.03379.x. 2.3, 2.5.3

Kito, T., C. Thomas, A. Rietbrock, E. J. Garnero, S. E. J. Nippress, and A. E. Heath (2008), Seismic evidence for a sharp lithospheric base persisting to the lowermost mantle beneath the caribbean, *Geophysical Journal International*, *174*(3), 1019–1028, doi:10.1111/j.1365-246X.2008.03880.x. 2.3, 4.2, 4.6.1, 4.7

Koper, K. D., and M. Dombrovskaya (2005), Seismic properties of the inner core boundary from PKiKP/P amplitude ratios, *Earth and Planetary Science Letters*, *237*(3-4), 680–694. 4.3.1

Koper, K. D., J. M. Franks, and M. Dombrovskaya (2004), Evidence for small-scale heterogeneity in earth's inner core from a global study of PKiKP coda waves, *Earth and Planetary Science Letters*, *228*(34), 227–241, doi:10.1016/j.epsl.2004.10.027. 2.3

Korn, M. (1997), Modelling the teleseismic P coda envelope: depth dependent scattering and deterministic structure, *Physics of the Earth and Planetary Interiors*, *104*(13), 23–36, doi:10.1016/S0031-9201(97)00044-7. 2.4.2

Korn, M., and H. Sato (2005), Synthesis of plane vector wave envelopes in two-dimensional random elastic media based on the markov approximation and comparison with finite-difference simulations, *Geophysical Journal International*, *161*(3), 839848, doi:10.1111/j.1365-246X.2005.02624.x. 2.4.2

Krüger, F., M. Baumann, F. Scherbaum, and M. Weber (2001), Mid mantle scatterers near the mariana slab detected with a double array method, *Geophysical Research Letters*, *28*(4), 667, doi:10.1029/2000GL011570. 1.6, 4.2, 4.6.1

Kurz, M. D., W. J. Jenkins, and S. R. Hart (1982), Helium isotopic systematics of oceanic islands and mantle heterogeneity, *Nature*, *297*(5861), 43–47, doi:10.1038/297043a0. 1.3

Latham, G., M. Ewing, J. Dorman, F. Press, N. Toksoz, G. Sutton, R. Meissner, F. Duennebier, Y. Nakamura, R. Kovach, and M. Yates (1970), Seismic data from man-made impacts on the moon, *Science*, *170*(3958), 620–626, doi:10.1126/science.170.3958.620. 2.1

Lay, T. (1987), Analysis of near-source contributions to early p-wave coda for underground explosions. II. frequency dependence, *Bulletin of the Seismological Society of America*, *77*(4), 1252–1273. 2.5.3

Lay, T., and D. V. Helmberger (1983), The shear-wave velocity gradient at the base of the mantle, *Journal of Geophysical Research: Solid Earth*, *88*(B10), 81608170, doi:10.1029/JB088iB10p08160. 1.2

Le Bars, M., and A. Davaille (2004), Whole layer convection in a heterogeneous planetary mantle, *Journal of Geophysical Research: Solid Earth*, *109*(B3), doi:10.1029/2003JB002617. 1.4

Lee, C., and S. D. King (2011), Dynamic buckling of subducting slabs reconciles geological and geophysical observations, *Earth and Planetary Science Letters*, *312*(34), 360–370, doi:10.1016/j.epsl.2011.10.033. 4.7, 4.7

Lee, C. T. A., and W. P. Chen (2007), Possible density segregation of subducted oceanic lithosphere along a weak serpentinite layer and implications for compositional stratification of the earth's mantle, *Earth and Planetary Science Letters*, *255*(3-4), 357–366, doi:http://0-dx.doi.org.wam.leeds.ac.uk/10.1016/j.epsl.2006.12.022. 1.5, 5.4.4

Lindquist, K. G., I. M. Tibuleac, and R. A. Hansen (2007), A semiautomatic calibration method applied to a small-aperture alaskan seismic array, *Bulletin of the Seismological Society of America*, *97*(1B), 100–113. 4.3.1, 4.4.3

Long, M. D., and P. G. Silver (2008), The subduction zone flow field from seismic anisotropy: A global view, *Science*, *319*(5861), 315–318, doi:10.1126/science.1150809, PMID: 18202286. 4.7

Lynnes, C. S., and T. Lay (1989), Inversion of p coda for isotropic scatterers at the yucca flat test site, *Bulletin of the Seismological Society of America*, *79*(3), 790–804. 2.5.3

Ma, P., P. Wang, L. Tenorio, M. V. de Hoop, and R. D. van der Hilst (2007), Imaging of structure at and near the core-mantle boundary using a generalized radon transform: 2. statistical inference of singularities, *Journal of Geophysical Research*, *112*(B8), doi:10.1029/2006JB004513. 2.5.3

Manga, M. (1996), Mixing of heterogeneities in the mantle: Effect of viscosity differences, *Geophysical Research Letters*, *23*(4), 403406, doi:10.1029/96GL00242. 1.4, 1.5

Margerin, L., and G. Nolet (2003a), Multiple scattering of high-frequency seismic waves in the deep Earth: Modeling and numerical examples, *Journal of Geophysical Research: Solid Earth*, *108*(B5), doi:10.1029/2002JB001974. 2.4.2, 3.2

Margerin, L., and G. Nolet (2003b), Multiple scattering of high-frequency seismic waves in the deep earth; PKP precursor analysis and inversion for mantle granularity, *Journal of Geophysical Research*, *108*(B11), 16, doi:http://0-dx.doi.org.wam.leeds.ac.uk/10.1029/2003JB002455. 3.2, 3.8.2

Margerin, L., M. Campillo, and B. van Tiggelen (1998), Radiative transfer and diffusion of waves in a layered medium: new insight into coda q, *Geophysical Journal International*, *134*(2), 596612, doi:10.1111/j.1365-246X.1998.tb07142.x. 2.4.2

Margerin, L., M. Campillo, and B. Van Tiggelen (2000), Monte carlo simulation of multiple scattering of elastic waves, *Journal of Geophysical Research: Solid Earth*, *105*(B4), 78737892, doi:10.1029/1999JB900359. 2.4.2

MathWorks (2013), Least-Squares (Model Fitting) Algorithms (r2013b), Accessed online October 1, 2013 from `http://www.mathworks.co.uk/help/optim/ug/least-squares-model-fitting-algorithms.html`. 3.3.4

McNamara, A. K., and S. Zhong (2005), Thermochemical structures beneath africa and the pacific ocean, *Nature*, *437*(7062), 1136–1139, doi:10.1038/nature04066. 1.4, 1.5

McNamara, A. K., P. E. van Keken, and S.-I. Karato (2002), Development of anisotropic structure in the earth's lower mantle by solid-state convection, *Nature*, *416*(6878), 310–314, doi:10.1038/416310a. 4.7

McNamara, A. K., P. E. van Keken, and S.-i. Karato (2003), Development of finite strain in the convecting lower mantle and its implications for seismic anisotropy, *Journal of Geophysical Research*, *108*(B5), 14, doi:http://0-dx.doi.org.wam.leeds.ac.uk/10.1029/2002JB001970. 4.7

Miller, M. S., and F. Niu (2008), Bulldozing the coremantle boundary: Localized seismic scatterers beneath the caribbean sea, *Physics of the Earth and Planetary Interiors*, *170*(12), 89–94, doi:10.1016/j.pepi.2008.07.044. 4.7

Miller, M. S., B. L. N. Kennett, and V. G. Toy (2006), Spatial and temporal evolution of the subducting pacific plate structure along the western pacific margin, *Journal of Geophysical Research: Solid Earth*, *111*(B2), doi:10.1029/2005JB003705. 4.7, 4.28

Murakami, M., K. Hirose, K. Kawamura, N. Sata, and Y. Ohishi (2004), Post-perovskite phase transition in MgSiO3, *Science*, *304*(5672), 855–858, doi:10.1126/science.1095932, PMID: 15073323. 1.2

Nakanishi, I. (1990), High-frequency waves following PKP-C (sub DIFF) at distances greater than 155 degrees, *Geophysical Research Letters*, *17*(5), 639–642, doi:http://0-dx.doi.org.wam.leeds.ac.uk/10.1029/GL017i005p00639. 3.2

Neidell, N. S., and M. T. Tanner (1971), Semblance and other coherency measures for multichannel data, *Geophysics*, *36*(3), 482, doi:10.1190/1.1440186. 4.4.2

Niu, F., and L. Wen (2001), Strong seismic scatterers near the core-mantle boundary west of mexico, *Geophysical Research Letters*, *28*(18), 3557–3560, doi:http://0-dx.doi.org.wam.leeds.ac.uk/10.1029/2001GL013270. 3.2

Niu, F., H. Kawakatsu, and Y. Fukao (2003), Seismic evidence for a chemical heterogeneity in the midmantle: A strong and slightly dipping seismic reflector beneath the mariana subduction zone, *Journal of Geophysical Research: Solid Earth*, *108*(B9), doi:10.1029/2002JB002384. 4.7, 6

Obayashi, M., J. Yoshimitsu, and Y. Fukao (2009), Tearing of stagnant slab, *Science*, *324*(5931), 1173–1175. 4.7

Oganov, A. R., and S. Ono (2004), Theoretical and experimental evidence for a post-perovskite phase of MgSiO3 in earth's d|[prime]| layer, *Nature*, *430*(6998), 445–448, doi:10.1038/nature02701. 1.2

Olson, P., D. A. Yuen, and D. Balsiger (1984), Mixing of passive heterogeneities by mantle convection, *Journal of Geophysical Research: Solid Earth*, *89*(B1), 425–436, doi:10.1029/JB089iB01p00425. 1.5

Ono, S. (2008), Experimental constraints on the temperature profile in the lower mantle, *Physics of the Earth and Planetary Interiors*, *170*, 267–273. 1.3

Plank, T., and P. E. van Keken (2008), Geodynamics: The ups and downs of sediments, *Nature Geoscience*, *1*(1), 17–18, doi:10.1038/ngeo.2007.68. 1.7, 5.5

Poupinet, G., and B. Kennett (2004), On the observation of high frequency PKiKP and its coda in australia, *Physics of the Earth and Planetary Interiors*, *146*(34), 497–511, doi:10.1016/j.pepi.2004.05.003. 2.3

Quinteros, J., S. V. Sobolev, and A. A. Popov (2010), Viscosity in transition zone and lower mantle: Implications for slab penetration, *Geophysical Research Letters*, *37*, 5 PP., doi:201010.1029/2010GL043140. 4.2

Rapp, R. P., T. Irifune, N. Shimizu, N. Nishiyama, M. D. Norman, and T. Inoue (2008), Subduction recycling of continental sediments and the origin of geochemically enriched reservoirs in the deep mantle, *Earth and Planetary Science Letters*, *271*(1-4), 14–23, doi:10.1016/j.epsl.2008.02.028. 1.1, 4.2

Revenaugh, J., and T. Jordan (1991), Mantle layering from scs reverberations .2. the transition zone, *Journal of Geophysical Research-Solid Earth*, *96*(B12), 19,763–19,780, doi:10.1029/91JB01486. 3.2, 4.3.2

Richards, M., and D. Engebretson (1992), Large-scale mantle convection and the history of subduction, *Nature*, *355*(6359), 437–440, doi:10.1038/355437a0. 4.6.1

Ringwood, A. (1970), Phase transformations and the constitution of the mantle, *Physics of the Earth and Planetary Interiors*, *3*, 109–155, doi:10.1016/0031-9201(70)90047-6. 1.2

Ritsema, J., H. J. van Heijst, and J. H. Woodhouse (1999), Complex shear wave velocity structure imaged beneath africa and iceland, *Science*, *286*(5446), 1925–1928, doi:10.1126/science.286.5446.1925. 4.2

Ritsema, J., H. J. van Heijst, and J. H. Woodhouse (2004), Global transition zone tomography, *Journal of Geophysical Research: Solid Earth*, *109*(B2), doi:10.1029/2003JB002610. 1.2

Ritsema, J., A. Deuss, H. J. van Heijst, and J. H. Woodhouse (2011), S40RTS: a degree-40 shear-velocity model for the mantle from new rayleigh wave dispersion, teleseismic traveltime and normal-mode splitting function measurements, *Geophysical Journal International*, *184*(3), 1223–1236, doi:10.1111/j.1365-246X.2010.04884.x. 1.2, 4.2, 4.6.1, 4.23, 4.7, 4.26, 4.7, 5.3.2

Rost, S., and P. S. Earle (2010), Identifying regions of strong scattering at the core-mantle boundary from analysis of PKKP precursor energy, *Earth and Planetary Science Letters*, *297*(3-4), 616–626, doi:10.1016/j.epsl.2010.07.014. 2.3

Rost, S., and C. Thomas (2002), Array seismology: Methods and applications, *Reviews of Geophysics*, *40*(3), doi:10.1029/2000RG000100. 2.4.1, 2.5.1, 2.5.2, 2.5.3

Rost, S., and C. Thomas (2009), Improving seismic resolution through array processing techniques, *Surveys in Geophysics*, *30*(4-5), 271–299, doi:10.1007/s10712-009-9070-6. 2.5.1, 2.5.2, 2.5.2, 2.5.3, 2.16

Rost, S., and M. Weber (2001), A reflector at 200 km depth beneath the northwest pacific, *Geophysical Journal International*, *147*(1), 12–28, doi:10.1046/j.1365-246X.2001.00497.x. 3.8.1, 4.4.1

Rost, S., and M. Weber (2002), The upper mantle transition zone discontinuities in the pacific as determined by short-period array data, *Earth and Planetary Science Letters*, *204*(3-4), 347–361, doi:10.1016/S0012-821X(02)00999-8. 3.2, 4.3.2, 4.4.2

Rost, S., M. S. Thorne, and E. J. Garnero (2006), Imaging global seismic phase arrivals by stacking array processed Short-Period data, *Seismological Research Letters. Vol. 77*, *697*(6). 2.3.1, 2.10, 3.3.1, 4.3.2, 4.4.1

Rost, S., E. J. Garnero, and Q. Williams (2008), Seismic array detection of subducted oceanic crust in the lower mantle, *Journal of Geophysical Research*, *113*, B06,303, doi:10.1029/2007JB005263. 1.6, 2.3, 2.3.1, 3.2, 3.3.1, 4.2, 4.2, 4.3.1, 4.3.2, 4.4, 4.4.1, 4.6.1, 4.6.1, 4.7, 4.7, 4.7, 5.3.2, 5.4.4

Sato, H., and M. C. Fehler (1998), *Seismic wave propagation and scattering in the heterogeneous Earth*, Springer-Verlag, New York. 3.2, 3.4, 3.4, 3.4

Sato, H., M. C. Fehler, and T. Maeda (2012), *Seismic Wave Propagation and Scattering in the Heterogeneous Earth : Second Edition: Second Edition*, Springer. 2.2.1

Schellart, W. P. (2011), A subduction zone reference frame based on slab geometry and subduction partitioning of plate motion and trench migration, *Geophysical Research Letters*, *38*(16), doi:10.1029/2011GL048197. 4.7

Scherbaum, F., F. Kr\ger, and M. Weber (1997), Double beam imaging: Mapping lower mantle heterogeneities using combinations of source and receiver arrays, *J. geophys. Res*, *102*(B1), 507522. 2.5.3

Schilling, J.-G. (1973), Iceland mantle plume: Geochemical study of reykjanes ridge, *Nature*, *242*(5400), 565–571, doi:10.1038/242565a0. 1.3

Schmerr, N., and C. Thomas (2011), Subducted lithosphere beneath the kuriles from migration of PP precursors, *Earth and Planetary Science Letters*, *311*(1-2), 101–111, doi:10.1016/j.epsl.2011.09.002. 2.3

Seno, T., and S. Maruyama (1984), Paleogeographic reconstruction and origin of the philippine sea, *Tectonophysics*, *102*(1-4), 53–84, doi:10.1016/0040-1951(84)90008-8. 4.6.1, 4.26, 4.7

Shearer, P. (2007), 1.20 - Deep Earth Structure - seismic scattering in the deep earth, in *Treatise on Geophysics*, edited by G. Schubert, pp. 695–729, Elsevier, Amsterdam. 2.4, 2.8, 2.4.2, 2.11, 3.2, 3.3.1, 3.3.5, 3.4

Shearer, P. M. (1990), Seismic imaging of upper-mantle structure with new evidence for a 520-km discontinuity, *Nature*, *344*(6262), 121–126. 2.3.1, 4.3.2

Shearer, P. M. (1999), *Introduction to seismology*, 274 pp., Cambridge University Press. 2.2.1, 3, 3.3.2

Shearer, P. M., and P. S. Earle (2004), The global short-period wavefield modelled with a Monte Carlo seismic phonon method, *Geophysical Journal International*, *158*(3), 1103–1117, doi:10.1111/j.1365-246X.2004.02378.x. 2.3, 2.4.1, 2.4.2, 2.4.2, 3.1, 3.2, 3.2, 3.3.2, 3.3.4, 3.4, 3.4, 3.13, 3.5, 3.6, 3.6, 3.6.1, 3.1, 3.16, 3, 5, 3.8.2, 5.3.1, 5.1, 5.4.4

Shearer, P. M., and P. S. Earle (2008), Observing and modeling elastic scattering in the deep earth, *Advances in Geophysics*, *50*(Chapter 6), 167–193. 2.4.1, 2.4.2, 3.4

Shearer, P. M., and T. G. Masters (1992), Global mapping of topography on the 660-km discontinuity, *Nature*, *355*(6363), 791–796. 3.8.1

Sheriff, R. E., and L. P. Geldart (1995), *Exploration seismology*, Cambridge University Press. 2.5.3

Shirey, S. B., and R. J. Walker (1998), The re-os isotope system in cosmochemistry and high-temperature geochemistry, *Annual Review of Earth and Planetary Sciences*, *26*, 423–500, doi:10.1146/annurev.earth.26.1.423. 1.3

Silver, P. G., R. W. Carlson, and P. Olson (1988), Deep slabs, geochemical heterogeneity, and the large-scale structure of mantle convection: Investigation of an enduring paradox, *Annual Review of Earth and Planetary Sciences*, *16*(1), 477–541, doi:10.1146/annurev.ea.16.050188.002401. 1.1, 1.3

Simmons, N. A., A. M. Forte, and S. P. Grand (2006), Constraining mantle flow with seismic and geodynamic data: A joint approach, *Earth and Planetary Science Letters*, *246*(1-2), 109–124, doi:10.1016/j.epsl.2006.04.003. 1.3

Spence, D. A., J. R. Ockendon, P. Wilmott, D. L. Turcotte, and L. H. Kellogg (1988), Convective mixing in the mantle: The role of viscosity differences, *Geophysical Journal International*, *95*(1), 79–86, doi:10.1111/j.1365-246X.1988.tb00452.x. 1.5, 1.5, 5.4.2

Stegman, D., R. Farrington, F. Capitanio, and W. Schellart (2010), A regime diagram for subduction styles from 3-d numerical models of free subduction, *Tectonophysics*, *483*(1-2), 29–45, doi:10.1016/j.tecto.2009.08.041. 4.7

Stein, S., and M. Wysession (2003), *An introduction to seismology, earthquakes and Earth structure*, Blackwell Publishing Ltd. 2.2.1, 2.3, 2.5.3, 3.3.4

Stixrude, L., and C. Lithgow-Bertelloni (2012), Geophysics of chemical heterogeneity in the mantle, *Annual Review of Earth and Planetary Sciences*, *40*(1), 569–595, doi:10.1146/annurev.earth.36.031207.124244. 1.5, 1.5, 1.8, 1.5, 1.10, 4.7, 5.4.2, 5.2, 5.4.2

Sugioka, H., D. Suetsugu, M. Obayashi, Y. Fukao, and G. Yuan (2010), Fast p- and s-wave velocities associated with the "cold" stagnant slab beneath the northern philippine sea, *Physics of the Earth and Planetary Interiors*, *179*(1-2), 1–6. 1.2

Tackley, P. J. (1998), Three-dimensional simulations of mantle convection with a thermo-chemical basal boundary layer; D"?, *Geodynamics Series*, *28*, 231–253. 1.4, 1.6

Tackley, P. J. (2000), Mantle convection and plate tectonics: Toward an integrated physical and chemical theory, *Science*, *288*(5473), 2002–2007, doi:10.1126/science.288.5473.2002. 1.6, 4.2

Tackley, P. J., D. J. Stevenson, G. A. Glatzmaier, and G. Schubert (1993), Effects of an endothermic phase transition at 670 km depth in a spherical model of convection in the earth's mantle, *Nature*, *361*, 699–704, doi:10.1038/361699a0. 1.3

Tackley, P. J., D. J. Stevenson, G. A. Glatzmaier, and G. Schubert (1994), Effects of multiple phase transitions in a three-dimensional spherical model of convection in earth's mantle, *Journal of Geophysical Research*, *99*(B8), 15,877, doi:199410.1029/94JB00853. 1.3

Thomas, C., M. Weber, C. W. Wicks, and F. Scherbaum (1999), Small scatterers in the lower mantle observed at german broadband arrays, *Journal of Geophysical Research: Solid Earth*, *104*(B7), 15,07315,088, doi:10.1029/1999JB900128. 2.5.3

Thomas, C., H. Igel, M. Weber, and F. Scherbaum (2000), Acoustic simulation of p-wave propagation in a heterogeneous spherical earth: numerical method and application to precursor waves to PKPdf, *Geophysical Journal International*, *141*(2), 307320, doi:10.1046/j.1365-246x.2000.00079.x. 2.4.2

Thomas, C., J.-M. Kendall, and J. Lowman (2004), Lower-mantle seismic discontinuities and the thermal morphology of subducted slabs, *Earth and Planetary Science Letters*, *225*(12), 105–113, doi:10.1016/j.epsl.2004.05.038. 2.5.3

Thorne, M. S., E. J. Garnero, and S. P. Grand (2004), Geographic correlation between hot spots and deep mantle lateral shear-wave velocity gradients, *Physics of the Earth and Planetary Interiors*, *146*(1-2), 47–63, doi:10.1016/j.pepi.2003.09.026. 4.6.1

Thorne, M. S., H. P. Crotwell, G. Jahnke, and H. Igel (2013), Animations of seismic wave propagation, Accessed online September 21, 2013 from `http://web.utah.edu/thorne/animations.html`. 2.1

Tkalcic, H., M. P. Flanagan, and V. F. Cormier (2006), Observation of near-podal P'P' precursors; evidence for back scattering from the 150-220 km zone in the earth's upper mantle, *Geophysical Research Letters*, *33*(3), 4, doi:http://0-dx.doi.org.wam.leeds.ac.uk/10.1029/2005GL024626. 3.2

Tono, Y., and K. Yomogida (1996), Complex scattering at the core-mantle boundary observed in short-period diffracted P-waves., *Journal of Physics of the Earth*, *44*(6), 729–744. 2.3, 3.2

Trampert, J., F. Deschamps, J. Resovsky, and D. Yuen (2004), Probabilistic tomography maps chemical heterogeneities throughout the lower mantle, *Science*, *306*(5697), 853–856, doi:10.1126/science.1101996. 1.2

van der Hilst, R., and T. Seno (1993), Effects of relative plate motion on the deep structure and penetration depth of slabs below the Izu-Bonin and mariana island arcs, *Earth and Planetary Science Letters*, *120*(3-4), 395–407. 1.2, 4.2, 4.7

van der Hilst, R. D., S. Widiyantoro, and E. R. Engdahl (1997), Evidence for deep mantle circulation from global tomography, *Nature*, *386*(6625), 578–584, doi:10.1038/386578a0. 1.2, 1.5

van der Hilst, R. D., H. Karason, and S. D. c. Malone (1999), The nature of the lower mantle; toward a hybrid convection model, *Seismological Research Letters*, *70*(2), 239. 4.2

Van der Hilst, R. D., M. V. De Hoop, P. Wang, S. H. Shim, P. Ma, and L. Tenorio (2007), Seismostratigraphy and thermal structure of earth's core-mantle boundary region, *science*, *315*(5820), 1813. 2.5.3

van Keken, P. E., S. Karato, and D. A. Yuen (1996), Rheological control of oceanic crust separation in the transition zone, *Geophysical Research Letters*, *23*(14), 18211824, doi:10.1029/96GL01594. 1.5, 5.4.4

van Keken, P. E., E. H. Hauri, and C. J. Ballentine (2002), MANTLE MIXING: the generation, preservation, and destruction of chemical heterogeneity, *Annual Review of Earth and Planetary Sciences*, *30*(1), 493–525, doi:10.1146/annurev.earth.30.091201.141236. 1.1, 1.4, 4.2, 4.7

Vanacore, E., F. Niu, and H. Kawakatsu (2006), Observations of the mid-mantle discontinuity beneath indonesia from S to P converted waveforms, *Geophysical Research Letters*, *33*(4), doi:10.1029/2005GL025106. 4.7

Vidale, J. E., and P. S. Earle (2000), Fine-scale heterogeneity in the earth's inner core, *Nature*, *404*(6775), 273–275, doi:10.1038/35005059. 2.3

Vinnik, L. (1981), Evaluation of the effective cross-section of scattering in the lithosphere, *Physics of the Earth and Planetary Interiors*, *26*(4), 268–284, doi:10.1016/0031-9201(81)90033-9. 2.3

Wagner, G. S., and C. A. Langston (1992), A numerical investigation of scattering effects for teleseismic plane wave propagation in a heterogeneous layer over a homogeneous half-space, *Geophysical Journal International*, *110*(3), 486500, doi:10.1111/j.1365-246X.1992.tb02087.x. 2.4.2

Wang, P., M. V. de Hoop, R. D. van der Hilst, P. Ma, and L. Tenorio (2006), Imaging of structure at and near the core mantle boundary using a generalized radon transform: 1. construction of image gathers, *Journal of Geophysical Research*, *111*(B12), doi:10.1029/2005JB004241. 2.5.3

Warren, L. M., and P. M. Shearer (2000), Investigating the frequency dependence of mantle q by stacking p and PP spectra, *Journal of Geophysical Research*, *105*(B11), 25,391–25,402, doi:http://0-dx.doi.org.wam.leeds.ac.uk/10.1029/2000JB900283. 3.5, 3.14, 3.6.1, 6.1

Weber, M., and C. W. Wicks (1996), Reflections from a distant subduction zone, *Geophysical Research Letters*, *23*(12), 1453, doi:10.1029/96GL01322. 1.6, 2.3, 2.3, 2.3.1, 3.2, 4.2, 4.3.2

Wen, L., and D. L. Anderson (1995), The fate of slabs inferred from seismic tomography and 130 million years of subduction, *Earth and Planetary Science Letters*, *133*(1-2), 185–198, doi:10.1016/0012-821X(95)00064-J. 1.2, 4.6.1

Wesley, J. P. (1965), Diffusion of seismic energy in the near range, *Journal of Geophysical Research*, *70*(20), 50995106, doi:10.1029/JZ070i020p05099. 2.4.2

Widiyantoro, S., B. L. N. Kennett, and R. D. van der Hilst (1999), Seismic tomography with p and s data reveals lateral variations in the rigidity of deep slabs, *Earth and Planetary Science Letters*, *173*(1-2), 91–100, doi:10.1016/S0012-821X(99)00216-2. 1.2, 4.7

Wolfe, C. J., S. C. Solomon, G. Laske, J. A. Collins, R. S. Detrick, J. A. Orcutt, D. Bercovici, and E. H. Hauri (2009), Mantle shear-wave velocity structure beneath the hawaiian hot spot, *Science*, *326*(5958), 1388–1390, doi:10.1126/science.1180165. 4.7

Wookey, J., J.-M. Kendall, and G. Barruol (2002), Mid-mantle deformation inferred from seismic anisotropy, *Nature*, *415*(6873), 777–780, doi:10.1038/415777a. 4.7

Wortel, M. J. R., and W. Spakman (2000), Subduction and slab detachment in the mediterranean-carpathian region, *Science*, *290*(5498), 1910–1917, doi:10.1126/science.290.5498.1910, PMID: 11110653. 1.2

Wright, C. (1972), Array studies of seismic waves arriving between p and PP in the distance range 90degrees to 115degrees, *Bulletin of the Seismological Society of America*, *62*(1), 385–400. 2.3.1, 3.3.1, 4.3.2

Wu, R., and K. Aki (1985), Scattering characteristics of elastic waves by an elastic heterogeneity, *Geophysics*, *50*(4), 582–595, doi:http://0-dx.doi.org.wam.leeds.ac.uk/10.1190/1.1441934. 2.2.1, 3.4

Wu, R., and K. Aki (1988), Introduction: Seismic wave scattering in three-dimensionally heterogeneous earth, *Pure and Applied Geophysics PAGEOPH*, *128*(1-2), 1–6, doi:10.1007/BF01772587. 2.2.1, 2.4.2

Wu, R.-S. (1985), Multiple scattering and energy transfer of seismic waves separation of scattering effect from intrinsic attenuation i. theoretical modelling, *Geophysical Journal International*, *82*(1), 57–80, doi:10.1111/j.1365-246X.1985.tb05128.x. 2.4.2, 3.4

Yilmaz, . (2001), *Seismic Data Analysis: Processing, Inversion, and Interpretation of Seismic Data*, SEG Books. 2.5.3, 2.5.3

Zhao, D. (2004), Global tomographic images of mantle plumes and subducting slabs: insight into deep earth dynamics, *Physics of The Earth and Planetary Interiors*, *146*(1-2), 3–34, doi:10.1016/j.pepi.2003.07.032. 1.2

Zhao, D., and E. Ohtani (2009), Deep slab subduction and dehydration and their geodynamic consequences; evidence from seismology and mineral physics, *Gondwana Research*, *16*(3-4), 401–413. 1.4, 4.1, 4.2

Appendix A

Global stack data periods

Network	Code	Start	Finish
Canadian National Network	CNN	01/01/2007	31/8/2012
Global Seismic Network	GAN	01/01/2004	31/08/2012
POLARIS	POL	02/05/2005	19/03/2009
USArray Temporary Array	TA	01/01/2004	27/12/2006
Canadian Northwest Experiment	ZN	01/01/2003	31/12/2005

Table A.1: Time periods in which data were downloaded for the networks and arrays used for global stacks of *PP*.

Appendix B

Summary of model parameters

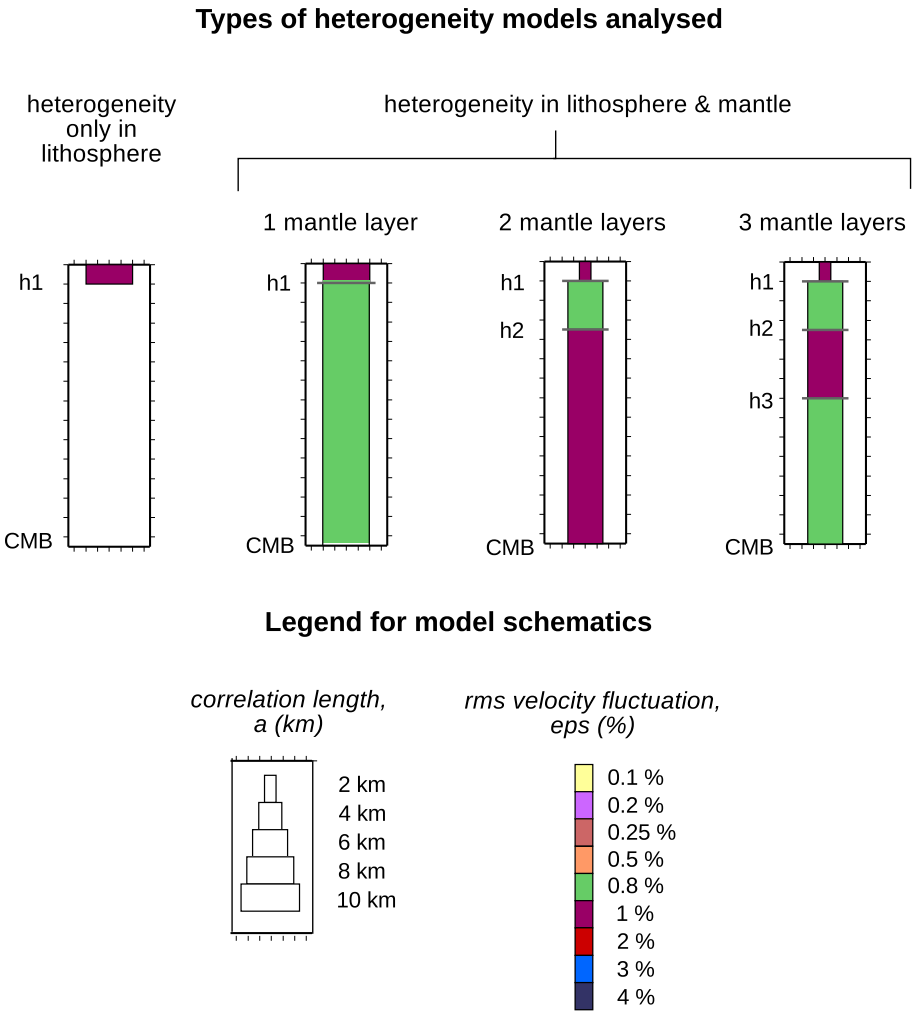

Figure B.1: Schematic depicting the types of models considered in this study and legend for model schematics showing correlation length, a and rms velocity fluctuation, ϵ (or eps).

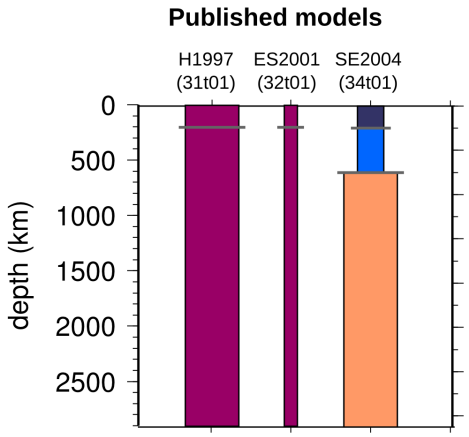

Figure B.2: Summary of model parameters from published models.

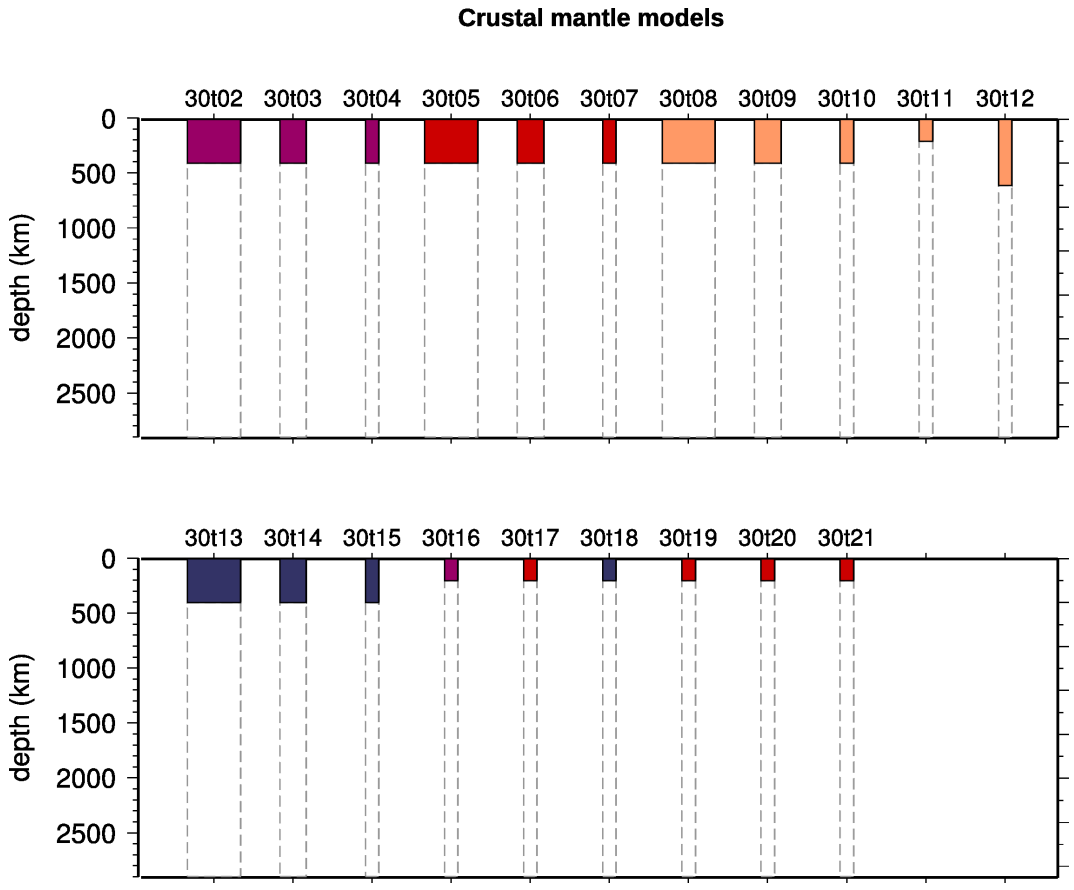

Figure B.3: Summary of model parameters from lithospheric heterogeneity models.

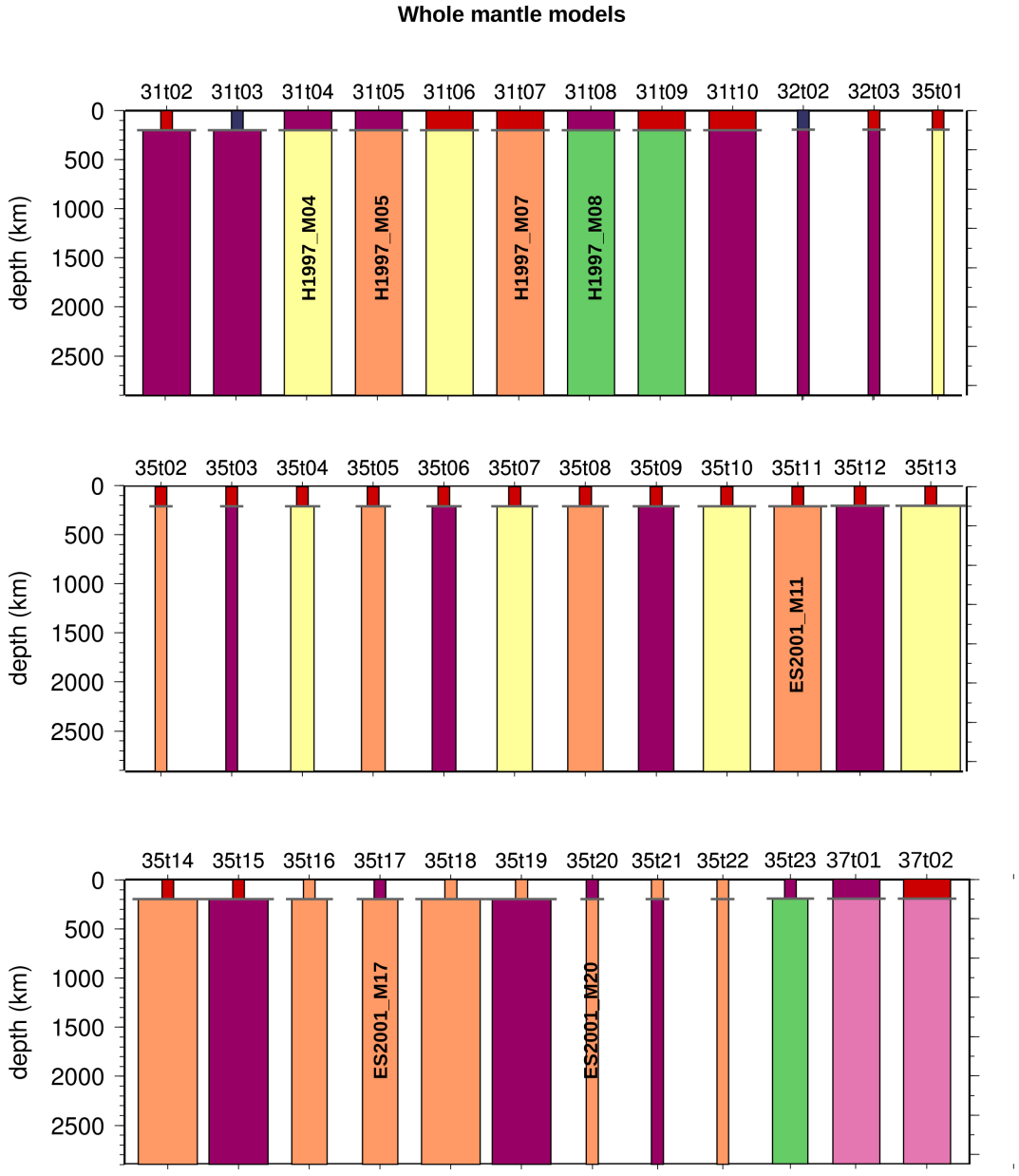

Figure B.4: Summary of model parameters from whole mantle heterogeneity models.

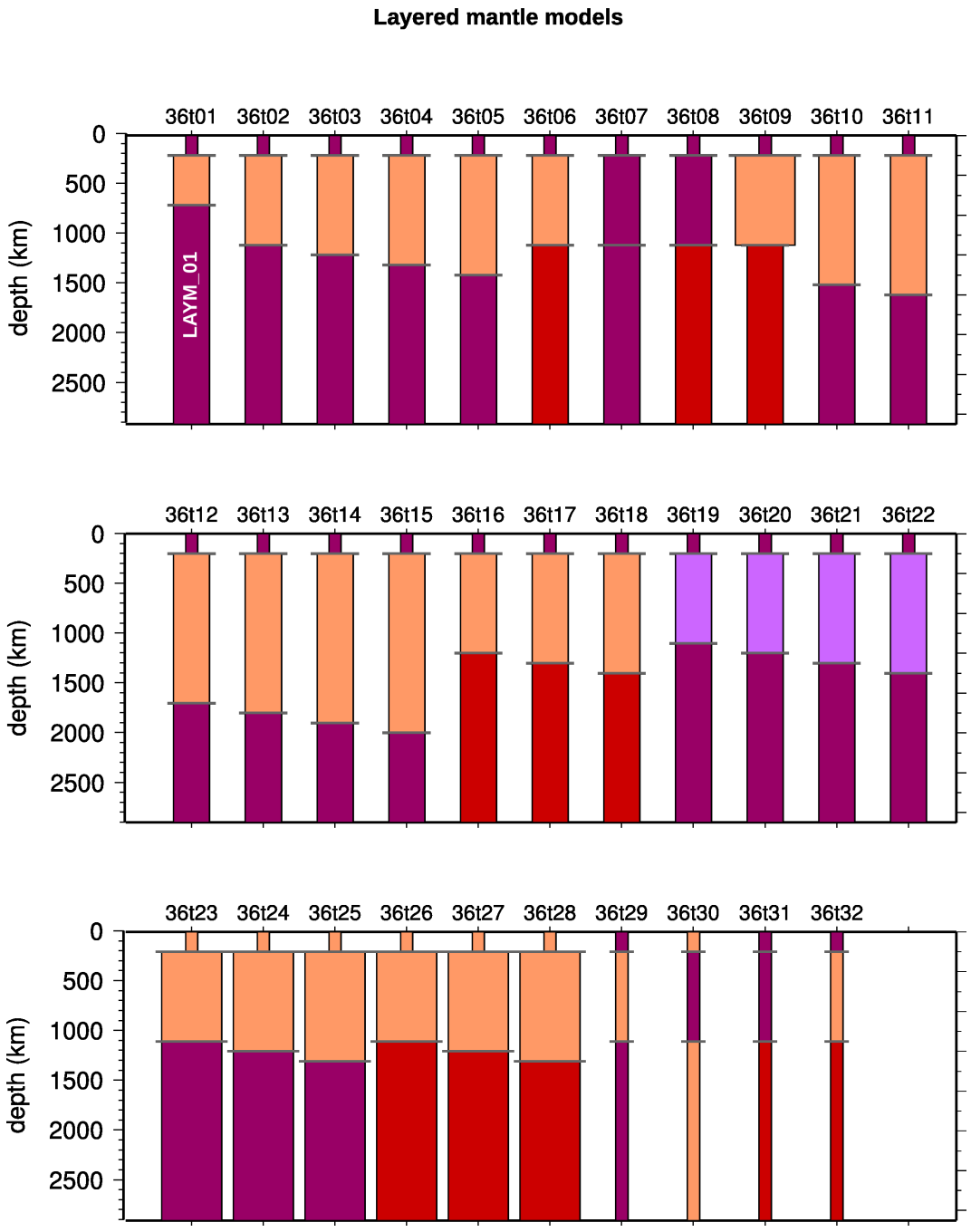

Figure B.5: Summary of model parameters from layered mantle heterogeneity models (1 of 2).

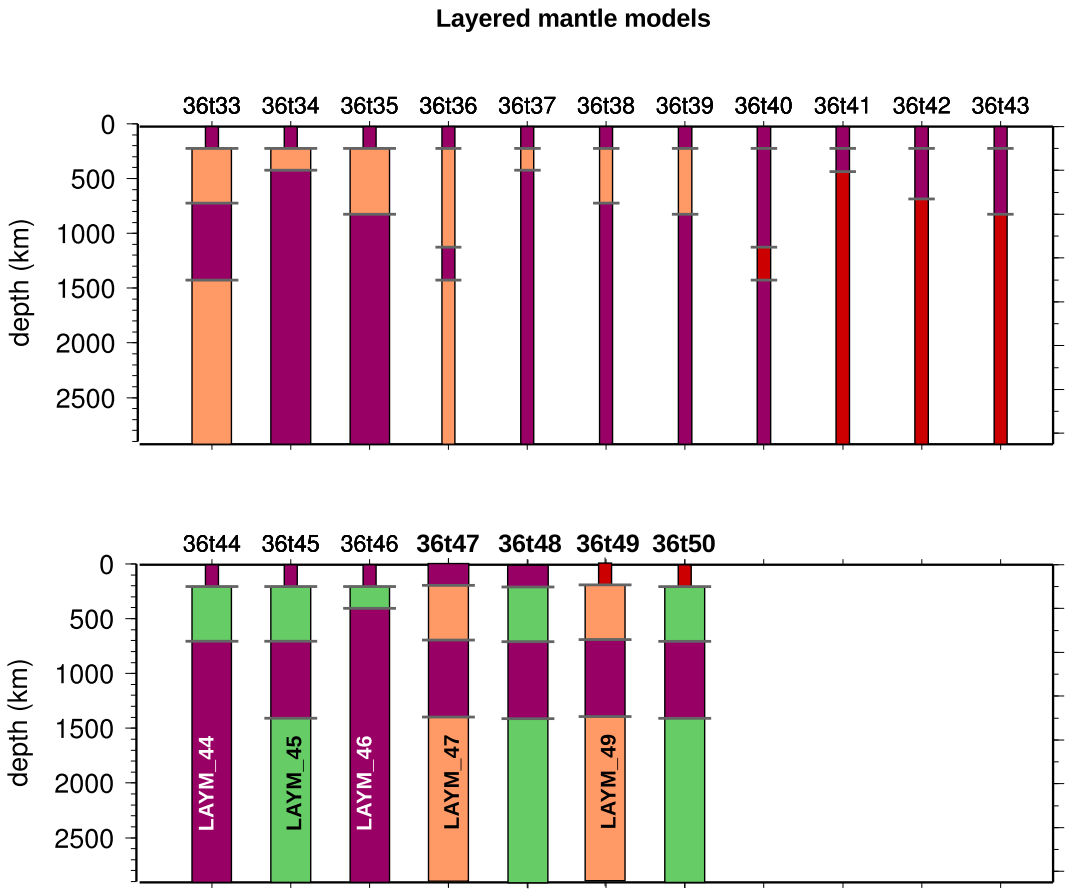

Figure B.6: Summary of model parameters from layered mantle heterogeneity models (2 of 2).

Appendix C

Comparison of model synthetics to data

C.1 Crustal models

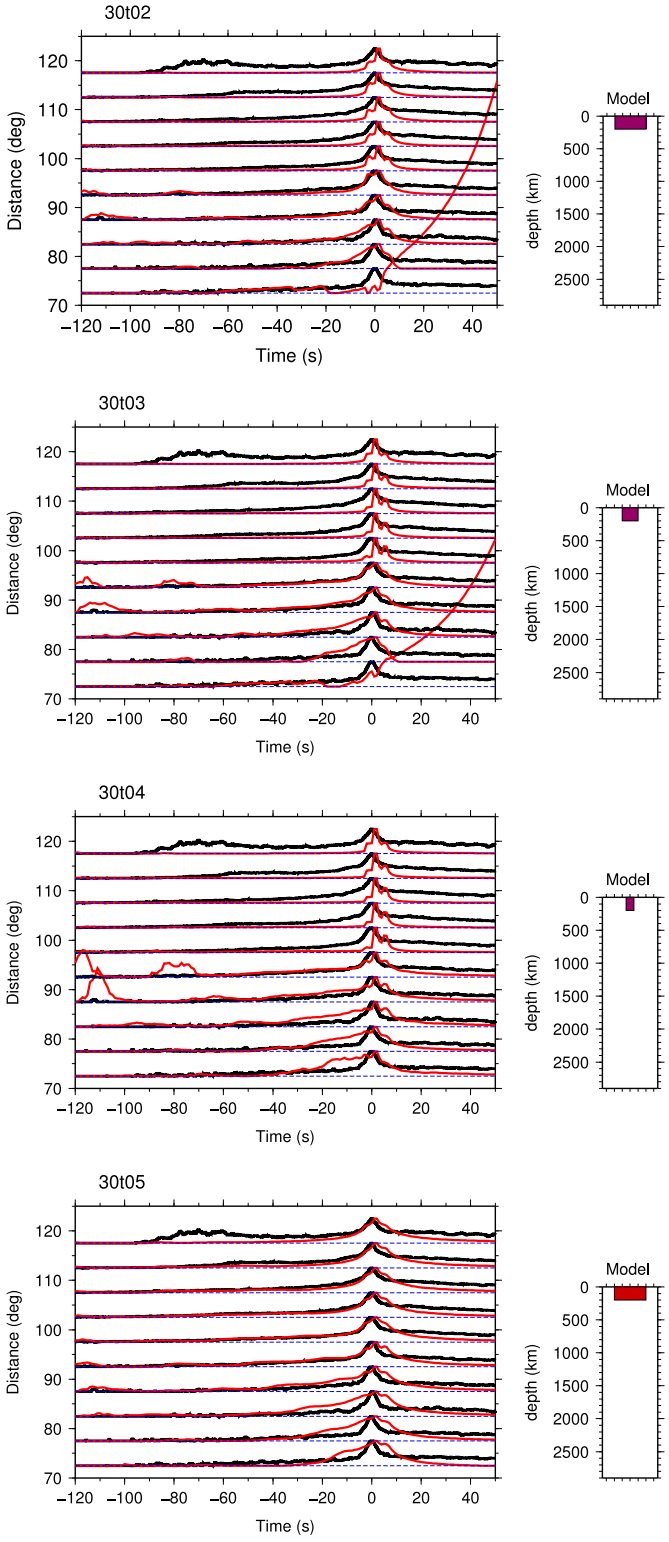

Figure C.1: Synthetic seismograms (red) generated with lithospheric heterogeneity models (right) compared to global stack data (black). *P* coda is removed for each seismogram prior to stacking in 5° distance bins.

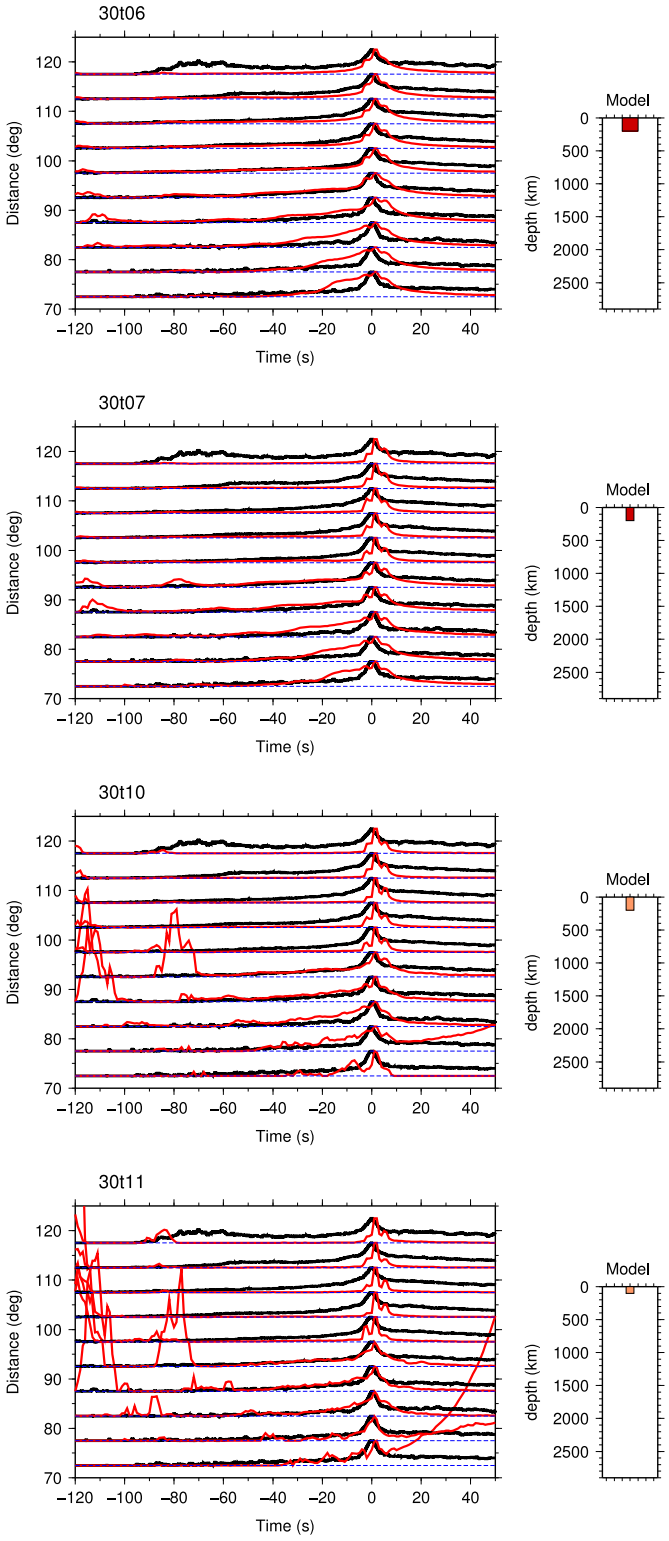

Figure C.2: Synthetic seismograms (red) generated with lithospheric heterogeneity models (right) compared to global stack data (black). *P* coda is removed for each seismogram prior to stacking in 5° distance bins.

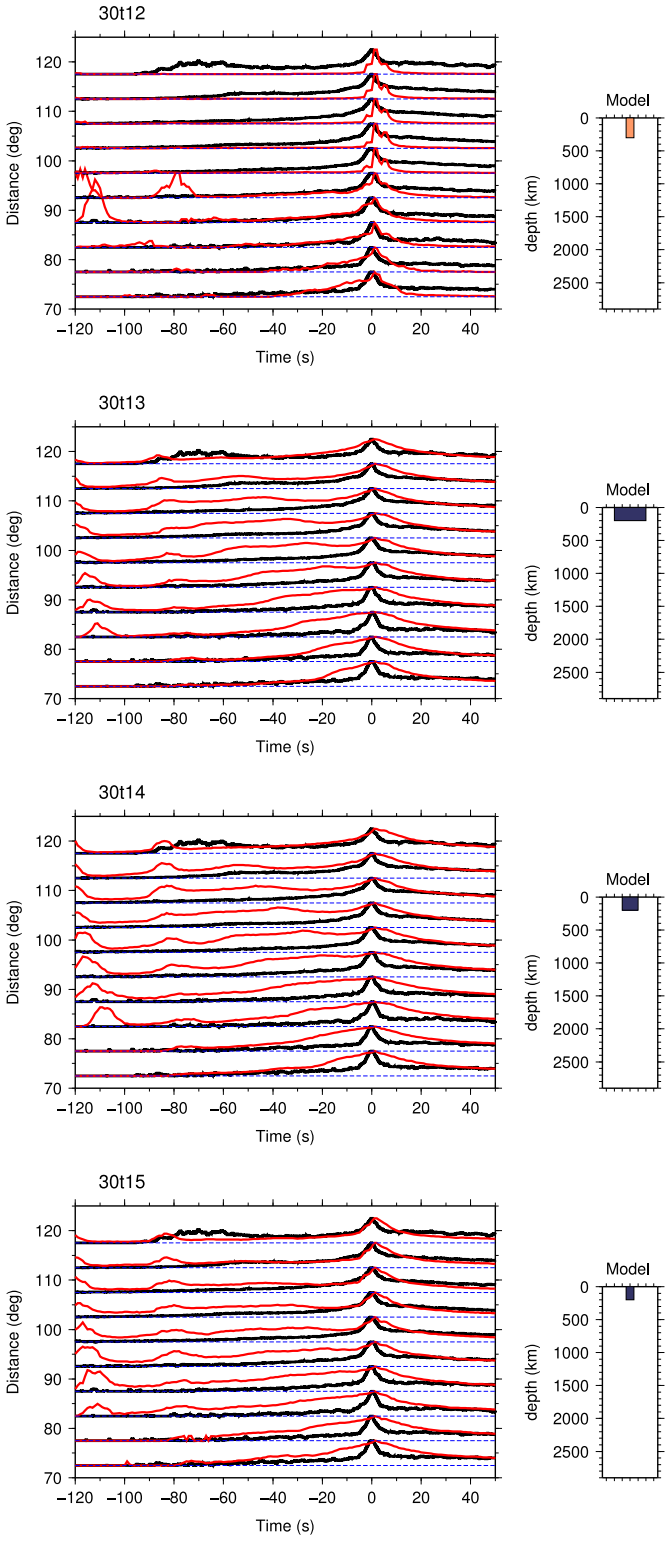

Figure C.3: Synthetic seismograms (red) generated with lithospheric heterogeneity models (right) compared to global stack data (black). *P* coda is removed for each seismogram prior to stacking in 5° distance bins.

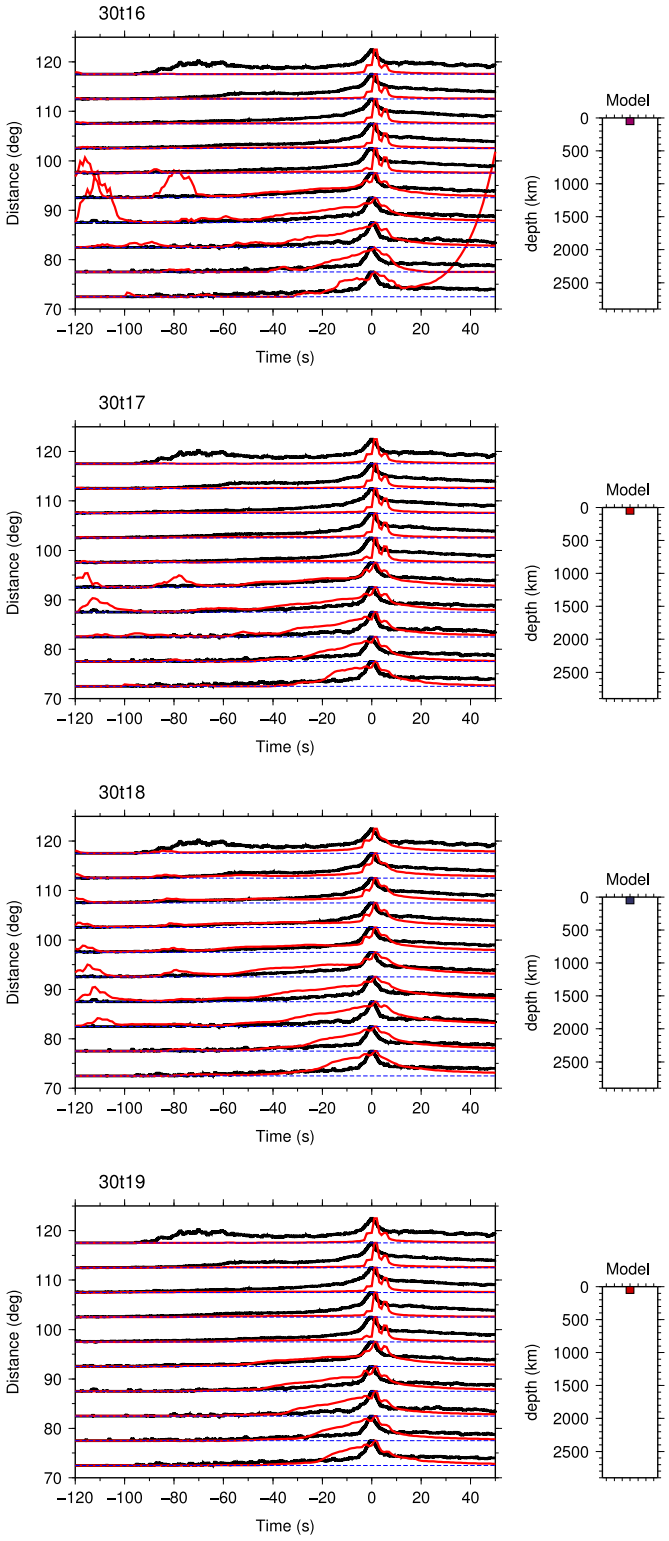

Figure C.4: Synthetic seismograms (red) generated with lithospheric heterogeneity models (right) compared to global stack data (black). *P* coda is removed for each seismogram prior to stacking in 5° distance bins.

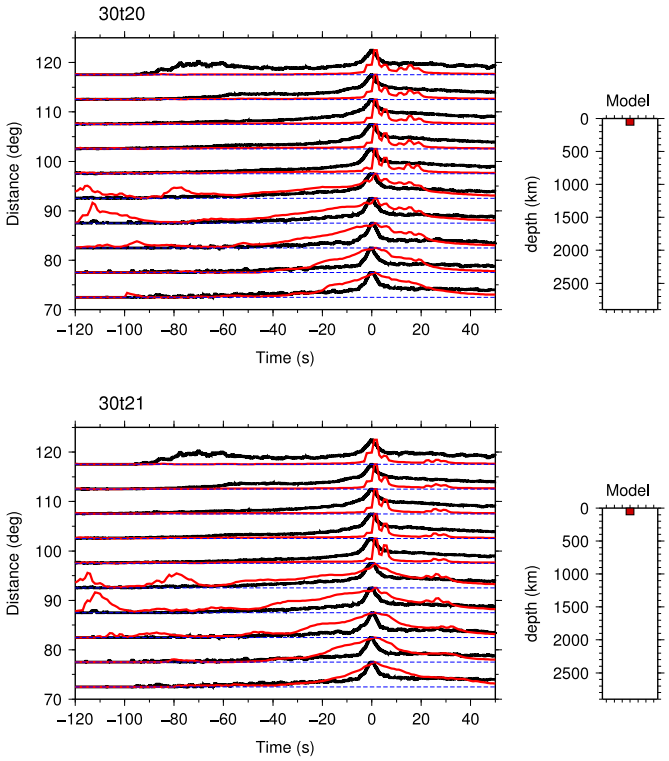

Figure C.5: Synthetic seismograms (red) generated with lithospheric heterogeneity models (right) compared to global stack data (black). *P* coda is removed for each seismogram prior to stacking in 5° distance bins.

C.2 Whole mantle models

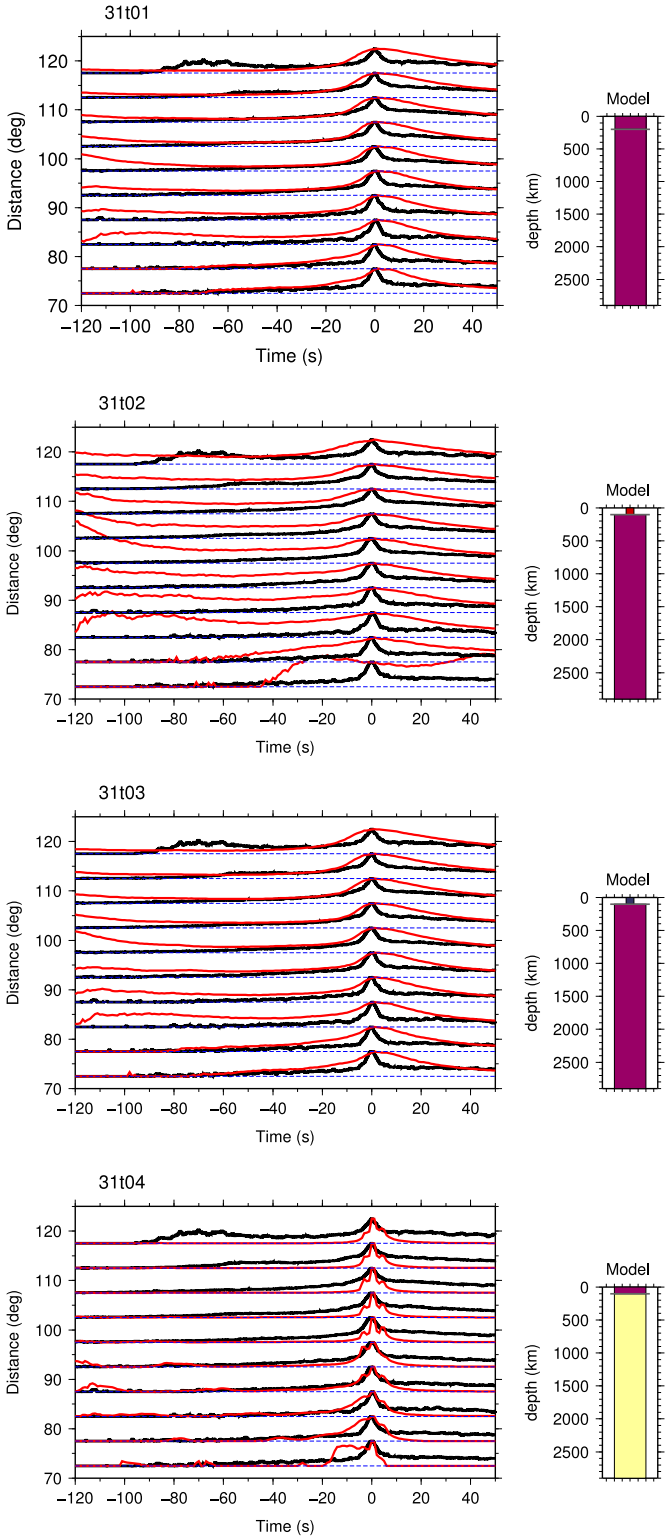

Figure C.6: Synthetic seismograms (red) generated with whole mantle heterogeneity models (right) compared to global stack data (black). *P* coda is removed for each seismogram prior to stacking in 5° distance bins.

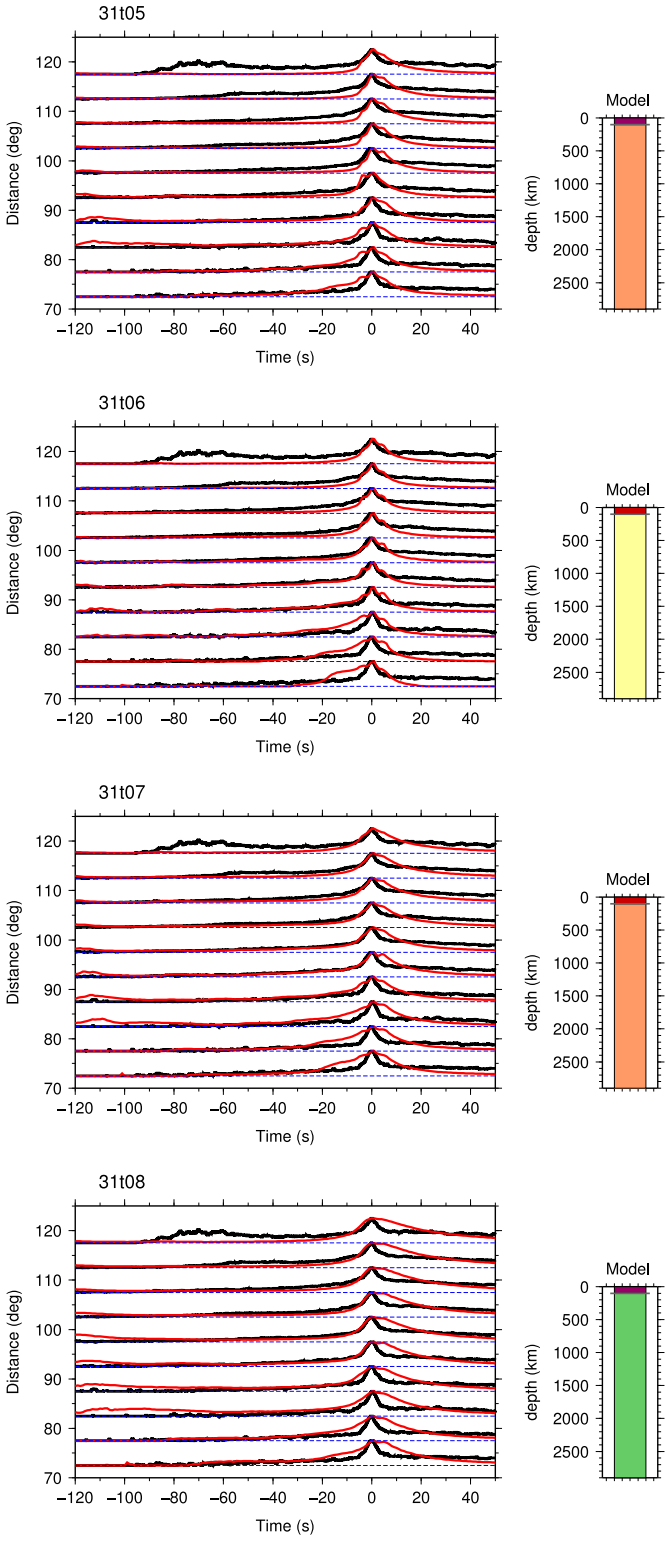

Figure C.7: Synthetic seismograms (red) generated with whole mantle heterogeneity models (right) compared to global stack data (black). *P* coda is removed for each seismogram prior to stacking in 5° distance bins.

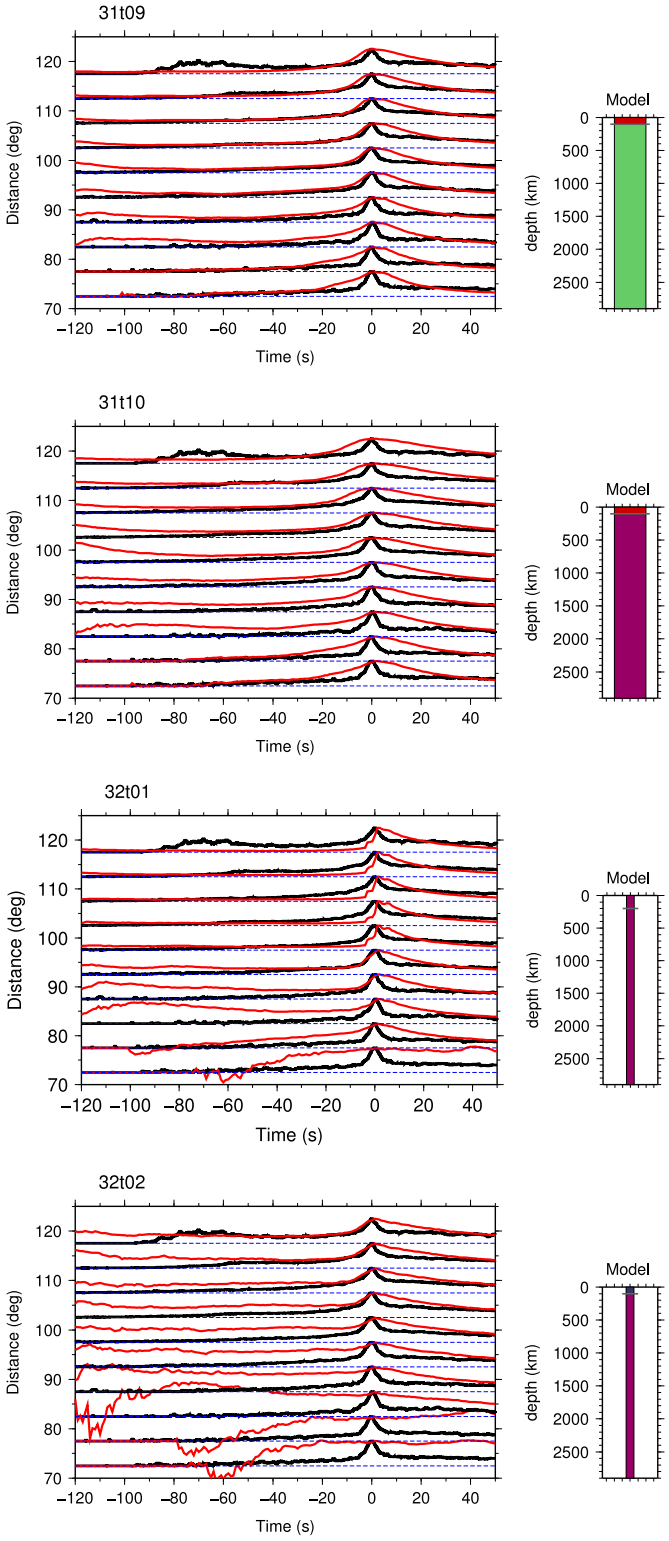

Figure C.8: Synthetic seismograms (red) generated with whole mantle heterogeneity models (right) compared to global stack data (black). *P* coda is removed for each seismogram prior to stacking in 5° distance bins.

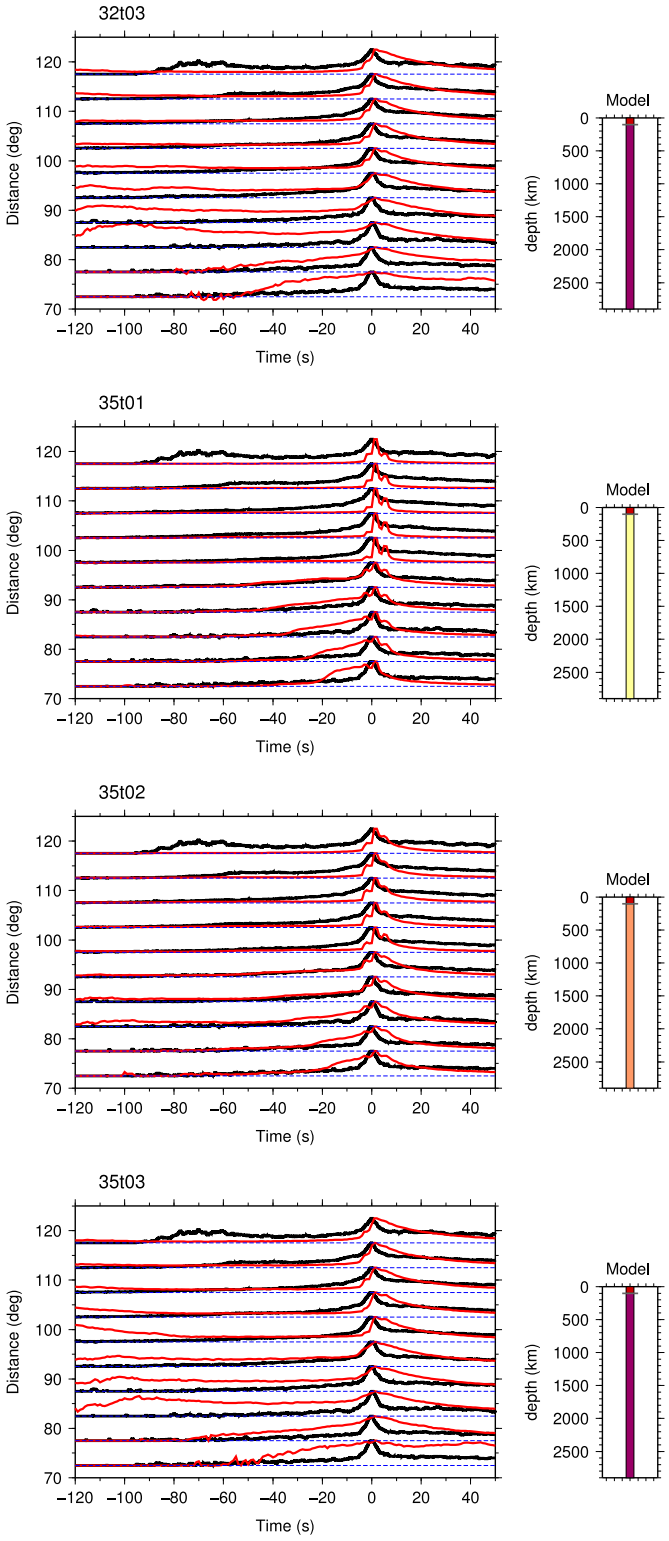

Figure C.9: Synthetic seismograms (red) generated with whole mantle heterogeneity models (right) compared to global stack data (black). *P* coda is removed for each seismogram prior to stacking in 5° distance bins.

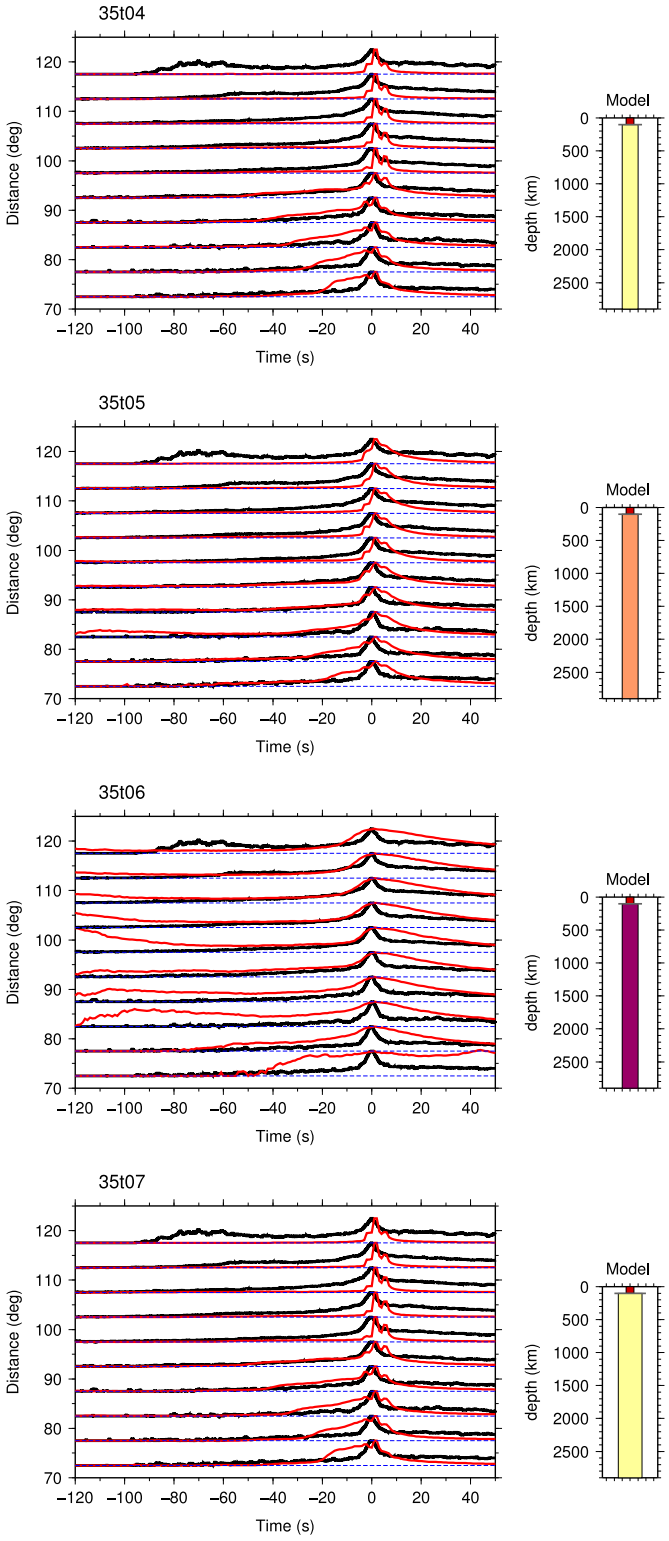

Figure C.10: Synthetic seismograms (red) generated with whole mantle heterogeneity models (right) compared to global stack data (black). *P* coda is removed for each seismogram prior to stacking in 5° distance bins.

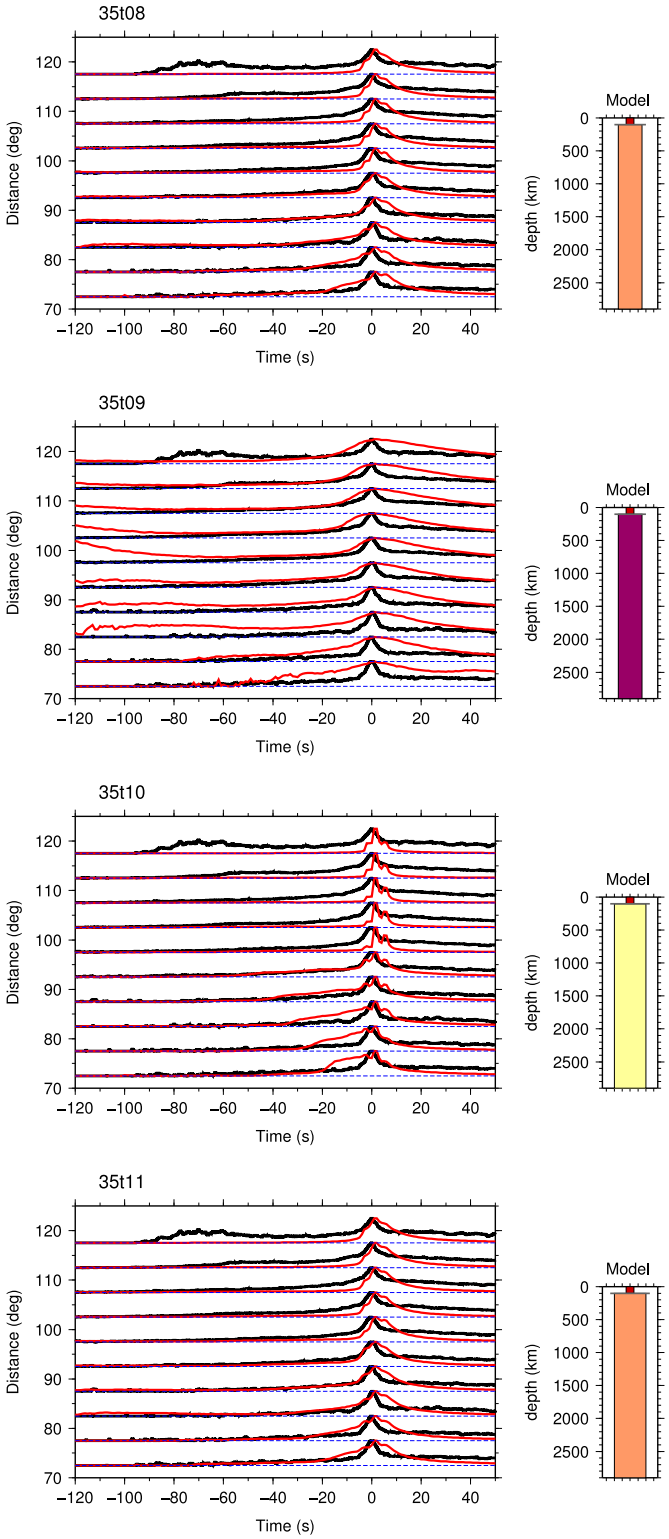

Figure C.11: Synthetic seismograms (red) generated with whole mantle heterogeneity models (right) compared to global stack data (black). *P* coda is removed for each seismogram prior to stacking in 5° distance bins.

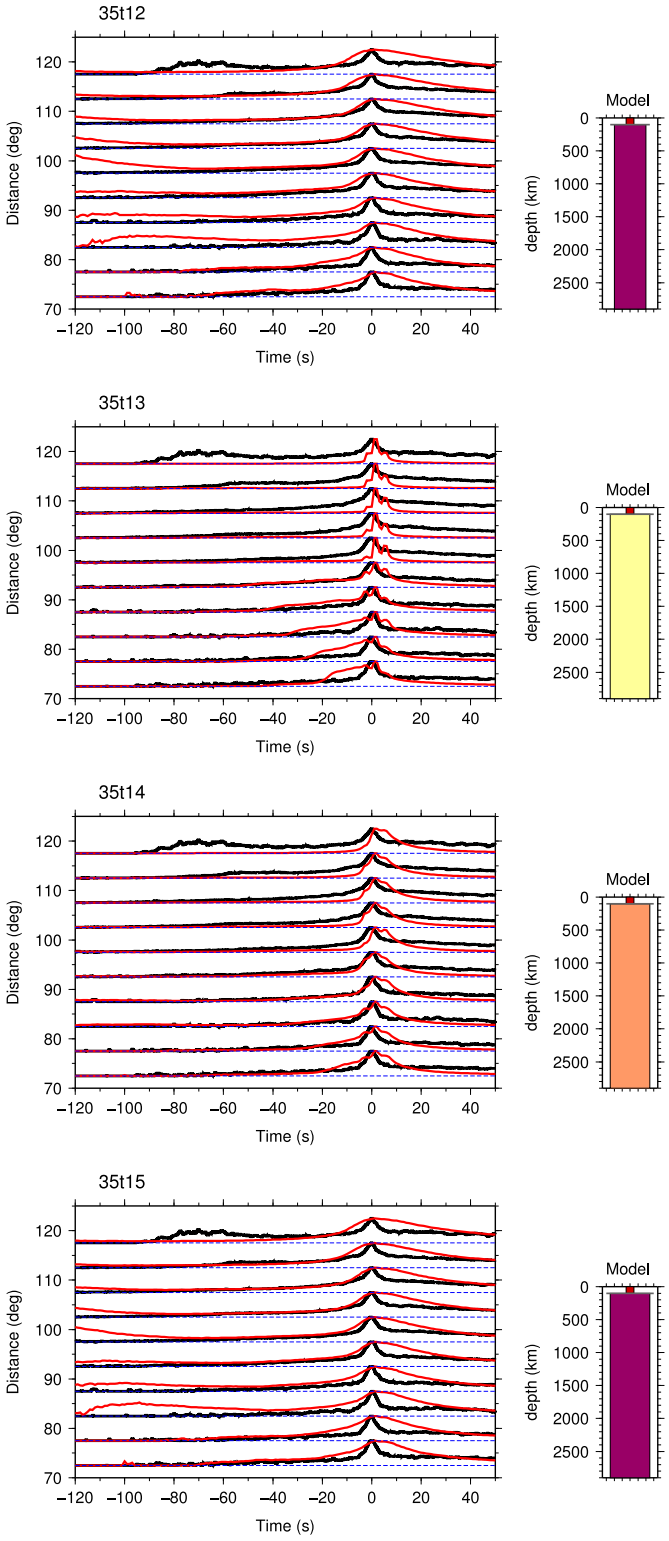

Figure C.12: Synthetic seismograms (red) generated with whole mantle heterogeneity models (right) compared to global stack data (black). *P* coda is removed for each seismogram prior to stacking in 5° distance bins.

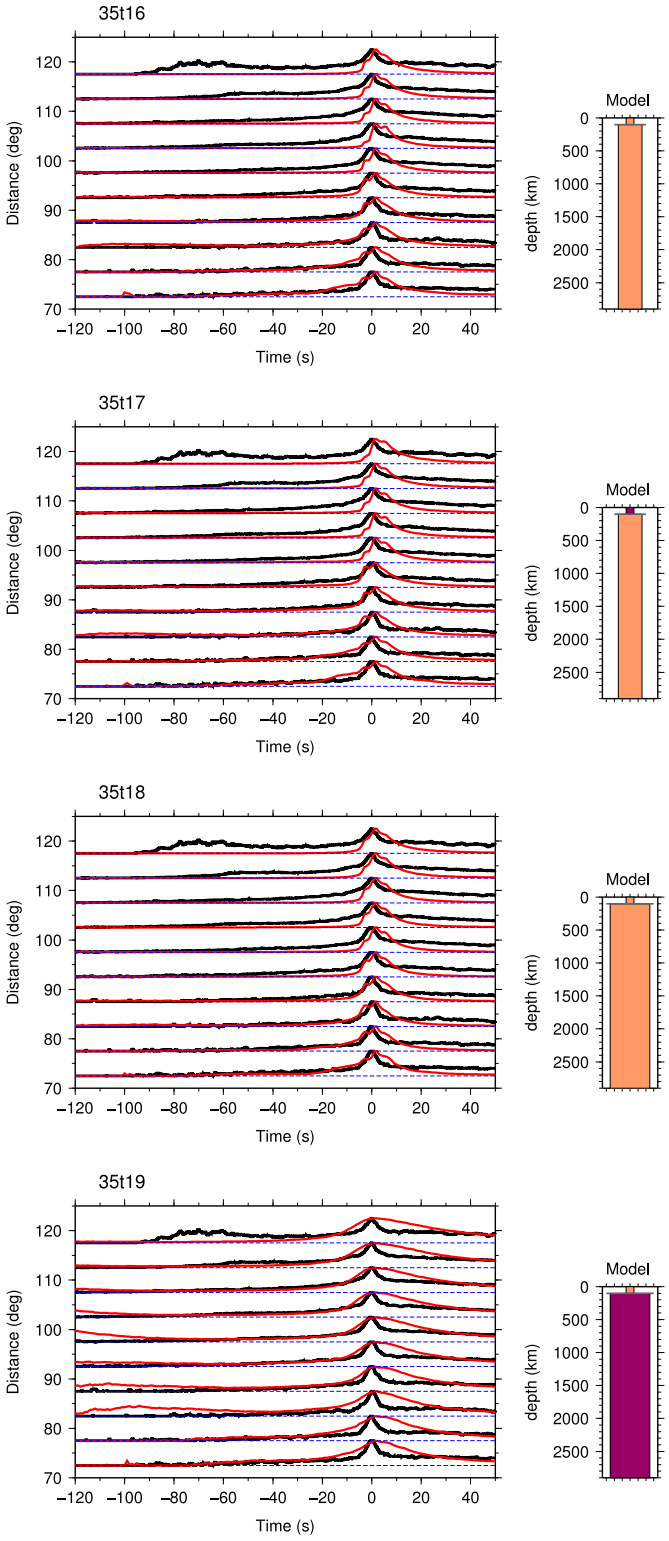

Figure C.13: Synthetic seismograms (red) generated with whole mantle heterogeneity models (right) compared to global stack data (black). *P* coda is removed for each seismogram prior to stacking in 5° distance bins.

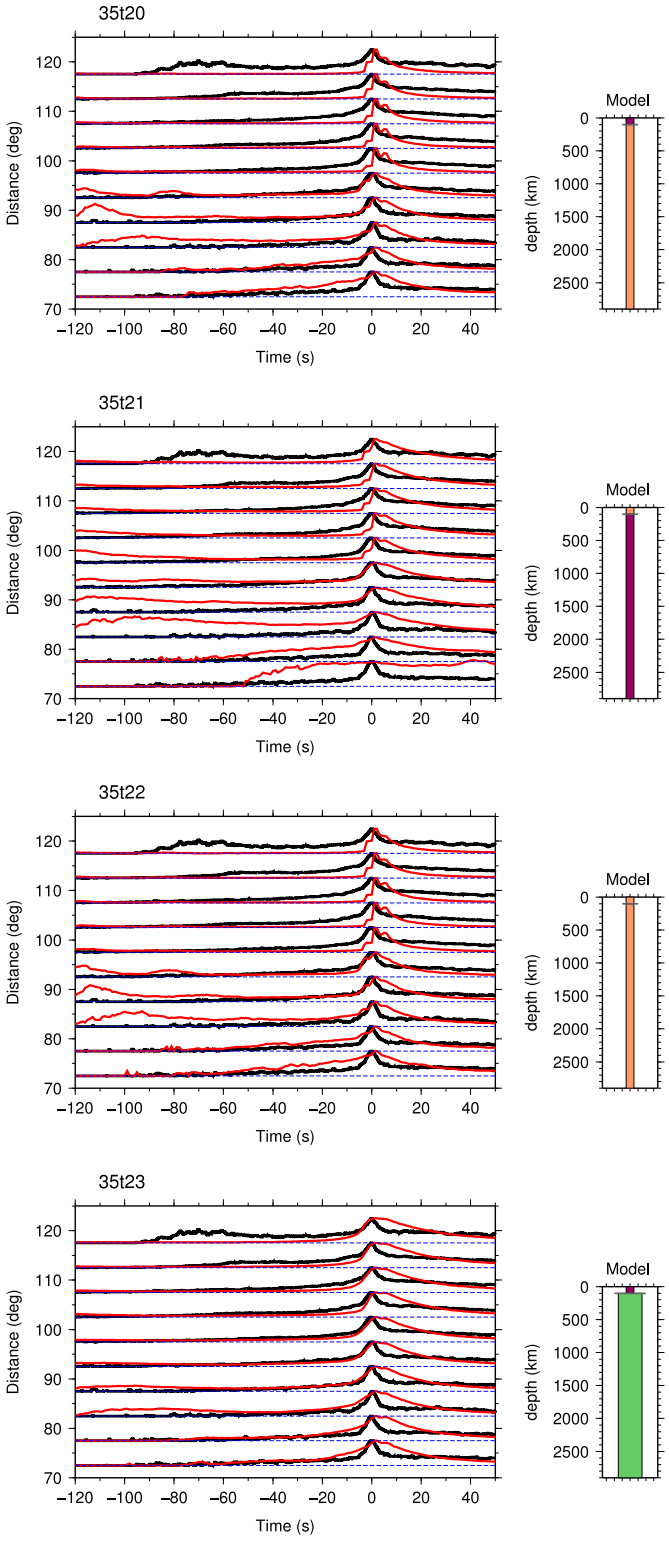

Figure C.14: Synthetic seismograms (red) generated with whole mantle heterogeneity models (right) compared to global stack data (black). *P* coda is removed for each seismogram prior to stacking in 5° distance bins.

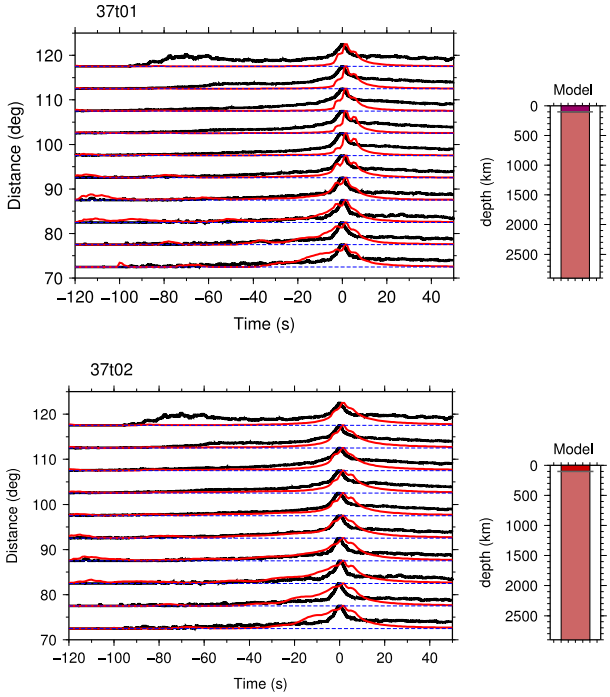

Figure C.15: Synthetic seismograms (red) generated with whole mantle heterogeneity models (right) compared to global stack data (black). *P* coda is removed for each seismogram prior to stacking in 5° distance bins.

C.3 Layered mantle models

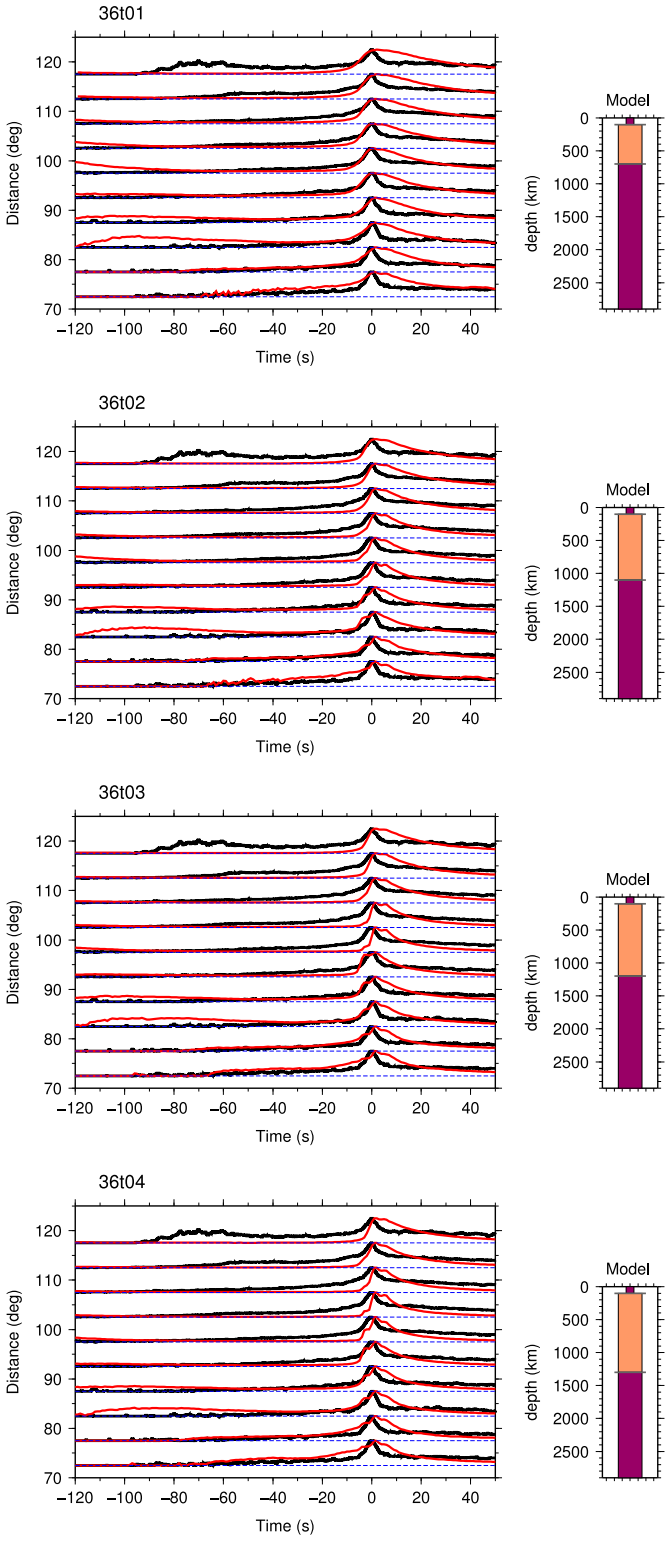

Figure C.16: Synthetic seismograms (red) generated with layered mantle heterogeneity models (right) compared to global stack data (black). *P* coda is removed for each seismogram prior to stacking in 5° distance bins.

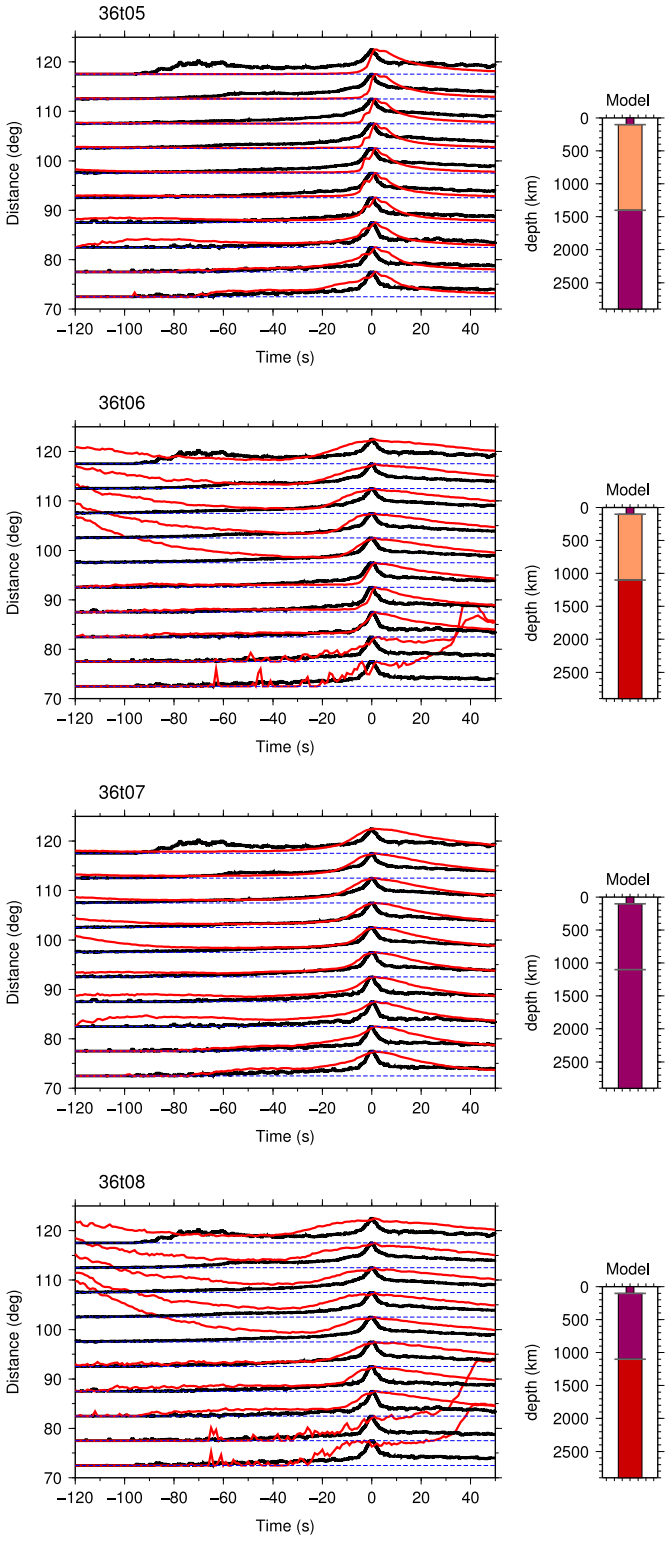

Figure C.17: Synthetic seismograms (red) generated with layered mantle heterogeneity models (right) compared to global stack data (black). *P* coda is removed for each seismogram prior to stacking in 5° distance bins.

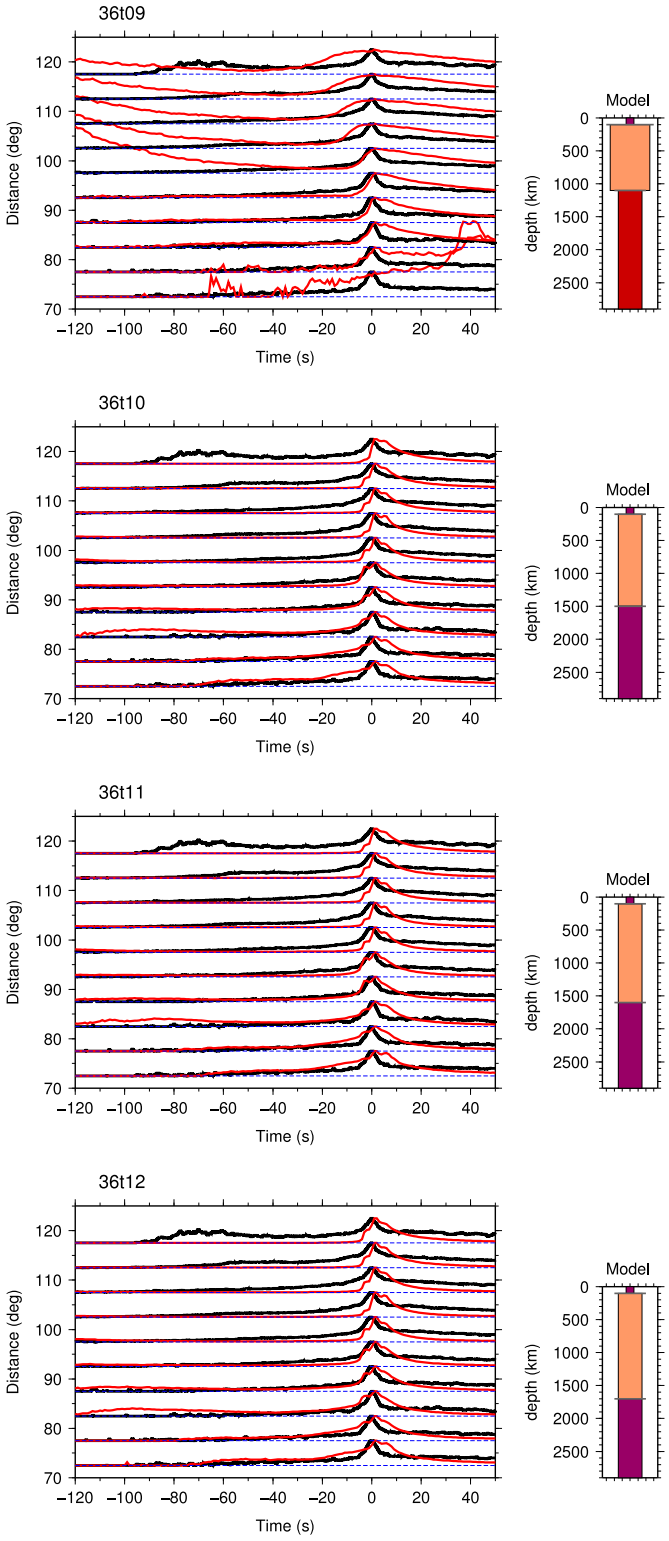

Figure C.18: Synthetic seismograms (red) generated with layered mantle heterogeneity models (right) compared to global stack data (black). *P* coda is removed for each seismogram prior to stacking in 5° distance bins.

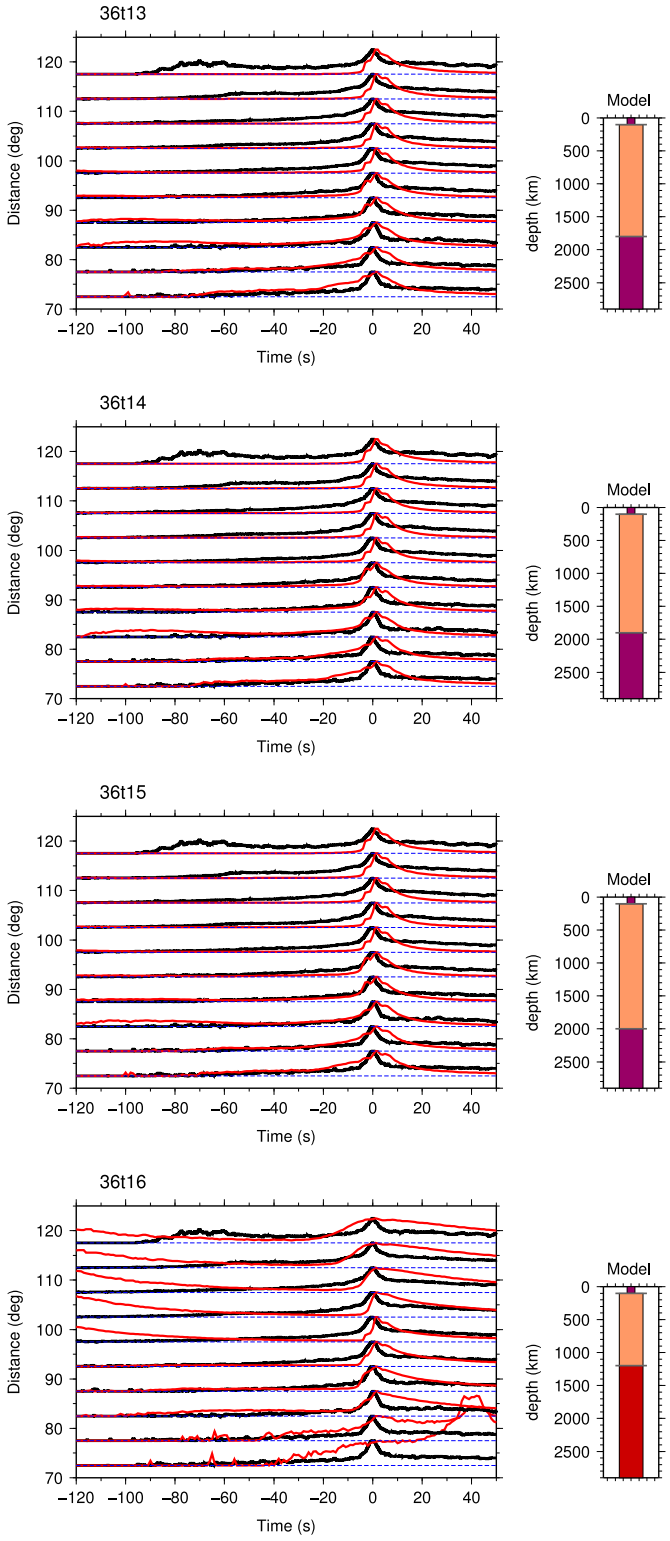

Figure C.19: Synthetic seismograms (red) generated with layered mantle heterogeneity models (right) compared to global stack data (black). *P* coda is removed for each seismogram prior to stacking in 5° distance bins.

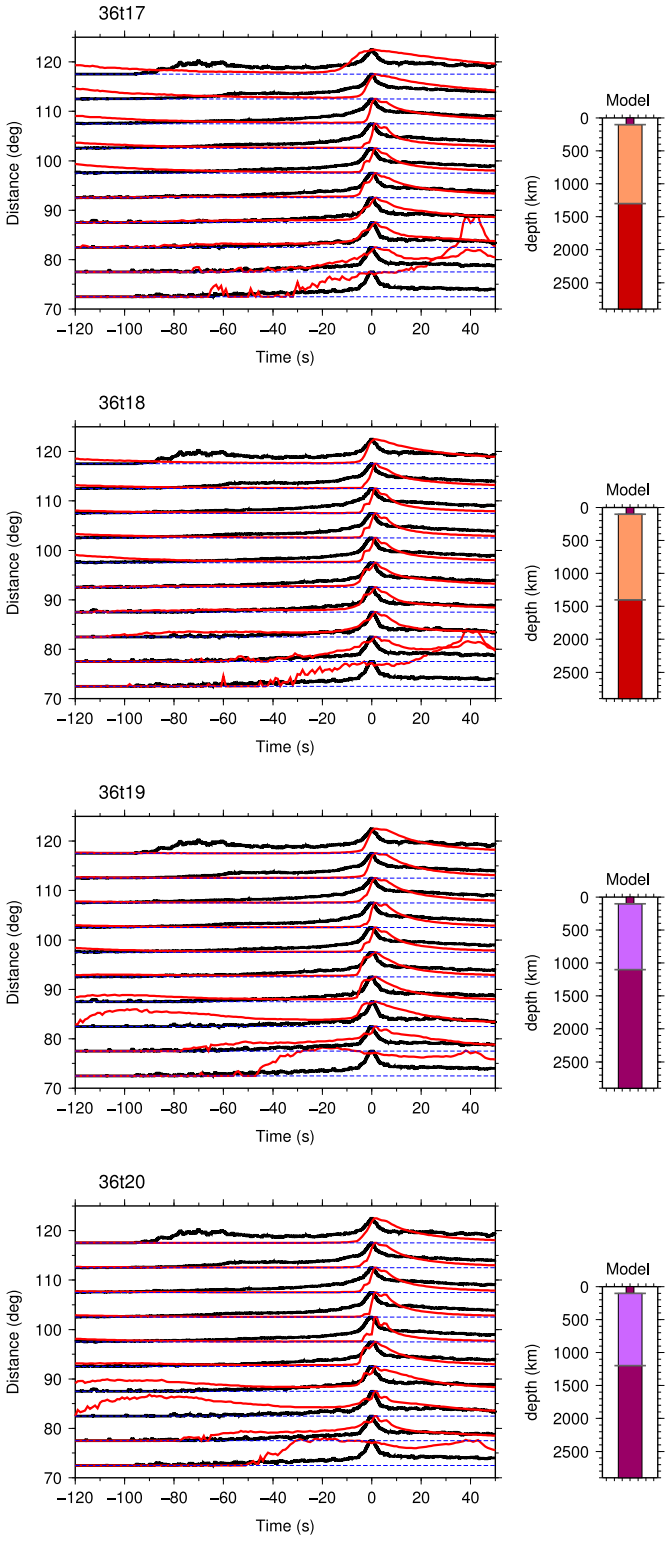

Figure C.20: Synthetic seismograms (red) generated with layered mantle heterogeneity models (right) compared to global stack data (black). *P* coda is removed for each seismogram prior to stacking in 5° distance bins.

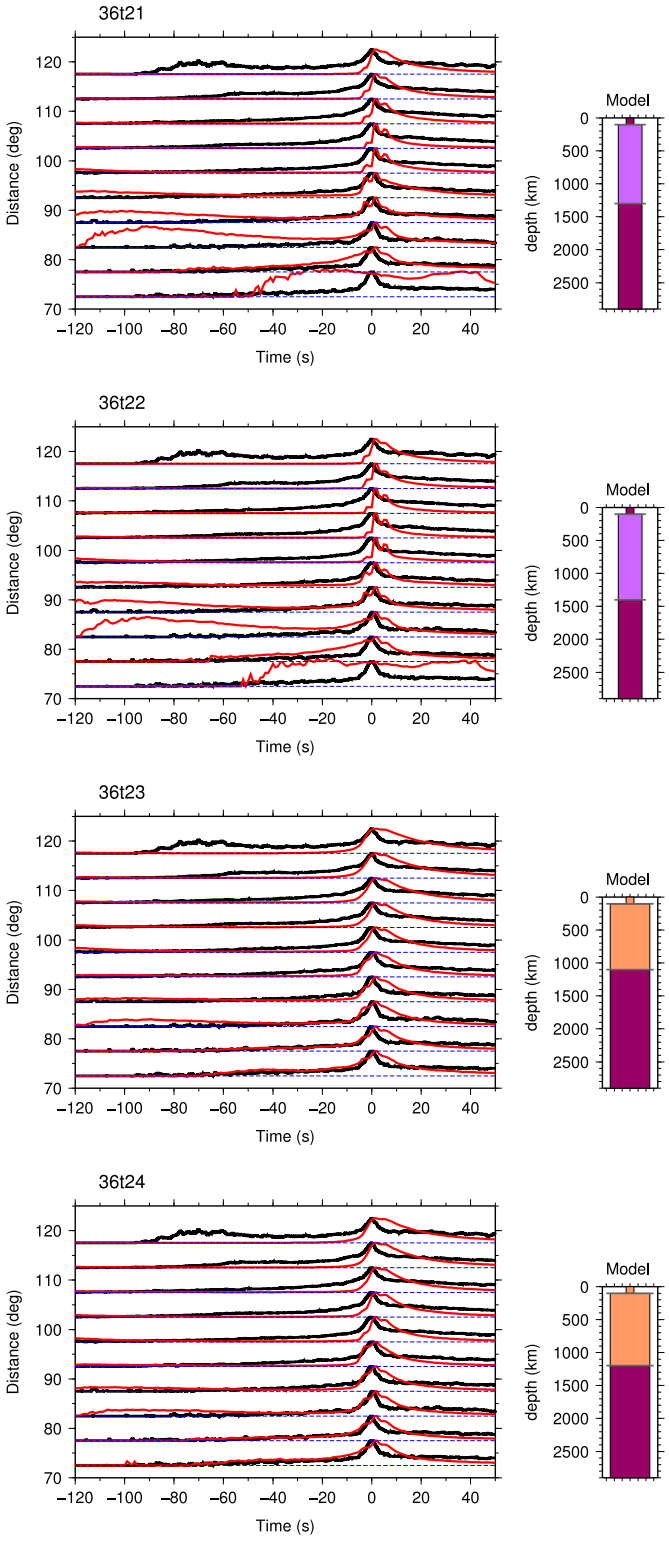

Figure C.21: Synthetic seismograms (red) generated with layered mantle heterogeneity models (right) compared to global stack data (black). *P* coda is removed for each seismogram prior to stacking in 5° distance bins.

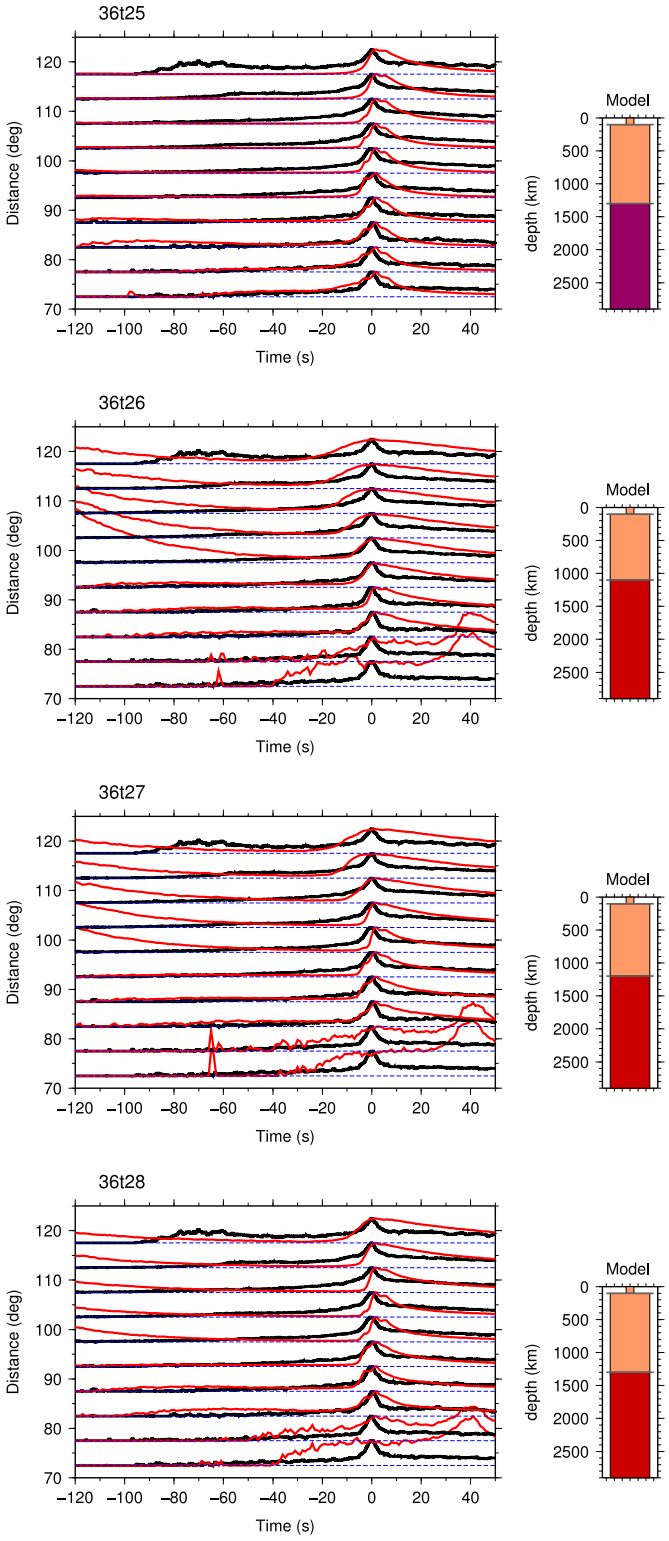

Figure C.22: Synthetic seismograms (red) generated with layered mantle heterogeneity models (right) compared to global stack data (black). *P* coda is removed for each seismogram prior to stacking in 5° distance bins.

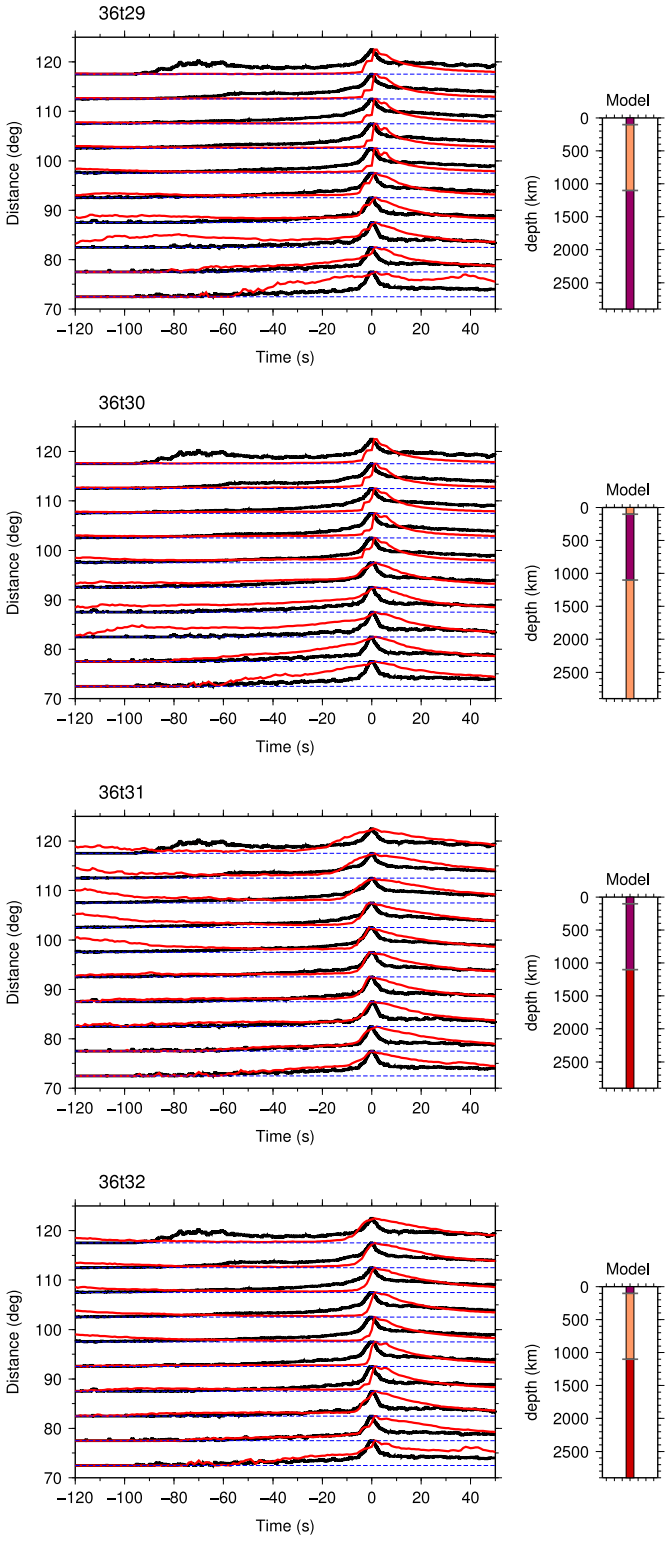

Figure C.23: Synthetic seismograms (red) generated with layered mantle heterogeneity models (right) compared to global stack data (black). *P* coda is removed for each seismogram prior to stacking in 5° distance bins.

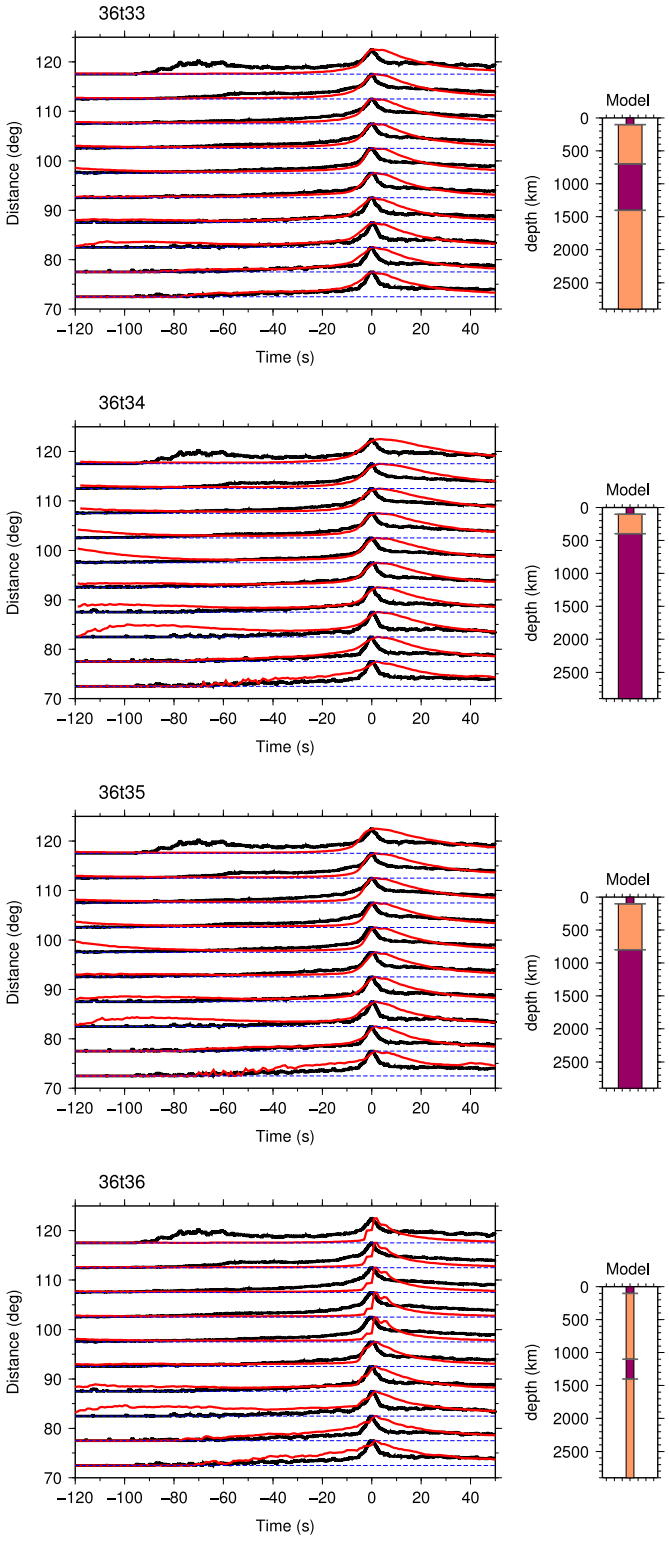

Figure C.24: Synthetic seismograms (red) generated with layered mantle heterogeneity models (right) compared to global stack data (black). *P* coda is removed for each seismogram prior to stacking in 5° distance bins.

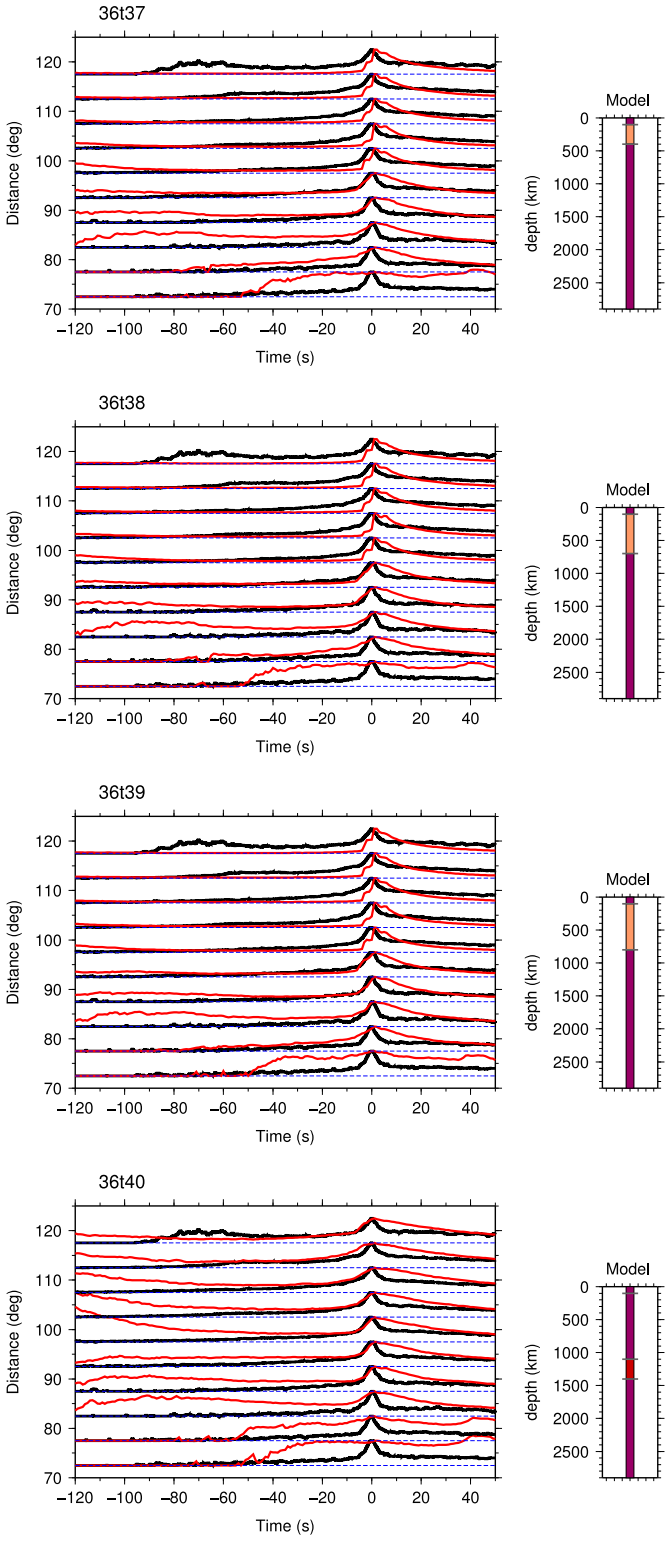

Figure C.25: Synthetic seismograms (red) generated with layered mantle heterogeneity models (right) compared to global stack data (black). *P* coda is removed for each seismogram prior to stacking in 5° distance bins.

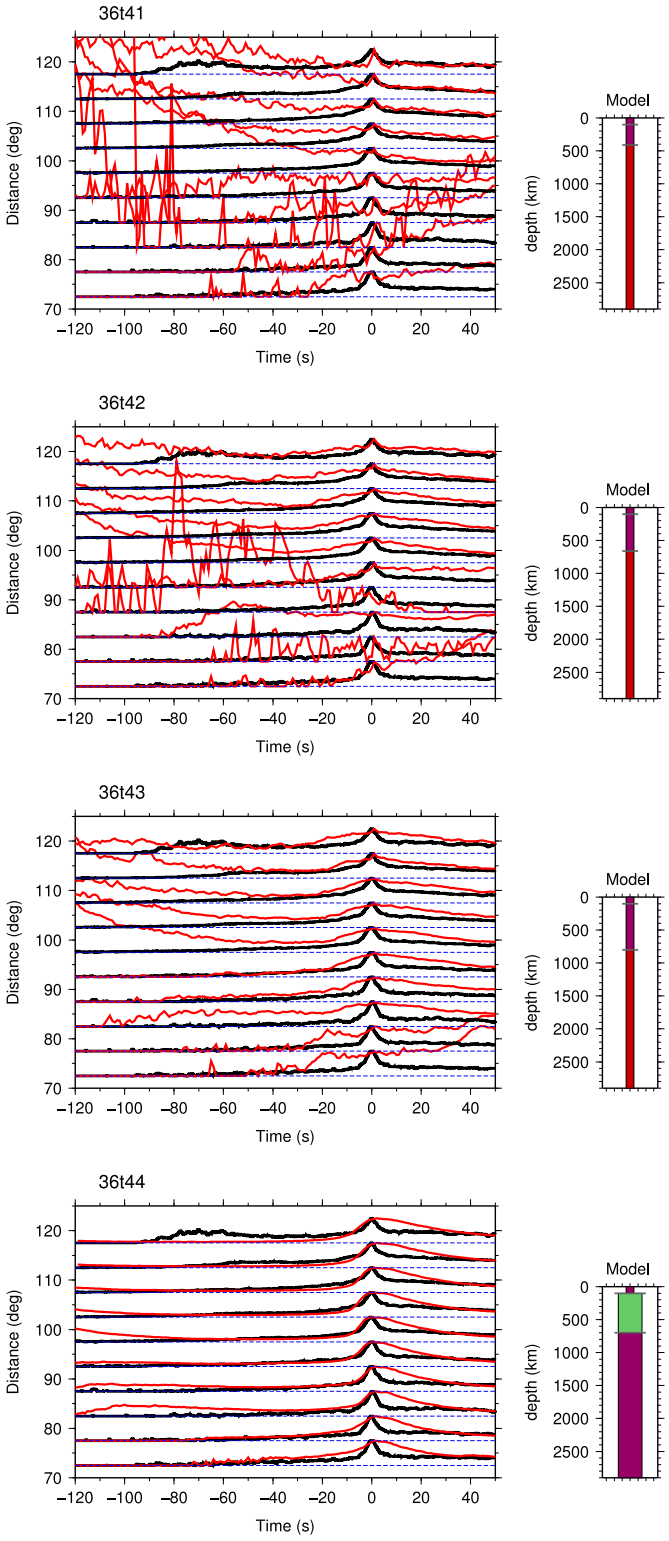

Figure C.26: Synthetic seismograms (red) generated with layered mantle heterogeneity models (right) compared to global stack data (black). *P* coda is removed for each seismogram prior to stacking in 5° distance bins.

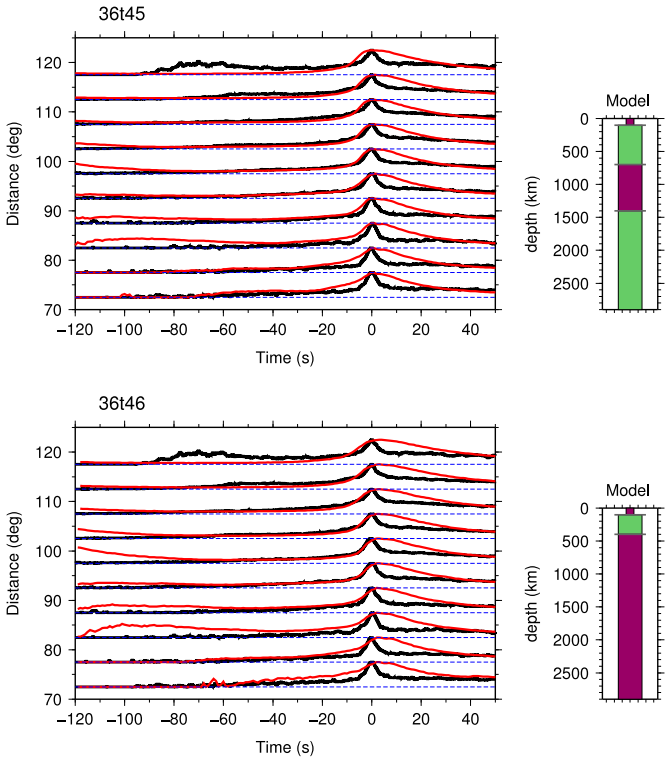

Figure C.27: Synthetic seismograms (red) generated with layered mantle heterogeneity models (right) compared to global stack data (black). *P* coda is removed for each seismogram prior to stacking in 5° distance bins.

Appendix D

Summary of model misfit

Model	Total misfit	Model	Total misfit	Model	Total misfit
31t1	10.12	35t17	9.35	36t22	13.41
31t2	22.26	35t18	9.74	36t23	9.46
31t3	11.18	35t19	8.72	36t24	9.35
31t4	10.26	35t20	9.71	36t25	9.64
31t5	8.93	35t21	12.83	36t26	11.8
31t6	9.12	35t22	10.19	36t27	11.21
31t7	8.47	35t23	7.95	36t28	11.96
31t8	7.85	37t1	9.63	36t29	10.83
31t9	8.81	37t2	8.75	36t30	12.41
31t10	13.59	36t1	8.57	36t31	8.73
32t1	12.55	36t2	9.46	36t32	9.97
32t2	21.03	36t3	8.94	36t33	7.61
32t3	13.03	36t4	9.98	36t34	8.59
34t1	32.48	36t5	9.73	36t35	8.75
35t1	10.76	36t6	10.87	36t36	9.74
35t2	9.59	36t7	9.86	36t37	12.51
35t3	12.66	36t8	15.55	36t38	11.74
35t4	10.8	36t9	11.45	36t39	11.16
35t5	8.79	36t10	9.94	36t40	14.05
35t6	12.72	36t11	9.57	36t41	28.38
35t7	10.54	36t12	9.61	36t42	31.4
35t8	8.53	36t13	9.47	36t43	15.31
35t9	12.39	36t14	9.35	36t44	8.36
35t10	10.47	36t15	9.1	36t45	7.92
35t11	8.49	36t16	10.63	36t46	8.99
35t12	10.44	36t17	11.05	36t47	7.23
35t13	10.48	36t18	11.54	36t48	8.17
35t14	8.58	36t19	13.95	36t49	7.25
35t15	9.58	36t20	13.46	36t50	9.11
35t16	9.52	36t21	13.73		

Table D.1: Total RMS misfit for models generated in Cheaper 3.

Appendix E

ILAR stations

Station	Latitude (°N)	Longitude (°E)	Elevation (km)
IL01	64.7716	-146.8861	0.418
IL02	64.7847	-146.8643	0.261
IL03	64.7714	-146.8512	0.440
IL04	64.7570	-146.8761	0.528
IL05	64.7731	-146.9229	0.389
IL06	64.7792	-146.9040	0.262
IL07	64.7993	-146.8393	0.401
IL08	64.7903	-146.7969	0.505
IL09	64.7681	-146.7832	0.494
IL10	64.7529	-146.8431	0.586
IL11	64.7415	-146.8974	0.444
IL12	64.7447	-146.9436	0.366
IL13	64.7479	-146.9865	0.367
IL14	64.7750	-146.9794	0.223
IL15	64.7777	-146.9428	0.336
IL16	64.7933	-146.9215	0.382
IL17	64.8072	-146.8898	0.357
IL18	64.7575	-146.7768	0.554
IL19	64.7461	-146.7974	0.549
IL31	64.7714	-146.8866	0.419

Table E.1: Eielson Array (ILAR) station coordinates and elevations

Appendix F

Earthquakes containing *P*P*

Table F.1: Event information for earthquake data processed at ILAR that contain P^*P including depth ($\boldsymbol{h}$), epicentral distance ($\boldsymbol{\Delta}$), azimuth ($\boldsymbol{\phi}$) and backazimuth ($\boldsymbol{\theta}$)

Event date	**Lat** (°)	**Lon** (°)	h **(km)**	Mw	Δ (°)	ϕ (°)	θ (°)
04-MAY-2000_04:21	-1.14	123.52	26	7.6	90.85	25.38	269.15
04-JUN-2000_16:28	-4.76	102.03	34.1	7.9	103.19	24.25	287.24
06-JUN-2000_09:58	-5.11	102.67	32	6.2	103.24	24.36	286.5
28-AUG-2000_15:05	-4.09	127.42	16	6.8	91.83	25.31	264.37
25-OCT-2000_09:32	-6.72	105.53	38	6.8	103.51	24.85	283.16
13-FEB-2001_19:28	-4.83	102.31	34	7.4	103.13	24.29	286.96
28-MAY-2001_08:37	-6.66	132.32	36.6	6	92.06	25.05	258.86
15-JUN-2001_16:19	13.87	51.67	26.8	6	100.33	7.97	341.69
19-OCT-2001_03:28	-4.12	123.93	29	7.5	93.35	25.42	267.51
27-JUN-2002_05:50	-6.97	103.97	11	6.5	104.39	24.71	284.5
15-AUG-2002_05:30	-1.27	121.29	20	6.2	91.92	25.38	271.11
13-SEP-2002_22:28	13.03	93.1	21	6.5	90.38	21.78	302.45
02-NOV-2002_01:26	2.82	96.08	30	7.4	98.65	22.72	295.85
02-NOV-2002_09:46	2.95	96.39	27	6.3	98.41	22.77	295.62
09-MAR-2003_10:36	-6.82	130.99	45	6	92.77	25.15	260
25-MAR-2003_02:53	-8.29	120.74	33	6.5	98.45	25.65	268.59
30-MAR-2003_18:13	-3.25	127.47	31	6.2	91.05	25.3	264.68
27-APR-2003_16:03	-20.94	169.77	77	6.3	91.7	17.12	219.93
04-MAY-2003_13:15	-30.68	-178.13	32	6.7	98.22	12.98	206.84
11-AUG-2003_21:22	12.12	93.53	100	6	91.06	21.89	301.72
03-JAN-2004_16:23	-22.25	169.68	22	7.1	92.97	17.16	219.63
22-FEB-2004_06:46	-1.56	100.49	42	6	100.91	23.76	290
23-APR-2004_01:50	-9.36	122.84	65	6.7	98.51	25.68	266.23
11-MAY-2004_08:28	0.41	97.82	21	6.1	100.18	23.18	293.28
02-JUN-2004_08:50	-32.88	-179.45	43	6.2	100.62	13.57	207.44
25-JUN-2004_02:35	-6.71	130.38	70	6.1	92.93	25.19	260.59
11-NOV-2004_21:26	-8.15	124.87	10	7.5	96.56	25.54	264.93
11-NOV-2004_22:49	-8.26	124.93	10	6.4	96.63	25.55	264.83
26-DEC-2004_04:21	6.91	92.96	39	7.2	96.07	21.88	300.31

Continued on next page

Table F.1 – continued from previous page

Event date	**Lat (°)**	**Lon (°)**	***h* (km)**	***Mw***	**Δ (°)**	***ϕ* (°)**	***θ* (°)**
26-DEC-2004_09:20	8.86	92.3	17.4	6.6	94.52	21.67	301.64
26-DEC-2004_10:19	13.46	92.74	26	6.3	90.11	21.7	302.93
26-DEC-2004_11:05	13.53	92.84	13	6.2	90.01	21.72	302.86
27-DEC-2004_09:39	5.35	94.65	35	6.1	96.88	22.3	298.15
29-DEC-2004_05:56	8.79	93.2	12	6.2	94.25	21.87	300.79
31-DEC-2004_02:24	7.12	92.53	14	6.1	96.04	21.78	300.78
01-JAN-2005_06:25	5.03	92.26	17.5	6.7	98.06	21.81	300.26
02-JAN-2005_15:35	6.36	92.79	30	6.4	96.64	21.87	300.26
04-JAN-2005_09:13	10.65	92.35	24.4	6.1	92.85	21.64	302.25
09-JAN-2005_22:12	4.93	95.11	40	6.1	97.09	22.42	297.57
26-FEB-2005_12:56	2.91	95.59	36	6.8	98.76	22.62	296.35
28-MAR-2005_16:09	2.06	97.06	33.7	8.6	98.97	22.94	294.64
28-MAR-2005_18:30	0.92	97.87	36	6.1	99.69	23.16	293.44
03-APR-2005_00:59	0.37	98.28	30	6	100.03	23.27	292.84
03-APR-2005_03:10	2.02	97.94	36	6.3	98.66	23.1	293.81
10-APR-2005_10:29	-1.64	99.61	19	6.7	101.33	23.63	290.79
10-APR-2005_17:24	-1.59	99.72	30	6.4	101.25	23.64	290.71
11-APR-2005_06:11	2.17	96.76	24	6.1	98.98	22.88	294.97
16-APR-2005_16:38	1.81	97.66	31	6.4	98.96	23.06	293.99
28-APR-2005_14:07	2.13	96.8	22	6.2	99	22.89	294.91
14-MAY-2005_05:05	0.5	98.35	34	6.7	99.89	23.27	292.82
16-MAY-2005_03:54	-32.59	-179.35	34	6.6	100.31	13.52	207.42
18-MAY-2005_11:37	5.6	93.3	44.5	6.1	97.15	22.01	299.5
08-JUN-2005_06:28	2.17	96.72	23	6.1	99	22.87	295
05-JUL-2005_01:52	1.8	97.05	21	6.7	99.21	22.96	294.55
30-DEC-2006_08:30	13.31	51.37	15	6.6	100.93	7.86	341.91
08-JAN-2007_12:48	8.08	92.44	11	6.1	95.18	21.72	301.22
31-JAN-2007_03:15	-29.78	-178	34	6.5	97.32	12.9	206.93
18-JUL-2007_00:07	-26.3	-177.74	10	6.1	93.89	12.73	207.48
17-AUG-2007_03:04	-5.26	129.43	10	6.4	92.02	25.23	262.06
12-SEP-2007_11:10	-4.44	101.37	34	8.5	103.17	24.13	287.99
13-SEP-2007_03:35	-2.13	99.63	22	7	101.77	23.67	290.57
13-SEP-2007_16:09	-3.17	101.52	53	6	101.95	24.04	288.38
14-SEP-2007_06:01	-4.07	101.17	23	6.4	102.91	24.07	288.33
20-SEP-2007_08:31	-2	100.14	30	6.7	101.45	23.74	290.15
27-SEP-2007_19:57	-21.1	169.28	9	6.1	91.99	17.28	220.32
24-OCT-2007_21:02	-3.9	101.02	21	6.8	102.82	24.03	288.54
15-DEC-2007_09:39	-6.62	131.09	57	6.4	92.54	25.14	259.99
04-JAN-2008_07:29	-2.79	100.92	40.6	6	101.86	23.92	289.1
22-JAN-2008_17:14	1.03	97.45	40.6	6.2	99.75	23.08	293.88
13-FEB-2008_19:58	-8.25	128.67	17.1	6.2	95.03	25.35	261.48
20-FEB-2008_08:08	2.76	95.96	31.4	7.4	98.75	22.7	295.94
25-FEB-2008_08:36	-2.49	99.92	29.8	7.2	101.98	23.75	290.15
25-FEB-2008_18:06	-2.38	99.86	33.1	6.6	101.91	23.73	290.25
25-FEB-2008_21:02	-2.24	99.81	33.3	6.7	101.81	23.71	290.36
15-MAR-2008_14:43	2.71	94.57	23.5	6	99.33	22.43	297.22

Continued on next page

Table F.1 – continued from previous page

Event date	**Lat** (°)	**Lon** (°)	h **(km)**	Mw	Δ (°)	ϕ (°)	θ (°)
29-MAR-2008_17:30	2.93	95.28	24.3	6.3	98.86	22.55	296.64
27-JUN-2008_11:40	11	91.84	27.6	6.6	92.71	21.51	302.84
28-JUN-2008_12:54	10.87	91.73	27.9	6.1	92.87	21.49	302.9
10-AUG-2008_08:20	11.02	91.83	29.1	6.2	92.69	21.51	302.87
29-SEP-2008_15:19	-30.1	-177.63	35	7	97.56	12.77	206.55
09-DEC-2008_06:23	-31.23	-176.92	18	6.8	98.53	12.53	205.69
18-JAN-2009_14:11	-30.23	-177.86	31.5	6.4	97.73	12.86	206.71
18-FEB-2009_21:53	-27.39	-176.24	28.2	7	94.66	12.17	205.93
19-MAR-2009_18:17	-23.16	-174.59	30.9	7.6	90.23	11.49	205.33
15-APR-2009_20:01	-3.13	100.46	27.8	6.3	102.35	23.88	289.39
16-MAY-2009_00:53	-31.45	-178.56	32.5	6.5	99.05	13.17	207.03
16-AUG-2009_07:38	-1.47	99.46	40.1	6.7	101.24	23.59	291
30-SEP-2009_10:16	-0.71	99.97	90.2	7.5	100.34	23.62	290.83
01-OCT-2009_01:52	-2.52	101.57	21.4	6.6	101.35	23.99	288.6
16-OCT-2009_09:52	-6.51	105.24	54.6	6.1	103.45	24.8	283.51
02-NOV-2009_10:47	-24.15	-175.09	13.9	6.2	91.29	11.69	205.58
08-NOV-2009_19:41	-8.28	118.67	32.1	6.6	99.33	25.66	270.46
10-NOV-2009_02:48	8.03	91.95	22.7	6	95.41	21.62	301.66
26-DEC-2009_08:57	-5.43	131.32	64.9	6.1	91.37	25.11	260.29
05-MAR-2010_16:06	-3.77	100.96	12	6.8	102.73	24.01	288.65

Appendix G

*P*P* detected using TOPCAT

Table G.1: Latitude, Longitude, depth (h), NSWB, backazimuth (θ), differential backazimuth ($\delta\theta$) and event information for all P^*P (precursors that are off great circle path by more than 5° ($\delta\theta > 5°$).

P*P	**Event**	**NSWB**	***h* (km)**	**Lat (°)**	**Lon (°)**	**θ (°)**	**θ_{PP} (°)**	**$\delta\theta$ (°)**
1	04-MAY-2000_04:21	0.2	150	37.51	168.61	245.6	252.4	-6.8
2	04-MAY-2000_04:21	0.18	95	39.82	147.46	268.9	252.4	16.5
3	04-MAY-2000_04:21	0.12	180	67.81	160.41	302	252.4	49.6
4	04-JUN-2000_16:28	0.13	145	20.3	133.04	270.1	287.4	-17.3
5	04-JUN-2000_16:28	0.11	440	35.28	135.02	276.7	287.4	-10.7
6	06-JUN-2000_09:58	0.16	100	53.07	148.65	281.1	294.3	-13.2
7	06-JUN-2000_09:58	0.15	225	53.2	172.05	260.3	294.3	-34
8	06-JUN-2000_09:58	0.1	90	58.28	168.29	273.9	294.3	-20.4
9	15-JUN-2001_16:19	0.15	120	33.55	76.07	324.2	340.3	-16.1
10	15-JUN-2001_16:19	0.1	985	48.08	131.38	289.2	340.3	-51.1
11	02-NOV-2002_01:26	0.14	85	55.85	179.56	257.2	306.5	-49.3
12	02-NOV-2002_09:46	0.18	40	53.35	142.12	286.4	292	-5.6
13	02-NOV-2002_09:46	0.14	105	45.59	142.79	277.9	292	-14.1
14	09-MAR-2003_10:36	0.11	220	20.61	141.6	262.4	254.1	8.3
15	27-APR-2003_16:03	0.18	525	26.61	-169.47	211.7	231.1	-19.4
16	04-MAY-2003_13:15	0.17	60	29.88	-163.09	204.1	213.9	-9.8
17	04-MAY-2003_13:15	0.16	90	44.14	-167.43	219	213.9	5.1
18	04-MAY-2003_13:15	0.11	270	26.86	-177.78	222.5	213.9	8.6
19	03-JAN-2004_16:23	0.18	180	35.31	-167.11	212.3	237.2	-24.9
20	03-JAN-2004_16:23	0.17	380	31.05	-174.59	220.5	237.2	-16.7
21	03-JAN-2004_16:23	0.15	310	-2.32	165.88	229.3	237.2	-7.9
22	03-JAN-2004_16:23	0.11	200	27.59	-169.63	212.3	237.2	-24.9
23	02-JUN-2004_08:50	0.2	145	33	-155.35	193.4	219.7	-26.3
24	02-JUN-2004_08:50	0.15	10	38.96	-180	232.9	219.7	13.2
25	01-JAN-2005_06:25	0.14	80	33.29	102.61	302.5	296	6.5
26	01-JAN-2005_06:25	0.13	75	40.19	101.52	306.7	296	10.7
27	02-JAN-2005_15:35	0.16	390	35.99	147.05	266.4	297	-30.6
28	02-JAN-2005_15:35	0.12	115	50.78	132.22	291	297	-6

Continued on next page

Table G.1 – continued from previous page

*P*P*	Event	NSWB	h (km)	Lat (°)	Lon (°)	θ (°)	θ_{PP} (°)	$\delta\theta$ (°)
29	04-JAN-2005_09:13	0.16	520	44.89	147.29	273.4	293.3	-19.9
30	04-JAN-2005_09:13	0.12	130	53.4	104.52	312.3	293.3	19
31	04-JAN-2005_09:13	0.12	390	40.25	131.29	283.2	293.3	-10.1
32	04-JAN-2005_09:13	0.11	35	70.74	137.11	315.9	293.3	22.6
33	09-JAN-2005_22:12	0.19	265	31.73	133.88	275.5	292.2	-16.7
34	03-APR-2005_00:59	0.19	195	52.6	145.2	283.2	302.7	-19.5
35	03-APR-2005_00:59	0.14	730	39.28	164.69	251.4	302.7	-51.3
36	03-APR-2005_00:59	0.13	225	61.57	159.82	287.1	302.7	-15.6
37	03-APR-2005_00:59	0.13	60	62.25	170.88	281.8	302.7	-20.9
38	03-APR-2005_00:59	0.13	150	61.14	162.59	284.4	302.7	-18.3
39	03-APR-2005_03:10	0.18	120	49.06	140.68	282.9	291.6	-8.7
40	16-MAY-2005_03:54	0.2	35	28.98	-164.79	206.2	225	-18.8
41	08-JUN-2005_06:28	0.11	195	46.65	106.28	306.7	293.4	13.3
42	30-DEC-2006_08:30	0.15	220	33.66	64.68	333.6	339.4	-5.8
43	08-JAN-2007_12:48	0.12	1080	41.83	164.87	253.5	301	-47.5
44	08-JAN-2007_12:48	0.11	680	32.19	142.02	268.5	301	-32.5
45	08-JAN-2007_12:48	0.11	0	71.48	133.92	318.3	301	17.3
46	31-JAN-2007_03:15	0.11	775	-0.6	162.38	233.3	223.9	9.4
47	18-JUL-2007_00:07	0.14	125	9.09	-167.12	203.9	222.4	-18.5
48	27-SEP-2007_19:57	0.17	455	30	161.47	248.1	209.9	38.2
49	04-JAN-2008_07:29	0.18	405	33.53	129.35	280.5	298.5	-18
50	04-JAN-2008_07:29	0.15	585	37.5	179.19	232.8	298.5	-65.7
51	29-SEP-2008_15:19	0.19	60	46.77	174.42	248	222.6	25.4
52	29-SEP-2008_15:19	0.16	690	28.19	170.98	236.6	222.6	14
53	29-SEP-2008_15:19	0.15	145	21.1	-174.14	215.6	222.6	-7
54	29-SEP-2008_15:19	0.13	385	9	-175.33	213.2	222.6	-9.4
55	09-DEC-2008_06:23	0.19	460	25.21	-174.38	217.5	224.3	-6.8
56	09-DEC-2008_06:23	0.14	305	8.13	-175.64	213.3	224.3	-11
57	18-JAN-2009_14:11	0.18	85	14.25	-169.94	208.4	222	-13.6
58	18-JAN-2009_14:11	0.15	420	43.16	168.61	250.7	222	28.7
59	18-JAN-2009_14:11	0.12	105	42.49	-157.19	199.7	222	-22.3
60	18-FEB-2009_21:53	0.11	80	35.13	-167.79	213.2	220.7	-7.5
61	19-MAR-2009_18:17	0.12	5	44.54	-163.9	213.3	218.9	-5.6
62	19-MAR-2009_18:17	0.11	210	14.26	-171.54	210.3	218.9	-8.6
63	16-MAY-2009_00:53	0.15	485	26.1	177.39	228	215	13
64	16-MAY-2009_00:53	0.12	145	44.4	-169.17	222.1	215	7.1
65	01-OCT-2009_01:52	0.15	125	49.27	125.63	294.5	284.3	10.2
66	02-NOV-2009_10:47	0.12	40	48.37	-140.17	164.4	215.9	-51.5
67	02-NOV-2009_10:47	0.11	170	43.52	-169.32	221.5	215.9	5.6
68	08-NOV-2009_19:41	0.17	100	25.57	153.41	253.7	270.2	-16.5
69	08-NOV-2009_19:41	0.1	155	53.06	176.2	255.4	270.2	-14.8
70	05-MAR-2010_16:06	0.13	320	9.53	131.18	266.8	283.3	-16.5
71	04-MAY-2000_04:21	0.29	110	46.47	160.99	262.3	252.4	9.9
72	04-JUN-2000_16:28	0.45	85	38	141.02	273.3	287.4	-14.1
73	06-JUN-2000_09:58	0.77	25	44.08	128.79	288	294.3	-6.3
74	06-JUN-2000_09:58	0.45	135	43.12	129.02	287.1	294.3	-7.2

Continued on next page

Table G.1 – continued from previous page

*P*P*	Event	NSWB	h (km)	Lat (°)	Lon (°)	θ (°)	θ_{PP} (°)	$\delta\theta$ (°)
75	06-JUN-2000_09:58	0.39	145	65.86	137.41	306.9	294.3	12.6
76	06-JUN-2000_09:58	0.38	70	55.06	125.36	299.9	294.3	5.6
77	06-JUN-2000_09:58	0.29	235	48.87	154.77	270.9	294.3	-23.4
78	06-JUN-2000_09:58	0.28	290	49.3	147.3	277.8	294.3	-16.5
79	06-JUN-2000_09:58	0.24	185	28.26	128.55	278.2	294.3	-16.1
80	06-JUN-2000_09:58	0.22	105	57	152.64	283.6	294.3	-10.7
81	06-JUN-2000_09:58	0.22	10	67.82	152	304.8	294.3	10.5
82	15-JUN-2001_16:19	0.36	145	50.53	87.21	322.3	340.3	-18
83	02-NOV-2002_01:26	1.35	25	43.43	121.27	293.4	306.5	-13.1
84	02-NOV-2002_01:26	0.9	215	48.01	121.82	296.3	306.5	-10.2
85	02-NOV-2002_01:26	0.89	100	40.45	126.19	287.5	306.5	-19
86	02-NOV-2002_01:26	0.82	10	59.29	143.24	293.4	306.5	-13.1
87	02-NOV-2002_01:26	0.39	120	47.92	122.26	295.9	306.5	-10.6
88	02-NOV-2002_01:26	0.36	140	56.36	160.19	276.8	306.5	-29.7
89	02-NOV-2002_01:26	0.32	25	62.56	164.23	286.7	306.5	-19.8
90	02-NOV-2002_01:26	0.3	185	47.31	130.01	289.6	306.5	-16.9
91	02-NOV-2002_01:26	0.23	265	37.54	113.74	295.7	306.5	-10.8
92	09-MAR-2003_10:36	0.59	230	25.39	162.89	243.9	254.1	-10.2
93	09-MAR-2003_10:36	0.37	90	18.44	134.14	268.2	254.1	14.1
94	09-MAR-2003_10:36	0.35	210	18	137.4	265	254.1	10.9
95	09-MAR-2003_10:36	0.34	70	30.88	140.47	269.1	254.1	15
96	09-MAR-2003_10:36	0.26	90	17.37	138.38	263.8	254.1	9.7
97	09-MAR-2003_10:36	0.25	85	5.57	122.2	273.2	254.1	19.1
98	09-MAR-2003_10:36	0.23	650	13.88	172.25	228.5	254.1	-25.6
99	09-MAR-2003_10:36	0.22	330	24.98	138.32	267.7	254.1	13.6
100	09-MAR-2003_10:36	0.21	100	18.13	155.18	248.1	254.1	-6
101	27-APR-2003_16:03	0.55	105	30.92	-172.54	217.7	231.1	-13.4
102	27-APR-2003_16:03	0.5	730	15.37	157.89	244.1	231.1	13
103	27-APR-2003_16:03	0.44	825	-0.61	152.78	242.5	231.1	11.4
104	27-APR-2003_16:03	0.42	110	11.98	179.11	220.3	231.1	-10.8
105	27-APR-2003_16:03	0.39	190	2.99	158.91	238	231.1	6.9
106	27-APR-2003_16:03	0.28	70	41.07	-168.18	217.6	231.1	-13.5
107	27-APR-2003_16:03	0.25	380	31.58	-178.44	225.8	231.1	-5.3
108	27-APR-2003_16:03	0.22	1265	11.29	145.21	254.6	231.1	23.5
109	04-MAY-2003_13:15	0.29	85	41.4	-169.41	219.8	213.9	5.9
110	04-MAY-2003_13:15	0.22	55	34.19	-177.38	226	213.9	12.1
111	03-JAN-2004_16:23	0.44	110	26.6	178.02	227.5	237.2	-9.7
112	03-JAN-2004_16:23	0.28	345	29.02	-177.65	223.4	237.2	-13.8
113	03-JAN-2004_16:23	0.25	250	41.37	-162.8	209	237.2	-28.2
114	03-JAN-2004_16:23	0.21	210	30.72	-170.18	214.4	237.2	-22.8
115	02-JUN-2004_08:50	0.39	15	32.84	-166.44	210.1	219.7	-9.6
116	02-JUN-2004_08:50	0.39	130	26.73	177.49	228.2	219.7	8.5
117	02-JUN-2004_08:50	0.24	45	41.66	-161.93	207.7	219.7	-12
118	02-JUN-2004_08:50	0.21	150	26.53	-169.34	211.5	219.7	-8.2
119	01-JAN-2005_06:25	0.25	140	42.52	128.85	286.8	296	-9.2
120	02-JAN-2005_15:35	0.44	55	46.55	134.08	285.8	297	-11.2

Continued on next page

Table G.1 – continued from previous page

*P*P*	Event	NSWB	h (km)	Lat (°)	Lon (°)	θ (°)	θ_{PP} (°)	$\delta\theta$ (°)
121	03-APR-2005_00:59	0.93	20	43.44	131.07	285.7	302.7	-17
122	03-APR-2005_00:59	0.73	45	50.88	138.39	286.5	302.7	-16.2
123	03-APR-2005_00:59	0.46	165	51.62	147.93	279.9	302.7	-22.8
124	03-APR-2005_00:59	0.45	215	44.27	131.87	285.7	302.7	-17
125	03-APR-2005_00:59	0.35	550	26.99	147.66	260.1	302.7	-42.6
126	03-APR-2005_00:59	0.26	645	22.52	150.3	255.1	302.7	-47.6
127	03-APR-2005_00:59	0.24	70	53.04	160.65	271.1	302.7	-31.6
128	03-APR-2005_03:10	0.32	145	31.41	128.14	280.3	291.6	-11.3
129	03-APR-2005_03:10	0.21	340	30.44	136.86	272.1	291.6	-19.5
130	16-MAY-2005_03:54	0.65	205	10.97	-156.37	191.5	225	-33.5
131	16-MAY-2005_03:54	0.61	5	32.76	-166.39	210	225	-15
132	16-MAY-2005_03:54	0.56	125	35.99	-168.35	214.5	225	-10.5
133	16-MAY-2005_03:54	0.56	25	24.01	-175.82	218.8	225	-6.2
134	16-MAY-2005_03:54	0.5	130	23.53	-168.86	209.8	225	-15.2
135	16-MAY-2005_03:54	0.45	185	17.41	-163.98	201.9	225	-23.1
136	16-MAY-2005_03:54	0.35	5	41.07	-157.79	200.1	225	-24.9
137	16-MAY-2005_03:54	0.34	50	34.98	179.17	231	225	6
138	16-MAY-2005_03:54	0.29	80	41.47	-159.82	203.9	225	-21.1
139	05-JUL-2005_01:52	0.47	15	57.32	145.19	289.3	284	5.3
140	05-JUL-2005_01:52	0.25	15	60.56	149.69	291.4	284	7.4
141	30-DEC-2006_08:30	0.62	0	50.59	50.5	347.8	339.4	8.4
142	30-DEC-2006_08:30	0.22	115	32.05	71.3	327.7	339.4	-11.7
143	31-JAN-2007_03:15	0.38	25	14.88	-175.05	214.6	223.9	-9.3
144	31-JAN-2007_03:15	0.24	300	-4.59	179.21	215.4	223.9	-8.5
145	31-JAN-2007_03:15	0.2	15	31.46	-171.68	216.8	223.9	-7.1
146	27-SEP-2007_19:57	0.68	1550	-1.1	144.12	250.4	209.9	40.5
147	27-SEP-2007_19:57	0.54	410	0.23	164.21	231.8	209.9	21.9
148	27-SEP-2007_19:57	0.43	310	6.96	165.34	233.1	209.9	23.2
149	27-SEP-2007_19:57	0.43	25	2.29	164.85	231.9	209.9	22
150	27-SEP-2007_19:57	0.33	440	31.09	-174.8	220.8	209.9	10.9
151	27-SEP-2007_19:57	0.3	1480	30.65	140.43	269	209.9	59.1
152	27-SEP-2007_19:57	0.25	240	17.17	159.99	242.8	209.9	32.9
153	27-SEP-2007_19:57	0.23	405	-17.86	153.85	235.1	209.9	25.2
154	04-JAN-2008_07:29	0.49	5	47.16	131.79	288.1	298.5	-10.4
155	04-JAN-2008_07:29	0.26	290	34.87	147.93	264.8	298.5	-33.7
156	04-JAN-2008_07:29	0.21	5	49.42	145.75	279.2	298.5	-19.3
157	29-SEP-2008_15:19	0.34	225	32.59	172.61	237.4	222.6	14.8
158	29-SEP-2008_15:19	0.3	15	31.52	-167.9	211.6	222.6	-11
159	09-DEC-2008_06:23	0.64	95	28.26	-168.83	211.5	224.3	-12.8
160	09-DEC-2008_06:23	0.49	75	31.01	-164.82	207	224.3	-17.3
161	09-DEC-2008_06:23	0.49	35	40.61	-157.91	200.1	224.3	-24.2
162	09-DEC-2008_06:23	0.48	30	12.05	-176.5	215.4	224.3	-8.9
163	09-DEC-2008_06:23	0.41	25	32.08	-164.12	206.4	224.3	-17.9
164	09-DEC-2008_06:23	0.4	140	29.2	-165.59	207.4	224.3	-16.9
165	09-DEC-2008_06:23	0.24	50	19.43	-173.15	213.8	224.3	-10.5
166	18-FEB-2009_21:53	0.4	35	13.46	-174.13	213.1	220.7	-7.6

Continued on next page

Table G.1 – continued from previous page

*P*P*	Event	NSWB	*h* (km)	Lat (°)	Lon (°)	θ (°)	θ_{PP} (°)	$\delta\theta$ (°)
167	18-FEB-2009_21:53	0.36	240	23.55	-167.77	208.4	220.7	-12.3
168	18-FEB-2009_21:53	0.25	205	15.79	-153.56	188.5	220.7	-32.2
169	18-FEB-2009_21:53	0.25	225	28.79	-168.75	211.6	220.7	-9.1
170	18-FEB-2009_21:53	0.25	55	34.05	-161.01	202.5	220.7	-18.2
171	19-MAR-2009_18:17	0.56	90	26.14	-169.53	211.6	218.9	-7.3
172	16-MAY-2009_00:53	0.62	35	13.85	-169.43	207.7	215	-7.3
173	16-MAY-2009_00:53	0.38	95	31.96	-158.84	198.5	215	-16.5
174	16-MAY-2009_00:53	0.33	105	31.6	-176.03	222.7	215	7.7
175	16-MAY-2009_00:53	0.29	65	31.42	-155.7	193.6	215	-21.4
176	16-MAY-2009_00:53	0.26	285	13.29	174.17	226.2	215	11.2
177	16-MAY-2009_00:53	0.24	260	14.63	-159.66	196	215	-19
178	02-NOV-2009_10:47	0.5	100	21.62	-162.98	201.6	215.9	-14.3
179	02-NOV-2009_10:47	0.31	400	-0.94	174.17	221.5	215.9	5.6
180	02-NOV-2009_10:47	0.27	225	6.86	170.38	227.9	215.9	12
181	08-NOV-2009_19:41	0.4	20	51.55	165.86	264	270.2	-6.2
182	05-MAR-2010_16:06	0.23	35	23.14	125.87	277.9	283.3	-5.4
183	05-MAR-2010_16:06	0.21	335	51.47	103.33	311.8	283.3	28.5
184	28-AUG-2000_15:05	0.1	25	38	139.54	274.6	260	14.6
185	25-OCT-2000_09:32	0.17	350	33.47	135.2	275.4	289.4	-14
186	25-OCT-2000_09:32	0.13	120	68.68	129.09	315.1	289.4	25.7
187	25-OCT-2000_09:32	0.12	60	60.26	170.07	277.1	289.4	-12.3
188	13-FEB-2001_19:28	0.11	45	66.17	169.25	294.3	286.9	7.4
189	28-MAY-2001_08:37	0.19	190	5.09	145.67	251.5	256.8	-5.3
190	28-MAY-2001_08:37	0.18	35	1.26	151.86	244.1	256.8	-12.7
191	28-MAY-2001_08:37	0.15	210	11.14	136.55	262.6	256.8	5.8
192	28-MAY-2001_08:37	0.13	140	8.03	149.82	248.8	256.8	-8
193	19-OCT-2001_03:28	0.14	80	63.16	154.68	293.4	255.6	37.8
194	19-OCT-2001_03:28	0.11	265	37.12	138.72	274.7	255.6	19.1
195	15-AUG-2002_05:30	0.13	40	28.12	139.24	268.6	274.7	-6.1
196	15-AUG-2002_05:30	0.12	55	49.16	-169.59	228.5	274.7	-46.2
197	15-AUG-2002_05:30	0.11	190	25.83	156.75	250.5	274.7	-24.2
198	13-SEP-2002_22:28	0.14	200	45.8	132.78	286.2	297.9	-11.7
199	25-MAR-2003_02:53	0.15	25	51.58	165.3	264.6	258.7	5.9
200	25-MAR-2003_02:53	0.14	45	52.41	141.88	285.5	258.7	26.8
201	30-MAR-2003_18:13	0.18	1880	28.55	93.13	308.3	257.5	50.8
202	11-AUG-2003_21:22	0.17	295	71.99	151.69	315	306.1	8.9
203	11-AUG-2003_21:22	0.16	120	34.35	116.63	291.6	306.1	-14.5
204	11-AUG-2003_21:22	0.13	415	43.86	127.05	289.2	306.1	-16.9
205	11-AUG-2003_21:22	0.12	75	56.86	136.2	294.7	306.1	-11.4
206	22-FEB-2004_06:46	0.19	125	50.88	113.79	304.2	295.8	8.4
207	22-FEB-2004_06:46	0.17	85	48.33	-179.14	241.8	295.8	-54
208	23-APR-2004_01:50	0.1	195	41.42	161.95	256.2	281	-24.8
209	11-MAY-2004_08:28	0.16	40	56.39	167.81	270.4	289.9	-19.5
210	11-MAY-2004_08:28	0.14	520	37.82	150.73	264.3	289.9	-25.6
211	11-MAY-2004_08:28	0.13	40	49.39	158.3	268.3	289.9	-21.6
212	11-MAY-2004_08:28	0.1	210	44.53	133.5	284.6	289.9	-5.3

Continued on next page

Table G.1 – continued from previous page

*P*P*	Event	NSWB	*h* (km)	Lat (°)	Lon (°)	θ (°)	θ_{PP} (°)	$\delta\theta$ (°)
213	25-JUN-2004_02:35	0.16	1385	16.62	105.97	292.4	259.5	32.9
214	25-JUN-2004_02:35	0.15	815	29.04	175.6	231.7	259.5	-27.8
215	25-JUN-2004_02:35	0.11	90	59.23	168.29	276	259.5	16.5
216	11-NOV-2004_21:26	0.16	460	14.67	116.9	281.9	262.2	19.7
217	11-NOV-2004_21:26	0.15	490	16.5	170.18	231.8	262.2	-30.4
218	11-NOV-2004_21:26	0.14	125	23.22	152.83	253	262.2	-9.2
219	11-NOV-2004_21:26	0.12	645	47.3	136.43	284.6	262.2	22.4
220	11-NOV-2004_21:26	0.12	1125	0.62	160.98	235.1	262.2	-27.1
221	11-NOV-2004_21:26	0.1	315	17.88	132.3	269.6	262.2	7.4
222	11-NOV-2004_22:49	0.12	235	37.56	137.01	276.5	259.2	17.3
223	26-DEC-2004_04:21	0.19	230	48.74	140.53	282.7	293.3	-10.6
224	26-DEC-2004_04:21	0.17	80	50.6	106.44	309.1	293.3	15.8
225	26-DEC-2004_09:20	0.11	225	32.25	120.56	287.2	309.1	-21.9
226	26-DEC-2004_10:19	0.16	125	36.29	122.97	287.5	298.3	-10.8
227	26-DEC-2004_10:19	0.1	1135	21.81	140.32	264.2	298.3	-34.1
228	27-DEC-2004_09:39	0.17	75	39.26	110.02	299.6	276.8	22.8
229	27-DEC-2004_09:39	0.12	615	45.78	75.28	328.8	276.8	52
230	29-DEC-2004_05:56	0.13	5	58.3	130.43	300.1	294.9	5.2
231	31-DEC-2004_02:24	0.18	325	45.32	152.45	269.2	295.8	-26.6
232	31-DEC-2004_02:24	0.12	360	37.24	142.66	271.3	295.8	-24.5
233	31-DEC-2004_02:24	0.12	70	26.12	117.67	286.5	295.8	-9.3
234	31-DEC-2004_02:24	0.11	105	73.5	133.81	322.3	295.8	26.5
235	26-FEB-2005_12:56	0.18	130	23.79	116.71	286.2	291.6	-5.4
236	26-FEB-2005_12:56	0.11	395	49.46	138.5	285	291.6	-6.6
237	28-MAR-2005_16:09	0.19	140	53.44	104.86	312.1	291.4	20.7
238	28-MAR-2005_18:30	0.15	20	75.02	135.93	325	287.8	37.2
239	28-MAR-2005_18:30	0.1	85	65.16	149.02	300.3	287.8	12.5
240	10-APR-2005_10:29	0.2	45	45.45	139.62	280.4	291.1	-10.7
241	10-APR-2005_10:29	0.16	5	53.91	158.23	274.5	291.1	-16.6
242	10-APR-2005_10:29	0.15	885	32.96	155.05	256.6	291.1	-34.5
243	10-APR-2005_17:24	0.18	290	54.58	141.23	288.5	298.4	-9.9
244	10-APR-2005_17:24	0.13	275	44.67	132.77	285.3	298.4	-13.1
245	10-APR-2005_17:24	0.13	10	56.45	-179.4	257.4	298.4	-41
246	11-APR-2005_06:11	0.12	120	48.46	138.17	284.3	290.5	-6.2
247	16-APR-2005_16:38	0.12	375	49.56	176.06	249.8	293.6	-43.8
248	28-APR-2005_14:07	0.15	515	31.99	136.44	273.4	300.5	-27.1
249	14-MAY-2005_05:05	0.2	405	31.43	129.54	279.1	286.8	-7.7
250	14-MAY-2005_05:05	0.18	50	56.02	168.45	269.1	286.8	-17.7
251	14-MAY-2005_05:05	0.16	190	45.43	159.03	263.1	286.8	-23.7
252	14-MAY-2005_05:05	0.14	0	60.47	173.11	275.3	286.8	-11.5
253	14-MAY-2005_05:05	0.13	1015	15.88	144.15	257.7	286.8	-29.1
254	14-MAY-2005_05:05	0.1	100	58.72	171.12	272.5	286.8	-14.3
255	18-MAY-2005_11:37	0.18	125	22.98	117.77	284.9	301.7	-16.8
256	18-MAY-2005_11:37	0.16	180	26.01	112.46	290.9	301.7	-10.8
257	18-MAY-2005_11:37	0.13	410	39.85	135.15	279.7	301.7	-22
258	18-MAY-2005_11:37	0.11	220	40.92	126.09	287.9	301.7	-13.8

Continued on next page

Table G.1 – continued from previous page

*P*P*	Event	NSWB	h (km)	Lat (°)	Lon (°)	θ (°)	θ_{PP} (°)	$\delta\theta$ (°)
259	17-AUG-2007_03:04	0.16	85	38.63	153.38	262.4	251.9	10.5
260	17-AUG-2007_03:04	0.15	105	42.51	152.93	266.1	251.9	14.2
261	17-AUG-2007_03:04	0.11	505	23.99	172	233.2	251.9	-18.7
262	17-AUG-2007_03:04	0.1	885	15.78	112.7	286.1	251.9	34.2
263	12-SEP-2007_11:10	0.16	70	32.85	107.5	298.3	288.1	10.2
264	13-SEP-2007_03:35	0.2	360	40.46	157.07	260.3	286.9	-26.6
265	13-SEP-2007_16:09	0.18	290	33.72	139.78	271.5	286.5	-15
266	13-SEP-2007_16:09	0.12	345	35.28	154.16	259.1	286.5	-27.4
267	13-SEP-2007_16:09	0.1	415	27.65	142.86	265	286.5	-21.5
268	14-SEP-2007_06:01	0.12	230	34.21	140.13	271.5	284.6	-13.1
269	20-SEP-2007_08:31	0.17	570	34.72	154.16	258.7	287.6	-28.9
270	20-SEP-2007_08:31	0.13	360	50.71	157.27	270.9	287.6	-16.7
271	24-OCT-2007_21:02	0.2	110	60.2	153.94	288.1	282.8	5.3
272	24-OCT-2007_21:02	0.19	255	57.92	119.09	306.7	282.8	23.9
273	24-OCT-2007_21:02	0.18	195	43.49	124.68	290.8	282.8	8
274	24-OCT-2007_21:02	0.17	0	55.09	160.52	274.4	282.8	-8.4
275	24-OCT-2007_21:02	0.13	495	33.81	95.62	308.4	282.8	25.6
276	15-DEC-2007_09:39	0.15	175	13	138.44	261.7	242.9	18.8
277	15-DEC-2007_09:39	0.14	865	25.56	-172	214.6	242.9	-28.3
278	15-DEC-2007_09:39	0.11	705	9.63	169.61	229.7	242.9	-13.2
279	22-JAN-2008_17:14	0.17	40	59.23	127.95	302.7	290.3	12.4
280	22-JAN-2008_17:14	0.15	130	57.02	104.39	315	290.3	24.7
281	13-FEB-2008_19:58	0.2	290	-3.38	157.81	236.7	258.8	-22.1
282	13-FEB-2008_19:58	0.13	1555	19.43	-163.93	202.3	258.8	-56.5
283	20-FEB-2008_08:08	0.14	430	38.05	144.2	270.5	294.7	-24.2
284	20-FEB-2008_08:08	0.12	0	73.14	171.33	317.7	294.7	23
285	20-FEB-2008_08:08	0.1	15	64.18	167.57	289.1	294.7	-5.6
286	25-FEB-2008_08:36	0.16	75	47.51	148.85	274.6	292.1	-17.5
287	25-FEB-2008_18:06	0.15	60	48.89	121.65	297.1	286.3	10.8
288	25-FEB-2008_18:06	0.12	185	55.24	163.16	272.4	286.3	-13.9
289	25-FEB-2008_21:02	0.12	30	54.83	160.98	273.6	279.6	-6
290	25-FEB-2008_21:02	0.11	135	47.02	151.37	271.9	279.6	-7.7
291	15-MAR-2008_14:43	0.14	975	34.06	-178.74	227.7	298.5	-70.8
292	15-MAR-2008_14:43	0.11	1740	30.77	-177.94	224.7	298.5	-73.8
293	29-MAR-2008_17:30	0.17	70	56.21	159.13	277.4	290.5	-13.1
294	29-MAR-2008_17:30	0.14	150	52.69	128.03	295.8	290.5	5.3
295	29-MAR-2008_17:30	0.12	275	47.25	141.85	280.2	290.5	-10.3
296	10-AUG-2008_08:20	0.12	160	50.78	129.48	293	285.9	7.1
297	16-AUG-2009_07:38	0.1	60	58.47	159.93	280.8	288.6	-7.8
298	30-SEP-2009_10:16	0.17	305	52.7	165.09	266.5	288.5	-22
299	30-SEP-2009_10:16	0.16	140	61.3	119.39	310	288.5	21.5
300	30-SEP-2009_10:16	0.15	235	48.84	162.11	264	288.5	-24.5
301	30-SEP-2009_10:16	0.13	330	42.66	166.35	252.7	288.5	-35.8
302	16-OCT-2009_09:52	0.2	240	30.14	106.79	297.6	278.6	19
303	16-OCT-2009_09:52	0.16	885	28.16	156.3	252.3	278.6	-26.3
304	16-OCT-2009_09:52	0.13	20	66.68	167.1	296.6	278.6	18

Continued on next page

Table G.1 – continued from previous page

*P*P*	Event	NSWB	h (km)	Lat (°)	Lon (°)	θ (°)	θ_{PP} (°)	$\delta\theta$ (°)
305	10-NOV-2009_02:48	0.19	150	29.78	121.6	285	292.7	-7.7
306	10-NOV-2009_02:48	0.19	245	35.69	129.01	282.1	292.7	-10.6
307	10-NOV-2009_02:48	0.18	465	39.47	140.65	274.7	292.7	-18
308	10-NOV-2009_02:48	0.18	360	22.3	127.89	275.7	292.7	-17
309	10-NOV-2009_02:48	0.16	140	63.61	124.57	309.9	292.7	17.2
310	26-DEC-2009_08:57	0.2	385	52.13	133.2	291.6	253.3	38.3
311	26-DEC-2009_08:57	0.18	255	36.18	172.29	240.3	253.3	-13
312	26-DEC-2009_08:57	0.17	570	35.61	129.66	281.5	253.3	28.2
313	25-OCT-2000_09:32	0.97	105	52.17	150.75	278.3	289.4	-11.1
314	25-OCT-2000_09:32	0.5	75	56.6	133.15	296.4	289.4	7
315	25-OCT-2000_09:32	0.27	285	43.56	157.82	262.4	289.4	-27
316	25-OCT-2000_09:32	0.25	70	38.96	135.58	278.7	289.4	-10.7
317	13-FEB-2001_19:28	0.5	160	42.29	138.16	279	286.9	-7.9
318	13-FEB-2001_19:28	0.32	55	65.17	122.61	312.9	286.9	26
319	19-OCT-2001_03:28	0.31	135	45.23	144.52	276.1	255.6	20.5
320	27-JUN-2002_05:50	0.56	40	38.14	123.37	288.3	297.9	-9.6
321	27-JUN-2002_05:50	0.5	155	51.9	132.19	292.1	297.9	-5.8
322	27-JUN-2002_05:50	0.46	20	32.96	131.39	278.4	297.9	-19.5
323	27-JUN-2002_05:50	0.46	65	37.05	124.74	286.5	297.9	-11.4
324	27-JUN-2002_05:50	0.38	60	44.65	124.84	291.5	297.9	-6.4
325	27-JUN-2002_05:50	0.24	105	43.63	139.8	278.7	297.9	-19.2
326	27-JUN-2002_05:50	0.21	70	55.18	160.47	274.6	297.9	-23.3
327	27-JUN-2002_05:50	0.21	10	20.32	125	277.3	297.9	-20.6
328	15-AUG-2002_05:30	0.23	155	10.48	145.36	254.1	274.7	-20.6
329	13-SEP-2002_22:28	0.21	240	51.14	137.29	287.6	297.9	-10.3
330	13-SEP-2002_22:28	0.21	180	25.48	115.21	288.3	297.9	-9.6
331	22-FEB-2004_06:46	0.5	25	58.49	152.35	286.2	295.8	-9.6
332	22-FEB-2004_06:46	0.29	135	39.4	138.05	276.9	295.8	-18.9
333	22-FEB-2004_06:46	0.28	5	53.42	136.44	290.6	295.8	-5.2
334	23-APR-2004_01:50	0.71	10	47.36	151.32	272.3	281	-8.7
335	23-APR-2004_01:50	0.57	110	36.92	158.97	255.5	281	-25.5
336	23-APR-2004_01:50	0.49	270	34.52	153.92	258.8	281	-22.2
337	23-APR-2004_01:50	0.37	115	52.47	166.07	265.2	281	-15.8
338	23-APR-2004_01:50	0.26	290	14.65	139.8	261.2	281	-19.8
339	23-APR-2004_01:50	0.25	1150	18.68	96.24	301.8	281	20.8
340	23-APR-2004_01:50	0.22	165	34.48	145.17	267.1	281	-13.9
341	23-APR-2004_01:50	0.22	355	41.55	166.1	251.9	281	-29.1
342	11-MAY-2004_08:28	0.75	90	38.26	132.76	280.6	289.9	-9.3
343	11-MAY-2004_08:28	0.54	120	39.32	131.35	282.5	289.9	-7.4
344	11-MAY-2004_08:28	0.23	140	40.93	130.41	284.4	289.9	-5.5
345	25-JUN-2004_02:35	0.15	310	24.67	121.59	282.4	259.5	22.9
346	25-JUN-2004_02:35	0.86	140	17.58	156.92	246.1	259.5	-13.4
347	25-JUN-2004_02:35	0.83	110	17.62	157.03	246	259.5	-13.5
348	25-JUN-2004_02:35	0.67	400	28.46	132.2	275.1	259.5	15.6
349	25-JUN-2004_02:35	0.47	440	6.47	157.94	240.3	259.5	-19.2
350	25-JUN-2004_02:35	0.21	35	13.33	130.3	269.3	259.5	9.8

Continued on next page

Table G.1 – continued from previous page

*P*P*	Event	NSWB	h (km)	Lat (°)	Lon (°)	θ (°)	θ_{PP} (°)	$\delta\theta$ (°)
351	11-NOV-2004_21:26	0.31	50	33.18	155.7	256.1	262.2	-6.1
352	11-NOV-2004_22:49	0.24	330	14.05	159.99	241.4	259.2	-17.8
353	11-NOV-2004_22:49	0.2	205	15.74	151.6	250.5	259.2	-8.7
354	26-DEC-2004_04:21	0.48	5	45	109.54	303.3	293.3	10
355	26-DEC-2004_04:21	0.31	85	51.43	113.81	304.6	293.3	11.3
356	26-DEC-2004_04:21	0.22	75	38.97	105.22	303.2	293.3	9.9
357	26-DEC-2004_09:20	0.69	25	56.64	124.08	302.3	309.1	-6.8
358	26-DEC-2004_09:20	0.37	10	45.96	110.21	303.4	309.1	-5.7
359	26-DEC-2004_10:19	0.26	80	57.33	145.93	288.8	298.3	-9.5
360	27-DEC-2004_09:39	0.27	30	64.65	154.61	296.6	276.8	19.8
361	27-DEC-2004_09:39	0.25	60	44.5	120.8	294.5	276.8	17.7
362	27-DEC-2004_09:39	0.24	125	60.04	154.56	287.4	276.8	10.6
363	26-FEB-2005_12:56	0.62	5	53.72	144.19	285.3	291.6	-6.3
364	26-FEB-2005_12:56	0.38	50	49.98	138.78	285.3	291.6	-6.3
365	26-FEB-2005_12:56	0.28	170	28.02	127.6	278.9	291.6	-12.7
366	26-FEB-2005_12:56	0.27	135	46.35	135.76	284.3	291.6	-7.3
367	28-MAR-2005_16:09	0.54	210	37.46	133.9	279.1	291.4	-12.3
368	28-MAR-2005_16:09	0.25	160	53.07	156.08	275.1	291.4	-16.3
369	28-MAR-2005_16:09	0.22	15	61.85	166.58	283.5	291.4	-7.9
370	28-MAR-2005_18:30	0.68	15	51.38	117.51	302	287.8	14.2
371	28-MAR-2005_18:30	0.52	40	55.49	115.56	306.7	287.8	18.9
372	28-MAR-2005_18:30	0.26	30	60.91	127.95	304.7	287.8	16.9
373	10-APR-2005_10:29	0.87	220	37.76	139.24	274.7	291.1	-16.4
374	10-APR-2005_10:29	0.54	225	44.94	134.65	284	291.1	-7.1
375	10-APR-2005_10:29	0.52	135	49.02	143.39	280.7	291.1	-10.4
376	10-APR-2005_10:29	0.47	95	53.03	154.94	276	291.1	-15.1
377	10-APR-2005_10:29	0.36	105	46.72	144.99	277.1	291.1	-14
378	10-APR-2005_10:29	0.31	75	60.58	164.32	282	291.1	-9.1
379	10-APR-2005_10:29	0.28	380	34.62	137.61	274	291.1	-17.1
380	10-APR-2005_10:29	0.27	290	40.66	135.61	279.9	291.1	-11.2
381	10-APR-2005_10:29	0.23	650	29.84	142.63	266.5	291.1	-24.6
382	10-APR-2005_17:24	0.77	30	49.91	131.81	290.5	298.4	-7.9
383	10-APR-2005_17:24	0.54	350	13.2	131.77	267.9	298.4	-30.5
384	10-APR-2005_17:24	0.42	250	43.43	138.53	279.6	298.4	-18.8
385	10-APR-2005_17:24	0.36	90	49.08	176.62	248.4	298.4	-50
386	10-APR-2005_17:24	0.3	230	43.19	138.89	279.1	298.4	-19.3
387	10-APR-2005_17:24	0.24	90	41.03	121.79	291.4	298.4	-7
388	10-APR-2005_17:24	0.23	180	47.4	128	291.2	298.4	-7.2
389	10-APR-2005_17:24	0.22	155	60.16	161.67	282.9	298.4	-15.5
390	10-APR-2005_17:24	0.21	305	47.73	153.11	271.1	298.4	-27.3
391	10-APR-2005_17:24	0.21	265	29.5	142.51	266.4	298.4	-32
392	16-APR-2005_16:38	0.54	0	57.82	150.35	286.5	293.6	-7.1
393	16-APR-2005_16:38	0.49	90	46.93	133.48	286.6	293.6	-7
394	16-APR-2005_16:38	0.22	30	56.29	165.78	272	293.6	-21.6
395	28-APR-2005_14:07	0.4	105	48.03	147.84	276	300.5	-24.5
396	28-APR-2005_14:07	0.23	250	46.23	149.55	272.7	300.5	-27.8

Continued on next page

Table G.1 – continued from previous page

*P*P*	Event	NSWB	h (km)	Lat (°)	Lon (°)	θ (°)	θ_{PP} (°)	$\delta\theta$ (°)
397	14-MAY-2005_05:05	0.61	25	36.9	118.01	291.9	286.8	5.1
398	14-MAY-2005_05:05	0.43	225	35.79	134.13	277.8	286.8	-9
399	18-MAY-2005_11:37	0.55	5	38.45	114.64	295.5	301.7	-6.2
400	18-MAY-2005_11:37	0.42	110	32.19	121.71	286.2	301.7	-15.5
401	18-MAY-2005_11:37	0.26	10	23.92	115.28	287.5	301.7	-14.2
402	12-SEP-2007_11:10	0.79	50	29.21	133.81	274.1	288.1	-14
403	12-SEP-2007_11:10	0.64	25	33.29	111.93	294.9	288.1	6.8
404	12-SEP-2007_11:10	0.41	60	50.58	168.19	260.2	288.1	-27.9
405	12-SEP-2007_11:10	0.33	5	46.26	146.47	275.4	288.1	-12.7
406	12-SEP-2007_11:10	0.26	75	51.55	166.36	263.5	288.1	-24.6
407	13-SEP-2007_03:35	0.22	10	50.11	158.53	269	286.9	-17.9
408	13-SEP-2007_16:09	0.59	65	33.48	130.71	279.3	286.5	-7.2
409	13-SEP-2007_16:09	0.5	65	47.56	162.05	262.5	286.5	-24
410	13-SEP-2007_16:09	0.34	315	36.18	138.79	274	286.5	-12.5
411	13-SEP-2007_16:09	0.29	15	63.9	158.71	292.9	286.5	6.4
412	14-SEP-2007_06:01	0.38	75	48.65	147.79	276.7	284.6	-7.9
413	14-SEP-2007_06:01	0.22	105	22.65	129.22	274.7	284.6	-9.9
414	20-SEP-2007_08:31	0.76	1625	20.99	168.34	235.8	287.6	-51.8
415	20-SEP-2007_08:31	0.51	95	52.22	150.09	278.9	287.6	-8.7
416	20-SEP-2007_08:31	0.4	175	44.88	145.08	275.3	287.6	-12.3
417	20-SEP-2007_08:31	0.35	190	47.52	144.96	277.9	287.6	-9.7
418	20-SEP-2007_08:31	0.34	120	42.42	120.15	293.6	287.6	6
419	24-OCT-2007_21:02	0.23	195	51.69	137.1	288.3	282.8	5.5
420	15-DEC-2007_09:39	0.32	180	6.53	147.16	250.7	242.9	7.8
421	15-DEC-2007_09:39	0.27	75	20.22	145.85	258.2	242.9	15.3
422	15-DEC-2007_09:39	0.24	160	8.03	144.02	254.3	242.9	11.4
423	15-DEC-2007_09:39	0.23	320	8.02	148.56	250	242.9	7.1
424	20-FEB-2008_08:08	0.51	185	37.81	127.98	284.3	294.7	-10.4
425	20-FEB-2008_08:08	0.32	35	54.7	141.99	288.1	294.7	-6.6
426	25-FEB-2008_08:36	0.25	0	57.91	157.99	281.2	292.1	-10.9
427	25-FEB-2008_18:06	0.92	45	37.99	133.38	279.9	286.3	-6.4
428	25-FEB-2008_18:06	0.45	35	47.35	126.09	292.6	286.3	6.3
429	25-FEB-2008_18:06	0.42	35	49.71	144.78	280.3	286.3	-6
430	25-FEB-2008_18:06	0.25	165	41.63	140.83	276.2	286.3	-10.1
431	25-FEB-2008_18:06	0.22	245	32.72	143.37	267.6	286.3	-18.7
432	25-FEB-2008_21:02	0.41	25	43.02	120.66	293.6	279.6	14
433	25-FEB-2008_21:02	0.28	35	49.22	133.9	288.3	279.6	8.7
434	25-FEB-2008_21:02	0.28	150	42.41	144.45	273.7	279.6	-5.9
435	25-FEB-2008_21:02	0.27	35	56.78	148.69	286.1	279.6	6.5
436	25-FEB-2008_21:02	0.26	85	52.76	163.6	268	279.6	-11.6
437	29-MAR-2008_17:30	0.48	10	56.46	132.9	296.4	290.5	5.9
438	29-MAR-2008_17:30	0.38	70	43.6	131.6	285.4	290.5	-5.1
439	27-JUN-2008_11:40	1.11	35	45.57	113.39	300.8	286.1	14.7
440	27-JUN-2008_11:40	0.44	175	42.14	118.5	294.7	286.1	8.6
441	27-JUN-2008_11:40	0.44	410	15.44	120.1	279.4	286.1	-6.7
442	27-JUN-2008_11:40	0.23	460	46.6	154.64	268.5	286.1	-17.6

Continued on next page

Table G.1 – continued from previous page

*P*P*	Event	NSWB	h (km)	Lat (°)	Lon (°)	θ (°)	θ_{PP} (°)	$\delta\theta$ (°)
443	27-JUN-2008_11:40	0.22	115	48.06	127.52	292.1	286.1	6
444	27-JUN-2008_11:40	0.21	165	48.92	124.97	294.7	286.1	8.6
445	27-JUN-2008_11:40	0.21	190	49.26	118.31	299.8	286.1	13.7
446	28-JUN-2008_12:54	0.5	320	28.75	130.79	276.5	291.4	-14.9
447	28-JUN-2008_12:54	0.25	100	37.59	108.75	299.7	291.4	8.3
448	28-JUN-2008_12:54	0.2	65	66.6	144.07	305.3	291.4	13.9
449	10-AUG-2008_08:20	0.66	90	51.67	111.6	306.3	285.9	20.4
450	10-AUG-2008_08:20	0.56	165	42.81	118.54	295.1	285.9	9.2
451	10-AUG-2008_08:20	0.22	185	56.02	121.27	303.5	285.9	17.6
452	10-AUG-2008_08:20	0.2	50	43.86	115.64	298	285.9	12.1
453	16-AUG-2009_07:38	0.43	180	41.63	144.85	272.7	288.6	-15.9
454	16-AUG-2009_07:38	0.37	170	47.91	154.67	269.9	288.6	-18.7
455	16-AUG-2009_07:38	0.29	100	57.63	170.12	270.9	288.6	-17.7
456	16-AUG-2009_07:38	0.25	0	56.94	-179.54	258.8	288.6	-29.8
457	16-AUG-2009_07:38	0.22	245	53.73	165.56	267.7	288.6	-20.9
458	16-AUG-2009_07:38	0.22	70	57.65	164.25	275.9	288.6	-12.7
459	30-SEP-2009_10:16	0.64	15	45.34	141.55	278.7	288.5	-9.8
460	16-OCT-2009_09:52	0.94	210	41.65	108.26	302.3	278.6	23.7
461	16-OCT-2009_09:52	0.7	5	53.69	131.46	294.4	278.6	15.8
462	16-OCT-2009_09:52	0.36	300	33.18	152.46	259.3	278.6	-19.3
463	16-OCT-2009_09:52	0.35	320	42.72	163.13	256.2	278.6	-22.4
464	16-OCT-2009_09:52	0.29	455	41.56	112.09	299.3	278.6	20.7
465	16-OCT-2009_09:52	0.25	10	65.08	150.38	299.5	278.6	20.9
466	16-OCT-2009_09:52	0.24	175	63.41	143.45	299.8	278.6	21.2
467	26-DEC-2009_08:57	0.79	10	24.37	135.55	269.9	253.3	16.6
468	26-DEC-2009_08:57	0.32	10	44.8	176.88	242.6	253.3	-10.7
469	26-DEC-2009_08:57	0.23	790	16.61	118.66	281.2	253.3	27.9